Cardiff
Catalysis Institute

Sefydliad Catalysis
Caerdydd

Towards the continuous production of supported metal nanoparticles and their application in hydrogenation reactions

Stefano Cattaneo

November 2018

Thesis submitted in accordance with the requirements of Cardiff University for the degree of Doctor of Philosophy

DECLARATION

This work has not been submitted in substance for any other degree or award at this or any other university or place of learning, nor is being submitted concurrently in candidature for any degree or other award.

Signed …… (candidate) Date ……

STATEMENT 1

This thesis is being submitted in partial fulfilment of the requirements for the degree of PhD.

Signed ……(candidate) Date ……

STATEMENT 2

This thesis is the result of my own independent work/investigation, except where otherwise stated, and the thesis has not been edited by a third party beyond what is permitted by Cardiff University's Policy on the Use of Third Party Editors by Research Degree Students. Other sources are acknowledged by explicit references. The views expressed are my own.

Signed …….. (candidate) Date ……

STATEMENT 3

I hereby give consent for my thesis, if accepted, to be available online in the University's Open Access repository and for inter-library loan, and for the title and summary to be made available to outside organisations.

Signed……. (candidate) Date ……

STATEMENT 4: PREVIOUSLY APPROVED BAR ON ACCESS

I hereby give consent for my thesis, if accepted, to be available online in the University's Open Access repository and for inter-library loans **after expiry of a bar on access previously approved by the Academic Standards & Quality Committee.**

Signed……(candidate) Date ……

"I wouldn't be the human I am
Without the friends that let me fly and help me land"

Acknowledgments

First and foremost, I would like to thank Professor Graham Hutchings for giving me the opportunity to study and work in such a prestigious and renowned University. His guidance and support during the past three years have been a guiding light along the tortuous pathway that was my PhD.

I would not have come such a long way without the constant supervision of Dr. Nikolaos Dimitratos and Dr. Meenakshisundaram Sankar; with their experience and passion, they provided me with moral and scientific support and helped keep me on track from day one until my very last day in Cardiff. I'm particularly grateful to my post-doctoral supervisor Simon Freakley for his constant presence, invaluable advice and everyday help; an additional thank for all the free-time he spent carefully correcting and proofreading this thesis, without his help it would not probably make any sense.

I would like to thank all the scientific personnel at Cardiff University, in particular Dr. Qian He and Dr. Thomas Davies for sharing all their knowledge in electron microscopy with me and for their assistance with SEM and TEM analysis and Dr. David Morgan for all the help in the interpretation of XPS data. A special thanks to Professor Chris Kiely and Sultan Althahban from Lehigh University for their incredible work on STEM and their invaluable inputs and stimulating discussions. I would also like to acknowledge Professor Asterios Gavriilidis and his research group at University College London for the long-lasting and fruitful collaboration that resulted in the publication of several collaborative scientific journal articles.

A special thanks to all the students, PhDs and post-docs of the Cardiff Catalysis Institute, because they made me feel welcome when I first arrived in Cardiff and provided me with a friendly and enjoyable work environment. Among them, I am particularly grateful to the MaxNet group, which I shared most of my ups and downs during my course of study. A big thank you also to Nikos' and Ceri's group for all the cheerful lunch-brakes and nights out. Finally, a special thanks to Alex, enthusiast student I had the pleasure to work with and the person who is going to take over my project; the best of luck for your PhD, I wish you it can be as rewarding as it has been for me.

Three years can be a very long time, especially if you are in another country and far away from your family and friends. Luckily, I had the fortune to meet a bunch of good people that made me feel like I never left home. Starting with Tom Tatchell, exceptional flatmate and landlord but friend before all; a big thank you for helping me to become familiar with

British customs and traditions and for sparking my passion for running. A place of honor in this list goes to Simon Dawson, the best labmate I could have ever asked for. Adventuring companion in most of the best memories I have inside and outside the Cardiff University walls, thank you for putting up with me during all these three years of PhD. A huge thanks to my second family in Wales, the Cardiff University Volleyball Team, and particularly to Georgie, Lucy, Morgan and Phil. I will never forget all the great moments we shared together. A special thanks to Amber, ginger earthquake, for making this last year so special.

Finally, I would like to thank all my friends back at home, because although we didn't spend much time together in the last three years, they made me feel like I'd never left home.

To conclude, I would like to quote a passage from my favorite movie: "True happiness can only be achieved through sacrifice, like the sacrifice our parents have made for us to be here today". To my parents, my sisters and all my family, for their unconditional love and support throughout this journey of mine: thank you.

Abstract

The research carried out in this thesis describes the synthesis and study of mono- and bi-metallic Au-Pd catalysts and their application in catalytic reactions, namely the nitrophenol reduction reaction and the selective hydrogenation of cinnamaldehyde.

In the first part, an innovative setup was assembled for the production of supported monometallic Au and Pd and bimetallic AuPd nanoparticles in a continuous fashion. The millifluidic reactor was firstly optimised for the production of Au colloid having a smaller mean particle size and size distribution compared to the batch benchmark method. During this procedure, several operational parameters, such as reaction conditions, solution residence time and mixing, were studied. A stream of a suspended solution of the support, namely TiO_2, was then integrated in the metal colloid stream in order to produce the whole supported metal nanoparticle catalyst in continuous mode. Moreover, different monometallic Au and Pd and bimetallic AuPd based catalysts were synthesised to demonstrate the applicability of the apparatus for the synthesis of various supported metal nanoparticles catalysts. Interestingly, no size-dependent alloy composition was observed during the synthesis of bimetallic AuPd catalysts in continuous, most likely due to a very fast deposition of the nanoparticles on the support surface that inhibits the Oswald ripening process responsible for metal rearrangements over time. The continuous prepared catalysts were finally tested in the model reaction of reduction of 4-nitrophenol to 4-aminophenol and showed consistently higher activity compared to that of the corresponding batch produced materials due to smaller mean nanoparticle size and uniform alloy composition.

In the second section of this thesis, the relation between metal particle size and catalytic activity was studied in the 4-nitrophenol reduction to 4-aminophenol using Au catalysts with different particle size. Despite the catalytic activity being ascribed indiscriminately to surface metal atoms by previous results, the tests carried out on Au/TiO_2 catalysts having mean particle size ranging from 4 nm to 30 nm showed a different behaviour. In order to isolate the active sites directly involved in the reaction, a mathematical model was applied: the Au nanoparticles were approximated to perfect hemi-icosahedrons and the number of Au atoms in vertex, edge, periphery and face positions were calculated from geometrical considerations. The rate of conversion of 4-nitrophenol was found to increase linearly with the number of peripheral and edge Au atoms in the catalyst.

Finally, in the third part, bimetallic AuPd-based catalysts were employed in the selective catalytic hydrogenation of cinnamaldehyde. Several parameters were varied in

order to observe changes in activity and selectivity, such as stirring speed, catalyst amount, hydrogen pressure, reaction temperature, solvent and support. After initial optimisation of the reaction conditions, such as stirring speed, catalyst amount, hydrogen pressure and reaction temperature, the effect of metal composition was studied. It was observed that a maximum in activity was reached with a Au : Pd relative molar composition of 50 : 50, while high selectivity towards the hydrogenation of the vinyl group was observed increasing the Pd concentration. The enhanced activity was attributed to a combination of ligand and ensemble effect caused by formation of bimetallic alloy, while the higher selectivity of Pd-rich catalysts was attributed to the presence of a Pd surface that favoured η^4 adsorption of the substrate and therefore the hydrogenation of the C=C bond. Deactivation phenomena caused by metal leaching and particle sintering was addressed by treating the catalysts at high temperature. In addition to a higher stability, the catalysts showed an enhanced selectivity towards the hydrogenation of the vinyl bond, attributed to the formation of Pd surface segregation during the high temperature oxidation step.

List of publications

1. N. Al-Rifai, F. Galvanin, M. Morad, E. Cao, S. Cattaneo, M. Sankar, V. Dua, G. J. Hutchings and A. Gavriilidis, Hydrodynamic effects on three phase micro-packed bed reactor performance - Gold-palladium catalysed benzyl alcohol oxidation. *Chemical Engineering Science*, **2016**, 149, 129-142.

2. N. Al-Rifai, P. J. Miedziak, M. Morad, M. Sankar, C. Waldron, S. Cattaneo, E. Cao, S. Pattisson, D. Morgan, D. Bethell, G. J. Hutchings and A. Gavriilidis, Deactivation Behavior of Supported Gold Palladium Nanoalloy Catalysts during the Selective Oxidation of Benzyl Alcohol in a Micropacked Bed Reactor. *Industrial and Engineering Chemistry Research*, **2017**, 54 (45), 12984-12993.

3. C. Waldron, E. Cao, S. Cattaneo, G. L. Brett, P. J. Miedziak, G. Wu, M. Sankar, G. J. Hutchings and A. Gavriilidis, Three step synthesis of benzylacetone and 4-(4-methoxyphenyl)butan-2-one in flow using micropacked bed reactors. *Chemical Engineering Journal*, **2018**, In Press, https://doi.org/10.1016/j.cej.2018.09.137

4. F. Galvanin, M. Sankar, S. Cattaneo, D. Bethell, V. Dua, G. J. Hutchings and A. Gavriilidis, On the development of kinetic models for solvent-free benzyl alcohol oxidation over a gold-palladium catalyst. *Chemical Engineering Journal*, **2018**, 342, 196-210.

5. S. Cattaneo, S. J. Freakley, D. J. Morgan, M. Sankar, N. Dimitratos and G. J. Hutchings, Cinnamaldehyde hydrogenation using Au-Pd catalysts prepared by sol immobilisation. *Catalysis Science & Technology*, **2018**, 8 (6), 1677-1685.

6. S. Cattaneo, S. Althahban, S. J. Freakley, M. Sankar, T. Davies, Q. He, N. Dimitratos, C. Kiely and G. J. Hutchings, Synthesis of Highly Uniform and Composition-Controlled Gold-Palladium Supported Nanoparticles in Continuous Flow. *Nanoscale*, **2019**, 11, 8247-8259.

Glossary

Term	Definition
2-NPH	2-nitrophenol
3-NPH	3-nitrophenol
4-APH	4-aminophenol
4-NAL	4-nitroaniline
4-NBA	4-nitrobenzyl alcohol
4-NPH	4-nitrophenol
4-NTL	4-nitrotoluene
A	Pre-exponential factor in the Arrhenius equation
ATR-FTIR	Attenuated total reflectance Fourier transform infrared spectroscopy
C_i	Concentration of the species “i”
CAL	Cinnamaldehyde
COH	Cinnamyl alcohol
DLS	Dynamic light scattering
DRIFT	Diffuse-reflectance Fourier transform infrared spectroscopy
E°	Standard electrode potential (V)
E_a	Activation energy
HCAL	Hydrocinnamaldehyde
HCOH	Hydrocinnamyl alcohol
IEP	Isoelectric point
k_i	Constant of the reaction “i”
L	Tubing diameter
Me	Metal
MP-AES	Microwave plasma atomic emission spectroscopy
Mw	Molecular weight
N_i	Number of moles of the species “i”
NBZ	Nitrobenzene
NPs	Nanoparticles
PPR	Phenyl propane
PVA	Poly(vinylalcohol)
PVP	Poly(vinylpyrrolydone)

PZC	Point of zero charge
R	Universal gas constant
Re	Reynolds number
S_i	Selectivity of the species “i”
SEM	Scanning electron microscopy
SMSI	Strong metal-support interaction
t	Time
T	Temperature
TEM	Transmission electron microscopy
TOF	Turnover frequency
u	Mean fluid velocity
UV-Vis	Ultraviolet-Visible spectroscopy
v	Kinematic viscosity
X	Conversion
XPS	X-ray photoelectron spectroscopy
XRD	Powder X-ray diffraction

Table of contents

Chapter 1

Introduction

1.1. Catalysis background

Society's development in the last 150 years has been possible, in part, thanks to the advancement of the chemistry industry. New and innovative materials have led the technological revolution in health, fuels, food production and disinfection; central to this is the field of catalysis. An example is the extensive work that resulted in Karl Ziegler and Giulio Natta being awarded the Nobel prize in Chemistry in 1963: the so-called "Ziegler-Natta catalysts" have completely revolutionised the polymer industry and the amount of plastic produced from these catalysts accounts for the largest volume commodity chemicals in the world[1].

The word "catalysis" was first used to describe the field in 1835 when Jöns Jacob Berzelius defined the "Catalytic Force" as "the property that simple and compound bodies, soluble and insoluble, exercising on other bodies an action very different from chemical affinity"[2]. Moreover, Berzelius observed that "the body effecting the changes does not take part in the reaction and remains unaltered through the reaction". In other words, a catalyst is a substance that increases the reaction rate without being consumed, and thus can be reused multiple times. Nowadays, almost 200 years after the observation of the catalytic force, catalysis is deeply integrated into our everyday lives, and over 90 % of all chemical industrial processes employ catalysts[3].

Catalysts decrease the activation energy of reactions, which effectively means that reactions can proceed either in milder conditions or shorter periods of time. They work by providing an alternative pathway involving transition states with lower activation energy (Figure 1.1). Only the kinetics of the process is affected, while the thermodynamics remain unaltered, as dictated by the second law of thermodynamics.

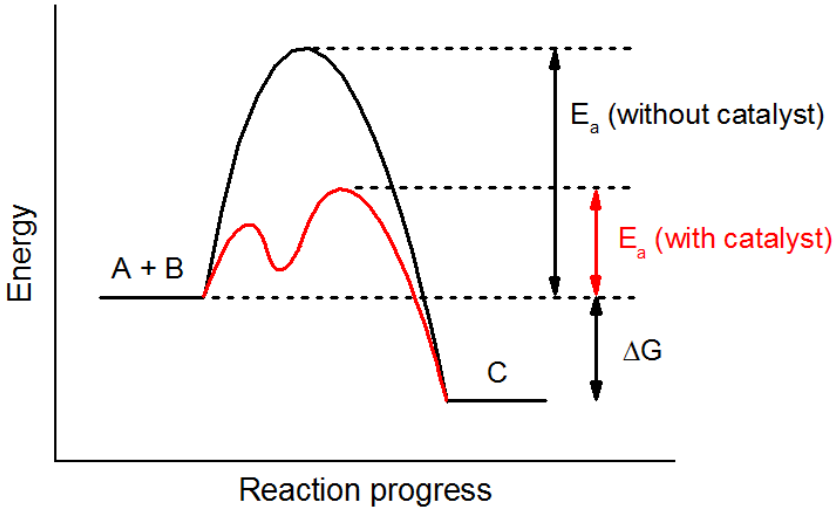

Figure 1.1: Potential energy diagram of an un-catlaysed and catalysed chemical reaction. The black line represent the uncatalysed reaction pathway, while the red line the catalysed reaction with lower activation energy (E_a).

Catalysts can be generally divided into two main groups depending on their chemical phase: if both catalyst and reagents are in the same phase, the catalysis is considered homogeneous, otherwise, when the reactants are in a different phase to the catalyst the system is called heterogeneous.

Homogeneous catalysts are usually coordination complexes composed by a metal centre bonded to organic ligands through a coordinate covalent bond. The nature and the oxidation state of the metal and the electronic properties of the ligands dominate the chemistry of such complexes. Despite this, homogeneous catalysts are often not economically viable at large scale mainly because of recycling/separation problems and as a result, they represent only 20 % of the total catalytic industrial processes[4]. Hydroformylation of olefins[5], acetic acid synthesis[6] and coupling reactions[7] are examples of industrial reactions that make use of homogeneous catalysts.

Heterogeneous catalysts are usually solid compounds that can be used either in gas or liquid phase reactions. Compared to homogeneous catalysts, they display several advantages, such as cheaper and easier recovery from the reaction medium and a higher thermal stability. They find applications in numerous industrial processes such as the Haber-Bosh process (synthesis of ammonia)[8], the catalytic reforming of crude oil and the Fischer-Tropsch process for the synthesis of hydrocarbons from syngas[9]. However, the complexity of the surface chemistry involved, and the challenge to attain a homogeneous population of catalytic sites, makes these catalysts generally less active and selective. The adsorption of reactants on the active sites and the consequent desorption of the products is often the rate-

limiting step, due to the low availability of active sites on the catalyst surface. For this reason, the catalyst surface area is a critical parameter since it determines the availability and population of catalytic sites.

Limitations in active site availability can be overcome by using supported metallic nanoparticles bonded on high surface area materials, usually metal oxides[10–12]. Metal nanoparticles are defined as particles with nanometre size range, typically composed by a single metal or a combination of two or more metals (often referred to as alloys if a metallic bond exists among them). Bulk materials possess chemical and physical properties that are independent of their size; however, as the dimensions of these materials decreases to the nano-scale, size-dependent properties begin to dominate[13]. This behaviour is related to different phenomena, such as a drastic increase of the surface area to volume ratio and quantum size effects[14].

For a spherical particle larger than a micron in diameter, the percentage of atoms at the surface is negligible compared to the atoms in a bulk environment; for example, in a Au sphere of 1 μm in diameter, the bulk atoms are 12 orders of magnitude more abundant than the surface atoms, while for a 3 nm sphere the ratio is about 1:1. The chemical and physical properties are therefore dominated by the large surface area of the material and often the properties of nanoparticles differ significantly from the properties of the bulk material. A clear example of this phenomena is the size dependency of the melting point (Figure 1.2); the energy required to break the strong metal-metal bonds decreases drastically in the nanometre range due to the relative abundance of low-coordination metal atoms compared to the higher-coordination ones[15].

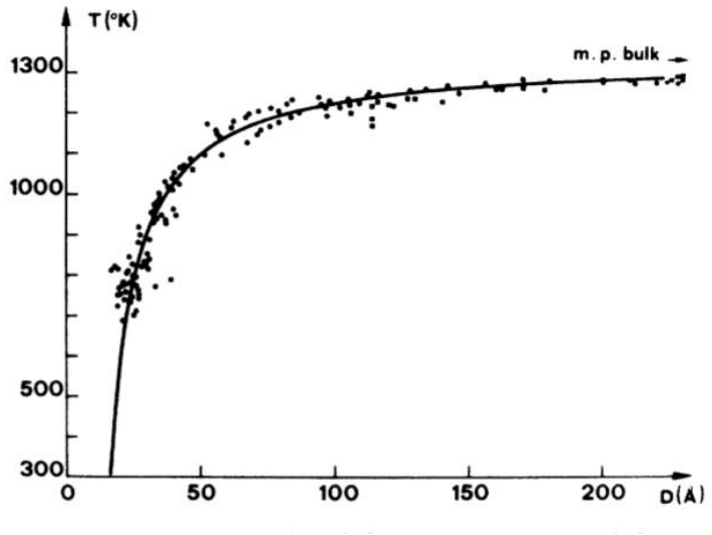

Figure 1.2: Change in melting point of gold with the decrease in nanoparticles dimension. Reprinted with permission from J-P Borel et al. Physical Review A, 1976, 2287-2298.

Quantum size effects are deviations in electronic and optical properties when the diameter of a material approaches the nanometre scale. At these small dimensions, the conduction and valence bands of metals and semiconductors assume discrete energy levels and, as a consequence, the band gap of the material change (Figure 1.3)[16]. An example of quantum size effect is the localised surface plasmon (LSP). LSP are coherent delocalised electron oscillations present at the surface of small nanomaterials and they greatly depend on the nature of the material and the particle size and shape[17].

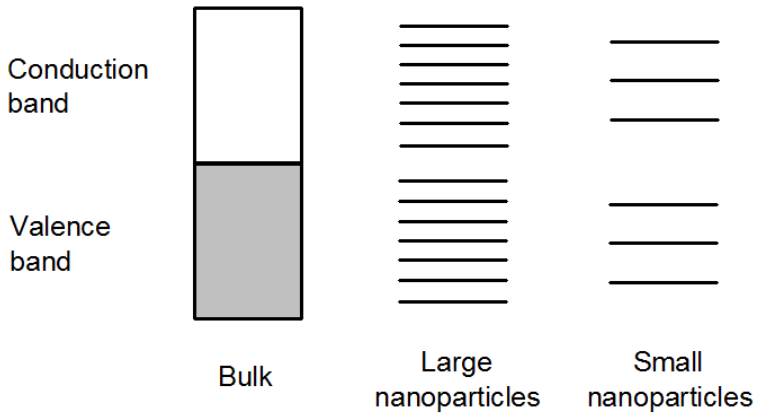

Figure 1.3: The increase in a semi-conductor bandgap with the decrease in dimension. In sufficiently small nanoparticles, the energy levels become discrete.

1.2. Noble metal catalysis

1.2.1. Catalysis by gold

In the collective imagination, gold is probably the most commonly thought of example of noble metal and it is appreciated for its resistance to corrosion and tarnishing in bulk form[18]. It has been used as a precious metal for jewellery, coins and other forms of art since early civilisations began, and still nowadays around 50 % of the gold demand comes from the jewellery sector, with the remaining half spread in investments and industrial applications[19]. Good thermal and electrical conductivity, malleability, ductility and biocompatibility allowed gold to be used in several sectors, such as medicine, electronics and astrophysics[20].

A particular and maybe counterintuitive sector of application is chemistry; although inert when present in bulk form, gold presents unique catalytic properties when finely dispersed. This incredible breakthrough was made in 1973 by Bond *et al.*, where it was demonstrated that tetrachloroauric acid impregnated onto metal oxides was very active for the hydrogenation and isomerisation of olefins[21]. More than 10 years later, Hutchings and Haruta disclosed the peculiar activity of this metal for ethylene hydrochlorination[22] and CO oxidation[23], and since then the research into gold as catalyst increased constantly, as demonstrated by the numerous reviews on this topic[24–27]. Milestones in this field were the discoveries made by Haruta, who showed that gold supported on titanium dioxide could be used in the oxidation of propene to propene oxide[28], and by Prati and Rossi, who demonstrated high activity and selectivity in ethylene glycol and 1,2-propandiol oxidation using gold on carbon catalysts[29]. Nowadays gold is widely studied in many organic reactions, including the hydrogenation of alkenes[30] and α,β-unsaturated aldehydes[31], oxidation of benzyl alcohol and glycerol[32], the water gas shift reaction[33] and the already cited CO oxidation[34] and acetylene hydrochlorination[35].

Gold has also been used in combination with other noble or non-noble metal such as palladium[36], platinum[37], silver[38] and copper[39] to create nano-alloys with better activity, selectivity and stability[40–42]. Gold-palladium catalysts, in particular, have attracted much attention in the last years and will be discussed later in Section 1.2.3.

1.2.2. Catalysis by palladium

Palladium has a far older history than gold as a catalyst, with the first study dating back to the nineteenth century. With his pioneering work, the Scottish chemist Thomas Graham reported the outstanding ability of palladium to absorb hydrogen compared to any other metal, followed by numerous studies on reactions catalysed by palladium black[43,44]. Since then, palladium has been largely used in heterogeneous and homogeneous catalysis in an increasing number of reactions, including hydrocarbon hydrogenations[45], selective alcohol oxidations[46] and hydrogenolysis of carbon-halogen bonds[46]. More than half of the palladium supply, however, finds application nowadays inside catalytic converters, where, along with other precious metal such as platinum and rhodium, it converts harmful gasses from vehicle exhaust into less toxic compounds[47].

Another major application of palladium catalysts, from both an industrial and academic point of view, is the recently developed cross coupling reaction, where two hydrocarbon fragments are coupled together by formation of a new carbon-carbon bond (Figure 1.4)[48]. In general, cross coupling reactions, can be divided in two categories depending on the nature of the two fragments: we talk about heterocouplings if the two fragments have different nature, while homocouplings if the fragments are identical. The development of palladium containing catalysts for such reactions won Heck, Negishi and Suzuki the Nobel prize in chemistry in 2010[49].

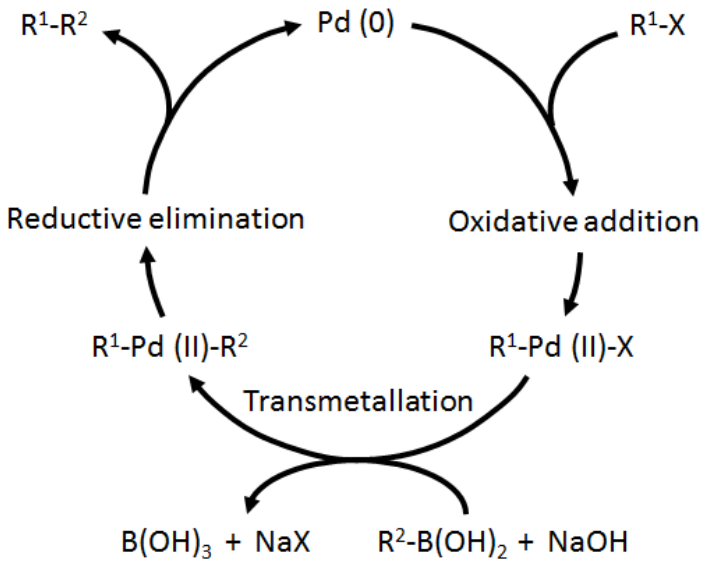

Figure 1.4: Palladium catalysed Suzuki coupling. The reaction consists in 3 main steps: 1) oxidative addition, 2) transmetallation and 3) reductive elimination.

1.2.3. Catalysis by bimetallic gold-palladium alloys

As mentioned previously, two metals can be effectively mixed together to produce a new material with unique properties depending on the final composition and its alloy structure. Two effects can be considered as being responsible for the enhancement in their chemical and physical properties, namely the ligand and ensemble effects[50]. The former, also called the electronic effect, refers to the electronic interactions between the two metal, such as charge redistribution and changes of the d-band electron structure, while the latter, also known as the geometric effect, refers to the changes in catalytic properties due to the change in chemical composition at the surface[51–53]. These two effects are deeply connected to each other and it is usually very difficult to clearly distinguish them and study them separately. For example, if the bulk composition of a catalyst is usually well known, the same cannot be said about the surface composition[50]. Moreover, varying the composition of the surface results in changes in the electronic structure of the alloy nanoparticle. Density Functional Theory (DFT) studies can help in this field, isolating the two effects by use of theoretical methods[50].

Among bimetallic nanoparticles, gold-palladium alloys have been extensively studied[54–56]. Gold is fully miscible with palladium in all ratios; depending on the synthesis technique and the experimental parameters, however, different alloy structures can be produced[57] and are categorised according to their mixing pattern as:

- Core-shell structure: where one metal completely encapsulates the other, forming a structure that resemble an egg, with the core being the yolk and the shell being the albumen.
- Segregated structure: where the two metals are isolated but share a common surface
- Mixed structure: where the metals are either ordered or solid solutions. The second ones are better known as random alloys.
- Multi-shelled structure: very similar to the core-shell, but with the presence of more than one shell.

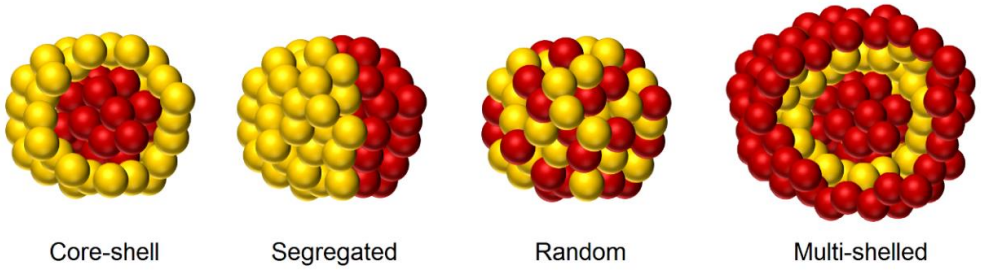

Figure 1.5: Representation of bimetallic structures: core-shell, segregated, random alloy and multi-shelled.

In addition to the structures reported above, it is worth mentioning a particular type of bimetallic catalyst that is in general not included in this list because it is not strictly an alloy: the physical mixture[58,59]. This particular nano-catalyst, as the name suggests, is simply a physical mixture of the two monometallic catalyst or refers to the presence of two monometallic structures present in the same catalyst.

Of all the structures, random-alloy and core-shell are the most common, and their superior performances have been reported for several reactions, such as selective oxidations of alcohols[55,60] and hydrocarbons[61], transformation of biomass to fuels and chemicals[62–64] and the already mentioned cross-coupling reactions[65,66] and CO oxidation[67]. A recent hot topic worth mentioning is the direct synthesis of hydrogen peroxide from hydrogen and oxygen, where the addition of palladium to gold containing catalysts let to an improvement in term of catalytic activity[68]. Hutchings et al., for example, reported an improvement in H_2O_2 productivity from 7 and 31 mol h^{-1} kg_{CAT}^{-1} for Au/TiO_2 and Pd/TiO_2 respectively to 64 mol h^{-1} kg_{CAT}^{-1} for a $AuPd/TiO_2$ catalyst with Au : Pd molar ratio of 1 : 1[69].

1.3. Catalyst preparation: an overview

The reason heterogeneous nanocatalysts are generally less active and selective than their homogeneous counterparts is that often more than one active site is present and it is usually very challenging to isolate and study them in isolation[70,71]. The performance of a heterogeneous catalyst, for example, can be related to the already mentioned quantum confinement[72,73], metal oxidation state[74–76] and co-ordination number[77,78], oxygen or hydrogen spill-over[79,80] and to various metal-support interactions such as the charge transfer[81,82] and the strong metal-support interaction (SMSI)[83]. The catalyst preparation method greatly influences all these properties and therefore it assumes a role of primary importance in the final catalyst performance. In general, the catalyst active phase (or its

precursor) can be produced simultaneously with the support or added to the already prepared support.

1.3.1. Simultaneous production of the active phase (or its precursor) and support

1.3.1.1. Sol-gel synthesis

The sol-gel process consists of a two-step procedure[84]. In the first step a colloidal sol is formed by hydrolysis and partial condensation of a metal precursor, usually either a metal alkoxide or an inorganic salt. In the second step a three-dimensional network is formed by condensation which traps the solvent inside the newly formed pores. This structure, called gel, undergoes an aging process where the solvent is either removed by simple evaporation, forming a xerogel, or by supercritical extraction, forming an aerogel. Several operational parameters can be changed to finely tune the properties of the final material, such as metal coordination number and oxidation state, pH and amount of solution used, as well as the already mentioned ageing step. The simultaneous production of support and active phase makes this method suitable for the synthesis of supported catalysts, even if the strong integration of the active phase in the support framework can sometimes make the activation step difficult.

1.3.1.2. Co-precipitation

This technique involves the simultaneous precipitation of two or more components from a homogeneous solution, after reaching supersaturation with respect to the precipitating solid[85]. The catalyst formed is a homogeneous distribution of active phase and support. Thermal decomposition of the metal precursor counter ions is usually required, and in many cases further thermal activation to form the active sites. Order and rate of addition of the components, nature of the precipitating agent and its addition procedure, solvent, temperature, mixing, initial and variation of the pH during the synthesis and ageing step greatly affect the process, making this methodology often difficult to control[86].

1.3.2. Deposition of the active phase (or its precursor) to the support

The active phase (or its precursor) is applied finely divided and uniformly onto the surface of the support. In this case, the support is usually synthesised in an early stage with the desired chemical-physical characteristics, such as specific composition, surface area, pore size and mechanical properties. All the methods reported in this category are governed by three variables: nucleation and growth, interactions at interphase and diffusive phenomena, and their occurrence, extent and control are the reason behind their final characteristics.

1.3.2.1. Impregnation

In this method, the support is mixed with a solution containing the metal precursor, so that the solution fills the pores of the support by capillary action[87]. The metal bonds to the support by weak interactions such as hydrogen bonds, van der Waals forces, dipole-dipole interactions and London dispersion forces. Impregnation can be categorised as dry or wet depending on the quantity of solution employed in the preparation. In particular, in the dry impregnation (also called incipient-wetness), the volume of metal precursor solution coincides with the support pore volume. In this way, an excess of precursor solution outside the pores is avoided thus leading to good particle dispersions. As a consequence, however, high metal loadings are generally not possible to prepare, due to the limitations given by the solubility of the precursor in the solvent used. In the wet impregnation (or diffusional impregnation), on the other hand, the support is firstly dispersed into the solvent and then mixed with the precursor solution, in order to have a final volume that is higher than the support pore volume; in this case, the precursor diffuses into the pores by concentration gradient.

The impregnation method was the technique used to synthesise the very first supported gold nanoparticles by Bond *et al.* in 1973[21] and it is perhaps the most commonly used technique from an industrial perspective due to its simplicity. Good metal dispersions can be achieved on numerous porous supports. However, the control over the particle size is generally poor due to sintering phenomena occurring during the heat treatment step, usually necessary to form the active site. A work recently published by Sankar *et al*., demonstrated the efficient synthesis of narrowly distributed sub 5 nm gold and gold-palladium nanoparticles with a modified impregnation method, where the presence of specific amount of chloride ions allows not only a better metal dispersion, but also a more homogeneous alloy composition[88].

1.3.2.2. Chemical Vapour Deposition

In the chemical vapour deposition (CVD), a solid metal precursor is vaporised by heating in a vacuum then deposited onto a solid support from the gas phase[89]. Depending on the method used to vaporise the solid precursor, the chemical vapour deposition can be categorised as plasma CVD, thermal laser CVD, photolytic CVD, fluidised-bed CVD and microwave plasma CVD. The immobilisation of the metal and the transformation to the active phase can be performed using different chemical processes, such as oxidation, reduction, nitridation, carbonisation, sulfurization, hydrolysis, disproportionation and thermal decomposition (pyrolysis). It is a very versatile and flexible process, often used in industry due to the ability of depositing any kind of metal and non-metal onto supports of almost any size and shape. Chemical precursors with high vapour pressure are however required and they are usually hazardous and very toxic; the decomposition of these chemicals produces by-products that are generally toxic and corrosive as well and require a neutralization step that increases the overall costs of the entire process.

1.3.2.3. Deposition-Precipitation

Deposition-precipitation is a preparation technique that allows the deposition of the active phase on the surface of finely dispersed supports by precipitation[85]. The metal precursor, as per wet-impregnation methods, is dissolved into a large volume of solvent and by use of a precipitating agent and specific reaction conditions, the nucleation is initiated onto the surface of the support. Precipitation can be achieved by changing the pH of the solution, changing the valency of a dissolved active precursor or increasing the concentration of a low solubility complex of the active precursor. The conditions are maintained so that the concentration of metal precursor does not exceed the limit of supersolubility in the bulk solution, but only at the support-solution interface due to the strong support-precursor interactions that decrease the nucleation barrier. Higher metal loadings can theoretically be achieved compared to the impregnation methods due to the large volume of solvent used. However, the necessity of rapid transport of the active precursor from the bulk solution to the support surface requires the support to have relatively high surface area to achieve a good dispersion.

1.3.2.4. Sol immobilisation

Most of the methods presented above have the common disadvantage of depositing the inactive metal precursor on the support surface, and thus they generally require an activation step to obtain the final active phase; this activation step may lead to changes in

surface morphology, particle size and metal dispersion. In the sol-immobilisation, the active phase is pre-formed in solution and then deposited onto the support surface[90]. Metal nanoparticles are generally formed by reduction of a metal salt or organometallic complex, or by thermal or photochemical decomposition of a metal precursor. The metal colloid is usually stabilised by a protecting agent against agglomeration phenomena that naturally occur due to attractive van der Waals forces between nanoparticles. The stabilisation can be either electrostatic or steric depending on the nature of the protective agent: if ionic species adsorb on the metal nanoparticles, they generate high charge density and thus the colloid is stabilised by repulsive Coulombs forces. On the other hand, if the protective agent is a long chain polymer, its adsorption leads to the formation of an isolating layer that reduces the reciprocal van der Waals interactions.

This technique offers great control over nanoparticles size, size distribution and shape, and almost any support can be used. The immobilisation step, in fact, depends only on the sol stabiliser and iso-electric point (IEP) of the support, and for this reason the choice of protective agent and working pH range is critical. The presence of a stabilising agent adsorbed onto the metal nanoparticles, however, can hinder the movement of a substrate in and out of the active site during a reaction, decreasing the overall activity of the catalyst[91]. For this reason, an additional washing step might be required to remove the protective agent from the active site. More details will be given in Section 4 and 5 of this Chapter.

1.3.3. Catalyst activation

Most of the catalyst preparation techniques described above allow the deposition of a precursor of the active phase on the surface of the chosen support; an additional step, called “activation”, is then required to transform the precursor into the final active phase[92]. This operation is generally a heat treatment in inert, oxidising (generally air or a mix of oxygen/inert gas) or reducing (usually a mix of hydrogen/inert gas) atmosphere and it can greatly influence the properties of the final catalyst. Heat treatments can in fact modify the dispersion degree of the metal nanoparticles (due to sintering phenomena) and change the interactions between precursor and support (strong metal-support interactions, SMSI), as well as alter the surface structure of the final catalyst (i.e. surface area and porosity)[93–95].

1.4. Theory of metal colloid formation and colloid deposition

As already mentioned above, the sol immobilisation method offers great advantages compared to other techniques, in particular for control of nanoparticle size and shape[96]. The possibility of using several protective and reducing agents, solvents and reaction conditions, allows control of the synthesis to obtain nanocrystals with various geometries and in a specific dimension range[97]. The formation of nanocrystals might look simple from a chemical point of view, where a simple reduction or decomposition reaction takes place to form the metallic nanoparticle. However, the formation mechanism behind this simple chemistry is extremely complicated and often hard to study.

The first reported synthesis of a metal colloid in liquid phase dates back to the 1857 with the pioneering work of Michael Faraday[98]. In his famous essay, he showed how gold nanoparticles could be produced by reduction of gold chloride with phosphorus; since then, hundreds of methods have been developed for the production of metal nanocrystals. In the last decade, however, the science reached a point where colloids can be produced with controlled morphologies, exceptional defined shapes, and low polydispersed sizes[99,100]. All the synthetic procedures follow a common 2-step mechanism: 1) nucleation and 2) growth, and they will be more extensively explained in the next sections[101].

1.4.1. Nucleation

Nucleation is the first step in the production of nanocrystals, and involves the production of zero-valent nuclei from a metal precursor by either a decomposition or reduction mechanism, depending on the original oxidation state of the metal. Two types of nucleation can be distinguished, namely homogeneous nucleation or heterogeneous nucleation[99]. Primary nucleation (or homogeneous) occurs when nuclei form uniformly in the liquid medium without the presence of other crystalline matter, while heterogeneous nucleation occurs when new nuclei are formed on structural inhomogeneity (dislocations of other nuclei, impurities, grain boundaries, support surface).

In the homogeneous nucleation, if the metal atom in the precursor is already in its zero-valent state, the precursor undergoes decomposition following a LaMer-type mechanism (Figure 1.6)[102]. In particular, the concentration of metal atoms in solution gradually increases with the decomposition of the precursor (generally by sonication or

heating), until it reaches a specific concentration, termed the level of minimum supersaturation. At this point, the atoms start to aggregate to form nuclei via homogeneous nucleation, which causes the concentration of dissolved metal atoms to fall back below the minimum supersaturation level, blocking any further nucleation. If the metal atom in the precursor is in higher oxidation state, a reduction step is also necessary; however, it is still unclear whether the precursor is reduced before aggregating into zero-valent nuclei or unreduced aggregates form prior reduction[100]. Theoretical studies suggest the latter mechanism, showing for example how charged Pt dimer and trimer exist when stabilised by Cl^- counter ions[103,104]. Also in this case, the formation of nuclei happens with a LaMer type mechanism.

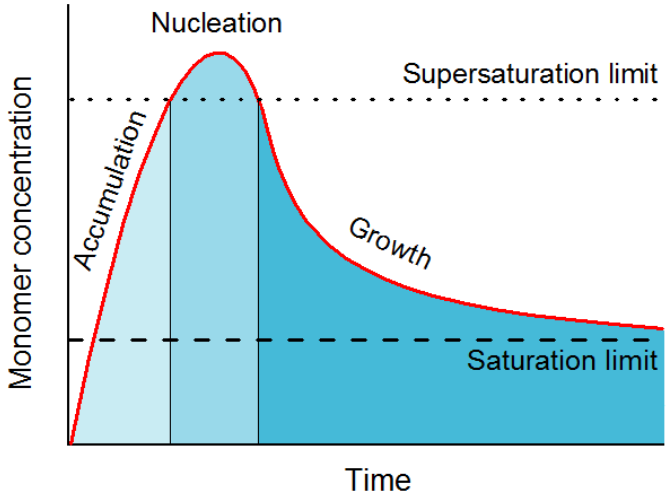

Figure 1.6: Phases of nanoparticles formation: accumulation of monomer in solution, rapid nucleation in small clusters and growth to nanoparticles.

Homogeneous nucleation is extremely sensitive to experimental conditions, such as stirring, temperature and presence of impurities, making this step critical for reproducibility between different batches[99]. Moreover, the study of this process presents big limitations, such as the lack of experimental tools capable to identify, observe and characterise the nuclei distribution in real space. Different approaches have been developed to try to overcome these limitations. Theoretical models, for example, try to predict the most stable nuclei configurations[105], while the atom nucleation on flat surfaces or the use of building blocks of much larger size allowed the study of the nucleation process in a similar reaction environment[106], even though drastic approximations are present in both cases. Alternatively, the use of organometallic complexes permits the synthesis of clusters with a specific number of atoms and thus their study[107,108]. Also in this case, however, significant differences are

likely to be present between the nuclei formed during the nucleation process and these synthetic organometallic clusters.

1.4.2. Growth

Until a certain critical size, nuclei are subjected to structural fluctuations that cause changing in the cluster morphology[109]. Above that critical size, these fluctuations become so energetically costly that the nuclei are stuck into well-defined structure. These structures, called seeds, may be composed by a single crystal or contain single or multiple twin defects[110,111]. Independently of their structure, the seeds can further grow in size by deposition of metallic atoms still present in solution. The overall growth of a seeds is energetically governed by two competitive forces: the decrease in bulk energy on particle growth and the increase in surface energy which favours the re-dissolution of the metallic atoms in solution. In general, however, the decrease in bulk energy dominates the equilibrium, leading to a constant growth of the nanocrystals. The growth process can be further limited by two factors: the diffusion of metallic atoms from the bulk solution to the seed surface or the adsorption reaction rate of these atoms on the surface[112].

Nanocrystals can further increase in dimension by coalescence[113] and Ostwald ripening[114]. The former simply happens when two or more nuclei merge together in larger nanoparticles to minimise their total surface energy, while the second is caused by differences in solubility between nanocrystals of different size; smaller clusters are more soluble due to their high surface energy and thus are more prone to re-dissolution, allowing larger nanoparticles to grow. Both these mechanisms, if not fully controlled or limited, can contribute to broadening the nanoparticle size distribution during the growth step of a synthetic procedure. As already mentioned, the initial seeds might be single crystals or possess single or multiple twin defects. The control over the formation of these different nano-geometries depends on the thermodynamic and the kinetic of the growth process. It is well known that typical chemical reactions can be thermodynamically or kinetically controlled; in particular, thermodynamics deals with the driving force of the system moving from the initial stage to the final product state, while kinetics deals with energy barriers present on the process pathway. For this reason, different products can be formed depending on whether they are the most stable final state or the product of pathway with the lowest energy barrier (Figure 1.7).

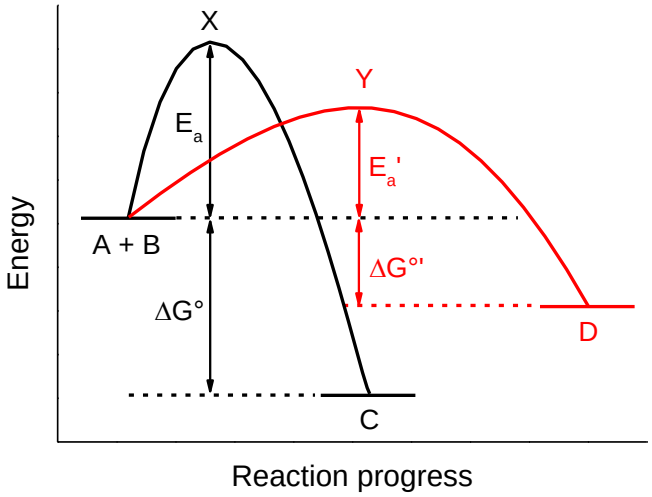

Figure 1.7: Potential energy diagram of a thermodynamically controlled reaction (black line) and a kinetically controlled reaction (red), with the product C being the most stable one, while the product D the fastest to produce.

The growth of a nanocrystal can be controlled thermodynamically or kinetically to obtain specific shapes (Figure 1.8)[110].

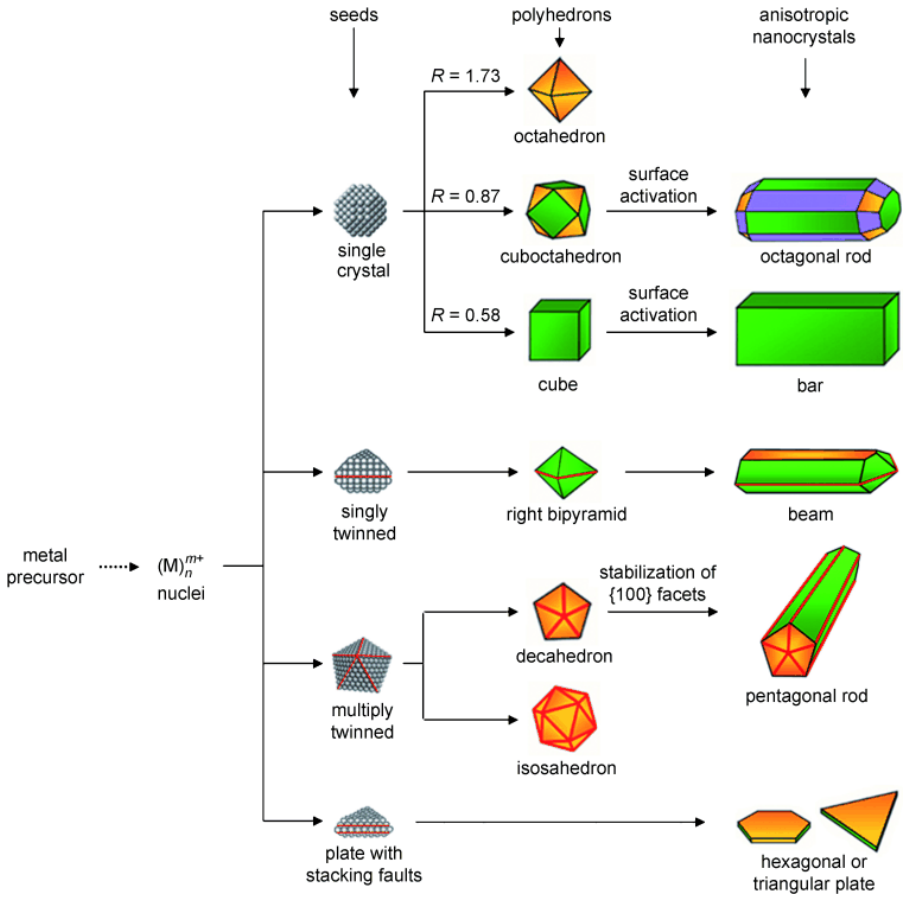

Figure 1.8: Different shapes that can be produced with accurate control over the reaction parameters. Image reprinted with permission from Y. Xia et al., Angew. Chem. Int. Ed. 2009, 48, 60-103.

1.4.3. Colloid immobilisation

Metal nanoparticles, as already explained before, have high surface energy and for this reason, if not effectively stabilised, tend to agglomerate into larger nanoparticles with higher surface area. A way to avoid agglomeration phenomena is the immobilisation of the metal colloid onto a solid support material. This is also beneficial from an application viewpoint, since the direct use of metal nanoparticles in catalytic reactions makes the separation step often tricky due to the very small dimension of the nanocrystals (for this reason, colloidal catalysts are generally referred to as quasi-homogeneous systems)[115]. Therefore, the first role of the support is to provide a stable environment to reduce nanoparticle agglomeration and to act as a carrier, sustaining the active phase and making it a heterogeneous catalyst in all respects. Many supports, moreover, can directly (i.e. providing acid/base sites) or indirectly (i.e. through strong metal-support interactions) contribute to the overall catalyst activity[116,117].

Many materials can be used as catalyst support, and most of them fit in one of the following 3 groups:

- Inorganic oxides: oxides of the IIa group of the periodic table (i.e. CaO and MgO), transition metal oxides (i.e. TiO_2, NiO, ZrO_2, WO_3, Nb_2O_5, Fe_2O_3 and CeO_2), silicas (i.e. amorphous and mesoporous SiO_2), aluminas (i.e. γ-Al_2O_3, α -Al_2O_3 and β-Al_2O_3) and complex multicomponent oxides (i.e. zeolites, hydrotalcites, hydroxylapatites, perovskites and clays).
- Carbon based materials: carbon allotropes such as activated carbon, graphite, nanotubes, nanofibers and graphene.
- Polymers and resins: dendrimers, polymer brushes, sulfonic resins and ion exchange resins are few of the most common polymers and resins employed.

An important parameter to take into consideration when a material is used as a support for metal nanoparticles is its isoelectric point (IEP), which is the pH value at which a generic molecule carries no net surface electrical charge[118,119]. It is often confused with the point of zero charge (PZC), although the latter refers to a zero surface charge density[120,121]. In other words, the IEP refers to a state of neutral net surface charge, while the PZC refers to the absence of any type of surface charge.

Metal oxides, from a bulk point of view, are simply composed of metal centres coordinated to oxygen atoms to form a stoichiometric compound (Figure 1.9)[118]. When exposed to water, however, the metal oxide can undergo hydration by 3 different

mechanisms: a) physical adsorption of water molecules by hydrogen bonding to surface oxygen atoms, b) chemisorption with consequent dissociation of water molecules, resulting in surface -MOH groups, and c) hydration reaction with conversion of oxide into oxyhydroxide or hydroxide (i.e. hydration of MgO to $Mg(OH)_2$).

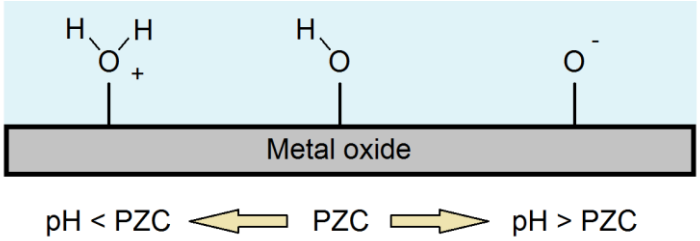

Figure 1.9: pH dependence of the point of zero charge (PZC) in a generic metal oxide.

Carbonaceous materials are mainly composed by sp^2-hybridised carbons, with layers of aromatic rings (graphene layers) held together by Van der Waals interactions. Numerous imperfections and defects (i.e. nonaromatic rings and structural carbon vacancies) populate the edges of these graphene layers, and their high density of unpaired electrons makes these carbons the most active sites[122]; on these sites, chemisorption of heteroatoms, such as oxygen, nitrogen and sulphur, is favoured. This opens the possibility to functionalise the carbon surface with several functional groups, such as carboxylic, phenolic, carbonylic, hydroxylic, nitro, amino, thiophenolic and sulphoxidic. Functional groups can form spontaneously during the synthesis of the carbon (most of the oxygenated groups and nitrogen and sulphur functionalities when present in the precursor) or can be introduced by specific chemical treatment (most of the nitrogen and sulphur containing groups)[122].

All these functional groups on the support surface can be easily polarised when in an aqueous solution, with the nature of the charge and its intensity depending on the pH value of the solution. Most of the metal oxide and carbonaceous materials are amphoteric, so that can be polarised either positively or negatively. Therefore, at the IEP, all the positive and negative charges (if present) are balanced to give a neutral net surface charge. However, if the pH of the solution is lower than the IEP, the support carries a positive net surface charge, while if the pH is higher than the IEP, then the surface is negatively charged. The interaction between the metal colloid and the support is therefore purely electrostatic[118]; metal nanoparticles are generally composed of an elemental zero-valent core surrounded by either a positive or a negative ionic double layer depending on the nature of the metal precursor, and for this reason they can interact with the surface of the support if opportunely polarised as well.

Some metal oxides, however, present a non-amphoteric behaviour, with the IEP that can be either very low or very high. In this case, the metal oxides can consequently adsorb only positively or negatively charged nanoparticles depending on its IEP. Some examples of non-amphoteric metal oxides are SiO_2 and MgO, with IEP of about 1 and 12 respectively, while a common amphoteric oxide is TiO_2, with an IEP of around 6 (Figure 1.10)[118].

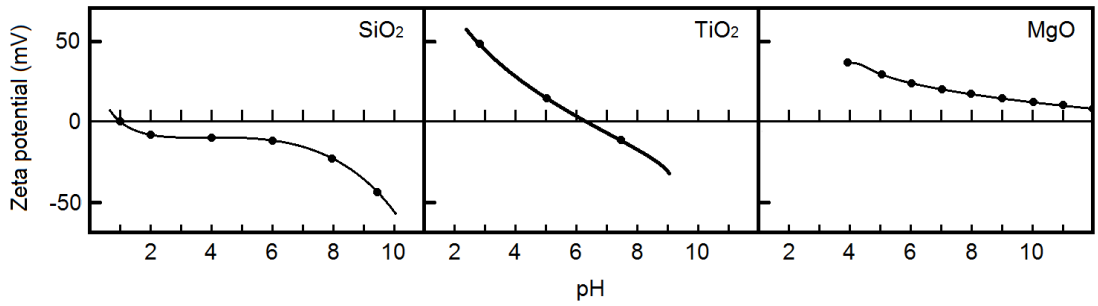

Figure 1.10: Acid (SiO_2), amphoteric (TiO_2) and basic (MgO) metal oxides and respective charge behaviour at different pH. Image modified with permission from J. P. Brunelle, Pure & Appl. Chem., 1978, 50, 1211-1229.

In this way, gold nanoparticles prepared by reduction of a $AuCl_4^-$ salt, for example, can be easily anchored onto the surface of TiO_2 suspended in an acidic water solution[118]. The reduced gold precursor, generates metal nanoparticles with a metallic core and adsorbed $AuCl_2^-$ ions on the surface, that confers a negative polarisation to the colloid (Figure 1.11). On the TiO_2 surface, hydroxylic groups are protonated by the acidic medium in which the support is suspended, and therefore can adsorb the negatively charged gold nanoparticles.

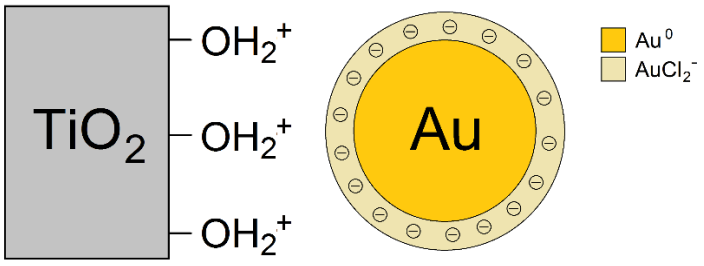

Figure 1.11: Interaction between a negatively charged gold nanoparticle and the positively charged titanium oxide surface.

In heterogeneous catalysis, the anchoring step is critical for several reasons. For example, metal nanoparticles can leach out in the reaction solution if the anchoring is too weak, causing several problems of product contamination, catalyst deactivation and catalyst reusability[123,124]. Similarly, a weak metal-support interaction can lead to particle sintering during thermal treatments[125–127]. For these reasons, a strong interaction between metal particles and support is always desirable and a great amount of work has been dedicated on this topic in the last few decades. In particular, studies have shown that when reducible metal

oxides are employed as support, the metal-support interaction can be strongly enhanced by heat treatments in a reducing atmosphere (usually pure H_2 or a mixture of H_2 and an inert gas)[117]. This effect, also called Strong Metal-Support Interaction (SMSI), is caused by a thin layer of reduced metal oxide that partially covers the metal particles thus increasing the metal-support interface[95].

1.5. Noble metal colloid synthesis: a practical approach

In the Section 1.3, several techniques have been described for the preparation of supported metal nanoparticles; except the deposition-precipitation and the sol-immobilisation methods, the other procedures involve the formation and subsequent growth of nanoparticles directly on the support surface. In Section 1.4, nanoparticle formation was analysed from a more theoretical point of view, exploring the mechanisms and the forces involved in the formation of metallic colloids. Here, the most common techniques for the production of the sole metal nanoparticles will be briefly described, with a particular emphasis on wet chemical methods and their characteristics.

The formation of nanoparticles of a specific dimension and with very narrow size distribution is always challenging due to the steps involved being challenging to measure and control: very small changes in the synthetic procedure can affect enormously the final product. For this reason, over the last century, several techniques have been developed in order to produce noble metal nanoparticles in solution with high control over the process parameters. Not only the quality of the colloids, but also the applicability of these techniques is a factor that must be taken into account: extremely expensive setups, or highly toxic precursors might lead to the production of nanocrystals with superior quality, but from an industrial point of view the process might not be viable.

1.5.1. Physical methods

In this section, physical methods are not identified simply as methods to produce nanoparticles in solution by direct application of a physical phenomenon, such as evaporation of metallic atoms by laser ablation, but also methods where the metal precursor reduction reaction is initiated by a physical phenomenon. For this reason, the reduction of a metal cation by a radical species will be accounted as a physical method, since the radical initiator was produced by ultrasonic or UV irradiation. Several methods are reported in

literature, with the most common being metal evaporation, laser pyrolysis, sonochemical synthesis, γ-radiolysis, photochemical reduction and microwave reduction[128].

- Metal Evaporation: In this method, metal vapours are generated through heating a high volatility metal precursor at low pressure. The heating can be carried out using either a Joule heating furnace or an electron-beam furnace. The vaporised metal atoms are then condensed generally in an organic solvent kept at low temperature. Gold[129,130], silver[131–133] and palladium[134] nanoparticles in a range of 3 – 30 nm have been successfully produced with this method, however, the control over the size distribution, and the use of toxic precursors and organic solvents, strongly limit this technique[128].
- Laser Pyrolysis: Similarly to metal evaporation, this synthetic route involves the evaporation of metallic atoms and the subsequent condensation into a solution. In this case, however, the precursor is simply a metallic plate immersed in an aqueous solution usually containing a stabilising agent. Metallic atoms evaporate by laser ablation and immediately condense into the solution. The use of greener solvents makes this technique more suitable for the production of colloids compared to the metal evaporation, even though inefficient control over the size distribution due to agglomeration phenomena still persists[135–137].
- Sonochemical Synthesis: This method is based on the cavitation process generated by ultrasonic irradiation. When the cavitation bubbles collapse, extremely high temperature and pressure are generated locally, and this leads to a radical splitting of solvent molecules at the liquid/gas interphase[138]. These radicals react with the metal precursor in solution, thus producing the final metal nanoparticles. This method has successfully been used for the production of stabilised gold[139], silver[140], platinum[141] and palladium[142] colloids.
- γ-Radiolysis: The reduction of the metal precursor present in solution happens by interaction with organic radicals generated by γ-irradiation. An example of organic radical initiator is iso-propyl alcohol, which generates $[(CH_3)_2C^{\bullet}(OH)]$ species that are able to produce rapidly and homogeneously a large number of metallic atoms in solution[143]. Good control over the nanoparticle size and size distribution can be reached, and this technique can efficiently be employed also in the growth of pre-existing metal seeds or in the synthesis of bimetallic core-shell structures[144–147].
- Photochemical Reduction: In this method, the slow reduction of the metal precursor is caused by UV irradiation. This technique is widely used in academia, especially for the synthesis of nanostructures with well-defined shape[148]. Gold and silver nanorods,

dendrites and nanoplates can be produced by choosing the right capping agent and carefully adjusting the concentration of metal precursor[149]. This synthesis is not limited to gold and palladium, but also platinum and palladium colloids are reported in literature[150,151].

- Microwave Reduction: In the microwave reduction, metal nanoparticles are generated by the heating effect of the microwave irradiation on the polar molecules of the solvent, rather than by the energy of the microwave quantum. This type of heating is much faster and more homogeneous than the conventional heating, and it causes therefore a more uniform nucleation step and shorter crystallisation time[152–154].

In addition to the techniques here above reported, thermal decomposition[155,156] and electrochemical reduction[157,158] are also methods that worthy of mention. In the former, metal nanoparticles are produced by thermal decomposition of a metalorganic precursor in an organic solvent, while the latter involves the use of a sacrificial anode made of the metal to be transformed in nanoparticles and the reduction is carried out by an electrochemical process. In both cases, however, the control over the particle size distribution is very hard, and for this reason these techniques find very limited application in academia[128].

1.5.2. Chemical methods

Most of the work found in literature regarding the synthesis of noble metal nanoparticles in solution involves the chemical reduction of a precious metal salt in an organic or aqueous medium. Nucleation and growth are the two key processes that govern the synthesis. In the nucleation, a metal precursor is reduced from the cationic form to its zero-valent state to form metallic clusters (nuclei) of very small dimension (< 3 nm). Once being formed, the nuclei can further grow into nanoparticles through several mechanisms, such as Ostwald ripening, heterogeneous nucleation on seeds and coalescence. Several parameters affect the outcome of the whole process, such as the reducing agent, the metal precursor, the solvent, the solution pH, the stabilising agent and the temperature.

1.5.2.1. The choice of the reducing agent

An enormous amount of reducing agents has been studied, with the most important being sodium borohydride ($NaBH_4$)[40,96,159], hydrazine (N_2H_4)[160,161], hydrogen[162,163], sodium citrate[164], ascorbic acid[165], ethanol[166], ethylene glycol[167], formaldehyde[168] and hydroxylamine[169]. The choose of the appropriate reducing agent depends on several factors,

such as the desired nanoparticle size that one wants to obtain, the type and nature of stabilising agent, the solvent used and the working temperature.

The reducing agents can be divided depending on their reducing power as either weak and strong. This reducing power is commonly referred in electrochemistry as the standard reduction potential (E°)[170] and is expressed in Volts (V). E° is a measure of individual potential of a reversible electrode at standard state (solute at concentration of 1 mol L^{-1}, pressure of 1 bar and temperature of 25 °C) against a reference electrode (standard hydrogen electrode). Without entering too much in the electrochemistry field, it is important to know that the lower the E°, and the stronger the reducing agent is. As a general rule, compounds with E° lower than -0.5 V are considered strong reducing agents, while reducing potentials higher than -0.5 V are generally characteristic of weak reducing agents[171]. Electrode potentials can be found in literature for the most common reducing agents and metal precursors, and a brief selection is reported here in Table 1.1.

The driving force of the redox reaction (Equation 1.1) is then the difference between the reduction potential of the metal reduction ($E°_M$) and the reduction potential of the oxidation reaction of the reducing agent ($-E°_{Red}$), and is usually indicated as ΔE°:

$$\Delta E° = E°_M - (-E°_{Red}) \qquad Equation\ 1.1$$

A reaction, in order to be thermodynamically spontaneous, must have a negative value of Gibbs free energy (ΔG°). Thus, from the relationship between ΔG° and ΔE° shown by the Equation 1.2[122], ΔE° must be positive.

$$\Delta G° = -nF\Delta E° \qquad Equation\ 1.2$$

Where n is the number of electrons exchanged in the reaction and F is the Faraday constant. In other words, the potential of the reducing agent must be higher in absolute value than the potential of the metal. For this reason, very electropositive metals (E° > 0.7 V) such as Au, Pd, Ir, Ag, Pt and Rh can easily react with both strong and weak reducing agents, while more electronegative metals, such as Ru and Cu, usually require strong reducing agents and harsh conditions of temperature and pressure. As general rule, the ΔE° should be higher than 0.3 – 0.4 V for the reaction to proceed and be of practical importance[172].

Table 1.1: Standard reduction potentials of the most commonly used noble metal precursors and reducing agents.

Redox half-reaction	E° [V]	Reference
$[B(OH)_4]^- + 2\ H_2 + 4\ e^- \Rightarrow [BH_4]^- + 4\ OH^-$	- 1.33	171,173
$[B(OH)_4]^- + 2\ H_2 + 4\ H^+ + 4\ e^- \Rightarrow [BH_4]^- + 4\ H_2O$	- 0.43	
$N_2 + 4\ H_2O + 4\ e^- \Rightarrow N_2H_4 + 4\ OH^-$	- 1.20	172
$N_2 + 5\ H^+ + 4\ e^- \Rightarrow [(N_2H_4)H]^+$	- 0.23	
$MeO + 2\ H^+ + 2\ e^- \Rightarrow MeOH$	- 0.34	174
$Ascorbic\ acid^{(OX)} + e^- \Rightarrow Ascorbic\ acid^{(RED)}$	- 0.28	175,176
$EtO + 2\ H^+\ 2\ e^- \Rightarrow EtOH$	- 0.20	177
$Sodium\ citrate^{(OX)} + e^- \Rightarrow Sodium\ citrate^{(RED)}$	- 0.18	177
$2\ H^+ + 2\ e^- \Rightarrow H_2$	0.00	178
$EtGly^{(OX)} + 2\ H^+ + 2\ e^- \Rightarrow EtGly^{(RED)}$	+ 0.16	174
$Cu^{2+} + 2\ e^- \Rightarrow Cu$	+ 0.34	178,179
$Ru^{3+} + 3\ e^- \Rightarrow Ru$	+ 0.60	178
$Rh^{3+} + 3\ e^- \Rightarrow Rh$	+ 0.76	178
$[PtCl_4]^{2-} + 2\ e^- \Rightarrow Pt + 4\ Cl^-$	+ 0.76	178,180
$Ag^+ + e^- \Rightarrow Ag$	+ 0.80	178,181
$[IrCl_6]^{2-} + 4\ e^- \Rightarrow Ir + 6\ Cl^-$	+ 0.84	178
$Pd^{2+} + 2\ e^- \Rightarrow Pd$	+ 0.92	178,180
$[AuCl_4]^- + 3\ e^- \Rightarrow Au + 4\ Cl^-$	+ 1.00	178

- Sodium borohydride: $NaBH_4$ is probably the most used strong reducing agent for the synthesis of small and monodisperse noble metal nanoparticles. Used widely in organic chemistry to reduce carbonyl, imine and nitro groups, in water it hydrolyses to Na_3BO_3 and H_2, especially in acidic conditions[171]. The very low E° value allows rapid reduction of all the metal precursor in a very short time, thus consuming all the metal in solution for the production of nuclei and not leaving remaining precursor for the growth step[182]. Sodium borohydride is usually added in excess, and the BH_4^- ions remaining in solution can stabilise the nanoparticles by electrostatic repulsion[183]. Due to the already mentioned hydrolysis, however, this stabilisation is only temporary and a stabilising agent is usually required to prevent agglomeration phenomena.
- Hydrazine: Another strong reducing agent widely used in the synthesis of metal colloids, even if its high toxicity limits the applicability of this material. The

mechanism of action is very similar to sodium borohydride, with an extremely fast nucleation step and an almost negligible growth of the nuclei formed[184]. Gold[185], palladium[186] and platinum[187] colloids can be easily synthesised with narrow size distribution. Due to the adsorption on specific crystallographic faces, hydrazine hydrate has also been used for the preparation of nanoparticles with different shapes[171].

- Sodium citrate: The reduction with salts derived from citric acid is one of the oldest methods for the synthesis of gold nanoparticles. Turkevitch reported in the early 50's a method to produce 20 nm gold nanoparticle by reduction of $HAuCl_4$ in an aqueous solution of sodium citrate[188]. The relatively low value of E° allows a quick nucleation step without consuming all the metal precursor, that is then available for the further growth of the seeds. In this process, citrate ions act also as stabilising agent adsorbing on the surface of the nanoparticles and creating a negatively charged layer that protects against agglomeration[189]. With the years, this method has been extended to all the noble metals and it's nowadays one of the most used for the production of medium-large size nanoparticles[143,190,191].
- Polyol: Primary alcohols such as methanol and ethanol can be used both as solvent and reducing agent, while alcohols containing multiple hydroxyl groups (polyols) may function as stabiliser as well[192]. Several studies have been published in literature regarding the preparation of gold, palladium, platinum, silver, ruthenium, rhodium, nickel and copper nanoparticles, showing the versatility of this particular technique[193,194]. The most common polyol used is ethylene glycol (EG) and it can be used in combination with other stabilising agents such as poly(vinylpyrrolidone) (PVP) at high temperature[195].

In addition to the ones described above, several other reducing agents find application in the chemical synthesis of noble metal nanoparticles, such as primary alcohols[196], ascorbic acid[197], gallic acid[198], gaseous hydrogen[199], carbon monoxide[200] and formaldehyde[201]. The choice of the appropriate reducing agent is not the only factor that affects the production of metal nanoparticles. Other parameters have a strong effect on the metal reduction process, such as the nature of the metal precursor, the solvent, the pH of the solution, the stabilising agent and the temperature.

1.5.2.2. The metal precursor

As already discussed above, ΔE° of more than 0.3 – 0.4 V is necessary for the reaction to proceed. For this reason, the selection of the appropriate reducing agent and metal

precursor is critical. Depending on the degree of complexation of the metal species, in fact, the E° value of the compound can be different than the fully dissociated ion. Complexation provides better stability to the metal centre, thus the reduction potential will be lower. The E° of completely dissociated Ag^+ ions, for example, is + 0.80 V, while the addition of more stable ligands decreases the reduction potential up to – 0.51 V (Table 1.2)[172]. The careful choice of the appropriate metal precursor can be thus used to tailor the reactivity of the species in a specific metal-reducing agent system.

Table 1.2: Redox half-reaction potentials for different Ag containing ions.

Redox half-reaction	**E° [V]**
$Ag^+ + e^- \Rightarrow Ag$	+ 0.80
$[Ag(NH_3)_2]^+ + e^- \Rightarrow Ag$	+ 0.38
$[Ag(SO_3)_2]^{3-} + e^- \Rightarrow Ag + 2\ SO_3^{2-}$	+ 0.29
$[Ag(S_2O_3)_2]^{3-} + e^- \Rightarrow Ag + 2\ S_2O_3^{2-}$	+ 0.01
$[AgI_4]^{3-} + e^- \Rightarrow Ag + 4\ I^-$	- 0.09
$[Ag(CN)_3]^{2-} + e^- \Rightarrow Ag + 3\ CN^-$	- 0.51

1.5.2.3. The solvent

Many of the nanoparticle preparation methods are performed in water, due to the high solubility of the reagents involved. The synthesis of metal colloids in organic mediums, although possible, usually presents some serious difficulties. The electron transfer, for example, can be difficult in low polarity solvents. Low solubility and dissociation of most metallic precursors and ionic reducing agents contribute to the limited applicability of low polarity liquids[202]. As already mentioned before, however, polar solvent such as primary alcohols and polyols can be easily used for the synthesis of several noble metal nanoparticles, the latter with the advantage of being used as in situ stabilising and reducing agents[196].

1.5.2.4. The pH

An important parameter to take into consideration, especially in aqueous mediums, is the pH of the solution. Most of the redox processes involve H^+ and OH^- ions and, as a result, the pH can greatly influence the outcome of the reaction. The Nernst equation expresses the relation between the reduction potential and the concentration of the species involved in the redox couple (Equation 1.3).

$$\Delta E = \Delta E° + \frac{RT}{nF} \ln \frac{\prod [Ox]_i^{\nu_{Ox}}}{\prod [Red]_i^{\ Red}} \qquad Equation\ 1.3$$

Where R is the gas constant, T is the temperature in Kelvin, n is the number of electrons transferred in the reaction, F is the Faraday constant and $[Ox]_i$ and $[Red]_i$ are the concentration of the oxidised and reduced species. Moreover, changes in pH might affect the degree of complexation of the metal precursor and the reducing agent behaviour. It is well known that some reducing agents strongly depend on the pH of the solution they are dissolved in. Redox diagrams combine both the effect of complexation and pH to give useful information on how to manipulate the redox reaction to produce colloids with the desired characteristics. Figure 1.12 gives an example of a redox diagram of a system composed by silver and palladium as metal precursor and hydrazine as reducing agent, with ammonia used to adjust the pH[203].

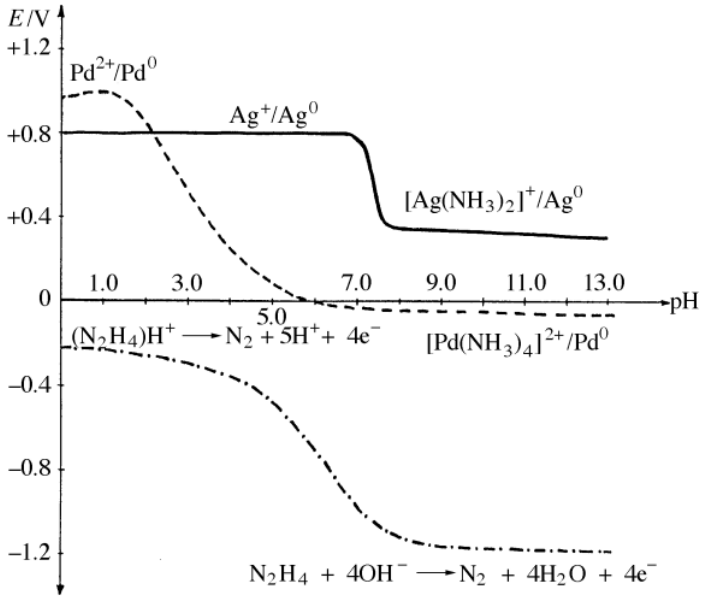

Figure 1.12: Influence of pH on reduction potential of some common metal precursors and reducing agents. Image reprinted with permission from D. V. Goia, Journal of Materials Chemistry, 2004, 14, 451-458.

1.5.2.5. The stabilising agent

The stabilising agent, as already mentioned in Section 1.4, has the role of protecting the nanoparticles from agglomeration. The stabilisation is generally due to either electrostatic repulsion or steric effect[117]. The former happens when the stabilising agent, usually small molecules, have a net surface charge. As a consequence, the adsorbed species will generate an electric double layer that stabilise the nanoparticles by repulsive Coulomb forces. Examples of electrostatic stabilisers are carboxylic acids, organosulfates,

tetraalkylammonium and tetraalkylphosphonium salts[128]. Steric stabilisation generally involves the addition of bulky polymers that adsorb on the particle surface. Long chain thiols, co-polymers and hydrogels are widely used steric stabilising agents for the synthesis of noble metal colloids[171]. Among them, of particular relevance is poly(vinylpyrrolidone) (PVP), a polymer made from the monomer N-vinylpyrrolidone (Figure 1.13)[117,128]. PVP, in fact, can preferentially adsorb on specific faces of the nanoparticles, thus promoting anisotropic growth[204]. Not only the type of stabilising agent affects the nanoparticle formation, but also its concentration and its molecular weight in the case of polymers: high concentrations and high molecular weight have been reported to decrease the particle size in different colloidal systems. Moreover, as already reported, some stabilising agents can act as both solvent and reducing agent, such as ethylene glycol[195].

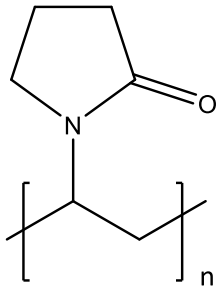

Figure 1.13: PVP monomer structure.

1.5.2.6. The temperature

Finally, the temperature of the reaction mixture can have a multiple effect on the quality of the final nanoparticles. In the first instance, it directly affects the reduction potential ΔE through the already mentioned Nernst equation (Equation 1.3). Thus, weak reducing agents at room temperature such as citric acid and alcohols, at high temperature are able to reduce most of the metal ions[205,206]. Additionally, higher temperatures often improve the solubility of metal precursors and ionic stabilising agents in low polarity solvents. On the other hand, high temperatures can also facilitate agglomeration and sintering phenomena, causing an uncontrolled increase in particle dimension and particle size distribution[207].

1.5.2.7. Bimetallic systems: a particular case

The nucleation and growth step in monometallic systems can be relatively easily controlled by careful adjustment of the reaction conditions. However, for bimetallic nanoparticles the situation is more complicated and accurate control can be challenging. In fact, the kinetic and thermodynamic parameters of the specific metals differ under the same

reaction conditions[171]. For this reason, in this case, the choice of the reducing and stabilising agent are crucial.

The challenge is related to the natural difference in reduction potential of different metal species. The larger the difference in E°, the greater the difference in nucleation rates between the two metals[208]. The species with more positive E°, in fact, will nucleate much faster than the one with lower E°, causing the nucleation of the second species on the surface of the already formed nuclei. This leads to formation of core-shell structures of anisotropic growth in case only one facet favours the deposition[171]. This is accentuated with strong reducing agents, while the use of weak reducing agents provides a more efficient control over the nucleation and growth processes. The use of stabilising agents, such as PVP and poly(2-ethyl-2-oxazoline), can decrease the production of aggregate in favours of alloys, as proved in gold-iron systems[209].

This difference in nucleation time can be used to prepare unique nano-objects. For example, hollow gold nanostructures can be prepared starting from a $AuCl_4^-/Ag^0$ system (Figure 1.14)[210]. The addition of gold precursor to a solution containing silver nanostructures, in fact, leads to the instauration of the following redox reaction, in which silver act as reducing agent due to the lower E° of the couple Ag^+/Ag (+ 0.80 V) than $AuCl_4^-/Au$ (+ 0.93 V).

$$3\,Ag + AuCl_4^- \rightarrow Au + 3\,Ag^+ + 4\,Cl^-$$

The zero-valent gold will then form at the interface of the silver/solution system, leading to the formation of a gold shell around the silver nanostructure. This shell, at the initial stage, has an open structure that allows continuous diffusion of gold precursor and Ag^+, until the whole silver nanostructure is completely consumed. Ostwald ripening process will finally complete the hollow structure at high temperature, to obtain the final desired nano-objects.

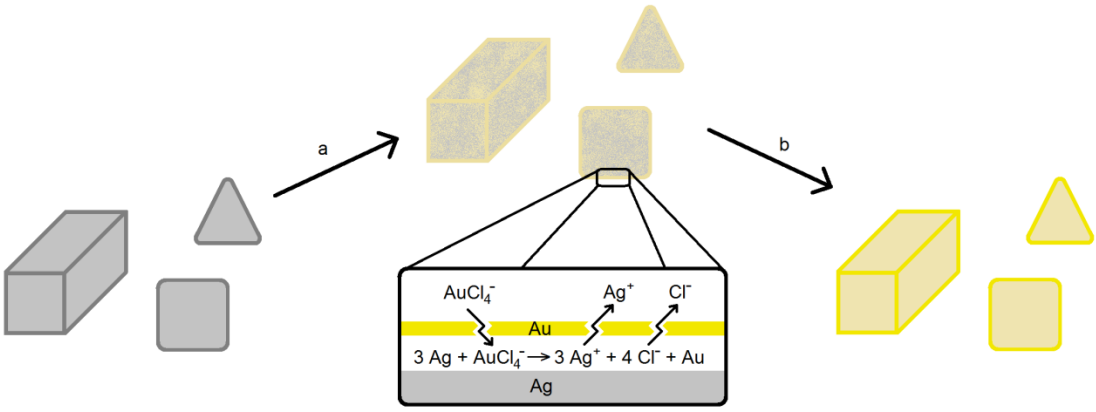

Figure 1.14: Synthesis of hollow nanostructures using silver as template. a) the gold precursor is reduced by the silver on the surface of the template, leading to slow formation of metallic gold cages. The products of reaction leave the cage by small pores in the gold structure. b) when the silver is consumed, the result is gold hollow nanostructures. Image modified with permission from Y. Sun et al. Nano Lett., 2002, 481.

1.5.3. From batch to continuous production

As already mentioned in Section 1, nanoparticles exhibit interesting size and shape dependent properties. For this reason, the production of uniform nanoparticles with controlled shape and size distribution is of a critical importance. A very fast nucleation step, compared with the relative growth time, is a necessary process to achieve this. In addition, all the nuclei should form and grow at the same time, and this can be achieved only if the chemical environment is extremely uniform throughout the reactor[211]. In fact, in case of a difference in physical and chemical conditions across the reaction vessel, the size and the relative growth rate of the formed nuclei will be affected by the location, leading to broad nanoparticle size distribution. Furthermore, for bimetallic particles, systematic composition variations with particle size almost always occur, which leads to the formation of nanoparticle populations that are rich in one or other metal component depending on particle size. This generally happens in conventional batch reactors, where turbulent flow caused by vigorous stirring is used to ensure a rapid mixing of the reactants, leading to batch-to-batch irreproducibility and thus problematic scale-up. Moreover, fast screening and optimisation of the synthesis conditions is often either impossible or very difficult[212].

In order to minimise these problems, in the last decade microfluidic systems (also called microreactors) have been employed in the continuous production of nanoparticles. Microreactors are simply continuous flow reactor with typical lateral dimensions below 1 mm

(Figure 1.15)[213]. Widely used also in chemical synthesis and as analytical tools[214], microreactors are able to combine several advantageous aspects, such as:

- Better control over the temperature or the temperature gradient along the reactor, combined with the possibility of rapidly cooling or heating the reaction mixture due to the large surface to volume ratio of the micro-channels[211].
- An efficient mixing of the reactant on a rapid time-scale that ensures a homogeneous reaction environment. Microreactors work in steady state, with control over composition and reproducibility, eliminating local variations in reaction conditions due to inhomogeneous mixing[215–217].
- The possibility to add reactants downstream as required, allowing control over the chemical composition in subsequent processes[211].
- The possibility of rapid, controlled and precise screening of parameters without consumption of large amounts of reagents or energy[216,218].
- The possibility to implement sensors and fast screening techniques for *in situ* monitoring, such as UV-Visible spectrometry and small-angle X-ray scattering (SAXS)[212,219].
- The superior ability to study the mechanism of nanoparticle formation due to the spatial separation of the nucleation and growth steps. *In situ* real time analysis can be performed with the aid of synchrotron based techniques, such as X-ray absorption spectroscopy (XAS) with a time resolution of up to 5 ms[213,220].
- An easy scale-up of the process by simply running the reactor in continuous or by using several reactors in parallel[221].

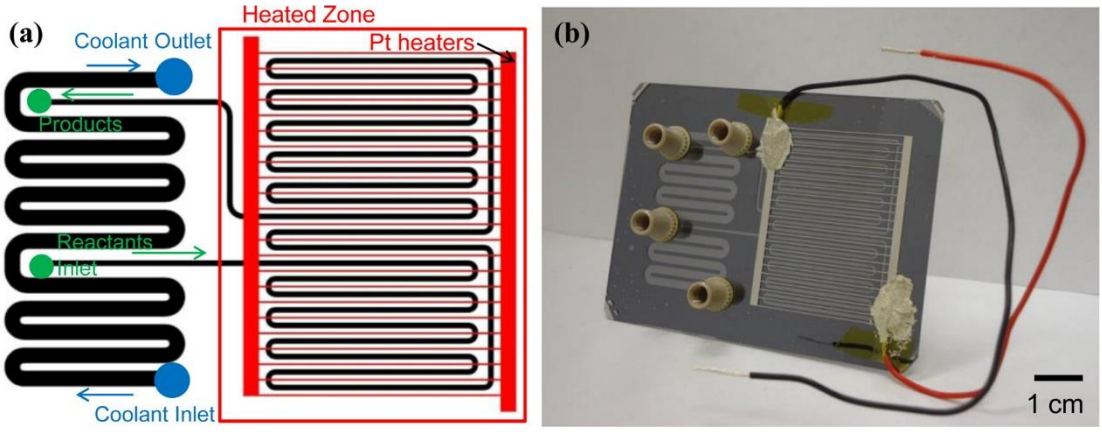

Figure 1.15: Example of a microreactor used for the synthesis of palladium nanoparticles. Image reprinted with permission from A. M. Karim et al., J. Phys. Chem. C, 2015, 119, 13257-13267.

Microreactors have successfully been employed not only in the synthesis of pseudo-spherical nanocrystals, but also for the production of many other different shapes, such as nanorods, hollow nanoparticles and nanocubes[222–225].

Microreactors, however, also suffer from some limitations. First of all, microfluidic devices are produced by photo-lithographic processes, which can be expensive[226]. Moreover, adsorption of metal on the internal walls of the microreactor is often reported and it can cause in some cases irreversible fouling[217,227]. Axial dispersion effects can also cause variations in residence time due to the fluid moving slower near the tube wall than in the centre, resulting in a broadening in nanoparticle size distribution[228] (more details on this mechanism will be given in Section 1.6).

To avoid both metal deposition and axial dispersion effects, segmented flow microreactors (Figure 1.16) can be used[229], where the use of an additional non-miscible solvent or gas creates a biphasic system and each "segment" can act as an independent microreactor[215,230,231]. In this way, the reaction mixture is not directly in contact with the tubing wall due to a very thin layer of the carrier solvent or gas, and the metal deposition is inhibited.

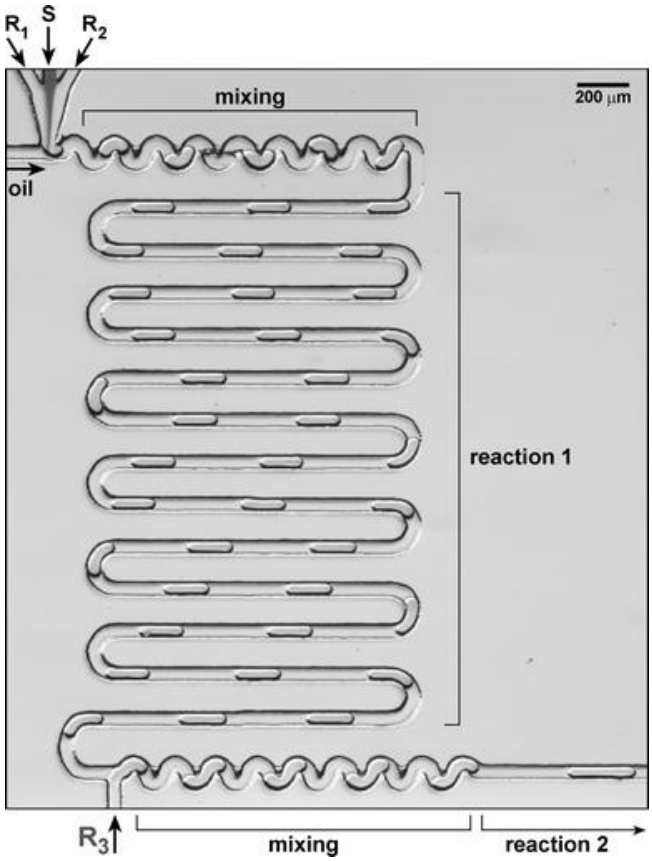

Figure 1.16: Example of a segmented flow microreactor used for the synthesis of semiconductors nanoparticles. Image reprinted with permission from I. Shestopalov et al., Lab on a Chip, 2004, 316-321.

Another option to partially solve the problems affecting microreactors is the use of millifluidic systems, which are reactors with channel diameter greater than 1 mm. Although providing the same advantages of classic microfluidic systems, these setups are easier to fabricate, fouling resistant and easier to integrate with *in situ* apparatus due to the larger channel size[232–234]. Moreover, the use of larger volumes allows the production of nanoparticles in a much larger scale, while maintaining the ease of flow-rate control and the ability to control reaction parameters.

1.6. Hydrodynamics at a small scale: an overview

Hydrodynamics is defined as the discipline of fluid mechanics that describes the flow of liquids and the forces acting on solid bodies immersed in liquids. In the context of micro- and milli-fluidic reactors, the study of hydrodynamics is needed to understand the dynamics and the forces that govern the motion of the fluid inside the channel. Hydrodynamically, microsystems are treated differently from general macroscopic cases due to effect of boundary conditions (i.e. the interaction between the solution and the channel wall, also

called no-slip condition) that become important only in the microscale because of the high surface area-volume ratio.

1.6.1. Flow regimes

Unidirectional flow regimes in a tube can be summarised as turbulent, transitional and laminar (Figure 1.17)[228,235]. Turbulent regimes refer to flows with a structure dominated by random and not predictable fluid motions. Laminar regime refers to flows that move in orderly sheets or lamina, and their motion is stable to perturbations. Finally, transitional regime refers to flows that are no longer laminar but yet not fully dominated by random fluid motion and thus cannot be described as turbulent. Flow regimes are characterised by a dimensionless quantity called Reynolds number (Re), and represented by the Equation 1.4:

$$Re = \frac{uL}{v} \qquad Equation\ 1.4$$

Where u is the mean velocity of the fluid in the tube, L is the diameter of the tube (hydraulic diameter if the cross-section is not circular) and v is the kinematic viscosity. From a physical point of view, the Reynolds number, is the ratio between inertial forces and viscous forces[214]. Fully turbulent flow is generally observed at Re > 4000, while laminar flow is characteristic of Re < 2300. Typically, milli- and micro-reactors work in very low Reynolds number regimes (laminar flow, Re < 150) due to the inherent small channel diameter of the devices used and low fluid velocities involved[236].

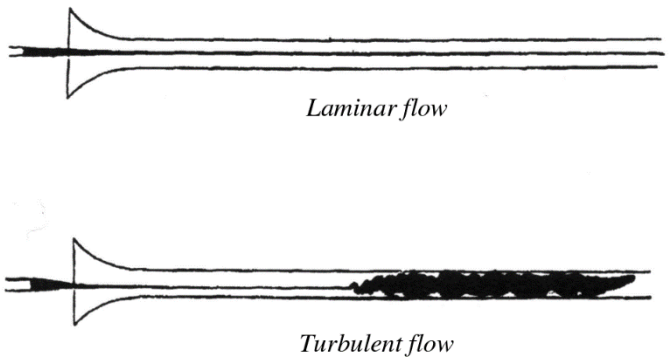

Figure 1.17: Original diagram from Reynolds' 1883 paper representing graphically the laminar and turbulent flow. Reprinted with permission from O. Reynolds, Proc. R. Soc. Lond., 1883, 84-99.

1.6.2. Transport phenomena

In a laminar regime, transport phenomena are described by three basic differential conservation equations[236], namely:

- Conservation of mass (continuity equation)
- Conservation of momentum (Navier-Stokes equation)
- Conservation of energy (energy equation)

In addition, if a reaction is carried out in the fluid, two more equations have to be added:

- Conservation of species (convective/diffusive equation)
- Laws of chemical reactions

The resolution of all these equations depends on the approximations considered and the boundary conditions, and allows to completely describe the flow under all its aspects and in any particular situation. One particular resolution of the conservation equations describes the pressure-driven laminar flow typical of microreactors: the so called Poiseuille flow, or more specifically Hagen-Poiseuille flow if channel cross-section is circular[237]. An important characteristic of this flow is the already mentioned no-slip condition, a boundary condition that refers to a fluid having zero velocity at a solid boundary. In other words, at the solid-fluid interface, the first fluid layer is not moving. The reason for this, is that adhesion forces between solid and fluid are stronger than the cohesive forces between the fluid particles, and thus the molecules of fluid in direct contact with the reactor wall are stuck to the surface past which they flow[236]. As a result, the typical Hagen-Poiseuille velocity distribution has a parabolic profile, with the layers at the centre of the channel that have higher velocities than the ones near the wall (Figure 1.18).

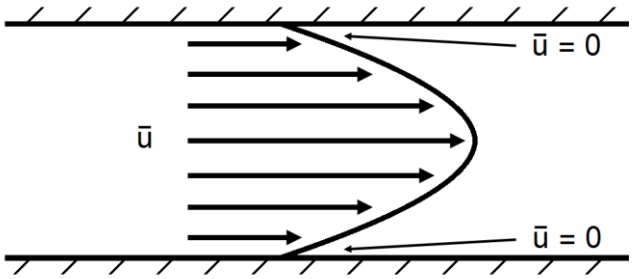

Figure 1.18: Typical parabolic profile flow of a laminar regime. This shape is caused by different velocities of the single fluid layers and the no-slip condition that imposes a null velocity of the layer directly in contact with the channel wall.

Transportation phenomena in a Hagen-Poiseuille flow can happen following three different yet inseparable mechanisms, specifically by molecular diffusion, Taylor dispersion and chaotic advection. The sum of these three components is often called convection[236].

1.6.2.1. Molecular diffusion

Molecular diffusion is simply the natural random thermal motion of atoms and molecules caused by Brownian motion[236]. Considering a single molecule of solute in a solution, the random path traced by the solute due to collision with the fast-moving molecules of the solution in which it is dissolved (Figure 1.19). In general, diffusion is driven by a concentration gradient, so that the molecules or atoms in the more concentrated solution will slowly migrate to the areas with lower concentration until neutralisation of the concentration gradient.

Molecular diffusion can be expressed by the diffusion coefficient (D_{ij}) calculated by the Stoke-Einstein equation, and it represents the ability of a certain atom or molecule (i) to diffuse into a specific medium (j):

$$D_{ij} = \frac{k_B T}{3\pi\mu_j\sigma_i} \qquad Equation\ 1.5$$

Where k_B is Boltzmann's constant, T is the absolute temperature, μ_j is the solvent viscosity and σ_i is the diameter of the solute molecule. In this equation, in particular, the numerator represents the kinetic energy of the solute, while the denominator represents the friction force acting on it.

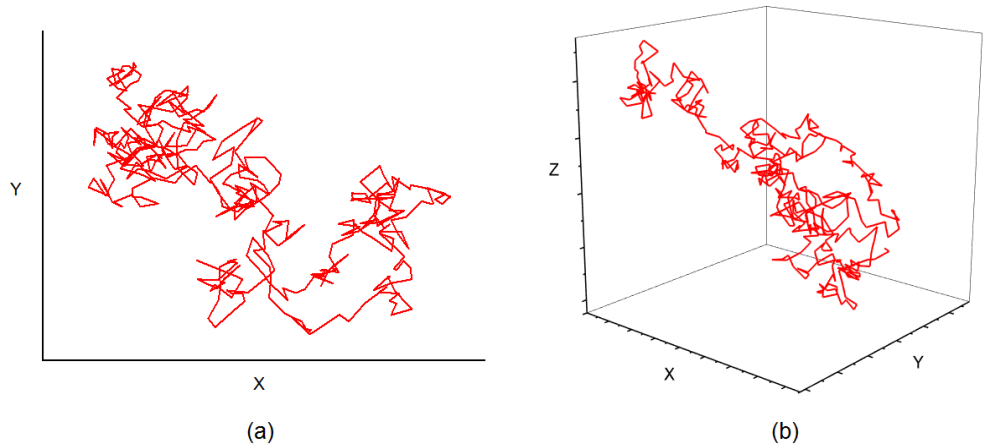

Figure 1.19: Random walk of a generic molecule in a solvent calculated in a (a) planar and a (b) three-dimensional space.

When considering two solutions "A" and "B" with the solution A containing a concentration "c_x" of a certain molecule, getting in contact in a microchannel (Figure 1.20), the solute will diffuse into the solution B through the interphase A/B until reaching concentration equilibrium[238]. The time needed to the solute to completely diffuse into a solution is called diffusion time (t_{DIFF}) and it is mathematically expressed as:

$$t_{DIFF} = \frac{a^2 Fo}{D} \qquad Equation\ 1.6$$

Where D is the diffusion coefficient, a is the diffusion length scale (the length over which the solute must diffuse) and Fo is the Fourier number, a dimensionless number generally in the range between 0.1 and 1. From the equation above, one can clearly see that the diffusion time strongly depend by the diffusion length scale. For this reason, in order to maximise the mixing and thus to minimise the diffusion time, it is necessary to reduce the diffusion length scale. Several methods can be applied to improve the mixing and will be reviewed later in this Section.

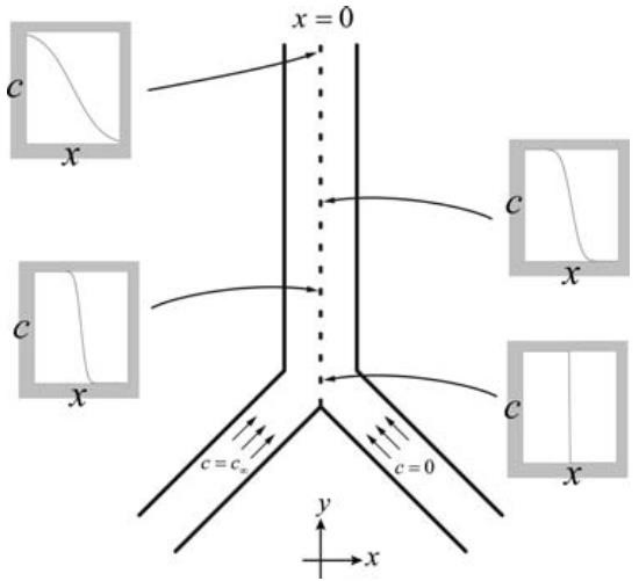

Figure 1.20: Mixing by molecular diffusion in a typical laminar regime flow in a straight channel. The four graphs show the variation in concentration along the direction x. Image reprinted with permission from B. Kirby, Micro- and Nanoscale Fluid Mechanics, 2013.

1.6.2.2. Taylor dispersion

Taylor dispersion is a typical mechanism of pressure-driven Poiseuille flows in microchannels[236]. In these flows, as already mentioned, the velocity distribution has a parabolic profile (Figure 1.21). Compared to an ideal plug-like flow, where the axial diffusion is due only to molecular diffusion, in the Poiseuille flow the fluid is more stretched in the

centre due to the parabolic velocity distribution, and the resulting concentration gradient between different fluid layers is blurred by diffusion in the radial direction. Therefore, the solute appears to diffuse at a faster rate than in the case of ordinary molecular diffusion.

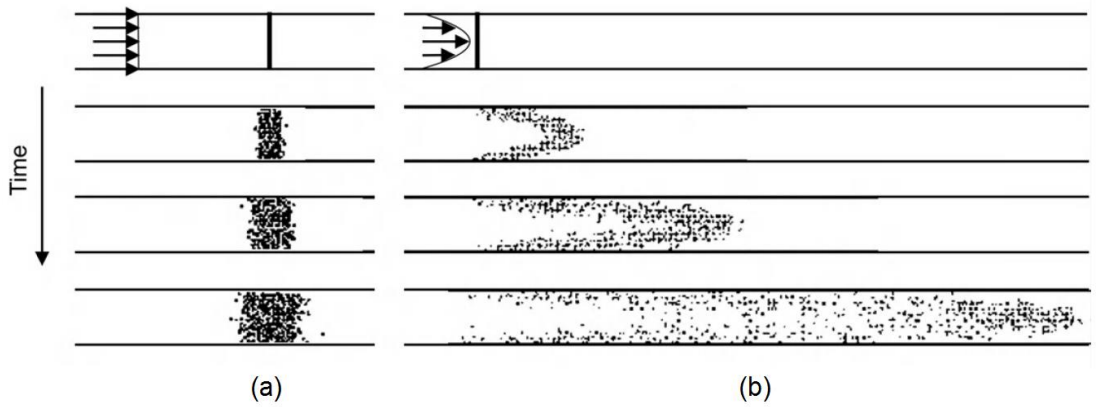

Figure 1.21: Graphical representation of the Taylor dispersion in (a) an ideal plug-flow reactor and in (b) a real Poiseuille flow regime. Image reprinted with permission from N-T. Nguyen, Micromixers, 2012.

1.6.2.3. Chaotic advection

An additional transportation phenomenon is chaotic advection, defined as the transport of a substance by bulk motion of the flow[236]. Considering for example two passive (inert and with hypothetical no mass) particles flowing next to each other in a plug-flow like field with no molecular diffusion, the two particles will run together along the channel in a steady state flow. However, under chaotic advection, the particles with initial nearby trajectories will diverge at an exponential rate creating an unsteady state flow and thus strongly enhancing the mixing between solvent and solute. This mechanism might be confused with the turbulent flow regime. However, there is an important difference between chaotic advection in laminar flows and turbulent regime: the velocity components of chaotic advection in a laminar flow remains constant over time at any point in space, while for the turbulent regime, these velocity components are completely random.

Chaotic advection must not also be confused with the non-chaotic advection mechanism. Non-chaotic advection is simply a transversal transport, where a perturbation of the system causes the fluid layers in a laminar flow to move from their position to another, but without generation of chaotic patterns. In this case, transversal transport simply generates new contact surface between the two solutions, and the observed improvement in the mixing is only due to molecular diffusion. An example of non-chaotic advection can be observed in curved pipes or channels in particular conditions. Considering a laminar flow in

a toroidal channel, the centrifugal force caused by the bent tube causes the fluid to move outward. As a result, two vortices will form from the motion of secondary flows; these vortices are usually called Dean vortices. In the situation depicted in Figure 1.22, however, Dean vortices will enhance the mixing only if the two solutions are introduced from the left and the right of the cross-section of the channel. If the two streams were introduced from the top and the bottom, in fact, the Dean vortices would keep them in their respective channel section and advection would not lead to any improvement by molecular diffusion.

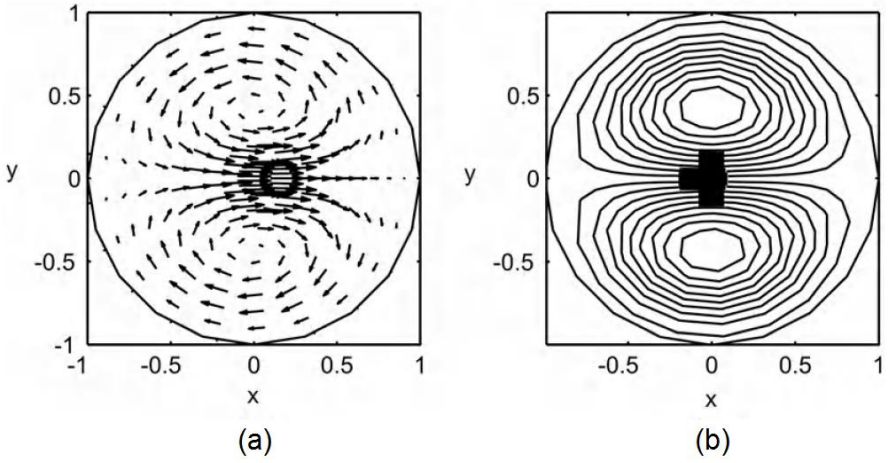

Figure 1.22: Representation of (a) secondary velocity field and (b) relative stream line of Dean vortices inside a curved tube. Image reprinted with permission from N-T. Nguyen, Micromixers, 2012.

The behaviour and intensity of Dean vortices in a bended pipe can be quantified with the Dean number (De), that numerically represents the ratio between centrifugal force and inertial force:

$$De = Re\sqrt{\frac{L}{R}} \qquad Equation\ 1.7$$

Where Re is the Reynolds number, L is the channel diameter and R is the radius of curvature. For Dean numbers lower than the critical Dean number (ca. 150), only a pair of two counter-rotating vortices are present, while for higher values the strong centrifugal force causes the formation of two additional vortices at the outer channel wall thus causing a displacement in the symmetry. The critical Dean number is, in other words, the border line between non-chaotic and chaotic advection mechanism in curved pipes. In the previous example then, chaotic advection can be achieved by either increasing the Reynolds number or increasing the L/R ratio.

Other examples of systems that can generate chaotic advection are helical and twisted pipes (where the term twisted pipe denotes curved pipe segments that are not all in the same plane)[239]. In these cases, the 3-dimensional geometry of the reactors increases the asymmetry and thus generates Dean vortices with different shapes.

1.6.3. Micromixers

Micromixers are devices that are designed to improve the mixing of two or more solutions flowing in a milli- or micro-reactor. Depending on how the mixing is carried out, micromixers can be divided into either passive and active (Figure 1.23)[236]. Passive micromixers do not require an external input to enhance the mixing and they can be further divided depending on the mixing mechanism that they enhance is molecular diffusion based or chaotic advection based. On the other hand, active micromixers rely on an external field, and the mixing mechanism is then related to the physical phenomena used.

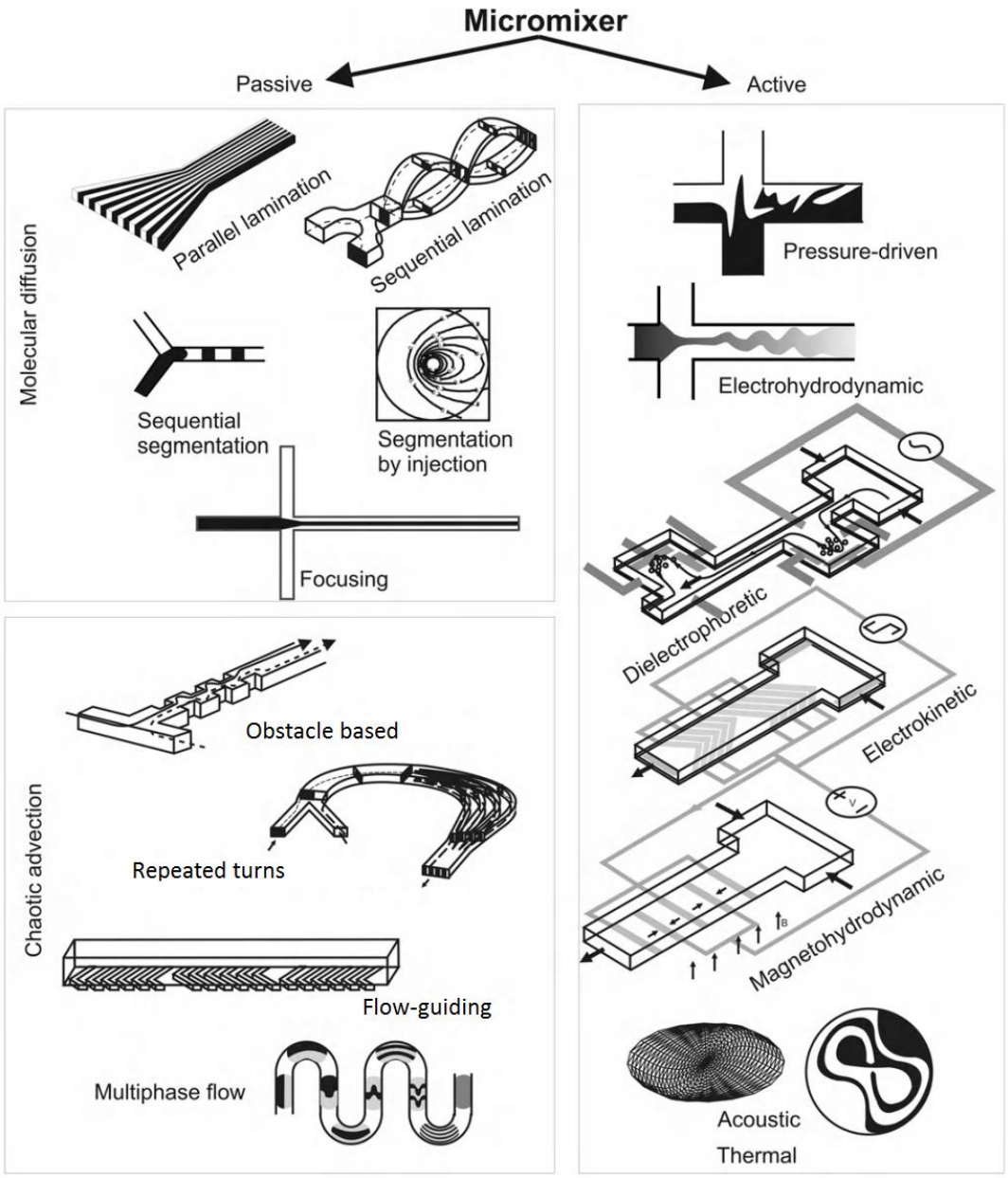

Figure 1.23: Micromixers can be categorised in passive or active depending on how the perturbation is introduced. Passive micromixers can be further divided in molecular diffusion based or chaotic advection based. Image reprinted with permission from N-T. Nguyen, Micromixers, 2012.

1.6.3.1. Passive micromixers

Molecular diffusion based micromixers

As already pointed out before, large concentration gradients, interfacial areas and diffusion coefficients are the parameters that can improve the diffusive flux. Gradient and diffusion coefficients can be controlled by adjusting the concentration and temperature or viscosity respectively, while geometric solutions are necessary to improve the interfacial area between the two solutions or to decrease their striation thickness. Parallel lamination mixers,

for example, increase the interfacial area and decrease the striation thickness by splitting the two solutions into smaller substreams and rejoining them in a single channel at a later moment[240]. In sequential lamination mixers, on the other hand, the two solutions are firstly joined together and then split into two channels and recombined[241]. This single transformation can be repeated several times in sequence to further improve the mixing. In sequential segmentation mixers, the two solutions are introduced in a channel in alternate segments[242]. In this case, the mixing by diffusion depends on the length of the single segment. Injection based segmentation mixers rely on a nozzle spraying one solution into a stream of the second solution[236], while in focusing mixers two streams of the same solution are injected into the stream of the second one, creating a sandwich-like flow configuration[243].

Chaotic advection based micromixers

In most passive diffusion based micromixers, the advection is parallel to the flow direction, and thus transverse transport is caused by molecular diffusion only. Advection in a three-dimensional pattern, as discussed before, can cause secondary transversal phenomena, called chaotic advection, and improve the mixing. In general, chaotic advection can be generated by stretching, folding or breaking of the laminar flow. The geometry of the micromixer and the flow Reynolds number strongly affect the efficiency of the mixing. T-shape connections can for example act as mixers at the appropriate Reynolds number regime[244]. Due to the sharp 90° turn, the large inertial force can in fact cause vortices that might lead to chaotic advection. T-shape mixers, however, are usually used in combination with other mixers, such as obstacle-based mixers[245] or repeated turns mixers[246,247]. The former are simple tubes with obstacles along the reactor channel; these obstacles, at high Reynolds numbers, disrupt the laminar flow thus inducing transversal transport. The latter, on the other hand, are formed by repeated steep turns that intensify the Dean vortices produced by the T-shape connection. These turns can be developed in three dimensions, such as helicoidal shapes, allowing complete mixing in a very short time. An interesting type of chaotic advection based micromixer is the flow-guiding structure mixer[248,249], where secondary flow patterns are generated by ridges or grooves placed at a channel wall and at a certain angle with respect to the direction of the flow. Multiphase mixers, on the other hand, take advantage of the presence of an additional solvent that functions as a carrier[250,251]. The simple generation of a droplet causes the formation of vortices due to the internal flow field. Finally, micromixers can also be made of a combination of two or more archetypes, thus creating complex structures that take advantage of steep turns and variation in velocity distribution to improve the mixing.

1.6.3.2. Active micromixers

Active mixers, as already mentioned before, induce disturbance by an external field. The external field is needed in order to make the interface between the two solutions unstable. The nature of the disturbance differentiates the various mixers. The most common active mixers are: pressure-driven[252], where the disturbance is created by external actuators in form of pressure pulses; electrohydrodynamic[253], where the mixing is achieved by the actuation of an electrical field on a dielectric fluid; thermal[254], where the disturbance is introduced by a temperature gradient. On top of them, other active mixers worth mentioning are dielectrophoretic[255], electrokinetic[256], magnetohydrodynamic[257] and acoustic[258].

1.7. Aim of the thesis

The aim of the thesis was the design and optimisation of a novel method for the synthesis of supported noble metal nanoparticles and the application of such materials in specific catalytic hydrogenation reactions. The first objective was then to build up and optimise a new setup that allowed the production of nanomaterials based on the well-known sol-immobilisation technique (Chapter 3). The novelty in this apparatus is the possibility to produce the entire supported metal nanoparticles (mono and bimetallic) directly in a continuous mode. The second objective was to study a model hydrogenation reaction, such as the nitrophenol reduction to aminophenol, using the catalysts produced with the newly optimised setup (Chapter 4). The flexibility of the catalyst synthetic technique allows the production of metal nanoparticle with a controlled size distribution, making the eventual correlation between catalytic activity and particle size much clearer and more accurate. Finally, the last objective was to deeply study a challenging hydrogenation reaction, such as the hydrogenation of cinnamaldehyde (Chapter 5); the presence of a conjugated vinyl and carbonyl group in this substrate served well the purpose.

1.8. References

1 G. Cecchin, G. Morini and F. Piemontesi, *Ziegler-Natta catalysts in Kirk-Othmer Encyclopedia of Chemical Technology*, 2003.

2 J. B. Robertson, *Platin. Met. Rev.*, 1975, **19**, 64–69.

3 J. Sá and J. Szlachetko, *Catal. Letters*, 2014, **144**, 197–203.

4 J. Hagen, *Industrial Catalysis: A Practical Approach*, Wiley, Third Edit., 2015.

5 C. Kohlpaintner, M. Schulte, J. Falbe, P. Lappe and J. Weber, *Aldehydes, Aliphatic and Araliphatic in Ullmann's Encyclopedia of Industrial Chemistry*, Wiley, 2005.

6 H. Cheung, R. S. Tanke and G. P. Torrence, *Acetic Acid in Ullmann's Encyclopedia of Industrial Chemistry*, 2005.

7 V. L. Budarin, P. S. Shuttleworth, J. H. Clark and R. Luque, *Curr. Org. Synth.*, 2010, **7**, 614–627.

8 M. Appl, *Ammonia in Ullmann's Encyclopedia of Industrial Chemistry*, 2005.

9 T. Kaneko, F. Derbishire, E. Makino, D. Gray and M. Tamura, *Coal Liquefaction in Ullmann's Encyclopedia of Industrial Chemistry*, 2005.

10 I. E. Wachs, *Catal. Today*, 1996, **27**, 437–455.

11 I. E. Wachs, *Catal. Today*, 2005, **100**, 79–94.

12 G. Martino, *Stud. Surf. Sci. Catal.*, 2000, **130**, 83–103.

13 H. Weller, *Curr. Opin. Colloid Interface Sci.*, 1998, **3**, 194–199.

14 Y. Wang and N. Herron, *J. Phys. Chem.*, 1991, **95**, 525–532.

15 P. Buffat and J. P. Borel, *Phys. Rev. A*, 1976, **13**, 2287–2298.

16 A. I. Ekimov, A. L. Efros and A. A. Onushchenko, *Solid State Commun.*, 1985, **56**, 921–924.

17 E. Hutter and J. H. Fendler, *Adv. Mater.*, 2004, **16**, 1685–1706.

18 L. Catherine and O. Pluchery, *Gold Nanoparticles in the Past: Before the Nanotechnology Era in Gold Nanoparticles for Physics, Chemistry and Biology*, 2012.

19 World Gold Council, Gold Demand Sectors, https://www.gold.org/about-gold/gold-demand/sectors-demand, (accessed 1 May 2018).

20 World Gold Council, New Uses for Gold, https://www.gold.org/about-gold/gold-demand/sectors-of-demand/uses-of-gold, (accessed 1 May 2018).

21 G. C. Bond and P. A. Sermon, *Gold Bull.*, 1973, **6**, 102–105.

22 G. Hutchings, *J. Catal.*, 1985, **96**, 292–295.

23 M. Haruta, T. Kobayashi, H. Sano and N. Yamada, *Chem. Lett.*, 1987, 405–408.

24 A. M. Echavarren, A. S. K. Hashmi and F. D. Toste, *Adv. Synth. Catal.*, 2016, **358**, 1347.

25 A. Corma and H. Garcia, *Chem. Soc. Rev.*, 2008, **37**, 2096–2126.

26 C. Della Pina, E. Falletta and M. Rossi, *Chem. Soc. Rev.*, 2012, **41**, 350–369.

27 G. C. Bond and D. T. Thompson, *Catal. Rev.*, 1999, **41**, 319–388.

28 T. Hayashi, L.-B. Han, S. Tsubota and M. Haruta, *Ind. Eng. Chem. Res.*, 1995, **34**, 2298–2304.

29 L. Prati and M. Rossi, *J. Catal.*, 1998, **176**, 552–560.

30 G. C. Bond, *Metal-Catalysed Reactions of Hydrocarbons*, 2005.

31 C. Milone, C. Crisafulli, R. Ingoglia, L. Schipilliti and S. Galvagno, *Catal. Today*, 2007, **122**, 341–351.

32 S. E. Davis, M. S. Ide and R. J. Davis, *Green Chem.*, 2013, **15**, 17–45.

33 J. A. Rodriguez, *Catal. Today*, 2011, **160**, 3–10.

34 N. Russo, D. Fino, G. Saracco and V. Specchia, *Catal. Today*, 2006, **117**, 214–219.

35 P. Johnston, N. Carthey and G. J. Hutchings, *J. Am. Chem. Soc.*, 2015, **137**, 14548–14557.

36 W. Hou, N. A. Dehm and R. W. J. Scott, *J. Catal.*, 2008, **253**, 22–27.

37 D. Mott, J. Luo, P. N. Njoki, Y. Lin, L. Wang and C.-J. Zhong, *Catal. Today*, 2007, **122**, 378–385.

38 S. A. Ojo, A. Lateef, M. A. Azeez, S. M. Oladejo, A. S. Akinwale, T. B. Asafa, T. A. Yekeen, A. Akinboro, I. C. Oladipo, E. B. Gueguim-Kana and L. S. Beukes, *IEEE Trans. Nanobioscience*, 2016, **15**, 433–442.

39 C. L. Bracey, P. R. Ellis and G. J. Hutchings, *Chem. Soc. Rev.*, 2009, **38**, 2231–2243.

40 M. Sankar, N. Dimitratos, P. J. Miedziak, P. P. Wells, C. J. Kiely and G. J. Hutchings, *Chem. Soc. Rev.*, 2012, **41**, 8099–8139.

41 D. M. Alonso, S. G. Wettstein and J. A. Dumesic, *Chem. Soc. Rev.*, 2012, **41**, 8075–8098.

42 L. Guczi, *Catal. Letters*, 1990, **7**, 205–212.

43 T. Graham, *Proc. R. Soc. London*, 1868, **17**, 212–220.

44 T. Graham, *Proc. R. Soc. London*, 1867, **16**, 422–427.

45 J. P. Boitiaux, J. Cosyns and S. Vasudevan, *Appl. Catal.*, 1983, **6**, 41–51.

46 J. Muzart, *Tetrahedron*, 2003, **59**, 5789–5816.

47 J. Emsley, *Nature's Building Blocks: An A-Z Guide to the Elements*, 2011.

48 N. Miyaura, T. Yanagi and A. Suzuki, *Synth. Commun.*, 1981, **11**, 513–519.

49 Nobel prize, The Nobel Prize in Chemistry 2010, https://www.nobelprize.org/nobel_prizes/chemistry/laureates/2010/, (accessed 1 May 2018).

50 P. Liu and J. K. Norskov, *Phys. Chem. Chem. Phys.*, 2001, **3**, 3814–3818.

51 R. Burch, *Acc. Chem. Res.*, 1982, **15**, 24–31.

52 M. Chen, D. Kumar, C.-W. Yi and D. W. Goodman, *Science*, 2005, **310**, 291–293.

53 F. Liu, D. Wechsler and P. Zhang, *Chem. Phys. Lett.*, 2008, **461**, 254–259.

54 O. Metin, X. Sun and S. Sun, *Nanoscale*, 2013, **5**, 910–912.

55 N. Dimitratos, J. A. Lopez-Sanchez, J. M. Anthonykutty, G. Brett, A. F. Carley, R. C. Tiruvalam, A. A. Herzing, C. J. Kiely, D. W. Knight and G. J. Hutchings, *Phys. Chem. Chem. Phys.*, 2009, **11**, 4952–4961.

56 G. J. Hutchings, *Chem. Commun.*, 2008, 1148–1164.

57 N. Bhattarai, S. Khanal, J. J. Velazquez-Salazar and M. Jose-Yacaman, eds. F. L. Deepak, A. Mayoral and R. Arenal, Springer International Publishing, Cham, 2015, pp. 59–91.

58 H. Gu, X. Xu, A. A. Chen, P. Ao and X. Yan, *Catal. Commun.*, 2013, **41**, 65–69.

59 R. Liu, Y. Yu, K. Yoshida, G. Li, H. Jiang, M. Zhang, F. Zhao, S. ichiro Fujita and M. Arai, *J. Catal.*, 2010, **269**, 191–200.

60 P. J. Miedziak, Q. He, J. K. Edwards, S. H. Taylor, D. W. Knight, B. Tarbit, C. J. Kiely and G. J. Hutchings, *Catal. Today*, 2011, **163**, 47–54.

61 L. Kesavan, R. Tiruvalam, M. H. A. Rahim, M. I. bin Saiman, D. I. Enache, R. L. Jenkins, N. Dimitratos, J. A. Lopez-Sanchez, S. H. Taylor, D. W. Knight, C. J. Kiely and G. J. Hutchings, *Science*, 2011, **331**, 195–199.

62 W. Luo, M. Sankar, A. M. Beale, Q. He, C. J. Kiely, P. C. A. Bruijnincx and B. M. Weckhuysen, *Nat. Commun.*, 2015, **6**, 6540, 1–10.

63 S. Nishimura, N. Ikeda and K. Ebitani, *Catal. Today*, 2014, **232**, 89–98.

64 C. Jiaying, M. Hong, Z. Junjie, S. Qi, D. Zhongtian, H. Yizheng and X. Jie, *Chem. – A Eur. J.*, 2013, **19**, 14215–14223.

65 H. A. Stephen K., L. Christian, D. René, R. Matthias, R. Tanuja D. and R. Frank, *Angew. Chemie Int. Ed.*, 2009, **48**, 8243–8246.

66 B. Panda and T. K. Sarkar, *Chem. Commun.*, 2010, **46**, 3131–3133.

67 A. M. Venezia, L. F. Liotta, G. Pantaleo, V. La Parola, G. Deganello, A. Beck, Z. Koppány, K. Frey, D. Horváth and L. Guczi, *Appl. Catal. A Gen.*, 2003, **251**, 359–368.

68 J. K. Edwards, A. F. Carley, A. A. Herzing, C. J. Kiely and G. J. Hutchings, *Faraday Discuss.*, 2008, **138**, 225–239.

69 J. K. Edwards and G. J. Hutchings, *Angew. Chem. Int. Ed. Engl.*, 2008, **47**, 9192–8.

70 J. K. Norskov, T. Bligaard, B. Hvolbaek, F. Abild-Pedersen, I. Chorkendorff and C. H. Christensen, *Chem. Soc. Rev.*, 2008, **37**, 2163–2171.

71 G. A. Somorjai, eds. D. D. Eley, H. Pines and P. B. B. T.-A. in C. Weisz, Academic Press, 1977, vol. 26, pp. 1–68.

72 Z. Yang, R. Wu and D. W. Goodman, *Phys. Rev. B*, 2000, **61**, 14066–14071.

73 Chen, Y. Cai, Z. Yan and D. W. Goodman, *J. Am. Chem. Soc.*, 2006, **128**, 6341–6346.

74 P. Haider, J.-D. Grunwaldt, R. Seidel and A. Baiker, *J. Catal.*, 2007, **250**, 313–323.

75 G. J. Hutchings, M. S. Hall, A. F. Carley, P. Landon, B. E. Solsona, C. J. Kiely, A. Herzing, M. Makkee, J. A. Moulijn, A. Overweg, J. C. Fierro-Gonzalez, J. Guzman and B. C. Gates, *J. Catal.*, 2006, **242**, 71–81.

76 J. Guzman and B. C. Gates, *J. Am. Chem. Soc.*, 2004, **126**, 2672–2673.

77 S. Carrettin, P. Concepción, A. Corma, M. J. López Nieto and V. F. Puntes, *Angew. Chemie Int. Ed.*, 2004, **43**, 2538–2540.

78 N. Lopez, T. V. W. Janssens, B. S. Clausen, Y. Xu, M. Mavrikakis, T. Bligaard and J. K. Nørskov, *J. Catal.*, 2004, **223**, 232–235.

79 M. F. Camellone and S. Fabris, *J. Am. Chem. Soc.*, 2009, **131**, 10473–10483.

80 T. Szumełda, A. Drelinkiewicz, R. Kosydar and J. Gurgul, *Appl. Catal. A Gen.*, 2014, **487**, 1–15.

81 J. A. van Bokhoven, C. Louis, J. T. Miller, M. Tromp, O. V. Safonova and P. Glatzel, *Angew. Chemie Int. Ed.*, 2006, **45**, 4651–4654.

82 A. Sanchez, S. Abbet, U. Heiz, W.-D. Schneider, H. Häkkinen, R. N. Barnett and U. Landman, *J. Phys. Chem. A*, 1999, **103**, 9573–9578.

83 L. Prati and A. Villa, *Catalysts*, 2012, **2**, 24–37.

84 M. V Landau, *Sol-Gel Process in Handbook of Heterogeneous Catalysis*, 2008.

85 F. Schuth, M. Hesse and K. K. Unger, *Precipitation and Coprecipitation in Handbook of Heterogeneous Catalysis*, 2008.

86 Q. He, S. J. Freakley, J. K. Edwards, A. F. Carley, A. Y. Borisevich, Y. Mineo, M. Haruta, G. J. Hutchings and C. J. Kiely, *Nat. Commun.*, 2016, **7**, 12905, 1–8.

87 E. Marceau, X. Carrier, M. Che, O. Clause and C. Marcilly, *Ion Exchange and Impregnation in Handbook of Heterogeneous Catalysis*, 2008.

88 M. Sankar, Q. He, M. Morad, J. Pritchard, S. J. Freakley, J. K. Edwards, S. H. Taylor, D. J. Morgan, A. F. Carley, D. W. Knight, C. J. Kiely and G. J. Hutchings, *ACS Nano*, 2012, **6**, 6600–6613.

89 M. Tada and Y. Iwasawa, *Supported Catalysts from Chemical Vapor Deposition and Related Techniques in Handbook of Heterogeneous Catalysis*, 2008.

90 P. Zhao, N. Li and D. Astruc, *Coord. Chem. Rev.*, 2013, **257**, 638–665.

91 G. Inaki, M. P. J., N. Ewa, D. Mark, M. D. J., H. G. J. and T. S. H., *ChemSusChem*, 2015, **8**, 473–480.

92 N. Pernicone and F. Traina, in *Preparation of Catalysts II*, eds. B. Delmon, P. Grange, P.

Jacobs and G. B. T.-S. in S. S. and C. Poncelet, Elsevier, 1979, vol. 3, pp. 321–351.

93 J. K. Edwards, J. Pritchard, M. Piccinini, G. Shaw, Q. He, A. F. Carley, C. J. Kiely and G. J. Hutchings, *J. Catal.*, 2012, **292**, 227–238.

94 C. W. B. Bezerra, L. Zhang, H. Liu, K. Lee, A. L. B. Marques, E. P. Marques, H. Wang and J. Zhang, *J. Power Sources*, 2007, **173**, 891–908.

95 P. Gallezot and D. Richard, *Selective Hydrogenation of α,β-Unsaturated Aldehydes*, 1998, vol. 40.

96 N. Dimitratos, J. A. Lopez-Sanchez, J. M. Anthonykutty, G. Brett, A. F. Carley, R. C. Tiruvalam, A. A. Herzing, C. J. Kiely, D. W. Knight and G. J. Hutchings, *Phys. Chem. Chem. Phys.*, 2009, **11**, 4952–4961.

97 I. Okura, *Encycl. Nanosci. Nanotechnol.*, 2004, **8**, 41–48.

98 D. Thompson, *Gold Bull.*, 2007, **40**, 267–269.

99 Y. Wang, J. He, C. Liu, W. H. Chong and H. Chen, *Angew. Chemie - Int. Ed.*, 2015, **54**, 2022–2051.

100 Y. Xia, Y. Xiong, B. Lim and S. E. Skrabalak, *Nanosctructures*, 2009, 60–103.

101 N. T. K. Thanh, N. Maclean and S. Mahiddine, *Chem. Rev.*, 2014, **3**, 7610–7630.

102 V. K. LaMer and R. H. Dinegar, *J. Am. Chem. Soc.*, 1950, **72**, 4847–4854.

103 L. Colombi Ciacchi, W. Pompe and A. De Vita, *J. Am. Chem. Soc.*, 2001, **123**, 7371–7380.

104 L. Colombi Ciacchi, W. Pompe and A. De Vita, *J. Phys. Chem. B*, 2003, **107**, 1755–1764.

105 S. Auer and D. Frenkel, *Nature*, 2001, **409**, 1020–1023.

106 U. Gasser, E. R. Weeks, A. Schofield, P. N. Pusey and D. A. Weitz, *Science*, 2001, **292**, 258–262.

107 M. G. Richmond, *Coord. Chem. Rev.*, 2003, **241**, 273–294.

108 S.-M. Lee and W.-T. Wong, *J. Clust. Sci.*, 1998, **9**, 417–444.

109 T. A. R., H. Susan and Y. Peidong, *Small*, 2008, **4**, 310–325.

110 X. Y. and X. Y., *Adv. Mater.*, 2007, **19**, 3385–3391.

111 B. Wiley, Y. Sun and Y. Xia, *Acc. Chem. Res.*, 2007, **40**, 1067–1076.

112 T. Sugimoto, *Growth in Monodispersed Particles*, 2001.

113 H. Zheng, R. K. Smith, Y. Jun, C. Kisielowski, U. Dahmen and A. P. Alivisatos, *Science*, 2009, **324**, 1309–1312.

114 P. W. Voorhees, *J. Stat. Phys.*, 1985, **38**, 231–252.

115 L. Prati and A. Villa, *Acc. Chem. Res.*, 2014, **47**, 855–863.

116 Y. Wang, Z. Xiao and L. Wu, *Curr. Org. Chem.*, 2013, **17**, 1325–1333.

117 C.-J. Jia and F. Schüth, *Phys. Chem. Chem. Phys.*, 2011, **13**, 2457–2487.

118 J. P. Brunelle, *Pure Appl. Chem.*, 1978, **50**, 1211–1229.

119 J. Lyklema, *Pure Appl. Chem.*, 1991, 63, 895–906.

120 D. H. Everett, *Pure Appl. Chem.*, 1972, 31, 577–638.

121 G. Ferard, *Pure Appl. Chem.*, 1994, 66, 891–896.

122 P. Serp and J. L. Figueiredo, *Carbon materials for catalysis*, 2009.

123 F. Zhao, M. Shirai, Y. Ikushima and M. Arai, *J. Mol. Catal. A Chem.*, 2002, **180**, 211–219.

124 D. Cantillo and O. C. Kappe, *ChemCatChem*, 2014, **6**, 3286–3305.

125 J. A. Farmer and C. T. Campbell, *Science*, 2010, **329**, 933–936.

126 C. T. Campbell, S. C. Parker and D. E. Starr, *Science*, 2002, **298**, 811–814.

127 C. T. Campbell, *Acc. Chem. Res.*, 2013, **46**, 1712–1719.

128 Y. Tan, Y. Li and D. Zhu, *Noble Metal Nanoparticles*, 2004, vol. 8.

129 A. W. Olsen and Z. H. Kafafi, *J. Am. Chem. Soc.*, 1991, **113**, 7758–7760.

130 E. B. Zuckerman, K. J. Klabunde, B. J. Olivier and C. M. Sorensen, *Chem. Mater.*, 1989, **1**, 12–14.

131 S. A. Harfenist, Z. L. Wang, M. M. Alvarez, I. Vezmar and R. L. Whetten, *J. Phys. Chem.*, 1996, **100**, 13904–13910.

132 H. S. A., W. Z. L., W. R. L., V. Igor and A. M. M., *Adv. Mater.*, 1997, **9**, 817–822.

133 Z. L. Wang, S. A. Harfenist, R. L. Whetten, J. Bentley and N. D. Evans, *J. Phys. Chem. B*, 1998, **102**, 3068–3072.

134 G. Cardenas-Trivino, K. J. Klabunde and E. B. Dale, *Langmuir*, 1987, **3**, 986–992.

135 Mafuné Fumitaka, J. Kohno, Y. Takeda and T. Kondow, *J. Phys. Chem. B*, 2002, **106**, 7575–7577.

136 Mafuné Fumitaka, J. Kohno, Y. Takeda, T. Kondow and H. Sawabe, *J. Phys. Chem. B*, 2001, **105**, 5114–5120.

137 Mafuné Fumitaka, J. Kohno, Y. Takeda, T. Kondow and H. Sawabe, *J. Phys. Chem. B*, 2000, **104**, 9111–9117.

138 T. J. Mason, *Advances in Sonochemistry, vol. 5*, 1999.

139 S. A. Yeung, R. Hobson, S. Biggs and F. Grieser, *J. Chem. Soc. Chem. Commun.*, 1993, 378–379.

140 Y. Nagata, Y. Watananabe, S. Fujita, T. Dohmaru and S. Taniguchi, *J. Chem. Soc. Chem. Commun.*, 1992, 1620–1622.

141 Y. Mizukoshi, R. Oshima, Y. Maeda and Y. Nagata, *Langmuir*, 1999, **15**, 2733–2737.

142 K. Okitsu, H. Bandow, Y. Maeda and Y. Nagata, *Chem. Mater.*, 1996, **8**, 315–317.

143 A. Henglein and M. Giersig, *J. Phys. Chem. B*, 1999, **103**, 9533–9539.

144 A. Henglein and D. Meisel, *Langmuir*, 1998, **14**, 7392–7396.

145 K. Kurihara, J. Kizling, P. Stenius and J. H. Fendler, *J. Am. Chem. Soc.*, 1983, **105**, 2574–

2579.

146 A. Henglein, *J. Phys. Chem. B*, 2000, **104**, 2201–2203.

147 R. Rafaeloff, Y. Haruvy, J. Binenboym, G. Baruch and L. A. Rajbenbach, *J. Mol. Catal.*, 1983, **22**, 219–233.

148 Y. Zhou, C. Y. Wang, Y. R. Zhu and Z. Y. Chen, *Chem. Mater.*, 1999, **11**, 2310–2312.

149 Z. Yong, Y. S. H., W. C. Y., L. X. G., Z. Y. R. and C. Z. Y., *Adv. Mater.*, 1999, **11**, 850–852.

150 N. Toshima, T. Takahashi and H. Hirai, *Chem. Lett.*, 1985, **14**, 1245–1248.

151 N. Toshima and T. Takahashi, *Bull. Chem. Soc. Jpn.*, 1992, **65**, 400–409.

152 S. Kundu, L. Peng and H. Liang, *Inorg. Chem.*, 2008, **47**, 6344–6352.

153 W. Yu, W. Tu and H. Liu, *Langmuir*, 1999, **15**, 6–9.

154 W. Tu and H. Liu, *Chem. Mater.*, 2000, **12**, 564–567.

155 T. Tano, K. Esumi and K. Meguro, *J. Colloid Interface Sci.*, 1989, **133**, 530–533.

156 K. Esumi, T. Tano and K. Meguro, *Langmuir*, 1989, **5**, 268–270.

157 R. M. T. and Q. S. A., *Angew. Chemie Int. Ed. English*, 2018, **34**, 2240–2241.

158 M. T. Reetz and W. Helbig, *J. Am. Chem. Soc.*, 1994, **116**, 7401–7402.

159 S. M. Rogers, C. R. A. Catlow, C. E. Chan-Thaw, D. Gianolio, E. K. Gibson, A. L. Gould, N. Jian, A. J. Logsdail, R. E. Palmer, L. Prati, N. Dimitratos, A. Villa and P. P. Wells, *ACS Catal.*, 2015, **5**, 4377–4384.

160 D. Burshtain, L. Zeiri and S. Efrima, *Langmuir*, 1999, **15**, 3050–3055.

161 R. S. Underhill and G. Liu, *Chem. Mater.*, 2000, **12**, 3633–3641.

162 T. S. Ahmadi, Z. L. Wang, T. C. Green, A. Henglein and M. A. El-Sayed, *Science*, 1996, **272**, 1924–1925.

163 A. Henglein, *J. Phys. Chem. B*, 2000, **104**, 6683–6685.

164 G. Frens, *Nat. Phys. Sci.*, 1973, **241**, 20–22.

165 N. R. Jana, L. Gearheart and C. J. Murphy, *Chem. Mater.*, 2001, **13**, 2313–2322.

166 S. Pathak, M. T. Greci, R. C. Kwong, K. Mercado, G. K. S. Prakash, G. A. Olah and M. E. Thompson, *Chem. Mater.*, 2000, **12**, 1985–1989.

167 Y. Wang, J. Ren, K. Deng, L. Gui and Y. Tang, *Chem. Mater.*, 2000, **12**, 1622–1627.

168 A. B. R. Mayer, W. Grebner and R. Wannemacher, *J. Phys. Chem. B*, 2000, **104**, 7278–7285.

169 K. R. Brown, D. G. Walter and M. J. Natan, *Chem. Mater.*, 2000, **12**, 306–313.

170 M. W. G. de Bolster, *Pure Appl. Chem.*, 1997, 69, 1251–1303.

171 A. D. Pomogailo and G. I. Dzhardimalieva, *Nanostructured materials preparation via condensation ways*, 2014, vol. 9789048125.

172 D. V. Goia and E. Matijević, *New J. Chem.*, 1998, **22**, 1203–1215.

173 S. Saha, A. Pal, S. Kundu, S. Basu and T. Pal, *Langmuir*, 2010, **26**, 2885–2893.

174 P. Wardman, *J. Phys. Chem. Ref. Data*, 1989, **18**, 1637–1755.

175 H. Borsook and G. Keighley, *Proc. Natl. Acad. Sci. U. S. A.*, 1933, **19**, 875–878.

176 H. Borsook, H. W. Davenport, C. E. P. Jeffreys and R. C. Warner, *J. Biol. Chem.*, 1937, **117**, 237–279.

177 N. L. Pacioni, C. D. Borsarelli, V. Rey and A. V Veglia, eds. E. I. Alarcon, M. Griffith and K. I. Udekwu, Springer International Publishing, Cham, 2015, pp. 13–46.

178 D. C. Harris, *Quantitative Chemical Analysis*, 2007.

179 A. J. Bard, *Standard Potentials in Aqueous Solution*, 1985.

180 A. J. Bard, *Electrochemical Methods. Fundamentals and Applications*, 2001.

181 W. M. Haynes, *Handbook of Chemistry and Physics*, 2014.

182 H. Tsunoyama, N. Ichikuni and T. Tsukuda, *Langmuir*, 2008, **24**, 11327–11330.

183 C. Deraedt, L. Salmon, S. Gatard, R. Ciganda, R. Hernandez, J. Ruiz and D. Astruc, *Chem. Commun.*, 2014, **50**, 14194–14196.

184 A. Krittayavathananon, P. Srimuk, S. Luanwuthi and M. Sawangphruk, *Anal. Chem.*, 2014, **86**, 12272–12278.

185 K. Esumi, N. Sato, K. Torigoe and K. Meguro, *J. Colloid Interface Sci.*, 1992, **149**, 295–298.

186 M. V Seregina, L. M. Bronstein, O. A. Platonova, D. M. Chernyshov, P. M. Valetsky, J. Hartmann, E. Wenz and M. Antonietti, *Chem. Mater.*, 1997, **9**, 923–931.

187 S. N. Sidorov, L. M. Bronstein, P. M. Valetsky, J. Hartmann, H. Cölfen, H. Schnablegger and M. Antonietti, *J. Colloid Interface Sci.*, 1999, **212**, 197–211.

188 M. Wuithschick, A. Birnbaum, S. Witte, M. Sztucki, U. Vainio, N. Pinna, K. Rademann, F. Emmerling, R. Kraehnert and J. Polte, *ACS Nano*, 2015, **9**, 7052–7071.

189 J. Polte, T. T. Ahner, F. Delissen, S. Sokolov, F. Emmerling, A. F. Thünemann and R. Kraehnert, *J. Am. Chem. Soc.*, 2010, **132**, 1296–1301.

190 G.-W. Wu, S.-B. He, H.-P. Peng, H.-H. Deng, A.-L. Liu, X.-H. Lin, X.-H. Xia and W. Chen, *Anal. Chem.*, 2014, **86**, 10955–10960.

191 X. Yujie, M. Joseph M., Y. Yadong and X. Younan, *Angew. Chemie*, 2006, **119**, 804–808.

192 S. Y. and X. Y., *Adv. Mater.*, 2002, **14**, 833–837.

193 L. C.-L., W. C.-C. and W. Y.-Y., *Adv. Funct. Mater.*, 2001, **11**, 344–347.

194 S. Ayyappan, R. S. Gopalan, G. N. Subbanna and C. N. R. Rao, *J. Mater. Res.*, 1997, **12**, 398–401.

195 Y. Sun, Y. Yin, B. T. Mayers, T. Herricks and Y. Xia, *Chem. Mater.*, 2002, **14**, 4736–4745.

196 H. Hirai, Y. Nakao and N. Toshima, *J. Macromol. Sci. Part A - Chem.*, 1979, **13**, 727–750.

197 J. N. R., G. L. and M. C. J., *Adv. Mater.*, 2001, **13**, 1389–1393.

198 W. Wang, Q. Chen, C. Jiang, D. Yang, X. Liu and S. Xu, *Colloids Surfaces A Physicochem. Eng. Asp.*, 2007, **301**, 73–79.

199 W. Yu and H. Liu, *Chem. Mater.*, 1998, **10**, 1205–1207.

200 J. Wu, A. Gross and H. Yang, *Nano Lett.*, 2011, **11**, 798–802.

201 K. Meguro, M. Torizuka and K. Esumi, *Bull. Chem. Soc. Jpn.*, 1988, **61**, 341–345.

202 H. Bonnemann and W. Brijoux, *Advanced Catalysts and Nanostructured Materials*, 1996.

203 D. V Goia, *J. Mater. Chem.*, 2004, **14**, 451–458.

204 I. Capek, *Noble Metal Nanoparticles*, 2017.

205 X. Liu, R. Huang and J. Zhu, *Chem. Mater.*, 2008, **20**, 192–197.

206 Z. J., L. H., W. Z. and M. N., *Adv. Funct. Mater.*, 2007, **17**, 3295–3303.

207 S. A. Tikhomirov, M. I. Alymov, I. V Tregubova and V. S. Shustov, *Nanotechnologies Russ.*, 2011, **6**, 268–273.

208 A. K. Sra and R. E. Schaak, *J. Am. Chem. Soc.*, 2004, **126**, 6667–6672.

209 Y. Vasquez, Z. Luo and R. E. Schaak, *J. Am. Chem. Soc.*, 2008, **130**, 11866–11867.

210 Y. Sun, B. T. Mayers and Y. Xia, *Nano Lett.*, 2002, **2**, 481–485.

211 J. DeMello and A. DeMello, *Lab Chip*, 2004, **4**, 11N–15N.

212 S. Marre and K. F. Jensen, *Chem. Soc. Rev.*, 2010, **39**, 1183–1202.

213 A. M. Karim, N. Al Hasan, S. Ivanov, S. Siefert, R. T. Kelly, N. G. Hallfors, A. Benavidez, L. Kovarik, A. Jenkins, R. E. Winans and A. K. Datye, *J. Phys. Chem. C*, 2015, **119**, 13257–13267.

214 K. S. Elvira, X. Casadevall i Solvas, R. C. R. Wootton and A. J. de Mello, *Nat. Chem.*, 2013, **5**, 905–915.

215 A. S. Martin and K. F. Jensen, *Langmuir*, 2004, **20**, 8604–8611.

216 S. Gómez-de Pedro, M. Puyol and J. Alonso-Chamarro, *Nanotechnology*, 2010, **21**, 415603, 1–6.

217 J. Wagner and J. M. Köhler, *Nano Lett.*, 2005, **7**, 1–7.

218 R. Gottesman, A. Tangy, I. Oussadon and D. Zitoun, *New J. Chem.*, 2012, **36**, 2456–2459.

219 J. Polte, R. Erler, A. F. Thünemann, S. Sokolov, T. T. Ahner, K. Rademann, F. Emmerling and R. Kraehnert, *ACS Nano*, 2010, **4**, 1076–1082.

220 D. Zhang, F. Wu, M. Peng, X. Wang, D. Xia and G. Guo, *J. Am. Chem. Soc.*, 2015, **137**, 6263–6269.

221 P. M. Valencia, O. C. Farokhzad, R. Karnik and R. Langer, *Nat. Nanotechnol.*, 2012, **7**,

623–629.

222 M. Thiele, J. Z. E. Soh, A. Knauer, D. Malsch, O. Stranik, R. Müller, A. Csáki, T. Henkel, J. M. Köhler and W. Fritzsche, *Chem. Eng. J.*, 2016, **288**, 432–440.

223 L. Uson, V. Sebastian, M. Arruebo and J. Santamaria, *Chem. Eng. J.*, 2016, **285**, 286–292.

224 J. Boleininger, A. Kurz, V. Reuss and C. Sönnichsen, *Phys. Chem. Chem. Phys.*, 2006, **8**, 3824–3827.

225 L. Gomez, V. Sebastian, S. Irusta, A. Ibarra, M. Arruebo and J. Santamaria, *Lab Chip*, 2014, **14**, 325–332.

226 S. Yujun, H. Josef and K. C. S. S. R., *Small*, 2008, **4**, 698–711.

227 J. Wagner, T. Kirner, G. Mayer, J. Albert and J. M. Kohler, *Chem. Eng. J.*, 2004, **101**, 251–260.

228 G. Karniadakis, A. Beskok and N. Aluru, in *Microflows and Nanoflows*, 2005, pp. 1–817.

229 I. Shestopalov, J. D. Tice and R. F. Ismagilov, *Lab Chip*, 2004, **4**, 316–321.

230 A. Günther, S. a Khan, M. Thalmann, F. Trachsel and K. F. Jensen, *Lab Chip*, 2004, **4**, 278–286.

231 J. T. Wang, J. Wang and J. J. Han, *Small*, 2011, **7**, 1728–1754.

232 H. Jun, T. Fabienne, M. Florent, P. Coulon, M. Nicolas and S. Olivier, *30th Anniv. Langmuir*, 2012, **28**, 15966–15974.

233 S. E. Lohse, J. R. Eller, S. T. Sivapalan, M. R. Plews and C. J. Murphy, *ACS Nano*, 2013, 4135–4150.

234 Y. Li, A. Sanampudi, V. Raji Reddy, S. Biswas, K. Nandakumar, D. Yemane, J. Goettert and C. S. S. R. Kumar, *Chem. Phys. Chem.*, 2012, **13**, 177–182.

235 O. Reynolds, *Proc. R. Soc. London*, 1883, 84–99.

236 N.-T. Nguyen, *Micromixers, Second Edition*, 2012.

237 N.-T. Nguyen and S. T. Wereley, *Fundamentals and Applications of Microfluidics*, 2006.

238 B. Kirby, *Micro- and Nanoscale Fluid Mechanics*, Cambridge University Press, 2013.

239 S. W. Jones, O. M. Thomas and H. Aref, *J. Fluid Mech.*, 1989, **209**, 335–357.

240 H. S. and S. F., *AIChE J.*, 2004, **49**, 578–584.

241 F. Schonfeld, V. Hessel and C. Hofmann, *Lab Chip*, 2004, **4**, 65–69.

242 C. K. L. Tan, M. C. Tracey, J. B. Davis and I. D. Johnston, *J. Micromechanics Microengineering*, 2005, **15**, 1885–1894.

243 J. B. Knight, A. Vishwanath, J. P. Brody and R. H. Austin, *Phys. Rev. Lett.*, 1998, **80**, 3863–3866.

244 D. Bothe, C. Stemich and H.-J. Warnecke, *Chem. Eng. Sci.*, 2006, **61**, 2950–2958.

245 Y. Lin, G. J. Gerfen, D. L. Rousseau and S.-R. Yeh, *Anal. Chem.*, 2003, **75**, 5381–5386.

246 R. H. Liu, M. A. Stremler, K. V Sharp, M. G. Olsen, J. G. Santiago, R. J. Adrian, H. Aref and D. J. Beebe, *J. Microelectromechanical Syst.*, 2000, **9**, 190–197.

247 J. F., D. K. S., H. S., K. M. and S. F., *AIChE J.*, 2004, **50**, 2297–2305.

248 A. D. Stroock and G. M. Whitesides, *Acc. Chem. Res.*, 2003, **36**, 597–604.

249 A. D. Stroock, S. K. W. Dertinger, A. Ajdari, I. Mezić, H. A. Stone and G. M. Whitesides, *Science*, 2002, **295**, 647–651.

250 G. I. Taylor, *Proc. R. Soc. London. Ser. A*, 1934, **146**, 501–523.

251 A. Gunther and K. F. Jensen, *Lab Chip*, 2006, **6**, 1487–1503.

252 Y.-K. Lee, J. Deval, P. Tabeling and C.-M. Ho, eds. M. Matlosz, W. Ehrfeld and J. P. Baselt, Springer Berlin Heidelberg, Berlin, Heidelberg, 2001, pp. 185–191.

253 A. O. El Moctar, N. Aubry and J. Batton, *Lab Chip*, 2003, **3**, 273–280.

254 A. A. Darhuber, J. P. Valentino, J. M. Davis and S. M. Troian, *Appl. Phys. Lett.*, 2003, **82**, 657–659.

255 J. Deval, P. Tabeling and C.-M. Ho, in *Technical Digest. MEMS 2002 IEEE International Conference. Fifteenth IEEE International Conference on Micro Electro Mechanical Systems (Cat. No.02CH37266)*, 2002, pp. 36–39.

256 F. Lung-Ming, Y. Ruey-Jen, L. Che-Hsin and C. Yu-Sheng, *Electrophoresis*, 2005, **26**, 1814–1824.

257 Y. Xiang and H. Bau, *Phys Rev E Stat Nonlin Soft Matter Phys*.

258 T. Rossing and N. H. Fletcher, *Principles of Vibration and Sound*, 2004.

Chapter 2

Experimental

2.1. List of chemicals

The chemicals used for all the experiments described in this thesis are listed in Table 2.1 with their purity and the supplier.

Substance	Supplier	Purity [%]
Acetone	VWR	99.98
Carbon, Darco G-60	Sigma-Aldrich	n.a.
Chloroauric acid	Sigma-Aldrich	≥ 99.999
Cinnamaldehyde	Sigma-Aldrich	≥ 99
Cinnamyl alcohol	Alpha-Aesar	≥ 95
Ethanol	Sigma-Aldrich	≥ 99.8
Hydrochloric acid	Sigma-Aldrich	37
Hydrocinnamaldehyde	Sigma-Aldrich	≥ 98
Hydrocinnamyl alcohol	Sigma-Aldrich	≥ 98
Iron nitrate nonahydrate	Sigma-Aldrich	≥ 98
Magnesium oxide	Fisher Scientific	n.a.
Nitric acid	Sigma-Aldrich	70
4-Nitroaniline	Sigma-Aldrich	≥ 99
Nitrobenzene	Sigma-Aldrich	≥ 99
4-Nitrobenzyl alcohol	Sigma-Aldrich	99
2-Nitrophenol	Sigma-Aldrich	98
3-Nitrophenol	Sigma-Aldrich	99
4-Nitrophenol	Sigma-Aldrich	≥ 99
4-Nitrotoluene	Sigma-Aldrich	99
Palladium chloride	Sigma-Aldrich	≥ 99.999
Phenylpropane	Sigma-Aldrich	≥ 98
2-Propanol	Sigma-Aldrich	≥ 99.5

Poly(vinylalcohol)	Sigma-Aldrich	Mw 10,000, 80 % hydrolysed
Sodium borohydride	Sigma-Aldrich	Granular, ≥ 99.99
Sodium carbonate	Sigma-Aldrich	≥ 99.9
Sulphuric acid	Sigma-Aldrich	98
Titania, P25	Degussa	≥ 99.5
Toluene	Sigma-Aldrich	≥ 99
o-Xylene	Sigma-Aldrich	97

Table 2.1: List of chemicals used with relative supplier and purity.

2.2. Catalyst preparation

2.2.1. Support synthesis

2.2.1.1. Preparation of α-Fe_2O_3 by co-precipitation

The α-Fe_2O_3 support was prepared by co-precipitation of $Fe(NO_3)_2.9H_2O$ and Na_2CO_3. In a standard 10 g preparation procedure, a 500 mL hot solution containing 48 g of $Fe(NO_3)_2$ and maintained at 80 °C was added to a 435 mL solution of Na_2CO_3 (23 g) maintained at the same temperature under vigorous stirring. After 1 hour, the precipitate was filtered, washed with 2 L of hot water to remove residual ions, dried at 110 °C for 16 hours and calcined for 3 hours in static air at 300 °C using a ramp rate of 20 °C/min. A schematic representation of the synthetic procedure is shown in Figure 2.1.

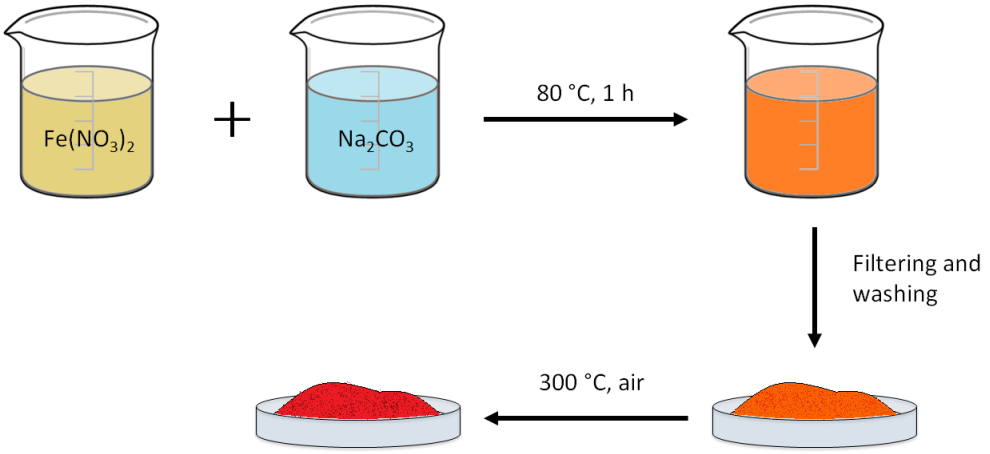

Figure 2.1: Schematic representation of the preparation of α-Fe_2O_3 by co-precipitation.

2.2.2. Catalyst synthesis

2.2.2.1. Preparation of monometallic Au and Pd catalysts by conventional sol-immobilisation

The following procedure applies to the preparation of 1 g of a 1 wt% Au or Pd (generically referred as "Me" from now on) catalyst on TiO_2, MgO, α-Fe_2O_3 or activated carbon.

$HAuCl_4.3H_2O$ (0.800 mL of a 12.5 mg_{Au}/mL solution) or $PdCl_2$ (1.665 mL of a 6.0 mg_{Pd}/mL solution containing 0.58 mol L^{-1} of HCl) was added to a beaker containing 400 mL of deionised H_2O. 0.65 mL of a 1 wt% solution of PVA (Mw 10,000, 80 % hydrolysed) was then added under vigorous stirring (PVA : Me weight ratio = 0.65). To this solution, the appropriate amount of a freshly prepared solution 0.1 M of $NaBH_4$ was rapidly added at room temperature ($NaBH_4$: Me molar ratio = 5), and the immediate formation of metallic colloid was confirmed by the change in colour of the solution to ruby red for gold or dark grey for palladium. After 30 minutes of sol generation, 0.99 g of support was introduced, and the solution was acidified to pH 1 by addition of few drops of concentrated H_2SO_4 (when MgO was used as support, no acidification step was required due to the basic nature of the support). After 1 hour of vigorous stirring, in which the sol immobilises onto the support, the slurry was filtered, washed thoroughly with 1 L of deionised H_2O, and the catalyst dried either at 110 °C for 16 h or at room temperature for 48 h. A schematic representation of the synthetic procedure is shown in Figure 2.2.

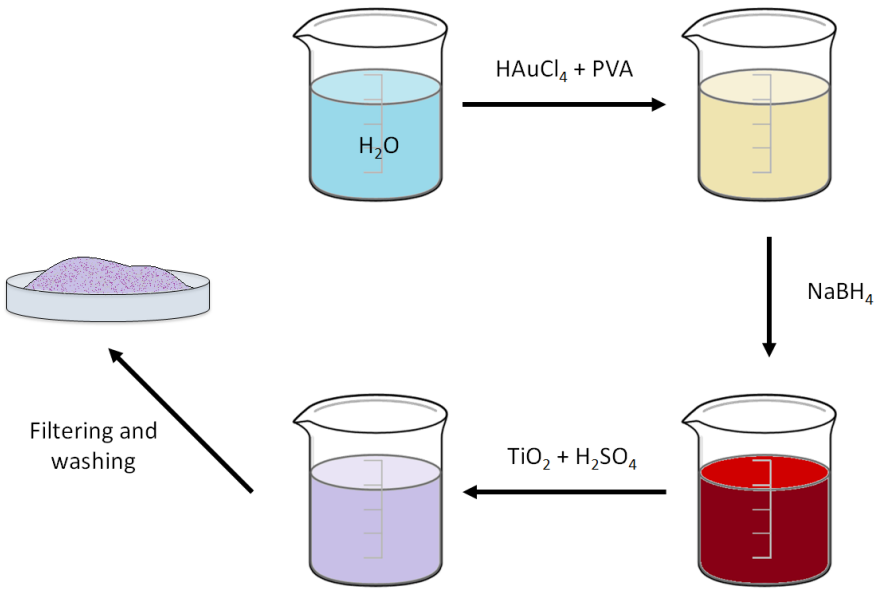

Figure 2.2: Schematic representation of the preparation of a monometallic Au/TiO_2 catalyst by conventional sol-immobilisation.

2.2.2.2. Preparation of bimetallic AuPd catalysts by conventional sol-immobilisation

The following procedure applies to the preparation of 1 g of a 1 wt% AuPd (generically referred as "Me" from now on) catalyst on TiO_2, MgO, α-Fe_2O_3 or activated carbon. The Au : Pd molar ratio is 50 : 50, but the same procedure has been applied to different Au : Pd ratios, namely 95 : 5, 65 : 35 and 35 : 65.

$HAuCl_4.3H_2O$ (0.519 mL of a 12.5 mg_{Au}/mL solution) and $PdCl_2$ (0.585 mL of a 6.0 mg_{Pd}/mL solution containing 0.58 mol L^{-1} of HCl) were added to a beaker containing 400 mL of deionised H_2O. 1.2 mL of a 1 wt% solution of PVA (Mw 10,000, 80 % hydrolysed) was then added under vigorous stirring (PVA : Me weight ratio = 1.2). To this solution, the appropriate amount of a freshly prepared solution 0.1 M of $NaBH_4$ was rapidly added ($NaBH_4$: Me molar ratio = 5), and the immediate formation of metallic colloid was confirmed by the change in colour of the solution to dark grey. After 30 minutes of sol generation, 0.99 g of support was introduced, and the solution was acidified to pH 1 by addition of few drops of concentrated H_2SO_4 (when MgO was used as support, no acidification step is required due to the basic nature of the support). After 1 hour of vigorous stirring, in which the sol immobilises onto the support, the slurry was filtered, washed thoroughly with 1 L of deionised H_2O, and the catalyst dried either at 110 °C for 16 h or at room temperature for 48 h.

2.2.2.3. Preparation of monometallic Au and Pd catalysts by semi-continuous sol-immobilisation

The following procedure applies to the preparation of 0.5 g of a 1 wt% Au or Pd (generically referred as "Me" from now on) catalyst on TiO_2 or activated carbon.

To a 100 mL solution containing 5 mg of Me, 0.325 mL of a 1 wt% solution of PVA was added (PVA : Me weight ratio = 0.65). In another beaker, the appropriate amount of a freshly prepared solution 0.1 M of $NaBH_4$ was added in 100 mL of deionised H_2O ($NaBH_4$: Me molar ratio = 5). The two solutions were pumped together with a peristaltic pump through either a PFA T-shape connection or in a 3D printed reactor. The metallic colloid prepared was pumped into microbore puri-flex tubing of the desired length connected to a UV-Vis flow-cell. At the end of the flow-cell, the colloid was allowed to flow into a beaker containing 0.495 g of support stirred in 50 mL of acidic deionised H_2O (3 drops of H_2SO_4 98 %, to reach pH 1). After all the metal colloid was immobilised onto the support, the suspension was filtered, washed with 1 L of deionised water and dried at room temperature for 48 hours. A schematic representation of the synthetic procedure is shown in Figure 2.3.

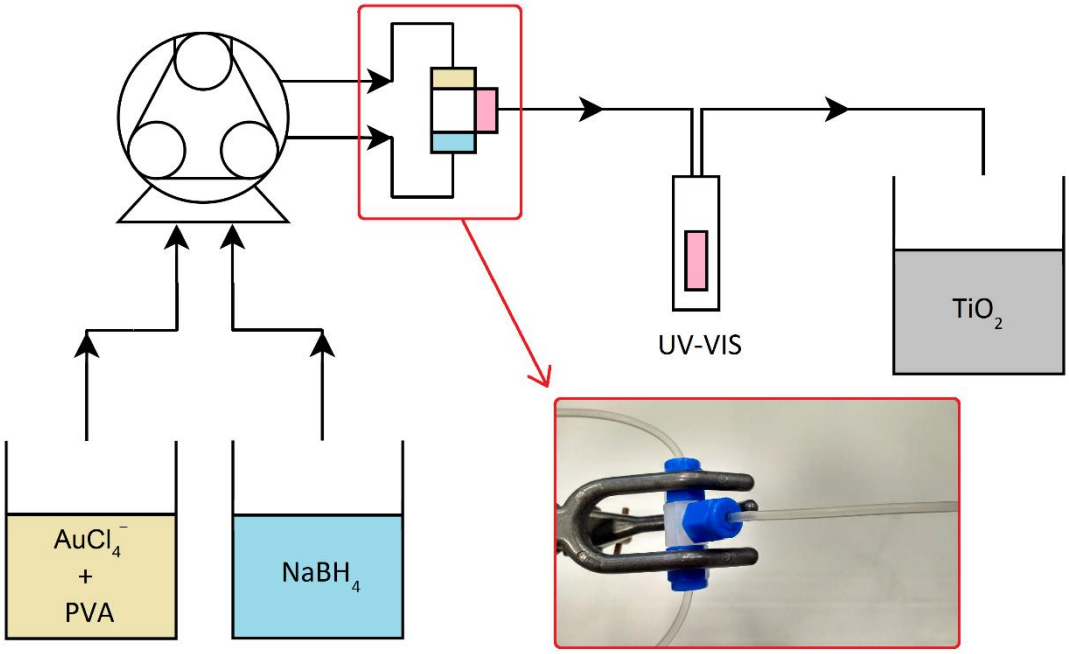

Figure 2.3: Schematic representation of the preparation of a monometallic Au/TiO_2 catalyst by semi continuous sol-immobilisation. The solutions are colour coded as follow: yellow is the metal precursor + PVA solution, blue is the $NaBH_4$ solution, red is the colloid solution and grey is the TiO_2 suspension. In the red box, a picture of the T-shape connection.

2.2.2.4. Preparation of bimetallic AuPd catalysts by semi-continuous sol-immobilisation

The following procedure applies to the preparation of 0.5 g of a 1 wt% AuPd (generically referred as "Me" from now on) catalyst on TiO_2 or activated carbon. The Au/Pd molar ratio is 50 : 50.

$HAuCl_4.3H_2O$ (0.260 mL of a 12.5 mg_{Au}/mL solution), $PdCl_2$ (0.293 mL of a 6.0 mg_{Pd}/mL solution containing 0.58 mol L^{-1} of HCl) and PVA (0.6 mL of a 1 wt% solution, PVA : Me weight ratio = 1.2) were added to a beaker containing 100 mL of deionised H_2O. In another beaker, the appropriate amount of a freshly prepared solution 0.1 M of $NaBH_4$ was added to 100 mL of deionised H_2O ($NaBH_4$: Me molar ratio = 5). The two solutions were pumped together through a peristaltic pump in either a PFA T-shape connection or in a 3D printed reactor. The metallic colloid prepared was pumped into microbore puri-flex tubing of the desired length connected to a UV-Vis flow-cell. At the end of the flow-cell, the colloid was allowed to flow into a beaker containing 0.495 g of support stirred in 50 mL of slightly acidic deionised H_2O (3 drops of H_2SO_4 98 %, to reach pH 1). After all the metal colloid was immobilised onto the support, the suspension was filtered, washed with 1 L of deionised water and dried at room temperature for 48 hours.

2.2.2.5. Preparation of monometallic Au and Pd catalysts by continuous sol-immobilisation

The following procedure applies to the preparation of 0.5 g of a 1 wt% Au or Pd (generically referred as "Me" from now on) catalyst on TiO_2 or activated carbon.

To a 100 mL solution containing 5 mg of Me, 0.325 mL of a 1 wt% solution of PVA was added (PVA : Me weight ratio = 0.65). In another beaker, the appropriate amount of a freshly prepared solution 0.1 M of $NaBH_4$ was added to 100 mL of deionised H_2O ($NaBH_4$: Me molar ratio = 5). The two solutions were pumped together through a peristaltic pump in either a PFA T-shape connection or in a 3D printed reactor. The metallic colloid prepared was pumped into microbore puri-flex tubing of the desired length connected to a UV-Vis flow-cell. In the meantime, a solution containing 0.495 g of support suspended in 100 mL of deionised water was vigorously stirred in a separate beaker. This solution was pumped into a T-shape connection with the colloidal stream coming from the UV-Vis flow cell. The resulting slurry was filtered with a Büchner funnel, washed with 1 L of deionised water and dried at room temperature for 48 hours. A schematic representation of the synthetic procedure is shown in Figure 2.4.

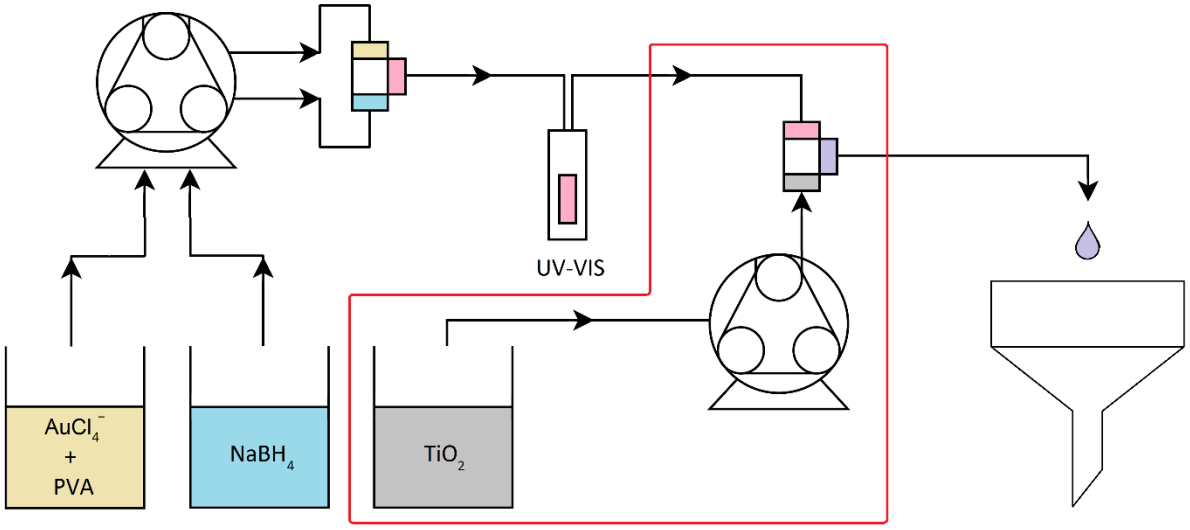

Figure 2.4: Schematic representation of the preparation of a monometallic Au/TiO_2 catalyst by continuous sol-immobilisation. The solutions are colour coded as follow: yellow is the metal precursor + PVA solution, blue is the $NaBH_4$ solution, red is the colloid solution, grey is the TiO_2 suspension and purple is the catalyst suspension. The red box emphasise the additional peristaltic pump and T-shape connection.

2.2.2.6. Preparation of bimetallic AuPd catalysts by continuous sol-immobilisation

The following procedure applies to the preparation of 0.5 g of a 1 wt% AuPd (generically referred as "Me" from now on) catalyst on TiO_2 or activated carbon. The Au/Pd molar ratio is 50 : 50.

$HAuCl_4.3H_2O$ (0.260 mL of a 12.5 mg_{Au}/mL solution), $PdCl_2$ (0.293 mL of a 6.0 mg_{Pd}/mL solution containing 0.58 mol L^{-1} of HCl) and PVA (0.6 mL of a 1 wt% solution, PVA : Me weight ratio = 1.2) were added to a beaker containing 100 mL of deionised H_2O. In another beaker, the appropriate amount of a freshly prepared solution 0.1 M of $NaBH_4$ was added in 100 mL of deionised H_2O ($NaBH_4$: Me molar ratio = 5). The two solutions were pumped together with a peristaltic pump in either a PFA T-shape connection or in a 3D printer reactor. The metallic colloid prepared was flowed into a microbore puri-flex tubing of the desired length connected to a UV-Vis flow-cell. In the meantime, a solution containing 0.495 g of support suspended in 100 mL of deionised water was vigorously stirred in a separate beaker. This solution was pumped into a T-shape connection with the colloidal stream coming from the UV-Vis flow cell. The resulting slurry was filtered with a Büchner funnel, washed with 1 L of deionised water and dried at room temperature for 48 hours.

2.2.3. Thermal treatment

High temperature treatments were carried out on the dried catalysts where specified. The procedure consists of a first calcination step for 3 hours in static air at either 200, 300 or 400 °C with a heating ramp rate of 10 °C/min. At the end of the calcination step and without cooling the furnace, the temperature was maintained for further 3 hours, introducing a constant flow of 5 % H_2/Ar. After the reducing step, the furnace was cooled down and the final catalyst collected from the quartz boat and stored into an air-tight glass vial.

2.3. 3D printing

3D printers are useful tools that allow the manufacture of custom three-dimensional objects in a fast and economic way. Over the last decade, the technology became significantly more affordable and 3D printers have recently found wide applications in several fields of science, such as in medical engineering, mechanical engineering, jewellery, dentistry, and chemistry[1,2]. There are several types of 3D printers commercially available, based on different

printing technology. The two most common, however, are the fused deposition modelling (FDM) printer and the stereolithography (SLA) printer. In FDM printers, the plastic filament is fed through a hot extruder that softens the plastic allowing the precise deposition of thin layers. In SLA printers the photopolymer is present in the liquid phase in a tank; a focussed UV beam is then applied to harden the resin in very thin layers (typically as thin as 25 µm) and create the final object; this process is called the curing process. The fast printing speed and the very cheap plastic filament cost make FDM printers ideal when rapid and low-cost prototyping is needed. The final quality of the printed objects, however, is much lower than models printed with SLA printers. The SLA technique, in fact, allows extremely smooth surfaces and intricate details due to the high resolution of the optical UV spot size. Figure 2.5 shows the difference in quality between an object printed with a FDM and a SLA printer. On the other hand, SLA printers are very limited in terms of type of plastic that can be used and the consumables are usually much more expensive than the materials used in FDM printers.

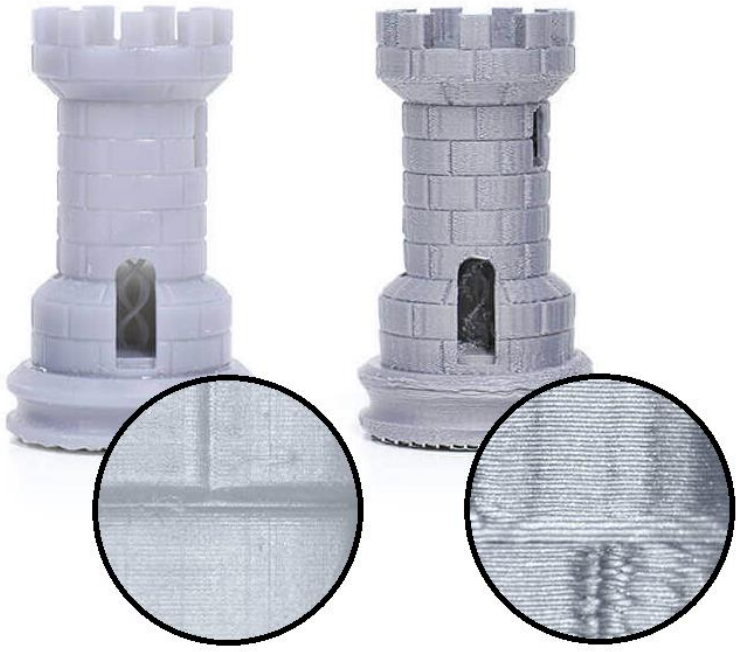

Figure 2.5: Comparison between two objects printed with different 3D printing technology; on the left SLA and on the right FDM. Image adapted with permission from Formlabs Inc.

For this work, a Formlabs Form 2 SLA 3D printer equipped with a standard clear photoreactive resin (mixture of methacrylic acid esters and photoinitiators) was used. A scheme of the printer is depicted in Figure 2.6. The objects to be printed were designed with a CAD software (Autodesk AutoCAD) and finalised with the printer software (PreForm). The layer thickness was set up to 50 µm in order to have a good compromise between quality and printing speed.

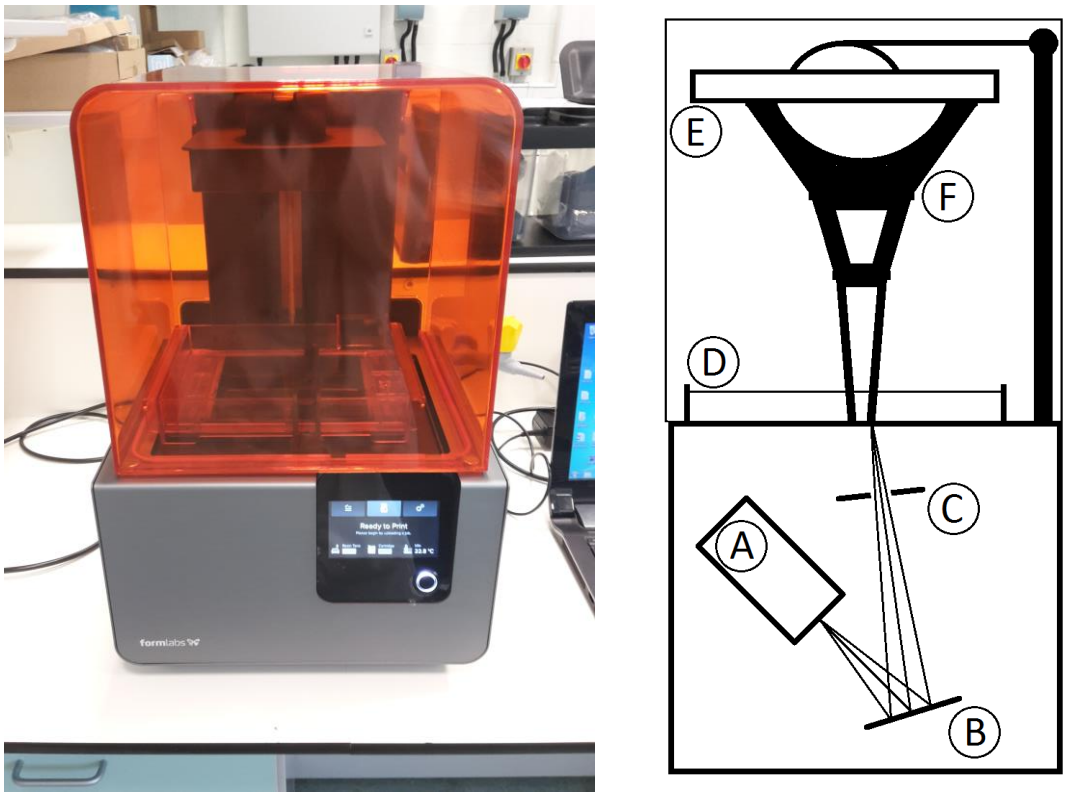

Figure 2.6: A picture (left) and a schematic representation (right) of the SLA 3D printer used. Specifically, (A) UV source, (B) mirror, (C) focussing lens, (D) resin tank, (E) building platform and (F) printed object.

In a typical printing procedure, the 3D object created in AutoCAD was imported into the PreForm software in file format .stl. Supports were added to the object in order to assist the printing of hanging parts. Once optimised, the file was sent to the printer and the printing started. After a few hours (depending on the dimension of the object and the layer thickness set up) the building platform was removed from the printer (Figure 2.7) and the object gently detached and immersed in a solution of 2-propanol for 10 minutes, in order to remove any residual liquid resin from the surface and eventual cavities. The object was then dried with compressed air and left overnight under a UV lamp set up at a fixed wavelength of 365 nm in order to complete the curing process. Finally the supports were removed with a cutter and the final object was ready to use.

Figure 2.7: Picture of a 3D printed reactor immediately after printing. It is still possible to observe liquid resin around it and the supports holding the object in place on the building platform.

2.4. Catalyst characterisation

2.4.1. Ultraviolet-Visible spectroscopy (UV-Vis)

UV-Vis spectroscopy is a common technique based on light absorption in the ultraviolet-visible spectral region. It is largely used in analytical chemistry to quantify specific chemicals in simple matrix (see Section 5.1 of this Chapter)[3]. In particular situations, UV-Vis can be used to characterise metallic nano-objects. For particular metal nanostructure, in fact, UV-Vis absorption can be caused by surface plasmon resonance[4]. As already mentioned in Chapter 1, localised surface plasmons are collective electron oscillations confined on the surface of metallic nano-objects that can resonate at specific wavelength depending on the nature, the dimension and the shape of the material (Figure 2.8)[5]. For certain metals, the resonance wavelength is in the UV-Vis part of the electromagnetic spectrum: an example is gold nanoparticles, which show surface plasmonic resonance at around 500 – 600 nm[6].

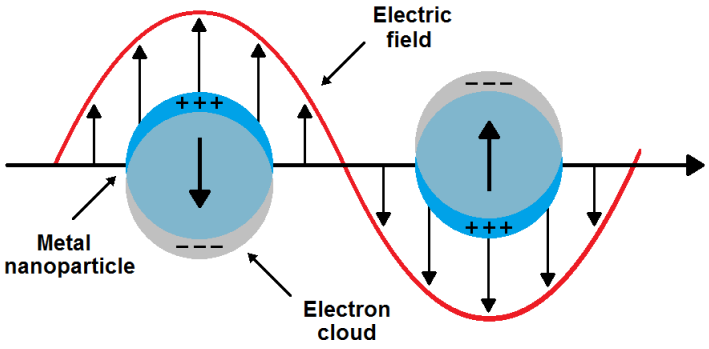

Figure 2.8: Schematic representation of the surface plasmon resonance.

Figure 2.9 shows the simplified scheme of a UV-Vis spectrophotometer with its main components. The light source generates electromagnetic radiation with a broad range of wavelength (usually between 200 – 1,000 nm), while the monochromator filters the light to the desired wavelength. The beam is then split into two by a beam chopper. One beam pass through the sample cell, while the other one through the reference (normally a cuvette filled with the solvent). The two beams are then directed towards two separate detectors. The detectors simply convert the incoming light into a current intensity. The absorbance at a specific wavelength (A_n) of the sample is then calculated according to the Equation 2.1:

$$A_n = \log \frac{I_0}{I_n} \qquad Equation\ 2.1$$

Where I_0 is the intensity of the reference and I_n is the intensity of the sample at the wavelength n.

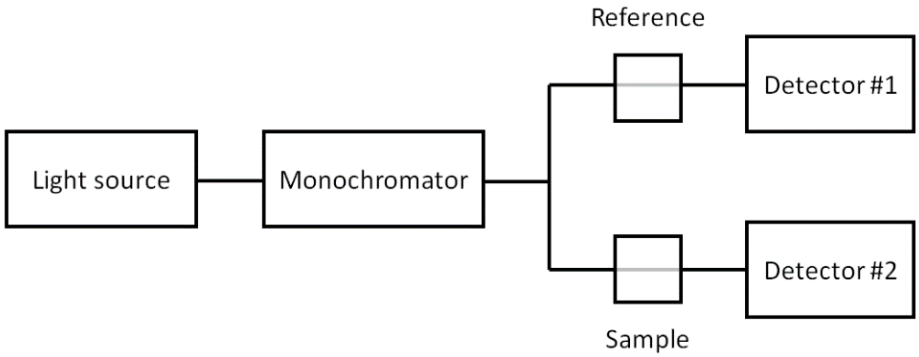

Figure 2.9: Schematic representation of a UV-Vis spectrophotometer components.

For this work, an Agilent Cary 60 double-beam UV-Vis spectrophotometer was used to determine the presence, position and intensity of the surface plasmon resonance of metallic nanoparticles. The light source was a xenon pulse light source with a wavelength range of 190 – 1100 nm. A scan rate of 400 nm s^{-1} provided fast monitoring of the whole spectral range in less than 3 seconds. The colloids were analysed either with a normal 3 mL quartz cuvette

or with an *in situ* quartz flow-through cell; in both cases the path length was 10 mm. The detector consisted of two silicon photodiodes for simultaneous sample beam and reference beam measurements. No pre-treatment of the sample was necessary, and the analysis was simply conducted placing ca. 1 mL of colloid solution into the quartz cuvette. The data was elaborated with Agilent software and analysed with OriginPro 9.0.

The same apparatus was used to monitor the catalytic reaction of nitroarenes reduction with $NaBH_4$ (Chapter 4) and more details on this use will be presented in Section 5.1 of this chapter.

2.4.2. Dynamic light scattering (DLS)

Monochromatic and coherent light is scattered when a solution containing particles smaller than its wavelength is irradiated. This scattering phenomenon undergoes fluctuations in intensity due to the Brownian motion of the particles which can then be correlated to the dimension of the nanoparticles in solution[7].

Figure 2.10 shows a simplified scheme of the instrument. A monochromatic light beam, usually produced by a laser, passes first through a polariser lens and then through the sample cell. Part of this beam is scattered in all the directions by the particles suspended in the sample solution. The detector, generally positioned at a fixed angle, monitor fluctuations of intensity generated by the Brownian motion of the particles: the smaller the particles, the stronger are these fluctuations (Figure 2.11). These changes in intensity are mathematically expressed by the decay rate (Γ), which can be defined as:

$$\Gamma = q^2 D \qquad Equation\ 2.2$$

Where q is the wave vector (that is function of the refractive index of the sample, the angle at which the detector is located and the incident laser wavelength) and D is the diffusion coefficient. The diffusion coefficient, in particular, can be correlated to the hydrodynamic radius (R) of the nanoparticles by means of the Stokes-Einstein equation:

$$D = \frac{k_B T}{6\pi\eta R} \qquad Equation\ 2.3$$

Where k_B is the Boltzmann constant, T is the temperature and η is the dynamic viscosity.

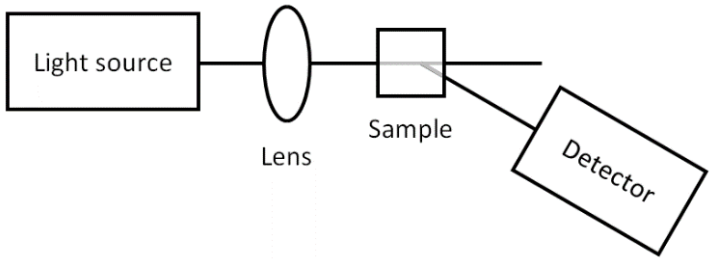

Figure 2.10: Schematic representation of a DLS instrument with the main components.

By the combination of Equation 2.2 and 2.3, it is therefore possible to calculate the average hydrodynamic radius from intensity fluctuations at a specific detection angle.

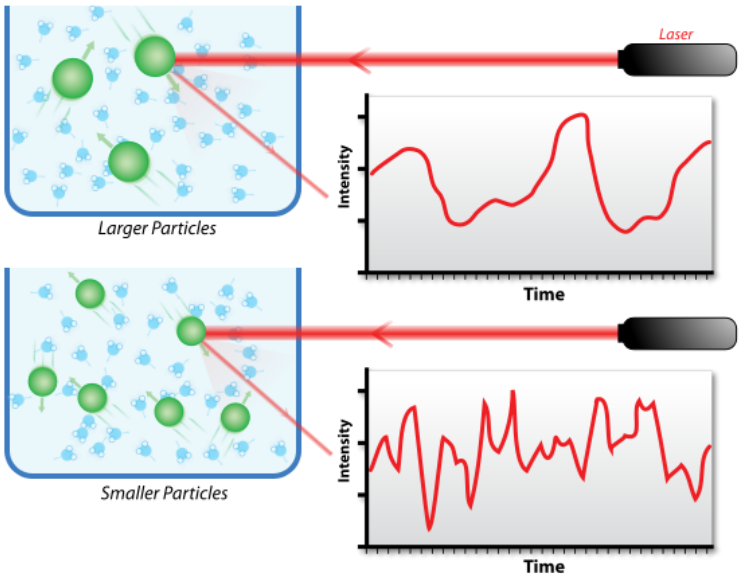

Figure 2.11: Graphical representation of a generic intensity fluctuation output for particles of different dimension. Large particles result in attenuated intensity fluctuations, while small particles produce strong intensity fluctuations. Image reprinted with permission from M. Jones, 2010, distributed under a CC BY-SA 3.0 licence.

DLS analysis presented in this thesis were performed with a Malvern Zetasizer Nano ZS. The light source was a He-Ne laser operating at a fixed wavelength of 633 nm, and the analysis were conducted in DLS disposable cuvettes at a constant temperature of 25 °C. Refractive indexes of Au and Pd were obtained from an online database (refractiveindex.info), while for AuPd alloys a weighted arithmetic mean of the pure metals was considered. At least three sets of analysis were conducted on every sample, and the coherent results averaged out. No pre-treatment of the sample was necessary, and the analysis was simply conducted placing 1 mL of colloid solution into a DLS disposable cuvette. The final data were elaborated by Malvern software and used as is.

2.4.3. Powder X-ray diffraction (XRD)

XRD is an analytical technique that is used to get structural information of crystalline solid materials[8]. Its main use, in particular, is for phase identification (crystalline structure) and crystallite size. The fundamental principle of this technique is that when incident X-ray irradiation contacts a surface, the beam elastically scatters and the resultant waves can undergo either destructive or constructive interference. With crystalline compounds, the strong constructive interference creates diffraction patterns that depend on the geometry of the crystal structure. This process is explained by the Bragg's equation (Equation 2.4), which correlates the angles of coherent X-ray scattering (θ) with the distance between two lattice planes (d).

$$n\lambda = 2d \sin\theta \qquad Equation\ 2.4$$

Where n is the order of reflection (a positive integer) and λ is the wavelength of the X-ray. A schematic representation of the X-ray diffraction through a crystalline solid is shown in Figure 2.12.

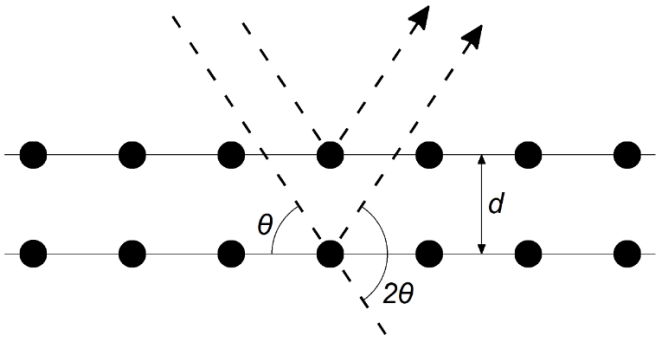

Figure 2.12: Bragg diffraction on a crystalline sample.

Other than the sample crystallinity, XRD can be used to measure the size of sub-micrometre crystallites[9]. In the context of nanocatalysts, this means that it can be used to estimate the size of nanoparticles. The Scherrer equation, in fact, relates the crystallite size (τ) with the peak broadening (β) in an XRD diffraction pattern (Equation 2.5).

$$\tau = \frac{K\lambda}{\beta \cos\theta} \qquad Equation\ 2.5$$

Where K is a dimensionless shape factor (typically with a value of about 0.9), λ is the X-ray wavelength and τ is the Bragg angle. The peak broadening is measured at half of the maximum intensity.

Figure 2.13 represent a simplified scheme of an XRD instrument components. X-rays are produced by bombarding a copper target with a beam of high energy electrons; K_α and K_β X-rays are emitted. A series of filters and electromagnetic lenses selects only the K_α X-rays to irradiate the sample. The scattered radiation is then focussed on the detector that converts the signal into electrical output that can be elaborated by a computer. During the analysis the angle of the X-ray source is typically varied from 10 ° to 80 ° and, as a consequence, the detector moves by the same angle as well in order to be in line with the scattered radiation.

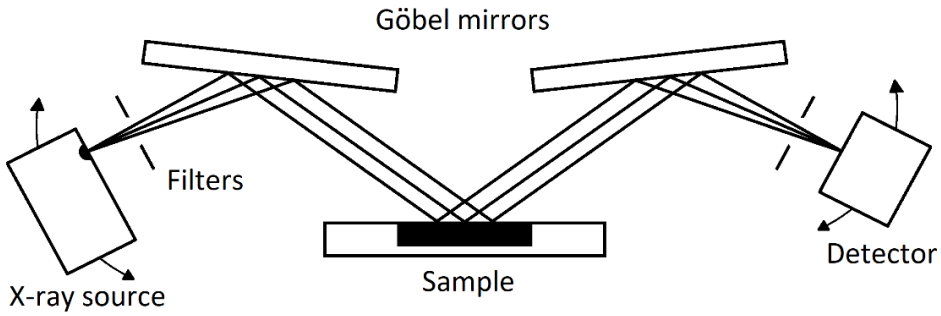

Figure 2.13: Schematic representation of an XRD setup.

XRD analysis were carried out at room temperature in a PANalytical X'PertPRO instrument using a Cu K_α radiation source (λ = 0.15418 nm) run at 40 kV and 40 mA. The diffractograms were collected by an X'Celerator detector over the 10 – 80 ° 2θ range at a rate of 1 °/min. The analysis were performed directly on the grinded catalysts loaded onto a silicon wafer. The results were finally compared with the data held in the ICDD library.

2.4.4. X-ray photoelectron spectroscopy (XPS)

XPS is an X-ray based technique that makes use of the photoelectric effect to gain information about chemical and electronic state of the elements within a material[8]. In a typical experiment, the sample is irradiated with an X-ray beam that causes the emission of electrons from the sample surface (Figure 2.14). This phenomenon happens when the energy of the incident photon is higher than the work function (electron binding energy) of the material. The kinetic energy (E_K) of the emitted electrons can be measured and correlated to the binding energy (E_b) through the Equation 2.6.

$$E_K = hv - E_b - \Phi \qquad Equation\ 2.6$$

Where hv is the energy of the X-ray photons used and Φ is the work function and depends on both material and instrument. The emitted electrons create holes in the electronic structure of the material that are filled by electrons of the outermost shell of the same atom. This process is sometimes accompanied by emission of additional electrons (Auger electrons, Figure 2.14).

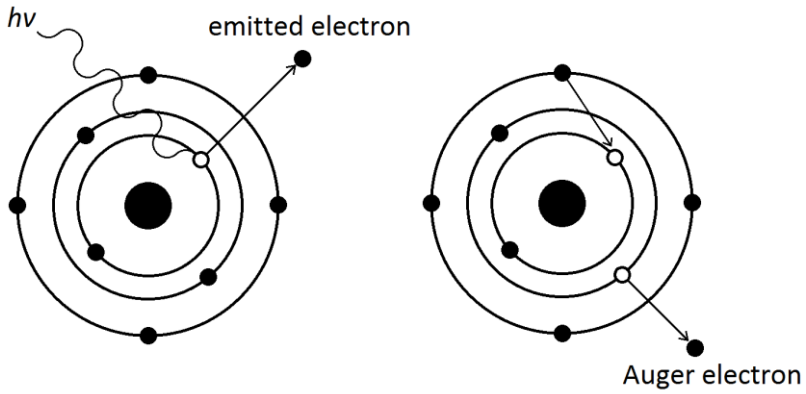

Figure 2.14: Photoelectric effect and Auger electron emission.

The measured binding energy is characteristic of the element that underwent electron emission. In the context of heterogeneous catalysis, the binding energy can therefore be used to identify elements in a sample and evaluate their oxidation state. Shifts in the binding energy can also evidence alloy states[10] or the presence of small metal particles[11]. Unlike XRD, XPS is a surface sensitive technique. Although the penetration depth of the X-ray beam is about 1 mm, in fact, the electrons mean free path in solids is usually not greater than 10 nm[12].

A schematic representation of a generic XPS spectrometer is shown in Figure 2.15. The X-ray source generates an X-ray beam that is focussed by electromagnetic lenses onto the sample surface. The electrons emitted are filtered by the energy analyser based on their kinetic energy and finally detected by the detector.

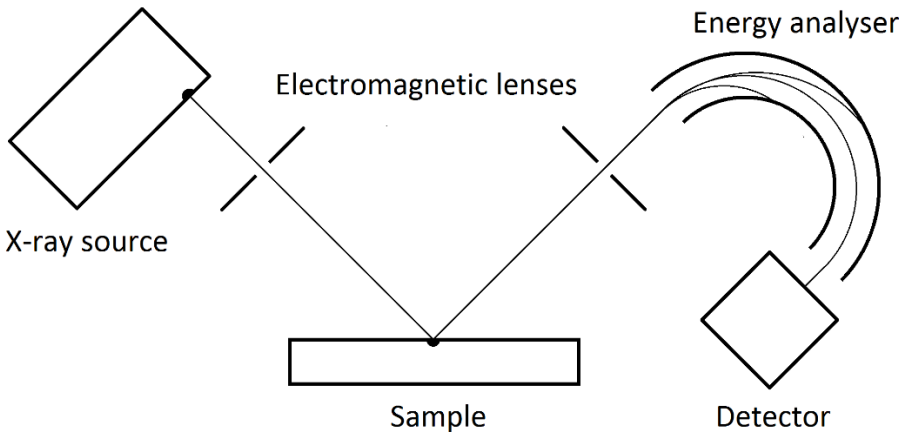

Figure 2.15: Schematic representation of an XPS instrument with its main components.

XPS analysis were performed at the XPS centre within the Cardiff Catalysis Institute at Cardiff University by Dr David Morgan. The instrument used was a Thermo Scientific K-alpha+ spectrometer and samples were analysed using a monochromatic Al X-ray source operating at 72 W. The data was recorded at pass energies of 150 eV for survey scans and 40 eV for high resolution scan with a 1eV and 0.1 eV step size respectively. Charge neutralisation of the sample was achieved using a combination of both low energy electrons and argon ions which gave a C(1s) binding energy of 284.8 eV. All data were analysed using the software CasaXPS.

2.4.5. Electron microscopy (EM)

An electron microscope is a tool used in several scientific fields to magnify and observe objects impossible to view simply with a traditional optical microscope[13]. The fundamental principle is similar, with the main difference being the type of irradiation used to illuminate the sample. In an optical microscope the source is visible light, while in an electron microscope the source is, as the name suggests, an electron beam. Optical microscopes suffer the well-known diffraction limit, which is the limit beyond which it is impossible to resolve separate points of an object due to diffraction phenomena. These effects become important when the wavelength of the illuminating source is in the same order of magnitude of the objects to be resolved, thus in the hundreds of nanometres scale. To overcome this limitation, electrons have been employed as illuminating source. Electrons, in fact, have a characteristic de Broglie wavelength smaller than 1 nm, thus in the picometre range (10^{-12} m), depending on the accelerating voltage: this allows atomic resolution to be achieved[14]. In particular, for a standard 200 keV transmission microscope, the electron wavelength is ca. 2.5 pm[13].

The most common electron microscopes are scanning electron microscope (SEM)[15] and the transmission electron microscope (TEM)[13]. The former uses secondary electrons emitted from the sample surface during irradiation with a focussed electron beam to produce the image, while the latter uses the electrons that manage to pass through the specimen. Figure 2.16 shows the mode of operation of a typical SEM and TEM.

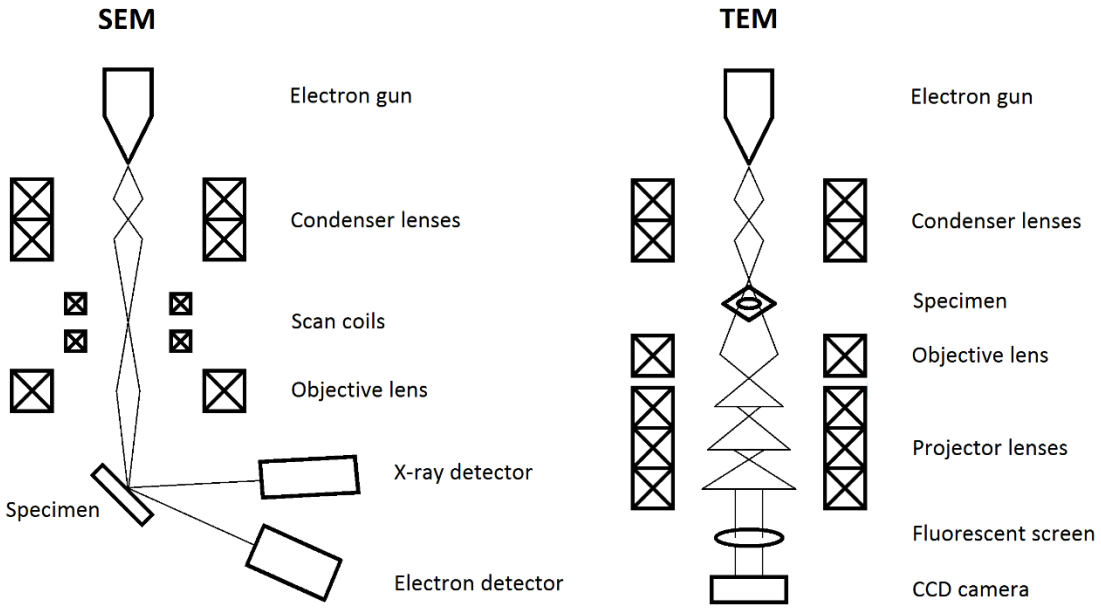

Figure 2.16: Schematic representation of a SEM and TEM with their main components.

In a SEM, the electron gun generates a high energy electron beam that passes through a first set of electromagnetic lenses (condenser lenses) that focuses the beam on a very narrow spot on the sample. The focus spot is moved over the selected sample by the scan coils. Secondary electrons and other radiation (such as X-ray or back-scattered electrons) are picked up by the specific detectors that translate them into electrical signal which can be elaborated by a computer. Secondary electrons are emitted from very close to the specimen surface and the resulting image will therefore carry information about the sample's surface topography. X-rays are also generated during the electron scanning and their energy is characteristic of specific elements. For this reason, X-ray analysis (Energy-dispersive X-ray, EDX) in SEM is widely used to get composition information of samples.

Similarly, in a TEM the electron gun produces an electron beam (usually at higher accelerations than in SEM) but the condenser lenses, in this case, focus the beam into a thin direct stream of electrons that passes through the specimen. The resulting beam is then focussed and magnified by a second set of lenses (objective and projector lenses) and it finally reaches either a fluorescent screen or a CCD camera detector. In "bright-field analysis"

the contrast in the image is generated by the difference in density and thickness in the sample; the thicker and denser the sample and the darker will result the image. Moreover, some electrons undergo diffraction when interacting with the sample. An annular dark field (ADF) detector can detect this signal and produce images. This process is at the base of the so-called "dark-field analysis". In contrast with bright-field, the formation of dark-field images is not dependent on thickness and density, but rather on the specific crystallographic orientation of a sample.

Bright-field TEM analysis were carried out on a JEOL JEM-2100 electron microscope with a 200 kV accelerating voltage. The samples were first dispersed in ethanol and sonicated for 5 minutes and then a drop was placed onto a 300 mesh carbon-coated copper grid. High angle annular dark-field STEM analysis (HAADF) were performed by Professor Chris Kiely and Sultan Althahban at Lehigh University (Pennsylvania, USA) on an aberration corrected JEM ARM-200CF microscope operating at 200 kV. The microscope was equipped with a JEOL Centurio silicon drift detector for X-ray energy dispersive spectroscopy (XEDS). In this case, the samples were prepared by dry-dispersing the catalyst powder onto a holey carbon film supported by a 300 mesh copper TEM grid. Particle size distribution analysis was performed using ImageJ software.

2.4.6. Microwave plasma atomic emission spectroscopy (MP-AES)

MP-AES is a widely used technique that can give quantitative elemental analysis of a liquid sample[16]. In a heterogeneous catalysis context, this technique can then be used to detect traces of leached metals in the reaction solution or to measure the metal loading of a catalyst after dissolution of the active metal in the liquid phase. When a given element is excited, the valence electrons can undergo transition to higher energy levels; as they relax to their original state, the element releases a quantum of energy in the form of a photon. These photons have wavelengths characteristic of the element that they generated from (Figure 2.17).

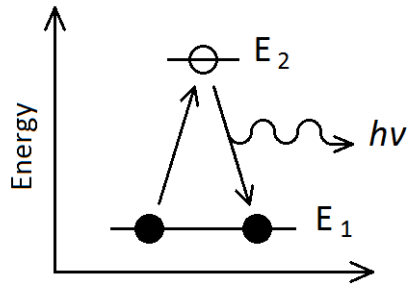

Figure 2.17: Photon emission after electron relaxation from a higher energy shell to a lower one.

Figure 2.18 shows a schematic representation of an instrument for MP-AES analysis. Nitrogen gas is first introduced in the torch and heated up to 5000 °C by microwave radiation. Under these conditions, the nitrogen molecules brake and ionise, generating a plasma. The sample is added to the torch and the molecules contained in it are immediately atomised. Photons are consequently emitted and focussed by mirrors and lenses to a monochromator that let through only specific wavelengths. Finally the detector (a charge-coupled device, CCD) converts photons in electrons, generating a signal that can be elaborated by a computer.

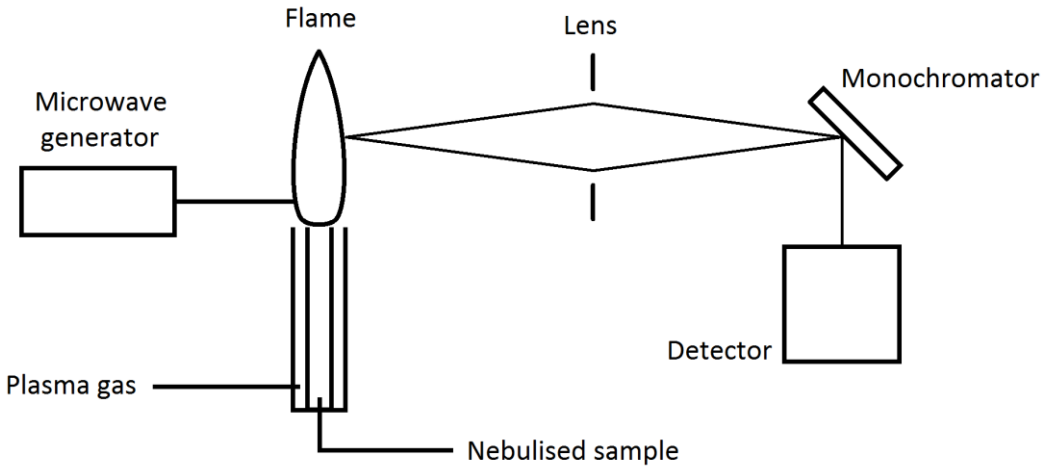

Figure 2.18: Schematic representation of a MP-AES apparatus and its main components.

For this work, an Agilent 4100 MP-AES spectrometer equipped with a nitrogen plasma was used. In a typical procedure for the quantification of the metal loading of a generic metal supported catalyst, 50 mg of sample were digested in 4 mL of aqua regia for 16 hours. The sample was then diluted to 50 mL with deionised water. The solution was then filtered to remove the undissolved support, and the concentration was evaluated against calibration solution freshly prepared before the analysis.

2.4.7. Fourier-transform infrared spectroscopy (FTIR)

Infrared (IR) spectroscopy is one of the most used technique to identify and study chemicals. The principle at the basis of this technique is that molecules possess discrete levels of vibrational and rotational energy, which are characteristic to their structure[8]. When IR radiation is shone onto a molecule, the photons excite the covalent bonds between atoms, causing them to vibrate. The number of vibrations a molecule with N atoms can undergo is defined by its vibrational mode number, which is 3N-5 for linear molecules or 3N-6 for nonlinear molecules. In order for a molecule to be IR-active, however, its resultant vibration must produce a change in the dipole moment. Nitrogen, for example, is a symmetrical diatomic molecule and vibrations on the N-N bond do not produce any change in the dipole moment; the molecule is therefore IR-inactive.

A Fourier transform (FT) is a mathematical operation used to decompose a signal into its constituent frequencies. This process is widely used in spectroscopy and allows one to collect high spectral-resolution data over a wide spectral range[17]. Unlike conventional spectrometers where absorbance or reflectance is measured for one wavelength at a time, FT spectrometers use a beam containing many frequencies of light at once. This is possible thanks to a Michelson interferometer, schematically shown in Figure 2.19. The IR beam is shone onto a beam splitter (M) that partially reflects it on the mirror M_1 and partially passes through and hit the mirror M_2. The two split beams are recombined on the beam splitter and detected by a detector. The relative position of M_2 with respect to M can be moved so one part of the beam covers a different path length. This configuration enables each wavelength of the beam to be transmitted and blocked periodically due to wave interference caused by the moving mirror.

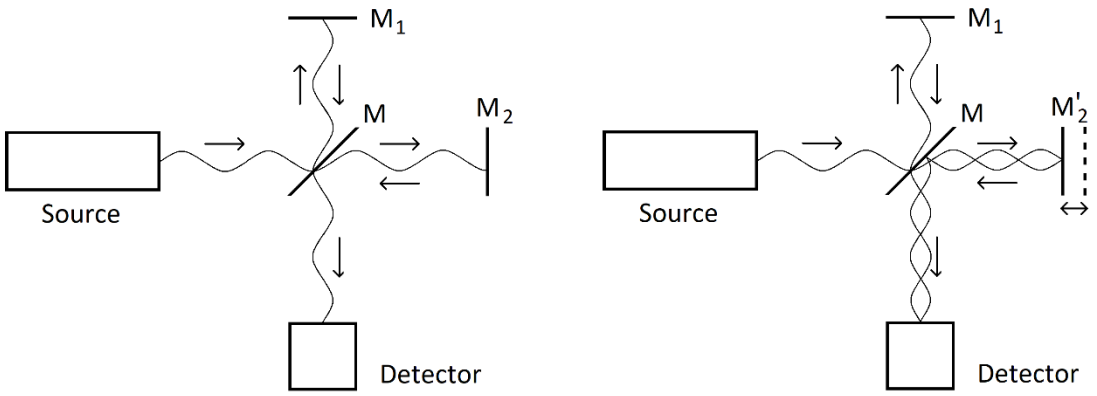

Figure 2.19: Schematic representation of Michelson interferometer.

In this thesis, two types of Fourier-transform infrared spectrometers have been used and will be briefly described below.

2.4.7.1. Attenuated total reflectance infrared spectroscopy (ATR)

ATR is an IR technique that enables the analysis of solid and liquid samples without further preparation. The setup make use of the total internal reflection property of a crystal to create evanescent waves that can pass through the sample[18]. In regions of the IR spectrum where the sample absorbs energy, the evanescent wave will be attenuated. The beam is then collected at the end of the crystal by a detector and the signal elaborated by Fourier transform. An example of ATR setup is depicted in Figure 2.20.

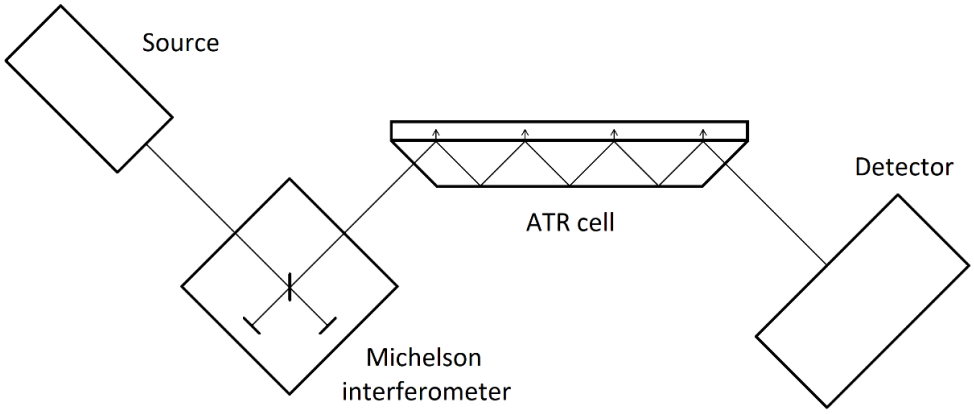

Figure 2.20: Schematic representation of an ATR spectrophotometer components.

ATR systems can be used to evaluate catalyst deactivation through the detection of organic species adsorbed on the catalyst surface. In this thesis an Agilent Cary 630 FTIR was used. The spectrophotometer was equipped with an ATR module using a ZnSe crystal. In a typical analysis, a very small amount of sample (ca. 1 mg) was placed on the ATR crystal and secured with the pressure clamp. The analysis was run with Agilent software and the data extracted and elaborated with OriginPro 9.0.

2.4.7.2. Diffuse-reflectance infrared Fourier-transform spectroscopy (DRIFT)

Similarly to ATR, DRIFT allows the analysis of solid sample without further preparation. The sample analysis, however, is carried out by taking advantage of the diffuse reflection phenomenon[19]. When an IR beam is shone on the sample, in fact, it interacts with surface and reflects in all directions as shown in Figure 2.21. The diffuse reflection is caused by the sample's surface roughness and it is collected by an ellipsoid or paraboloid mirror that focuses the photons to a detector. In heterogeneous catalysis, DRIFTs is mainly used to evaluate acid/base properties and active sites of the catalysts. In order to do so, probe

molecules are commonly used; these probe molecules reversibly adsorb on specific sites of the catalyst, helping one to understand the physical and chemical surface properties of the materials. Specifically, CO is used to study metal sites while pyridine is used to evaluate the presence of acid/base functional groups on the support.

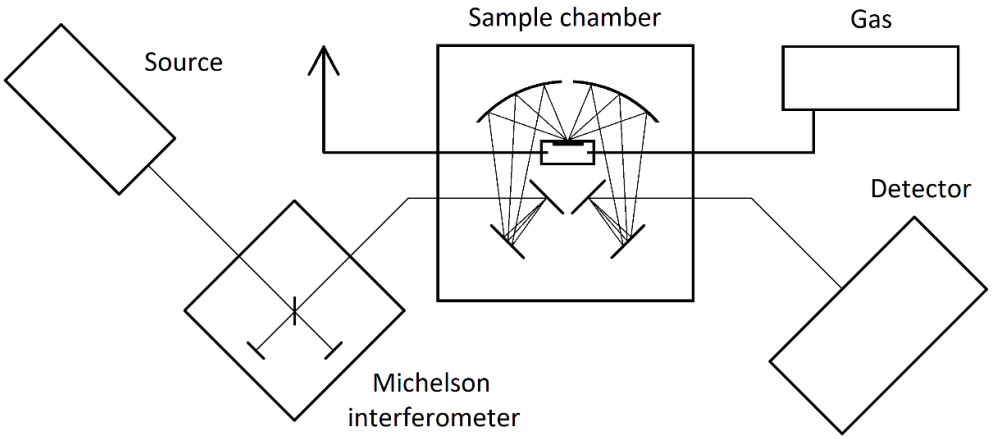

Figure 2.21: Schematic representation of a DRIFT setup and its main components.

DRIFT analysis were carried out with a Bruker Tensor 27 spectrometer fitted with a HgCdTe (MCT) detector and operated with OPUS software. The Harrick Praying Mantis HVC-DRP-4 sample cell was equipped with ZnSe windows and included gas inlet and outlet and vacuum ports as well as capabilities for heating and cooling. For CO adsorption studies, the required gas flow was introduced using a 2 % CO/N_2 gas mixture at 40 mL min^{-1} over a period of 60 minutes. The mixture composition and flow rate was controlled by mass-flow controllers. Each absorbance spectrum represents an average of 64 scans with a spectral resolution of 2 cm^{-1}. Prior to analysis, the gas-phase CO signal was removed by subtracting the spectra recorded under CO containing atmosphere, followed by background and normalisation of the spectra. No high temperature pretreatments were performed on the catalysts in order to avoid sintering of metal nanoparticles. When pyridine was employed as probe molecule, a 60 mL min^{-1} flow of N_2 was bubbled into a sealed flask containing pure pyridine and successively into the cell maintained at a constant temperature of 30 °C. After 15 minutes, the gas flow was switched off while opening the vacuum line, and the analysis started. The temperature was gradually increased up to 480 °C by consecutive steps of 50 °C and maintained for 15 minutes, at the end of which, spectra were collected. As for CO spectra, each absorbance spectrum represented an average of 64 scans with a spectral

resolution of 2 cm^{-1}. All the samples were previously pre-treated at 150 °C under static air for 1 h in order to remove all the adsorbed H_2O. Background and normalisation of the spectra were performed on dehydrated KBr.

2.5. Catalyst testing

2.5.1. Nitroarenes reduction reaction

Nitroarenes are organic molecules containing conjugated bonding systems and they can therefore absorb electromagnetic radiation in the UV-Visible spectral region. Molecules containing π-electrons or non-bonding electrons (n-electrons), in fact, can absorb energy to excite electrons from low energy bonding orbitals (HOMO) to higher anti-bonding molecular orbitals (LUMO)[3]. The energy difference between these two orbitals, often called HOMO-LUMO gap, is responsible for the colours of organic molecules and inorganic complexes. In nitroarenes, the conjugation of the electrons in the aromatic ring with the electrons in the nitro group is responsible for their pale yellow colouration when dissolved in water. For this reason, UV-Vis spectrometry can be used to monitor the evolution of nitroarenes reduction reactions.

The concentration of a known substance dissolved in a UV-Vis transparent solvent (C_x) is directly correlated to its absorbance at a specific wavelength (A_x) through the Beer-Lambert equation (Equation 2.7).

$$A_x = \varepsilon C_x l \qquad Equation\ 2.7$$

Where ε is the molar attenuation coefficient and l is the optical pathlength (usually 1 cm in a typical UV-Vis spectrophotometer). The reaction conversion (X) can therefore be expressed simply by the ratio between the absorption after a reaction time "t" (A_t) and the absorption at the beginning of the reaction (A_0), as shown by Equation 2.8.

$$X = \frac{A_0 - A_t}{A_0} \times 100 \qquad Equation\ 2.8$$

The instrument used was an Agilent Cary 60 double-beam UV-Vis spectrophotometer. All the specifications are reported in Section 4.1 of this Chapter (Ultraviolet-Visible spectroscopy). In a typical 4-NPH reduction reaction with a 1 wt% Au/TiO_2 catalyst, 2.4 mg of catalyst were placed in a quartz cuvette. 2 mL of a 1.5 x 10^{-4} mol L^{-1} solution of 4-NPH were then added, in order to have a metal-to-substrate molar ratio of 1 : 2.5. The cuvette was then

placed into the spectrophotometer at room temperature and the analysis started setting up the instrument in a 200 - 500 nm scan range and with a 400 nm s^{-1} scan rate. No conversion was recorded due to the absence of the reducing agent. A $NaBH_4$ solution was then prepared dissolving 0.0113 g in 10 mL of deionised water (3 x 10^{-2} mol L^{-1}) and 1 mL of this freshly prepared solution was quickly added into the cuvette (final Au : 4-NPH : $NaBH_4$ molar ratio of 1 : 2.5 : 250). Immediately the reaction started and the absorbance at 400 nm was monitored over time. The collected data were finally exported in .txt file and analysed with OriginPro 9.0.

The same procedure was followed for the reduction of other nitroarenes substrates and other catalysts, simply adjusting the quantities where necessary in order to maintain the metal-to-substrate-to-reducing agent molar ratio of 1 : 2.5 : 250.

2.5.2. Cinnamaldehyde hydrogenation reaction

Cinnamaldehyde hydrogenation reactions were carried out in a Radleys StarFish work station composed of 5 parallel 50 mL glass reactors magnetically stirred with a stirring bar. In a typical reaction, 50 mg of catalyst (metal-to-substrate molar ratio of 1 : 1200) were charged in each of the 5 round-bottom flasks with 0.5 mL of cinnamaldehyde (4 x 10^{-3} mol) and 5 mL of solvent at room temperature. Hydrogen was then purged 5 times before the reactors were pressurised (typically at 1 bar of H_2) and left connected to the gas-line to replenish the hydrogen consumed during reaction. The reactors were loaded into a preheated heating block, which was maintained at the desired reaction temperature (typically 100 °C), and the reaction started by commencing stirring inside the reactors (1000 rpm). After the desired reaction time, the reactors were disconnected from the gas line, removed from the work station and cooled down in an ice bath for 5 minutes to quench the reaction. The reaction mixture was then filtered and an aliquot (0.5 mL) diluted with an external standard solution (0.5 mL of a 0.7 M solution of o-xylene in the appropriate solvent) for GC measurement.

The catalyst reusability was carried out using the following experimental procedure. After 90 minutes of reaction, the flask was cooled to room temperature in an ice bath and the catalyst allowed to settle at the bottom of the flask. The supernatant liquid reaction mixture was removed carefully and the solid catalyst was washed with acetone 2 times and allowed to dry in air. A second reaction was then started with the washed catalyst. This procedure was repeated 4 times.

For the analysis of the products, a gas chromatographer (GC) was used. Gas chromatography is a widely used technique to separate and quantify different substances in the gas phase. The fundamental principle is similar to column chromatography, *i.e.* silica columns for the product separation in organic synthesis, with the difference that the separation process in gas chromatography is carried out between a liquid stationary phase and a gas mobile phase, while in column chromatography the stationary phase is solid and the mobile phase is liquid[20]. The separation process is based on differential partitioning between the mobile phase and the stationary phase. Differences in the partition coefficient of the single substances in the mobile phase, in fact, result in diverse retention on the stationary phase and thus affect the separation.

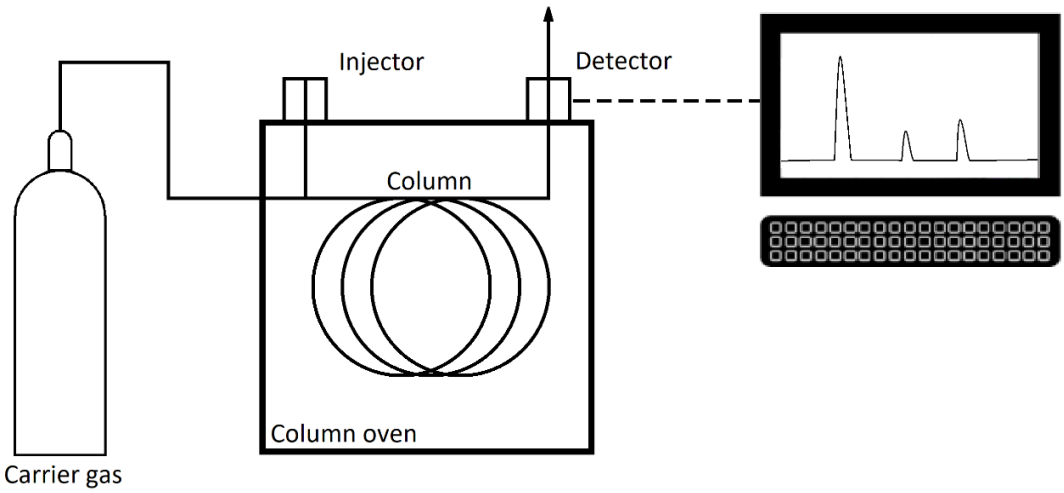

Figure 2.22: Schematic representation of a GC and its main components.

A simplified diagram of a GC is represented in Figure 2.22. The carrier gas, usually helium, nitrogen or a mixture of the two gas, is the mobile phase. The sample is injected into the carrier gas flow through an injector (also called inlet) that has also the purpose of vaporise the sample in case it is liquid. The mobile phase with the mixture of substances injected passes through a narrow tube containing the stationary phase (column) and where the separation happens. Several types of column can be installed depending on the application and the specific needs; the most common type, however, is the capillary column. Capillary columns are very thin (usually 0.1 – 0.5 mm internal diameter) and long (typically 15 – 60 m) columns with the stationary phase coating the interior surface. The stationary phase can be polar or non-polar depending on the needs. The separated compounds reach finally the detector where they are detected and identified. Several type of detectors are commercially available, but the two most commonly used are the flame ionization detector (FID) and the thermal conductivity detector (TCD). The former is based on the detection of ions formed

during combustion of organic compounds in a hydrogen flame, while the latter detects changes in the thermal conductivity of the column effluent and compares it to a reference flow of carrier gas. The advantages of using the FID compared to the TCD are that FID is cheaper and more resistant, it requires little maintenance and has a very low concentration detection limit. On the other hand, FIDs cannot detect some highly oxygenated or functionalised organic species and inorganic compounds, such as CO, CO_2 and H_2O, and they are a destructive detection tool, since they oxidise all the compounds that pass through them. A schematic representation of how a FID and a TCD work is depicted in Figure 2.23.

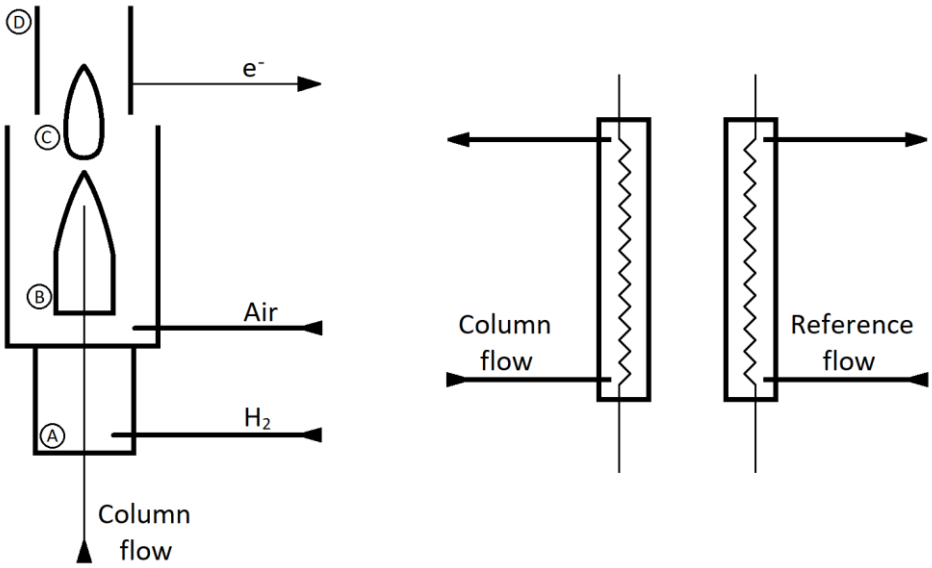

Figure 2.23: Schematic representation of a FID (left) and TCD (right) detector. In particular, (A) FID detector oven, (B) nozzle, (C) ion flame and (D) collector plates.

For the quantification of the amounts of reactants consumed and products generated during the reaction of hydrogenation of cinnamaldehyde, an Agilent 7820A GC was used. The GC was equipped with a non-polar Agilent HP-5 column (30 m x 320 µm x 0.25 µm column) and a FID.

2.6. References

1 M. D. Symes, P. J. Kitson, J. Yan, C. J. Richmond, G. J. T. Cooper, R. W. Bowman, T. Vilbrandt and L. Cronin, *Nat. Chem.*, 2012, **4**, 349–354.

2 B. Berman, *Bus. Horiz.*, 2012, **55**, 155–162.

3 H. Förster, eds. H. G. Karge and J. Weitkamp, Springer Berlin Heidelberg, Berlin, Heidelberg, 2004, pp. 337–426.

4 W. Haiss, N. T. K. Thanh, J. Aveyard and D. G. Fernig, *Anal. Chem.*, 2007, **79**, 4215–4221.

5 E. Hutter and J. H. Fendler, *Adv. Mater.*, 2004, **16**, 1685–1706.

6 V. Amendola, R. Pilot, M. Frasconi, O. M. Maragò and M. A. Iatì, *J. Phys. Condens. Matter*, 2017, **29**, 203002, 1–48.

7 B. Chu, eds. R. Borsali and R. Pecora, Springer Netherlands, Dordrecht, 2008, pp. 335–372.

8 I. Chorkendorff and J. W. Niemantsverdriet, *Concepts of Modern Catalysis and Kinetics*, 2003.

9 U. Holzwarth and N. Gibson, *Nat. Nanotechnol.*, 2011, **6**, 534.

10 A. M. Venezia, L. F. Liotta, G. Pantaleo, V. La Parola, G. Deganello, A. Beck, Z. Koppány, K. Frey, D. Horváth and L. Guczi, *Appl. Catal. A Gen.*, 2003, **251**, 359–368.

11 D. Goodman, *Catalysis by Supported Gold Nanoclusters in Dekker Encyclopedia of Nanoscience and Nanotechnology*, 2008.

12 J. F. Watts and J. Wolstenholme, *Surface Analysis by XPS and AES*, 2003.

13 D. B. Williams and C. B. Carter, *Transmission Electron Microscopy*, 2009.

14 L. V. P. R. de Broglie, *Recherches sur la théorie des quanta*, 1924.

15 J. D. C., *Mater. Sci. Technol.*, 2006.

16 W. Li, P. Simmons, D. Shrader, T. J. Herrman and S. Y. Dai, *Talanta*, 2013, **112**, 43–48.

17 J. B. Bates, *Science*, 1976, **191**, 31–37.

18 J. Fahrenfort, *Spectrochim. Acta*, 1961, **17**, 698–709.

19 J. Torrent and V. Barron, *Diffuse Reflectance Spectroscopy in Methods of Soils Analysis*, 2008.

20 R. L. Grob and E. F. Barry, *Modern Practice of Gas Chromatography*, 2004.

Chapter 3

Continuous production of supported metal nanoparticles

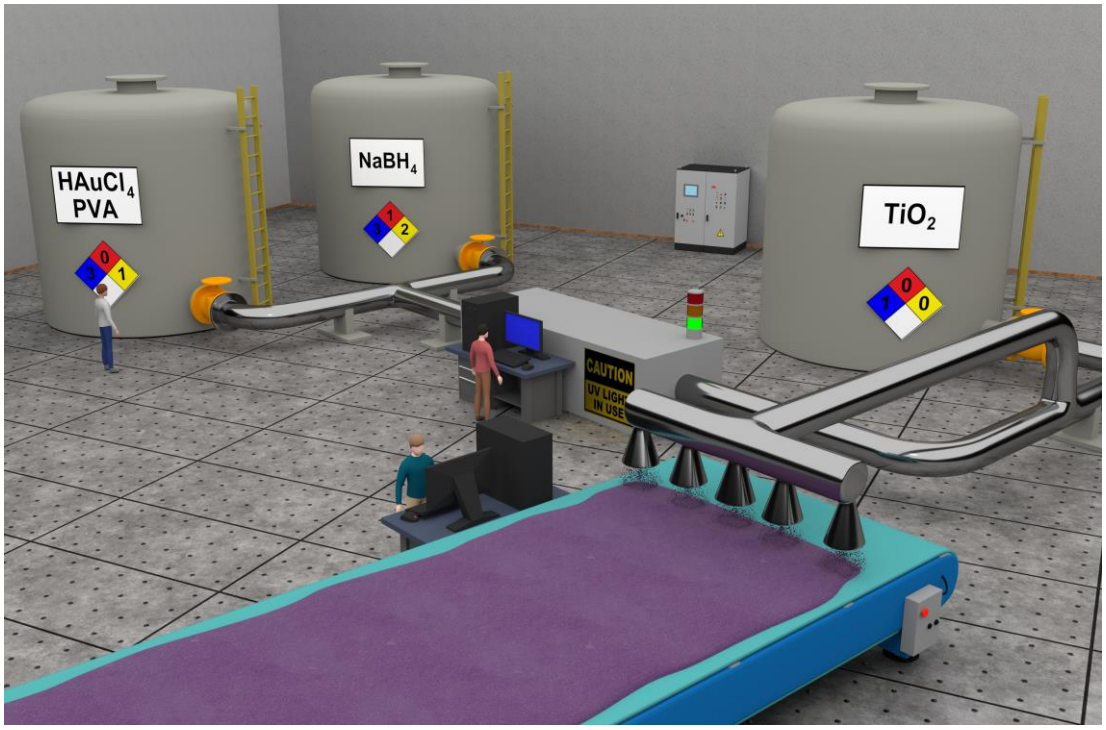

3.1. Introduction

3.1.1. The Production of metal nanoparticles in continuous systems - background

The advantages of using micro- or milli-fluidic devices over traditional batch techniques for the synthesis of metal nanoparticles were thoroughly reviewed in Chapter 1.5.3. The synthesis of colloidal solutions in continuous mode increases control over local concentration and temperature gradients and allows fast screening and optimisation of the synthesis conditions[1]. Moreover, scale-up of batch synthesis processes are often problematic due to the high volumes involved and the batch-to-batch irreproducibility problems already described[2]. To obtain small and monodisperse metal nanoparticles, it is therefore important to ensure a very fast nucleation step compared to the relative growth time and a homogeneous physical-chemical environment for the nuclei to form[3–5].

The first use of a microreactor for the synthesis of nanoparticles dates back to 2002, when *deMello* and co-workers reported the production of cadmium sulphide nanoparticles within a controlled size range (3 – 12 nm) via a microfluidic procedure[6]. In their work, the superior nanoparticle quality was ascribed to a much better thermal and chemical homogeneity due to the small size of the reactor. The same year, *Maeda* and colleagues applied a similar approach to the preparation of 10 nm titanium oxide nanoparticles in a ceramic microreactor[7]; two immiscible fluids were used in this case to provide a small volume reactor vessel and thus generate TiO_2 nanoparticles via rapid hydrolysis of titanium alkoxide. Two years later, *Köhler* and co-workers reported the first synthesis of metal nanoparticles in a continuous flow system[8]. Specifically, 12 nm Au seeds prepared in batch were injected into the reactor and their size was controlled by ascorbic acid reduction of a chloroauric acid solution onto the seeds. Although the initial seeds were not synthesised in the microreactor, this work can be considered as the first report of metal nanoparticle processing in a continuous flow system. The same group later described the full seed-mediated growth synthesis of Au nanoparticles in a microreactor, with a nanoparticles size of 5 to 50 nm [9]. The problem of reactor fouling was reduced by chemical modification of the inner walls of the microreactor.

Since then, several papers have appeared in the chemical and engineering literature regarding the production of metal nanoparticles in a continuous fashion[10–15]. Among all the continuous flow techniques developed, the most promising are the segmented flow synthesis[16] and millifluidic synthesis[17]. In the former, the use of an additional non-miscible

solvent or gas creates a biphasic system where each segment acts as an independent microreactor, while in the latter, reactors with channel diameter greater than 1 mm are used. The advantage of using a biphasic system is that metal deposition on the inner walls is greatly reduced since the reaction mixture is not directly in contact with the tubing due to the presence of a very thin layer of the carrier solvent or gas[18]. Moreover, the parabolic flow profile typical of laminar flows is strongly reduced due to internal mixing in the single independent microreactor[19]. The use of a biphasic system, however, can complicate the whole apparatus due to addition of extra instrumentation such as pumps and in-line biphasic separators thus increasing the overall cost of the setup[20]. In addition, the carrier phase is often an organic solvent and health and safety issues can arise from excessive exposure and more complicated solvent processing is required during scale up[16,21].

The millifluidic synthesis, in contrast, simply makes use of reactors with an internal channel diameter greater than 1 mm. Although providing the same benefits as the classic microreactors, these setups proved to be more resistant against fouling and easier to fabricate and integrate with *in situ* apparatus[22,23]. The possibility of using higher volumes and higher flow rates, without any problem of backpressure, makes the scale-up of these systems easier compared to microreactors[17].

3.1.2. Aims and objectives of the chapter

The aim of this chapter was to build and optimise a new millifluidic setup for the continuous production of supported metal nanoparticles for applications in catalysis. The optimisation was carried out by producing the colloid only in continuous mode and varying several operational parameters, such as reaction conditions, solution residence time and mixing, in order to produce small and monodispersed nanoparticles. The synthesised colloids were then immobilised onto a suitable support to produce the final catalyst.

Once optimised, the setup was further upgraded for the production of the whole supported metal nanoparticles in continuous mode by simply integrating the metal colloid stream with a suspended solution of the support. The applicability of this apparatus was tested for the production of different monometallic Au and Pd and bimetallic AuPd based catalysts.

The catalysts produced were fully characterised with UV-Vis, DLS, MP-AES and STEM to evaluate metal loading and particle dimension. Moreover, on the most promising

catalysts, DR-UV-Vis, XPS, AC-TEM and EDX analysis were performed to have a better understanding on the nature of the catalysts produced.

3.2. The batch benchmark catalyst

For the continuous synthesis of nanoparticles, gold was first chosen as test metal. The reason behind this is that gold is widely used as catalyst for several reactions, such as alcohol oxidations[24], CO oxidation[25] and the direct synthesis of hydrogen peroxide[26] and most importantly Au nanoparticles can be easily characterised by means of UV-Vis spectroscopy[27]. Gold shows surface plasmonic resonance in the visible range of the electromagnetic spectrum when finely dispersed in the nanometre scale[28]. The intensity and position of the resonance generates one or more absorption peaks (called plasmonic peaks) that strongly depend on the size and shape of the nanostructure[29]. By exciting gold nanoparticles with a light source, the resulting plasmonic peak detected by the spectrophotometer centered at around 520 nm can give qualitative and quantitative information about the average nanoparticles size and shape (see Chapter 2.4.1)[30].

The approach was to use a well know colloidal method for the production of supported metal nanoparticles in batch and to try to adapt the preparation method into a continuous fashion. The synthetic procedure taken as a benchmark was the catalyst preparation protocol based on the Brust-Schiffrin method[31] and then further developed by Prati and coworkers[32,33]. The synthetic procedure is reported in Chapter 2.3.2 and depicted in Figure 3.1. This method involves the reduction of a metal salt ($HAuCl_4$) dissolved in H_2O by a strong reducing agent ($NaBH_4$) in the presence of a stabilising agent (usually PVA or PVP). The role of the stabilising agent is to protect the newly formed nanoparticles from agglomeration and coalescence by forming a protective surface layer. As described in Chapter 1, the temperature plays an important role in the nanoparticles synthesis; all throughout this work, the catalyst synthesis were conducted at room temperature (25 °C).

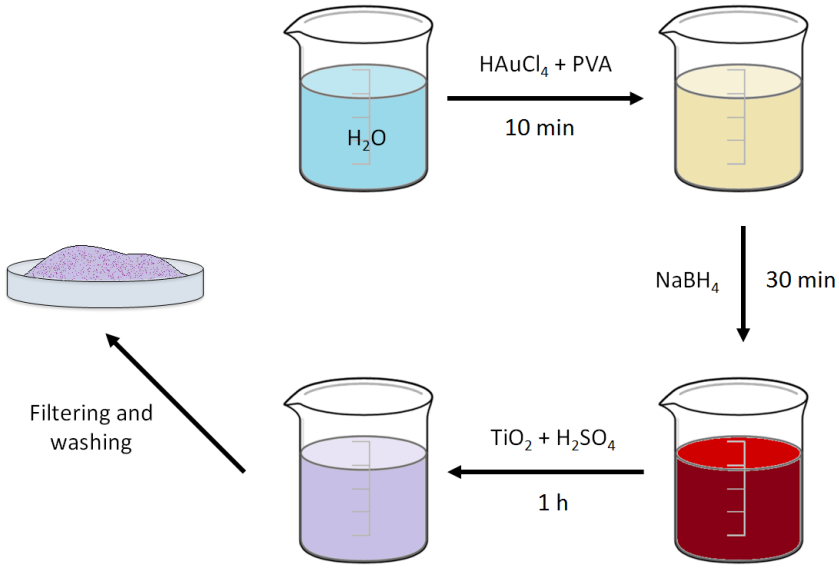

Figure 3.1: Schematic procedure for the synthesis of Au nanoparticles supported on TiO_2 with the batch procedure.

The colloid formed presented a dark red colouration typical of nanoparticles in the 3 to 6 nm range. UV-Vis analysis confirmed the presence of very small nanoparticles, with localised surface plasmon resonance centred at ca. 520 nm (Figure 3.2)[34–36]. Typically, the optical extinction spectrum of a colloidal solution of spherical Au nanoparticles is characterised by a surface plasmon resonance band centred at approximatively 520 nm[37]. This band, however, is partially superposed to the tail of interband transitions (i.e. single particle excitations from the occupied 5d valence band to the unoccupied 6s-6p conduction bands of Au) at shorter wavelengths (Figure 3.3)[38,39]. This overlap partially reduces Au plasmon intensity. In addition, there are several factors that can shift the plasmon resonance band towards higher or lower wavelengths (respectively called redshift and blueshift), such as the physical-chemical environment and the size, shape and composition of the metal nanoparticles[37]. The lower intensity of the plasmonic resonance peak in Figure 3.2 compared to the reference peak in Figure 3.3 is mainly due to intrinsic size effects, that are caused by modification of the metal optical constant when the size of Au nanoparticles is below 30 nm[39]. When the particle size is lower than ca. 30 nm, in fact, the free electron scattering at the particle surface is no longer negligible and causes a damping of the surface plasmon resonance band for decreasing particle size[38,40,41]. This quenching is further enhanced when the particle size is smaller than ca. 2 nm due to quantum size effects[42,43]. In this range, in fact, the energy quantisation of the electronic levels becomes too large for the collective oscillations to develop and such particles no longer support plasmon resonance. Dynamic light scattering (DLS) analysis was also conducted on the freshly prepared colloid and the

results indicated the presence of nanoparticles with a hydrodynamic diameter of 5.6 ± 1.7 nm. It should be pointed out that the hydrodynamic diameter includes not only the actual metal nanoparticle, but also the solvation/polymer shell (Chapter 2.4.2)[44].

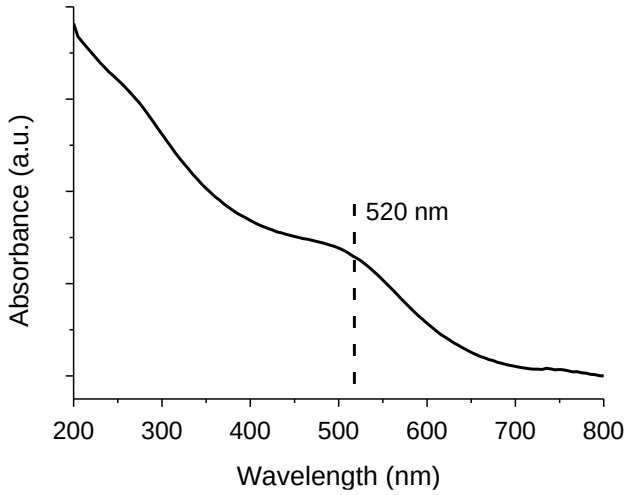

Figure 3.2: UV-Vis analysis of the Au colloid prepared with the batch technique. The surface plasmon resonance is centred at ca. 520 nm.

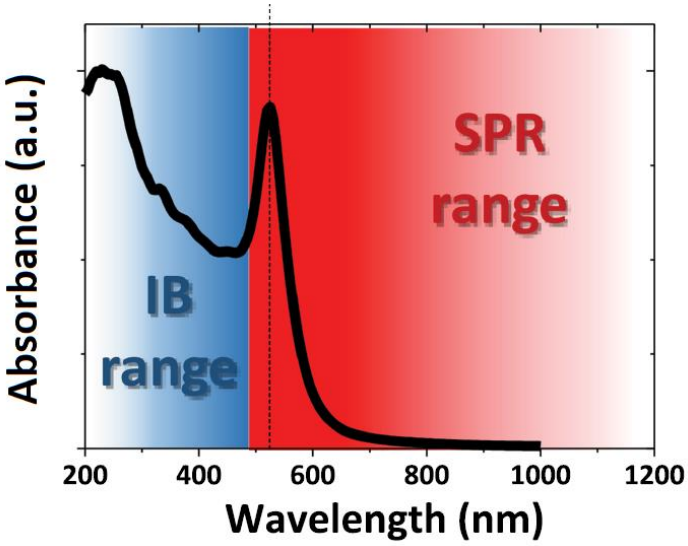

Figure 3.3: Extinction spectrum of spherical Au NPs (20 nm diameter, in water, calculated with the Mie model). Onset of IB and SPR regions are highlighted in blue and red, respectively. Image adapted with permission from Amendola et al., J. Phys. Condens. Matter 2017, 29, 1-48.

Once the Au colloid is prepared, the support was added in order to immobilise the nanoparticles onto its surface. The final washing step is crucial to remove all the unwanted ions resulting from the synthetic procedure. The absence of any residual Au precursor or Au nanoparticle not efficiently immobilised on the support was confirmed by UV-Vis analysis on the filtrate solution.

The catalyst was finally dried at room temperature for 48 hours, crushed with pestle and mortar and sieved using a 60 Mesh sieve (0.250 mm). Scanning transmission electron microscopy analysis (STEM) was performed on the final catalyst to assess the particle dimension and size distribution (Figure 3.4); the results indicated a mean nanoparticle size of 5.6 nm and a size distribution of ± 1.6. In addition, a sample of the catalyst was treated with aqua regia to leach the gold nanoparticles immobilised; the resulting solution was analysed at the MP-AES to verify the final metal loading. The effective Au loading was slightly lower than the target 1 wt% (0.94 %), probably due to systematic errors in the preparation of the Au stock solution and weighing of reagents.

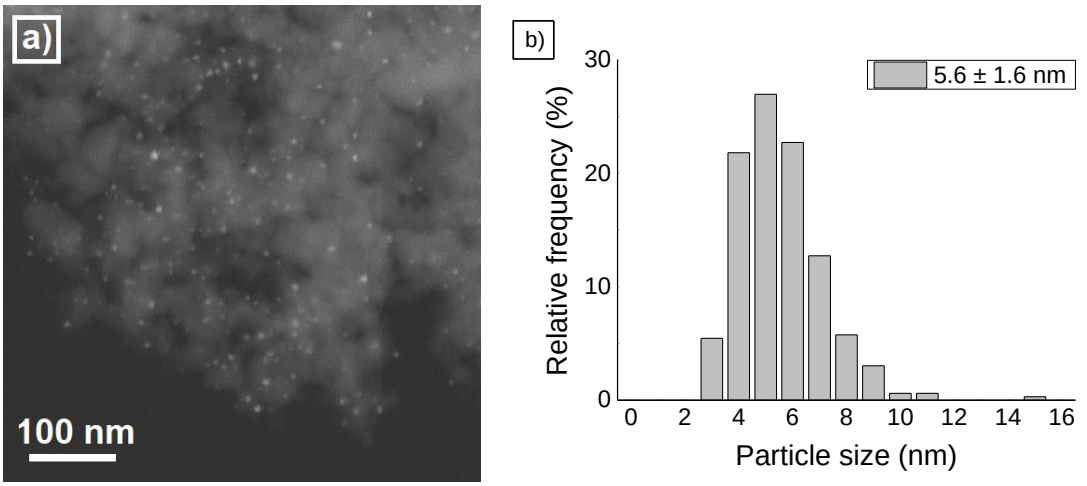

Figure 3.4: Representative STEM michrograph of the Au/TiO_2 catalyst prepared with the batch technique and relative size distribution isthograph.

3.3. Semi-continuous setup optimisation

3.3.1. The semi-continuous setup

A scheme of the experimental setup used to produce colloidal Au particles in continuous flow is reported in Figure 3.5. From now on it will be referred as “semi-continuous”, since only the metal nanoparticles were produced in continuous mode, while the immobilisation step was carried out in batch as previously described.

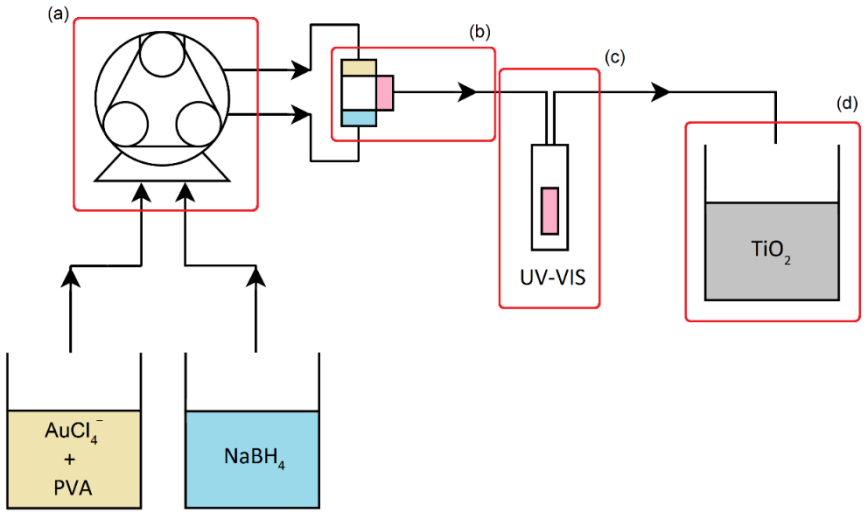

Figure 3.5: Schematic representation of the semi-continuous setup for the synthesis of Au/TiO_2 catalyst. (a) peristaltic pump, (b) reactor composed by a T-shape connection and tube of a specific length, (c) in-line UV-Vis flow cell and (d) beaker containing the support suspended in H_2O.

The setup consists of a dual-channel peristaltic pump, a reactor (composed of a connection and tubing), an in-line UV-Vis flow cell and a glass container for the immobilisation of the colloid. The detailed operational procedure is reported in Chapter 2.3.2. One solution containing the metal precursor and the stabilising agent and a second solution containing the reducing agent are pumped into the reactor by the peristaltic pump. The colloid produced then passes through the in-line UV-Vis flow cell and then drops into a beaker containing the support stirred in an acidified water solution. All the reaction parameters were kept similar to the batch protocol for a suitable comparison. Specifically, PVA : Au ratio (0.65 weight : weight), $NaBH_4$: Au ratio (5 mol : mol) and Au concentration (0.127 mmol L^{-1}) were kept consistent with the batch protocol. The dual-channel peristaltic pump can work over a 1 – 24 mL min^{-1} flow range depending on the drive rpm and tubing size. When not specified, the overall flow rate was 6 mL min^{-1} (3 mL min^{-1} each channel), the reactor was made from a perfluoroalkoxy alkane (PFA) T-shape connection attached to a straight tube for a total reactor length of 80 cm (50 cm from the tee connection and the UV-Vis flow cell plus 30 cm from the flow cell to the beaker), to give a final residence time of 8 seconds. The whole setup was kept at a constant room temperature of 25 °C. A picture of the working setup is represented in Figure 3.6.

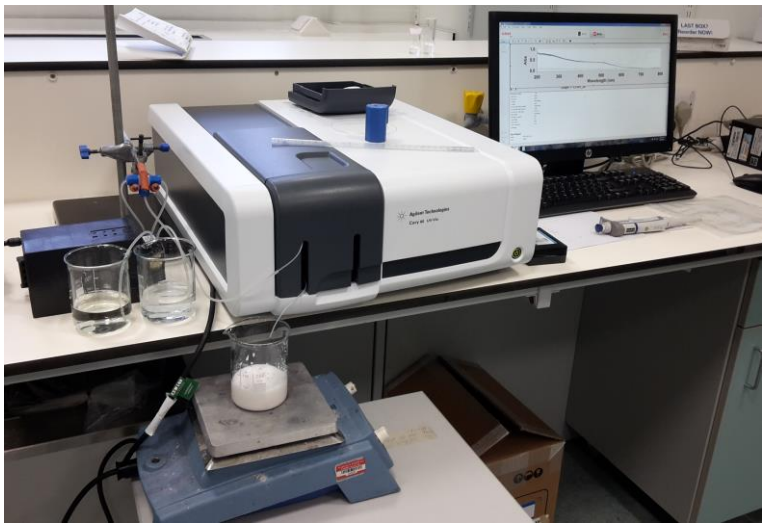

Figure 3. 6: Picture of the semi-continuous setup during the synthesis of a Au/TiO_2 catalyst. The reactor is connected to the UV-Vis spectrophotometer for the in-line analysis of the Au plasmon resonance.

A first catalyst was synthesised with the semi-continuous setup using the operational parameters described above. The in-line UV-Vis flow cell provided a useful tool for the real time monitoring of the Au nanoparticles being produced. In a typical synthesis of 0.5 g of 1 wt% catalyst, for example, the setup was left running for ca. 35 minutes; comparing the plasmonic resonance of the Au nanoparticles produced at the beginning of the synthetic procedure (5 minutes) to the end of the procedure (30 minutes), no difference was detected in either shape, intensity or shift of the surface plasmon resonance (Figure 3.7), with the two spectra perfectly overlapping. These results confirm that the production of Au nanoparticles in the semi continuous system occurs with no loss in quality during the synthetic procedure.

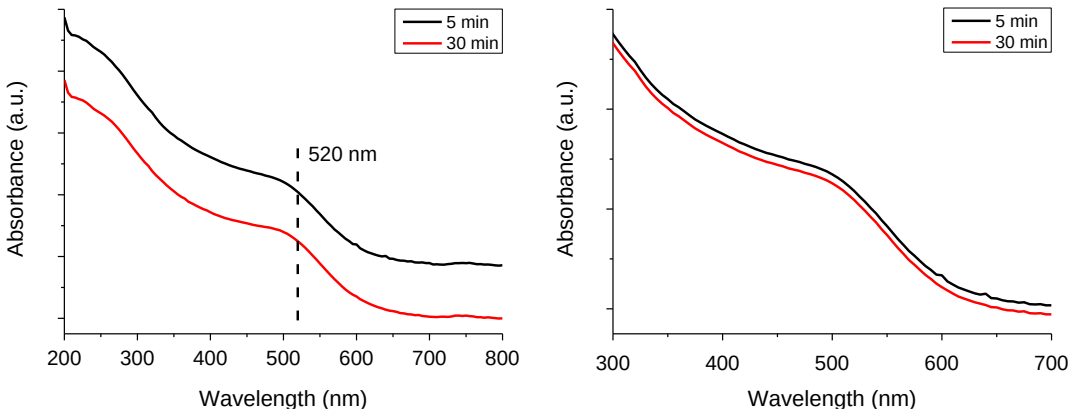

Figure 3.7: UV-Vis analysis of the Au colloid prepared with the semi-continuous technique after 5 and 30 minutes (left). On the right, a zoom-in on the plasmonic region (the two spectra have been vertically shifted in order to avoid complete overlap). Reaction conditions: total flow rate 6 mL min^{-1}, reactor length 80 cm (residence time 8 s), Au concentration 0.127 mmol L^{-1}, PVA : Au weight ratio 0.65, $NaBH_4$: Au molar ratio 5, temperature 25 °C.

Interestingly, comparing the semi-continuous catalyst with the batch, the plasmonic peak seems to be shifted towards smaller wavelengths (Figure 3.8, from ca. 520 nm to ca. 500 nm), although a precise evaluation of the resonance maxima is difficult due to the low peak intensity. Blueshifts of the surface plasmon resonance are usually ascribed to a decrease in particle size. For particle size below ca. 10 nm, in fact, lattice contractions cause an increase in electron density, that push the plasmon resonance towards higher frequencies (lower wavelengths)[43]. STEM analysis, however, revealed the presence of slightly bigger nanoparticles (Table 3.1, 6.5 ± 1.7 nm compared to 5.6 ± 1.6 nm of the batch catalyst), in apparent contradiction with the UV-Vis analysis. It is possible that the increase in particle dimension for the semi-continuous catalyst happened during the immobilisation step rather than during the particle formation. The UV-Vis analysis, in fact, suggests the presence of smaller nanoparticles in the colloid prepared with the semi-continuous setup. Indeed, the immobilisation step is different for the two techniques. In the batch method, all the Au nanoparticles are immobilised at the same time with addition of support, while in the semi-continuous method small amounts of Au are immobilised over time (generally 30 minutes for a standard preparation of 0.5 g) by dropping the colloid in a beaker containing the support. This could lead to bigger particles due to coalescence of newly introduced particles with already immobilised ones.

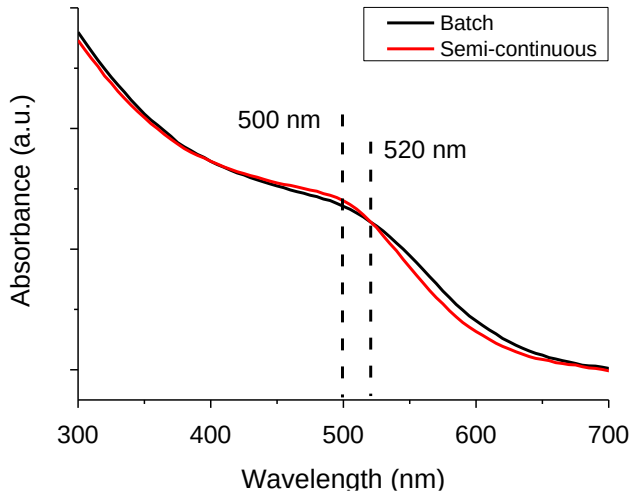

Figure 3.8: Comparison between the Au plasmonic resonance of the batch and semi-continuous colloids.

Table 3.1: Au plasmonic resonance, particle dimension and metal loading of the catalysts prepared with different technique: batch, semi-continuous and continuous.

Catalyst	Particle size [nm]		Metal loading [wt%]
	DLS	STEM	
Batch	5.6 ± 1.7	5.6 ± 1.6	0.94
Semi-continuous	5.5 ± 1.7	6.5 ± 1.7	0.94

During the Au reduction, noble metal build-up was observed on the inner wall of the T-shape connection and the tube. After ca. 30 minutes, a thin dark purple layer was clearly observable, but it was limited to the first 2 - 3 cm of the tubing and the connection (Figure 3.9). To evaluate the actual amount of metal lost due to deposition, an aqueous solution of aqua regia (HCl : HNO_3 3 : 1 mol : mol) was passed through the connection and tubing, in order to fully dissolve the metallic Au. The solution was further diluted and analysed at the MP-AES. The results show a total metal loss of only 0.27 %, with an amount of Au deposited of 27 µg per 10 mg of Au colloid produced. These results were further confirmed by MP-AES analysis on the catalyst synthesised, resulting in an effective metal loading that perfectly matches the one obtained with the batch catalyst (0.94 wt%).

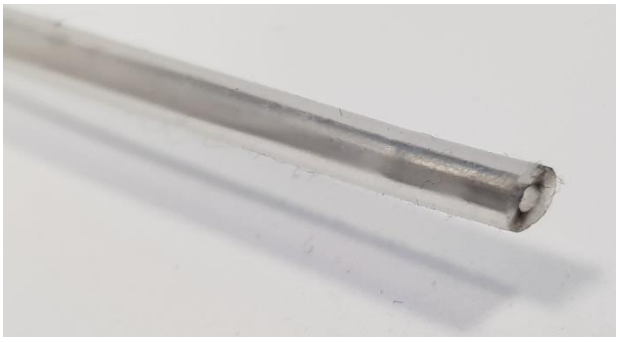

Figure 3.9: Examlpe of Au deposition on the tube inner walls.

In order to try to obtain the best performance from the semi-continuous setup, several parameters were optimised. In particular, the three main factors that affect the quality of the nanoparticles produced are the reaction parameters, the colloid residence time and the solution mixing.

3.3.2. Reaction parameters

The formation of stabilised metal nanoparticles in solution has been explained in details in the introduction chapter (Chapter 1.4 and 1.5). Several parameters can affect the efficient reduction of the metal precursor and the subsequent stabilisation of the nanoparticles formed. Among them, the concentration of metal, stabiliser and reducing agent and the solution pH were studied and the optimum conditions for the production of small and monodisperse metal nanoparticles were identified.

3.3.2.1. Stabiliser concentration

The concentration of stabiliser agent was changed relative to the concentration of Au in solution. In the batch synthetic procedure, a PVA : Au weight ratio of 0.65 was used. Au colloids were further produced doubling the ratio to 1.3 and without using stabilising agent (Table 3.2). The absence of PVA, as expected, led to the production of large nanoparticles with a broad particle size distribution (14.5 ± 8.7 nm, Figure 3.10). On the other hand, the presence of an excess of PVA did not significantly change the characteristics of the Au colloid produced, and small well uniform Au NPs were efficiently produced with a PVA : Au ratio of 1.3 (6.0 ± 1.4 nm). However, from a catalytic point of view, it is always desirable to use the lowest amount of stabilising agent, since it may block or decrease the accessibility of the metal active sites from the substrate, affect adsorption/desorption of substrates/products and thus decrease the overall activity. The presence of a thicker polymeric layer was confirmed by DLS analysis, with the hydrodynamic diameter increasing from 5.5 ± 1.7 nm with a PVA Au ratio of 0.65 to 7.0 ± 1.3 nm with a ratio of 1.3 (Table 3.2). Interestingly, DLS analysis of the catalyst produced with no PVA gave a smaller particle size compared to STEM analysis. It is possible again that particle growth happened during the immobilisation step. Unstable Au particles, in fact, might have undergone coalescence and growth once added into the beaker containing the support, with the already immobilised particles acting as seeds for further growth.

Table 3.2: Stabiliser concentration effect on Au plasmonic resonance, particle dimension and metal loading.

PVA : Au [wt : wt]	Particle size [nm]		Metal loading [wt%]
	DLS	STEM	
0	10.5 ± 2.9	14.5 ± 8.7	0.97
0.65	5.5 ± 1.7	6.5 ± 1.7	0.94
1.3	7.0 ± 1.3	6.0 ± 1.4	0.93

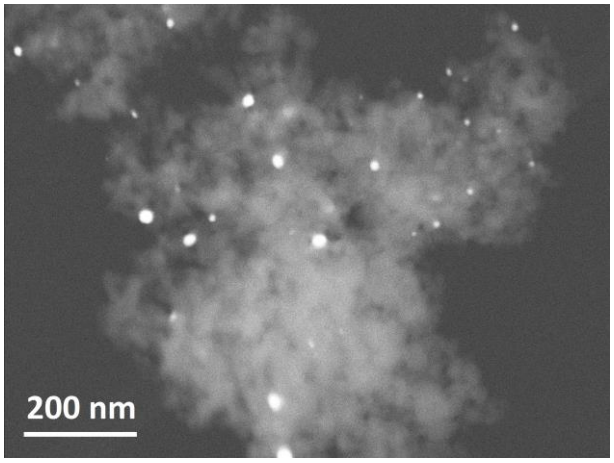

Figure 3.10: Representative STEM image of the catalyst prepared without PVA.

Figure 3.11 shows the UV-Vis analysis of the Au nanoparticles produced with different PVA : Au weight ratios. It is interesting to notice a marked difference in the interband region between the catalysts produced with the use of stabilising agent and the one without PVA (green box in Figure 3.11 - left). A decreased intensity in that region of the spectrum could suggest a not complete reduction of the metal precursor; the intensity of interband absorption is in fact proportional to the amount of Au(0) present in solution[45]. MP-AES analysis (Table 3.2), however, shows a similar metal loading among the three samples, meaning that eventual unreduced Au precursor is ultimately reduced at the end of the synthesis, possibly in the beaker during the immobilisation step. Changes in the surface plasmon resonance are also observable from Figure 3.11 - right. For both 0.65 and 1.3 PVA : Au weight ratio, in fact, the plasmon resonance maximum is centred at ca. 500 nm, while when no stabiliser was used the peak maximum shifted slightly towards higher wavelengths. At the same time, the catalyst with no PVA shows a lower plasmon resonance damping, that is indicative of the presence of bigger nanoparticles as previously mentioned[38,40,41].

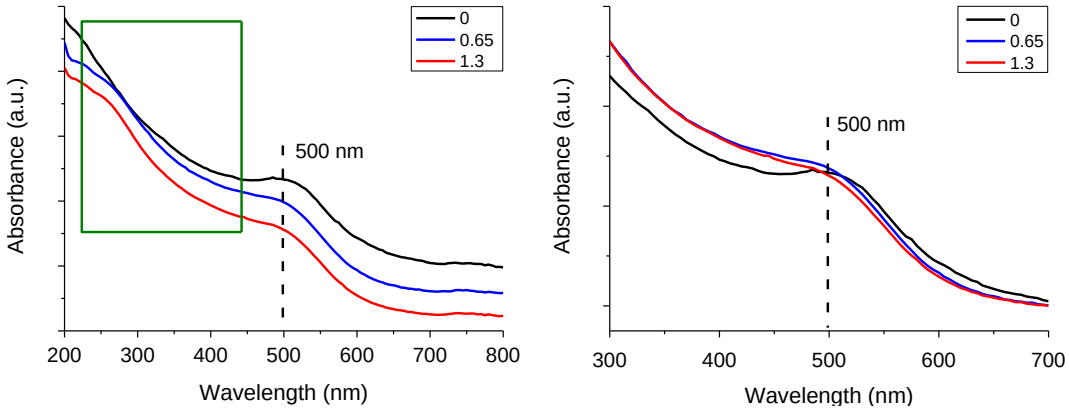

Figure 3.11: Comparison between the Au plasmonic resonance of the nanoparticles prepared with different PVA : Au ratio (left); the spectra have been vertically shifted in order to avoid complete overlap. The green box highlights differences in the interband region. On the right, a zoom-in on the plasmonic region of the overlapped spectra. Reaction conditions: total flow rate 6 mL min^{-1}, reactor length 80 cm (residence time 8 s), Au concentration 0.127 mmol L^{-1}, $NaBH_4$: Au molar ratio 5, temperature 25 °C.

3.3.2.2. Reducing agent concentration

The reductant, $NaBH_4$, is typically used in excess in order to accomplish full and fast reduction of the $AuCl_4^-$ species[46]. A broad range of $NaBH_4$: Au molar ratios (from 1 to 7.5) was investigated and an optimum value identified. Even when the lowest ratio was used, the $NaBH_4$ concentration was higher than the stoichiometric value. The reduction reaction, in fact, generates zero-valent Au atoms according to the following reaction:

$$8\,HAuCl_4 + 3\,NaBH_4 + 12\,H_2O \rightarrow 8\,Au + 3\,NaB(OH)_4 + 32\,HCl$$

Therefore, due to the stoichiometry of the reaction, one molecule of $NaBH_4$ can reduce ca. 2.7 molecules of $HAuCl_4$. However, $NaBH_4$ slowly decomposes in water according to the following reaction[47]:

$$BH_4^- + 2\,H_2O \rightarrow BO_2^- + 4\,H_2$$

When a $NaBH_4$: Au molar ratio of 1 was used, less than half of the metal was successfully deposited onto the support leaving the filtrated solution rich in Au^{3+}. These results were further confirmed by analysis of the absorbance intensity at 400 nm in the UV-Vis spectra. It has been reported in the literature that at this wavelength a correlation exists between absorbance intensity and Au(0) concentration (more detail will be given in the next section)[45]. Figure 3.12 confirms a very low intensity of absorbance at 400 nm compared to the other catalysts, indicating incomplete reduction of the Au precursor. Moreover, the

nanoparticles produced were very large in size compared to the batch protocol and with a broad particle size distribution (22.9 ± 8.2 nm), as confirmed by STEM analysis and by the strong shift of the plasmonic peak to higher wavelengths (ca. 540 nm) in Figure 3.13 - right. It is therefore clear that, despite $NaBH_4$ being present in concentration higher than the stoichiometric amount, the reducing agent cannot efficiently and rapidly reduce the Au precursor. The presence of unreduced Au precursor is further confirmed by the presence of a small peak at ca. 300 nm characteristic of the $AuCl_4^-$ precursor.

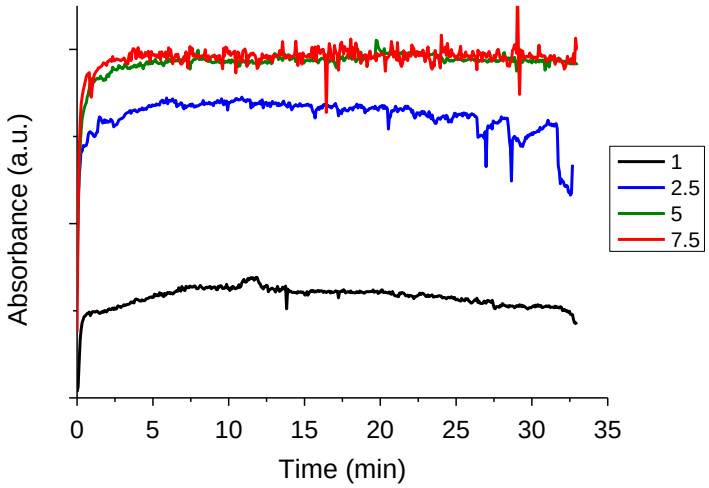

Figure 3.12: Variation over time of the intensity at 400 nm as indication of the complete reduction of Au(III) precursor.

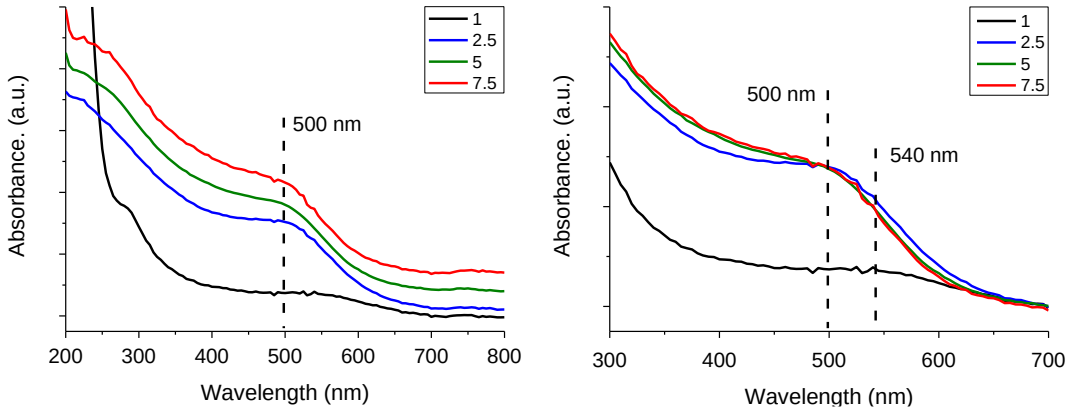

Figure 3.13: Comparison between the Au plasmonic resonance of the nanoparticles prepared with different $NaBH_4$: Au ratio (left); the spectra have been vertically shifted in order to avoid complete overlap. On the right, a zoom-in on the plasmonic region of the overlapped spectra. Reaction conditions: total flow rate 6 mL min^{-1}, reactor length 80 cm (residence time 8 s), Au concentration 0.127 mmol L^{-1}, PVA : Au weight ratio 0.65, temperature 25 °C.

On increasing the $NaBH_4$ concentration, small nanoparticles were produced. In particular, 9.0 ± 2.8 nm nanoparticles were produced with a $NaBH_4$: Au ratio of 2.5, and 6.5 ± 1.7 nm with a ratio of 5 (Table 3.3). As a consequence, the plasmonic peak shifted to lower wavelengths (Figure 3.13). An excess of reducing agent ($NaBH_4$: Au - 7.5), however, caused again the production of bigger nanoparticles (11.3 ± 4.0 nm). This effect is possibly caused by destabilisation triggered by the excess of electrolytes (Na^+, BH_4^-, $B(OH)_4^-$ and BO_2^- among others) in solution as it has been previously reported[48]. The UV-Vis analysis, however, does not show any appreciable change in either resonance shift or damping; it is therefore possible that the destabilisation happened during the immobilisation step rather than during the particle formation.

Table 3.3: Reducing agent concentration effect on Au plasmonic resonance, particle dimension and metal loading.

$NaBH_4$: Au [mol : mol]	**Particle size [nm]**		**Metal loading [wt%]**
	DLS	**STEM**	
1	50.9 ± 3.0	22.9 ± 8.2	0.41
2.5	6.7 ± 1.9	9.0 ± 2.8	0.90
5	5.5 ± 1.7	6.5 ± 1.7	0.94
7.5	16.1 ± 2.2	11.3 ± 4.0	0.92

3.3.2.3. Metal concentration

The concentration of metal precursor was varied in the range 0.102 to 0.254 mmol L^{-1}, changing the PVA and $NaBH_4$ concentrations accordingly (the ratios PVA : Au and $NaBH_4$: Au were kept constant). Comparing the UV-Vis spectra, it is possible to notice that when increasing the Au concentration, the intensity of absorbance increases accordingly (Figure 3.14). Ideally, this concentration effect should be described by the well-known Beer-Lambert law (Equation 3.1):

$$A_\lambda = \varepsilon_\lambda l C \qquad Equation\ 3.1$$

Where A_λ is the sample absorbance at a certain wavelength λ, ε_λ is the sample molar attenuation coefficient, l is the path length of the beam of light through the material sample and C is the sample concentration.

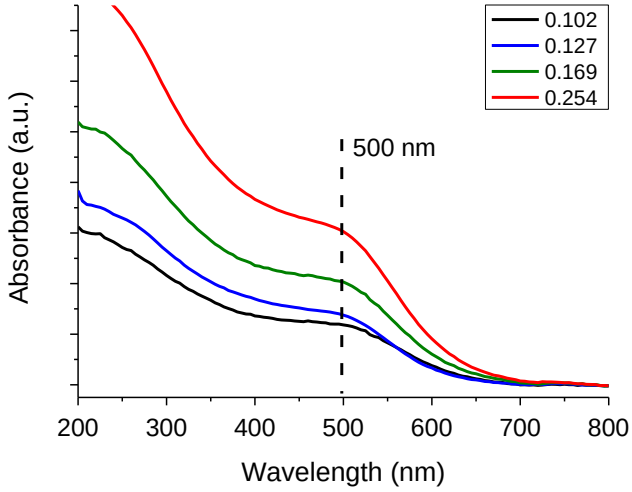

Figure 3.14: Comparison between the Au plasmonic resonance of the nanoparticles prepared with different Au precursor concentration. Reaction conditions: total flow rate 6 mL min^{-1}, reactor length 80 cm (residence time 8 s), PVA : Au weight ratio 0.65, $NaBH_4$: Au molar ratio 5, temperature 25 °C.

The strong dependency of surface plasmon resonance to size and shape of the nanoparticles and the surrounding environment, however, makes the application of the Beer-Lambert law difficult. A recent report suggested to use the absorption at 400 nm as a reference to evaluate the concentration of Au(0) in gold nanoparticles[45]. At this wavelength, in fact, the plasmonic resonances contribute only a small amount of absorption to the overall intensity, while organic and inorganic molecule present in solution (ions, stabilising agent, etc.) are usually colourless due to absorption in the UV region only. The absorbance at this wavelength is then only due to interband transition of gold (particularly from the occupied 5d valence band to the unoccupied levels of the 6s-6p conduction band), and therefore to its concentration in solution[37]. This method has proved to be effective for the evaluation of the concentration of Au(0) in particles of a 2 – 30 nm range and in a similar chemical-physical environment (same solvent, temperature and pressure)[45]. To validate this hypothesis, the absorbance intensity at 400 nm was plotted for the four different concentrations used. The results (Figure 3.15) show a very linear correlation in the range studied, with a calculated molar attenuation coefficient of 2.81 L $mmol^{-1}$ cm^{-1}, a value in line with what obtained by Hendel and colleagues in their work[45].

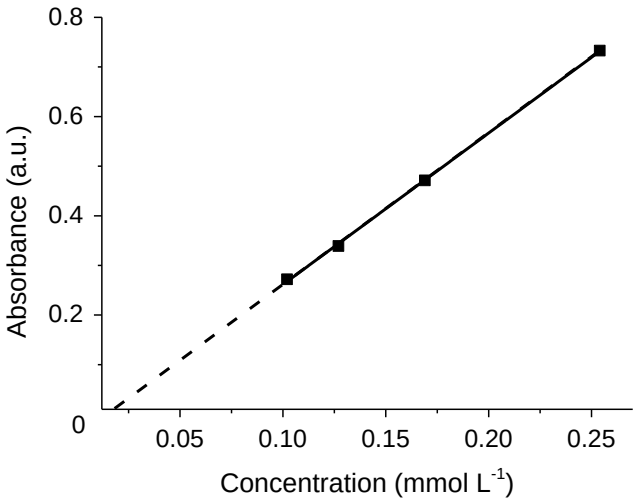

Figure 3.15: Relation between absorbance intensity at 375 nm and Au nanoparticle concentration for the range studied. The molar coefficient was calculated as the slope of the linear fitting.

The change in metal precursor concentration did not have a strong effect on the particle dimensions, as shown by UV-Vis analysis (Figure 3.14); no appreciable variation in plasmon resonance was observable, since variation in intensity of the plasmonic peak can be simply correlated to the different concentration of the Au(0) present in solution rather than changes in particle size. DLS analysis, however, shows an increase in hydrodynamic diameter from 5.5 ± 1.7 nm to 8.0 ± 1.7 nm with a concentration of 0.127 mmol L^{-1} and 0.102 mmol L^{-1} respectively, and to 7.4 ± 1.5 nm with a concentration of 0.254 mmol L^{-1}, suggesting an optimum Au precursor concentration of 0.127 mmol L^{-1} for the production of smaller nanoparticles (Table 3.4).

Table 3.4: Au precursor concentration effect on plasmonic resonance, particle dimension and metal loading.

C_{Au} [mmol L^{-1}]	Particle size [nm]		Metal loading [wt%]
	DLS	STEM	
0.102	8.0 ± 1.7	n.a.	0.94
0.127	5.5 ± 1.7	6.5 ± 1.7	0.94
0.169	7.4 ± 1.5	n.a.	0.93
0.254	7.4 ± 1.5	n.a.	0.96

3.3.2.4. pH

When preparing the solution to be used in catalyst synthesis, a specific amount of stock tetrachloroauric acid ($HAuCl_4$) solution was diluted to obtain the desired Au concentration (usually 0.127 mmol L^{-1}). The pH of this solution was 3.6, and the only Au(III) species present is $AuCl_4^-$. Simply by changing the pH, it is possible to induce Au speciation and thus obtain different Au(III) species (Figure 3.16)[49]: $AuCl_3(OH)^-$, $AuCl_2(OH)_2^-$, $AuCl(OH)_3^-$ and $Au(OH)_4^-$. Every species exists in a specific range of pH and has its own reducing potential. In particular, increasing the number of OH groups on the Au(III) ion, the reduction potential decreases (Table 3.5)[50]. It is therefore expected that the reduction reaction will take longer when species with low reduction potential are used, which in turn results in bigger nanoparticles.

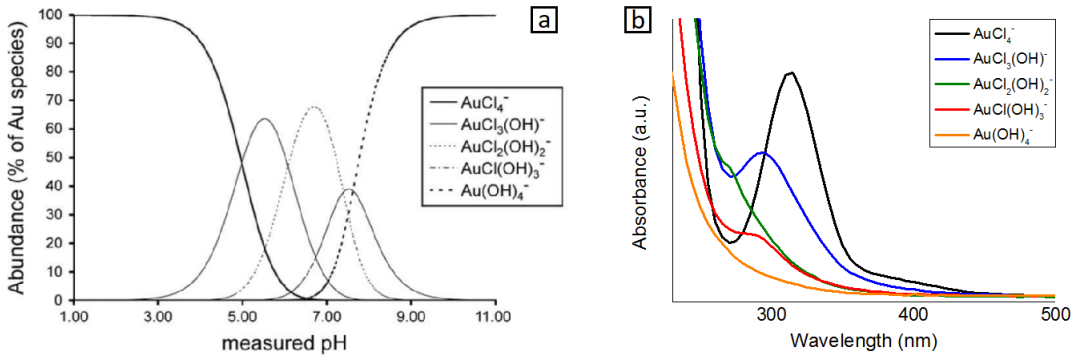

Figure 3.16: a) Relative Au(III) species abundance in aqueous solution at different pH. b) UV-Vis spectra of the different Au(III) species. Image a) reprinted with permission from A. Usher et al., Geochimica et Cosmochimica acta, 2009, 3359-3380.

Table 3.5: Reduction potential (E°) of the different Au(III) precursors.

Reduction reaction	**E° [V][a]**
$AuCl_4^- + 3\ e^- \Rightarrow Au + 4\ Cl^-$	+ 1.00
$AuCl_3(OH)^- + 3\ e^- \Rightarrow Au + 3\ Cl^- + OH^-$	n.a.
$AuCl_2(OH)_2^- + 3\ e^- \Rightarrow Au + 2\ Cl^- + 2\ OH^-$	+ 0.94
$AuCl(OH)_3^- + 3\ e^- \Rightarrow Au + Cl^- + 3\ OH^-$	+ 0.69
$Au(OH)_4^- + 3\ e^- \Rightarrow Au + 4\ OH^-$	+ 0.60

[a] *M. L. Machesky. Chemical Geology, 1992, 53-71.*

Three different pH values were studied, in order to obtain the species $AuCl_4^-$, $AuCl_2(OH)_2^-$ and $Au(OH)_4^-$. The pH was controlled by addition of a diluted solution of sodium hydroxide to obtain 6.9 and 9.6 (Table 3.6). As expected, bigger nanoparticles were produced at higher pH (from 5.5 ± 1.7 with $AuCl_4^-$ to 7.5 ± 2.4 nm with $Au(OH)_4^-$), as indicated by both DLS and UV-Vis analysis (Figure 3.17). The lower reduction potential of the metal precursor,

in fact, slows down the whole reduction process leaving more time for the unreduced Au(III) to be used in the growth step rather than in the nucleation step. The small increase in nanoparticles dimension once again results in a large redshift of the plasmonic resonance band, with the peak shifting from ca. 500 nm to ca. 540 nm. This enhanced redshift is probably due to the changed surrounding environment (Figure 3.17)[29].

Table 3.6: pH effect on Au plasmonic resonance, particle dimension and metal loading.

pH	Particle size [nm]		Metal loading [wt%]
	DLS	STEM	
3.6	5.5 ± 1.7	6.5 ± 1.7	0.94
6.9	6.3 ± 1.8	n.a.	0.95
9.6	7.5 ± 2.4	n.a	0.97

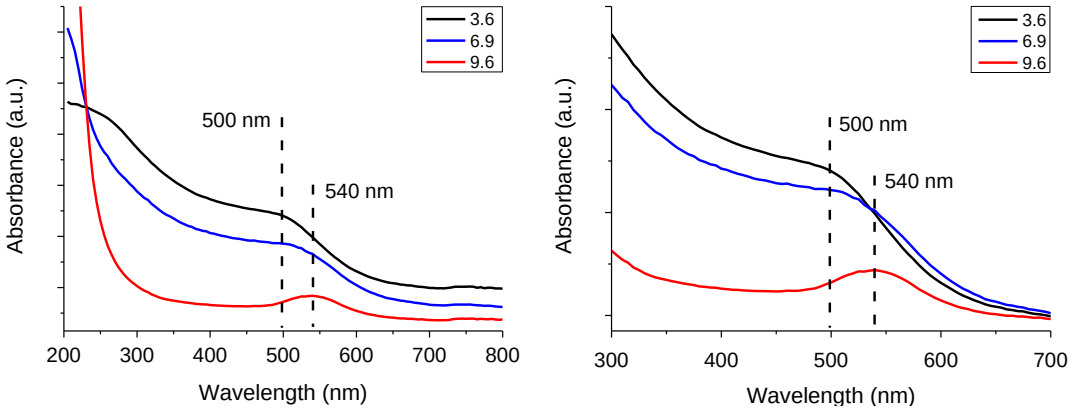

Figure 3.17: Comparison between the Au plasmonic resonance of the nanoparticles prepared starting with different Au(III) solution pH (left); the spectra have been vertically shifted in order to avoid complete overlap. On the right, a zoom-in on the plasmonic region of the overlapped spectra. Reaction conditions: total flow rate 6 mL min^{-1}, reactor length 80 cm (residence time 8 s), Au concentration 0.127 mmol L^{-1}, PVA : Au weight ratio 0.65, $NaBH_4$: Au molar ratio 5, temperature 25 °C.

A longer reduction time, in a continuous flow reactor, means a longer residence time for the reaction to be completed and thus a longer reactor. Since the reactor length from the T-shape connection to the in-line UV-Vis flow cell was kept constant at 50 cm, it is not surprising that the intensity at 400 nm markedly decreased (Figure 3.17). A further confirmation can be drawn simply by looking at the tubing used for the synthesis of the three catalysts at different pH (Figure 3.18). The Au deposition can be seen as a clear indication of where the nucleation step takes place. The tube used at pH 3.6 shows Au deposition at the very beginning, at the junction with the T-shape connection, while the tube used at pH 6.9 shows Au deposition further on the tube, approximatively 3 – 5 cm from the connection.

Finally, the tube used at pH 9.6 presents no clear Au deposition throughout the tube length, because most of the nucleation step took place either in the tubing after the in-line UV-Vis flow cell or directly in the beaker containing TiO_2. From MP-AES analysis on the final catalyst, the metal loading was close to 1 wt% for all the catalysts, proving that all the metal had ultimately been deposited on the surface of the support.

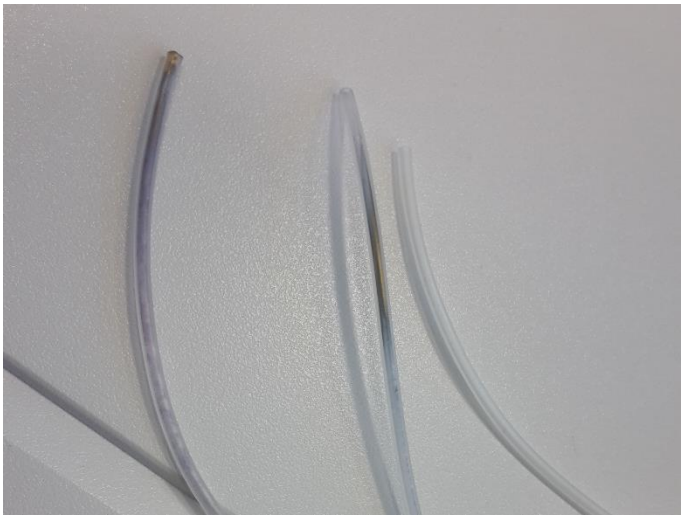

Figure 3.18: Au deposition on the tubing used with different Au(III) species as precursor. From left: pH 3.6, pH 6.9 and pH 9.6.

3.3.3. Residence time

The time that the two solutions take to pass through the whole reactor (from when they make contact until the colloid reaches the beaker containing the support) is defined as the residence time. Long residence times are often desired in the synthesis of relatively big nanoparticles (10 – 100 nm) via a seed mediated growth mechanism; in this way, the formed nuclei have time to grow and thus the final nanoparticle dimensions can be tuned simply by changing the residence time. On the other hand, in the Brust-Schiffrin based methods, the residence time does not significantly influence the final particle size. The use of a strong reducing agent, in fact, consumes the whole metal precursor in a very short time, greatly enhancing the production of nuclei and leaving no metal precursor for the growth step. In this context, short residence time are more desirable to avoid potential particle coalescence and to rapidly remove unwanted species present in the reaction media that can interfere with the reduction/stabilisation process (presence of chloride and sulphate ions and products of $NaBH_4$ decomposition). The residence time can be varied simply by changing either the

reactor length or the solution's flow rate. The latter, however, has a strong influence on the mixing as well, and therefore it will be analysed in the mixing Section (Chapter 3.3.4).

3.3.3.1. Reactor length

As reported in other studies[51,52], the reactor length should be optimised in order to achieve complete reduction of the metal precursor whilst avoiding unwanted growth or coalescence of the NPs. For this reason, the reactor length was varied from 80 to 130 cm by changing the tubing between the T-shape connection and the in-line UV-Vis cuvette. The flow was maintained at a constant value of 6 mL min^{-1}. The residence time was consequently varied from 8 to 13 s using 80 and 130 cm long reactors.

Since all the metal precursor was efficiently reduced using only 50 cm of reactor, the use of longer tubing should only result in larger nanoparticles with broader distributions. In fact, increasing the reactor length from 80 cm to 130 cm, the mean particle size increased from 6.5 nm to 7.2 nm (Table 3.7), with the size distribution increasing as well from ± 1.7 to ± 2.6 nm. It is possible that the interaction between the plastic of the inner walls of the tubing with the stabilising agent PVA causes a destabilisation effect that enhances coalescence phenomena. The type of tubing, in fact, can affect the quality of the nanoparticles produced due to the different surface chemistry of various materials[53].

Shorter reactor length of 30 cm was achieved by bypassing the in-situ cuvette, for a residence time of 3 s. UV-Vis spectra were recorded collecting a small amount of colloid produced at the end of the tubing. A further decrease in reactor length produced even smaller nanoparticles (5.7 ± 1.3 nm). UV-Vis analysis do not show any particular change in either surface plasmon resonance shift or damping (Figure 3.19); the catalyst produced with 30 cm of reactor displayed a slightly different plasmon resonance compared to the other catalysts, although this change could be attributed to the different acquisition method (in-situ versus ex-situ).

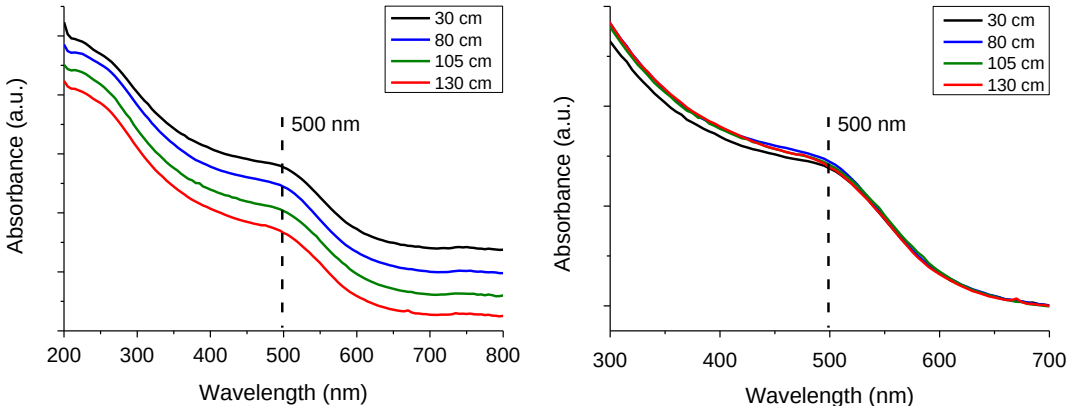

Figure 3.19: Comparison between the Au plasmonic resonance of the nanoparticles prepared using different reactor lengths (left); the spectra have been vertically shifted in order to avoid complete overlap. On the right, a zoom-in on the plasmonic region of the overlapped spectra. Reaction conditions: total flow rate 6 mL min^{-1}, Au concentration 0.127 mmol L^{-1}, PVA : Au weight ratio 0.65, $NaBH_4$: Au molar ratio 5, temperature 25 °C.

Table 3.7: Reactor length effect on Au plasmonic resonance, particle dimension and metal loading.

Reactor length [cm]	Particle size [nm]		Metal loading [wt%]
	DLS	STEM	
130	6.8 ± 1.8	7.2 ± 2.6	0.92
105	6.1 ± 1.7	7.0 ± 2.1	0.95
80	5.5 ± 1.7	6.5 ± 1.7	0.94
30	5.9 ± 1.7	5.7 ± 1.3	0.95

3.3.4. Mixing

One of the most critical parameter in producing uniform metallic nanoparticles in a continuous fashion is the efficient mixing of the two solutions inside the tubing. Of paramount importance of the mixing in flow micro- and milli-reactors has been extensively described in Chapter 1.6. In general, from both a macro- and microscopic point of view, mixing follows a two-step sequence: lamination followed by inter-diffusion[19]. A heterogeneous mixture of two fluids is formed by convection, and can be easily reached macroscopically through vigorous mechanical stirring. In the straight channels of micro- and milli-fluidic devices, mixing is more problematic due to laminar flow and the absence of mechanical stirring.

To solve this problem, mixing can be induced by either increasing the flow rate of the reactant solutions or by modifying the geometry of the reactor. As already mentioned in

Chapter 1.6, there are two dimensionless numbers that characterise the flow of a fluid in a channel, namely the Reynolds number and the Dean number. Mathematically they can be expressed by Equation 3.2 and 3.3:

$$Re = \frac{uL}{v} \qquad Equation\ 3.2$$

$$De = Re\sqrt{\frac{L}{R}} \qquad Equation\ 3.3$$

where u is the mean velocity of the fluid in the tube, L is the diameter of the tube, v is the kinematic viscosity and R is the radius of curvature of the tube. For higher De, the mixing is more efficient due to the formation of the so-called Dean vortices. For a simple curved channel with aspect ratio (R / L) of 40, for example, Dean vortices start to form at De ca. 40 – 60 and they become stable at De higher than ca. 60 – 75[54]. The generation of Dean vortices, however, strictly depends on the curvature ratio, thus prediction *a priori* of their behaviour is very difficult[19].

From these two equations it is clear which parameters can affect the formation of the Dean vortices and thus improve the solutions mixing. Considering the viscosity constant (the solutions are very diluted), the mixing can be improved by increasing the flow rate (u) and by modifying the reactor geometry (increasing L or decreasing R).

3.3.4.1. Flow rate

The flow rate was varied between 1 and 24 mL min^{-1}, causing a change in residence time between 2 and 48 seconds considering a reactor length of 80 cm. Reynolds numbers were calculated using the Equation 3.2; for all the flow rates used, the Re varies from 13 at 1 mL min^{-1} up to 320 at 24 mL min^{-1}, confirming the presence of a laminar flow environment (Re < 2,300)[16]. Laminar flows are desired, since back mixing phenomena characteristic of the turbulent regime lead to differences in the residence times of single volume units and thus to broader size distribution of the NPs produced[16]. Laminar flows, however, can also have disadvantages; the first is that the mixing between solutions is dominated by molecular diffusion, that is a slower process compared to advection. The second is that due to friction between the fluid and the wall of the tubing, the flow profile assumes a parabolic shape, resulting in differences in contact times along the radial cross section of the tubing. Varying

the flow velocity and the tubing material can reduce this parabolic profile due to friction reduction[55–58].

In addition, the flow rate can strongly affect the conditions inside the T-shape connection, the part of the reactor where the two feeding streams are merged. The presence of sharp turns, in general, leads to formation of vortices analogous to Dean vortices characteristic of flow in curved pipe that are caused by the large inertial force of the flow[59]. In a T-shape connection, in particular, 2 sub-regimes can be distinguished based on the Reynolds number[59]. At Re < 50, the two streams do not have inertial force high enough to create vortices and thus they simply flow side by side; the only mixing mechanism is thus molecular diffusion. The mixing is enhanced at Re higher than 50, where vortices start to appear. This mechanism can be better visualized in Figure 3.20.

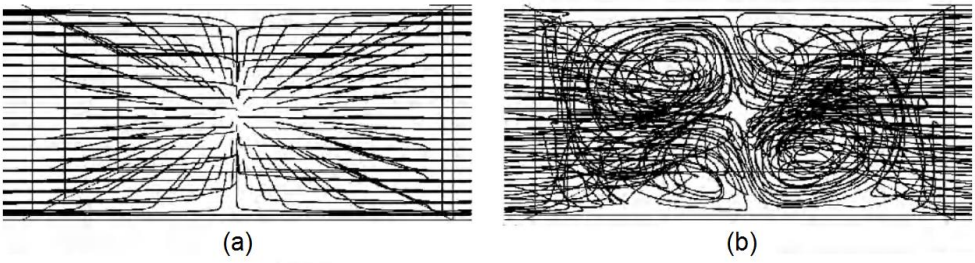

Figure 3.20: Trajectory inside a T-mixer at (a) Re <50 and (b) Re > 50. In (a) the flow is perfectly laminar, and the mixing is by molecular diffusion, while in (b) asymmetrical Dean vortices cause chaotic advection, greatly improving the mixing. Image adapted with permission from D. Bothe et al., Chem. Eng. Sci., 2006, 2950-2958.

At a total flow rate equal or lower than 4 mL min^{-1} (Re < 50), the mixing is then entirely dominated by molecular diffusion. This led to bigger nanoparticles with a broader size distribution due to a slow and inefficient mixing (Table 3.8). The mean nanoparticles size, in fact, increases from 7.0 ± 6.2 at 4 mL min^{-1} to 15.1 ± 6.2 nm at 1 mL min^{-1}. Particularly big nanoparticles were produced at a flow rate of 1 mL min^{-1} due to $NaBH_4$ decomposition, as is demonstrated later on this chapter. An increase in flow rate enhanced the chaotic advection caused by the Dean-type vortices and this is reflected on the size of the particles produced (6.5 ± 1.7 nm and 5.4 ± 0.9 nm with a flow rate of 6 and 8 mL min^{-1} respectively). A further increase in flow rate did not reveal a significant change in the particle size and size distribution (Table 3.8), suggesting that the mixing caused by variation of flow velocity is already optimised for values as low as 8 mL min^{-1}.

Table 3.8: Flow rate effect on Reynolds number, Au plasmonic resonance, particle dimension and metal loading.

Flow rate [mL min^{-1}]	Re	Particle size [nm]		Metal loading [wt%]
		DLS	STEM	
1	13	18.3 ± 2.1	15.1 ± 6.2	0.81
2	27	6.8 ± 2.0	6.7 ± 1.5	0.87
4	53	6.1 ± 1.6	7.0 ± 2.0	0.88
6	80	5.5 ± 1.7	6.5 ± 1.7	0.94
8	107	6.0 ± 1.7	5.4 ± 0.9	0.92
24	320	5.9 ± 1.7	5.6 ± 1.3	0.94

Figure 3.21 reports the in-line UV-Vis analysis after 30 minutes at different flow rates. The complete reduction of the Au precursor was very quick, as confirmed by the absorbance intensity at 400 nm in the in-line UV-Vis spectra of the colloid prepared with a 24 mL min^{-1} flow. A small increase in intensity of the plasmon resonance is noticeable only in the colloid prepared at a flow rate of 1 mL min^{-1}, suggesting the presence of bigger nanoparticles.

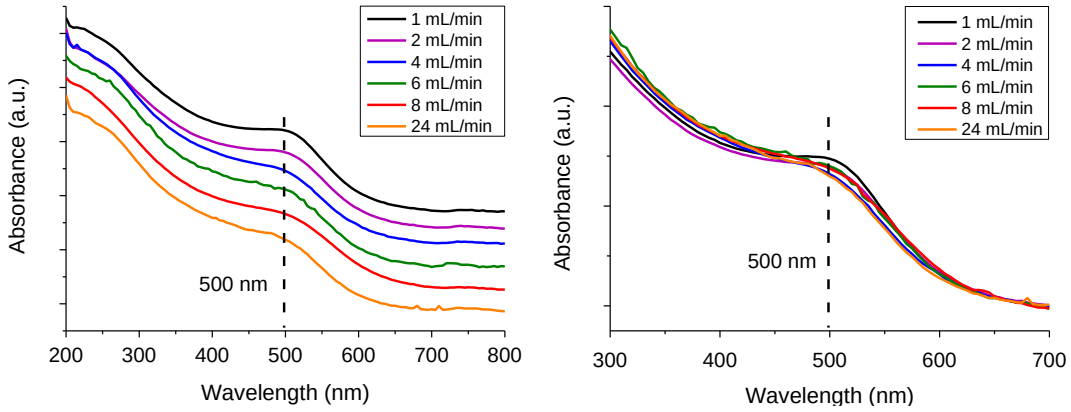

Figure 3.21: Comparison between the Au plasmonic resonance of the nanoparticles prepared using different flow rates (left); the spectra have been vertically shifted in order to avoid complete overlap. On the right, a zoom-in on the plasmonic region of the overlapped spectra. Reaction conditions: reactor length 80 cm, Au concentration 0.127 mmol L^{-1}, PVA : Au weight ratio 0.65, $NaBH_4$: Au molar ratio 5, temperature 25 °C.

The evolution of the Au plasmonic peak over extended continuous operation during the synthesis of Au colloid with a flow rate of 1 mL min^{-1} is depicted in Figure 3.22. Stable and uniform Au colloids were produced for the first 65 minutes of continuous flow, as confirmed by the position of the plasmonic peak (position constant to ca. 500 nm), and after which, structural changes were observed. A slow and constant redshift of the plasmon resonance

was noticeable from 65 to 140 minutes, as clear indication of the production of bigger NPs. The redshift of the plasmonic peak continues until it reaches a value of ca. 520 nm after 200 minutes. This effect is due to the progressive decomposition of $NaBH_4$ in H_2O. As already mentioned, in fact, the reducing agent slowly decomposes in aqueous solution[47]. To confirm this hypothesis, the absorbance at 400 nm was plotted over time (Figure 3.23). The study of the intensity at 400 nm, as already mentioned, is a powerful tool to detect any change in Au nanoparticles concentration. The graph shows constant intensity up until 35 minutes, after which a slow decrease was measured, meaning that some unreduced Au(III) precursor was still in solution. From ca. 145 minutes onward, the intensity at 400 nm dropped significantly, clearly indicating the inefficient reduction of the Au(III) ions. These results are reflected in the final catalyst metal loading: the catalyst prepared with a flow rate of 1 mL min^{-1} showed a lower metal loading compared with the one prepared at 6 mL min^{-1} (0.81 % and 0.94 % respectively). The $NaBH_4$ decomposition effect was observed on the catalysts produced with a 2 mL min^{-1} and 4 mL min^{-1} flow rates as well, but in much smaller extent. These results confirm that $NaBH_4$ can be used without concerns about its decomposition only for catalyst preparations that require a reaction time lower than ca. 35 minutes. For longer reaction times, the $NaBH_4$ solution needs to be constantly replaced with a fresh one.

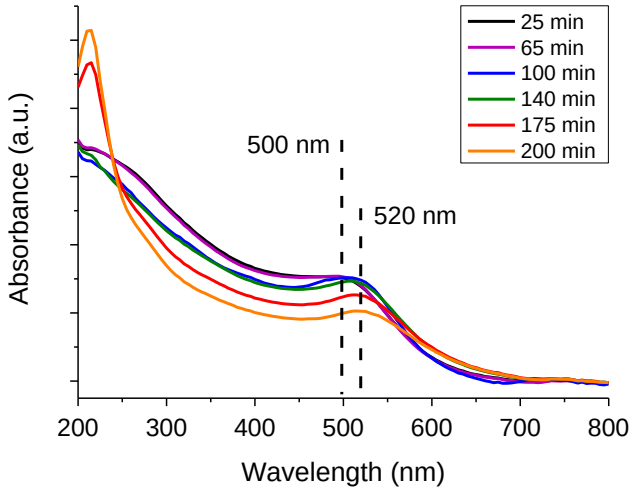

Figure 3.22: Comparison between the Au plasmonic resonance of the nanoparticles during the synthesis of the colloid prepared with a flow rate of 1 mL min^{-1}. Reaction conditions: total flow rate 1 mL min^{-1}, reactor length 80 cm (residence time 48 s), Au concentration 0.127 mmol L^{-1}, PVA : Au weight ratio 0.65, $NaBH_4$: Au molar ratio 5, temperature 25 °C.

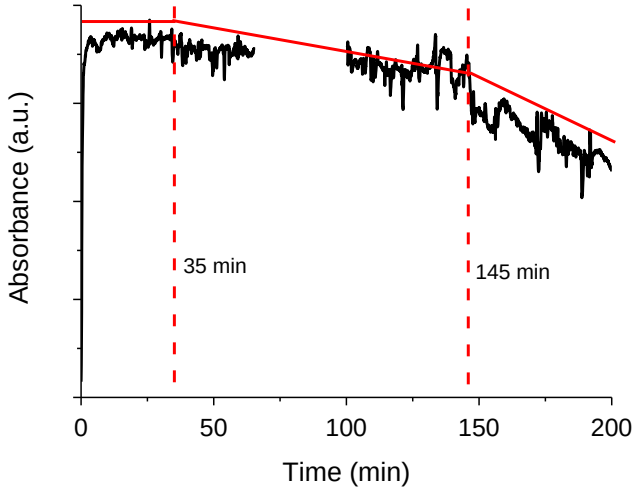

Figure 3.23: Variation over time of the intensity at 400 nm as indication of the complete reduction of Au(III) precursor during the synthesis of nanoparticles with a flow rate of 1 mL min^{-1}.

3.3.4.2. Reactor geometry

Different reactors geometries were designed using CAD software and then printed with a stereolithography 3D printer (see Chapter 2.3). The new printed parts were made of a different material compared to the standard PFA/Puriflex of the connection and tubing used so far in the study. Since it has been previously reported that the tubing material can affect the quality of the metal colloid produced and result in differences in the quality of the NPs produced[53], a printed T-shape connection was initially used and the catalyst produced compared with the standard PFA T-shape connection (Figure 3.24). Both of the connections were identical in characteristics (same length, internal diameter and contact angle) except for the construction material. As predicted, differences in nanoparticle size and size distribution were observed during STEM analysis: smaller and more uniform NPs were produced with the standard PFA T-shape connection (6.5 ± 1.7 nm) compared to the 3D printed one (7.0 ± 1.9 nm). From UV-Vis analysis (Figure 3.25), the plasmonic peak of the Au nanoparticles produced with the 3D printed connection is slightly broader. For this reason, all the new designs were compared with a printed T-shape connection.

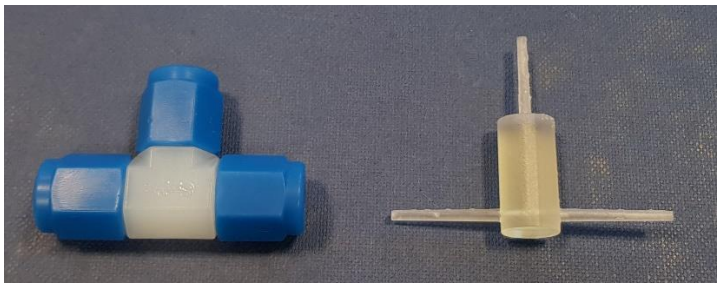

Figure 3.24: Picture of the PFA (left) and 3D printed (right) T-shape connections.

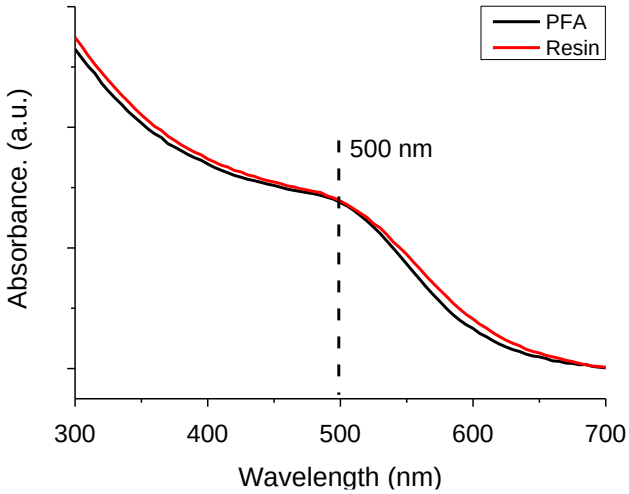

Figure 3.25: Comparison between the Au plasmonic resonance of the nanoparticles prepared using the PFA and the 3D printed T-shape connections. Reaction conditions: total flow rate 6 mL min^{-1}, reactor length 80 cm (residence time 8 s), Au concentration 0.127 mmol L^{-1}, PVA : Au weight ratio 0.65, $NaBH_4$: Au molar ratio 5, temperature 25 °C.

The connection shape can strongly influence the mixing of the two solutions, as discussed in Chapter 1.6. Two types of connections were initially studied (Figure 3.26) and compared with the standard T-shape. The Y-shape connection simply allows the merging of the two streams with a contact angle of 90 °, while the I-shape was designed in such a way to have a coaxial mixing, therefore with a contact angle of 0 ° (Figure 3.27). The comparison between the T-connection and the other geometries is reported in Table 3.9. Decreasing the contact angle from 180 ° to 90 ° (from T-shape to Y-shape), as expected, both nanoparticle dimension and size distribution increase (from 7.0 ± 1.9 nm to 7.4 ± 2.2 nm). The intensity of the Dean vortices, in fact, greatly decreases with the contact angle[19]. Surprisingly, using the I-shape connection, the particle dimension decreased back to 6.4 ± 1.5 nm. This effect is due to the particular design of this connection, where the solution on the outside ($AuCl_4^-$ + PVA) is forced into the solution on the inside ($NaBH_4$). The tube restriction happens in a very short distance, and thus technically the contact angle is not 0 ° but much higher (in this particular

situation the effective contact angle was calculated to be 43 °). Moreover, having one solution flowing into the other one enhances the contact area between the two streams and thus the molecular diffusion is accelerated.

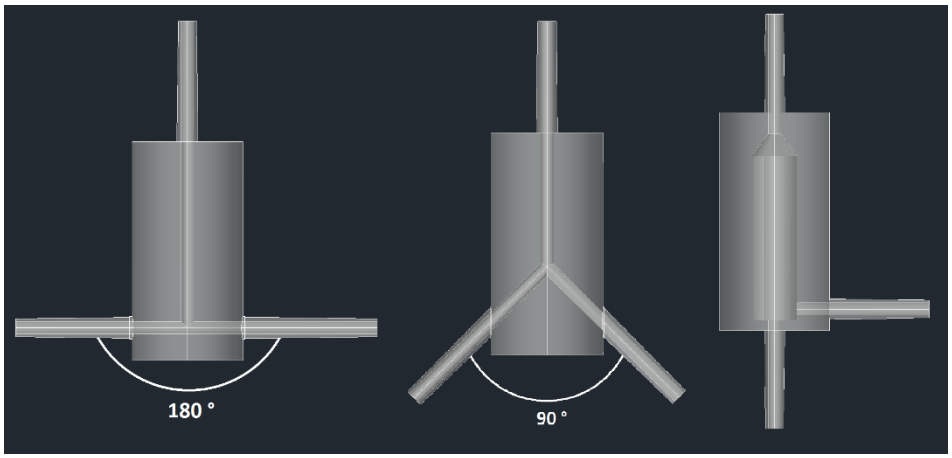

Figure 3.26: Schematic representations of the 3D printed connections with relative contact angles. From left to right: T-shape, Y-shape and I-shape.

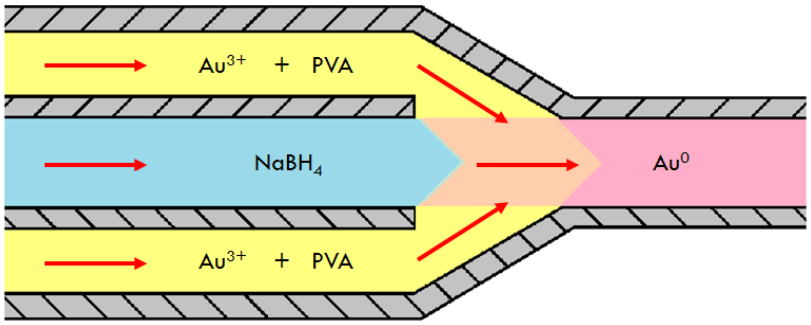

Figure 3.27: Schematic representation of the solutions mixing inside the I-shape connection.

Table 3.9: Connection shape effect on Au plasmonic resonance, particle dimension and metal loading.

Reactor	Particle size [nm]		Metal loading [wt%]
	DLS	STEM	
PFA-T	5.5 ± 1.7	6.5 ± 1.7	0.94
T-shape	5.9 ± 1.7	7.0 ± 1.9	0.95
Y-shape	6.2 ± 2.1	7.4 ± 2.2	0.97
I-shape	5.6 ± 1.8	6.4 ± 1.5	0.96

The mixing can be further improved by modifying the geometry of the reactor tube. Recent studies, in fact, have shown that very fast mixing inside a micro-reactor can be achieved by either increasing the molecular diffusion (by lamination, segmentation or

focussing) or the chaotic advection (by changing the reactor shape). Two additional types of reactor were designed in this study, namely Helix and Plait-like, and are schematically represented in Figure 3.28. The Helix reactor is an 8-turn helicoidal-shape reactor that takes advantage of its 3-dimentional curves to intensify the Dean vortices created by the T-shape connection. The plait-like is a device based on sequential lamination mechanism combined with repeated turns, where the two solutions split and recombine multiple times along their pathway.

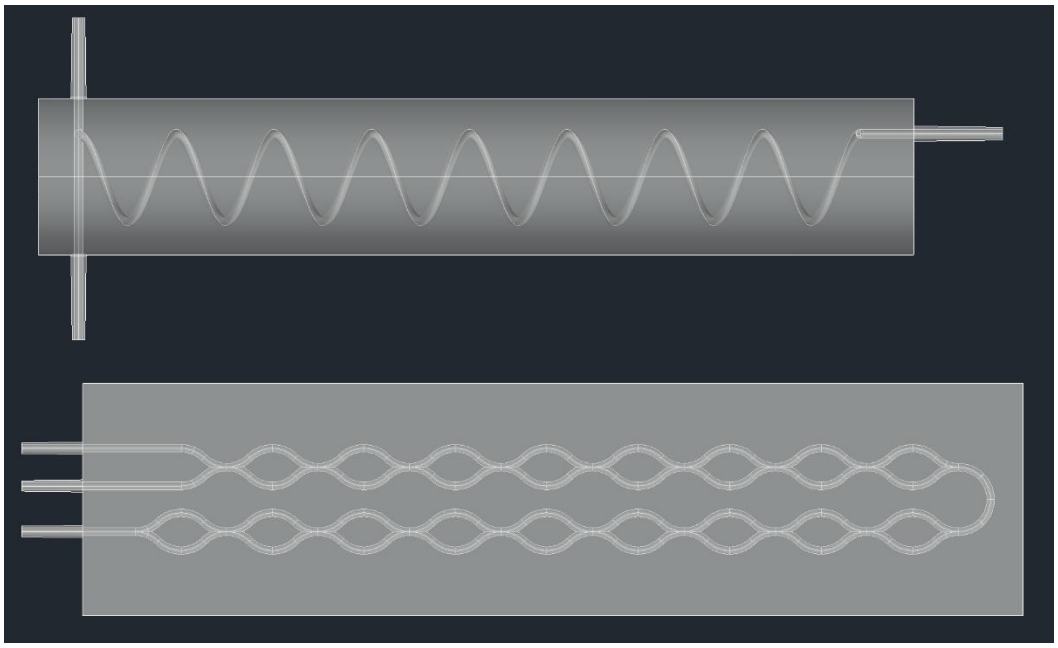

Figure 3.28: Schematic representation of the 3D printed reactors. From top: Helix-shape and Plait-like.

The two reactors were compared with the standard printed T-shape connection, and the results are reported in Table 3.10. Both Helix and Plait-like reactors produced smaller nanoparticles, confirming the better mixing of the two printed reactors. In particular, the mixing caused by intensification of Dean vortices was shown to be more effective than the mixing caused by lamination mechanism (6.3 ± 1.3 nm with the Helix reactor versus 7.5 ± 2.5 nm with the Plait-like reactor). This is expected, since sequential lamination enhances the mixing only by molecular diffusion, which is a slower process compared to chaotic advection generated by the curved tube in the Helix reactor[19]. Dean numbers were calculated for all the range of possible flow rate that can be used with the semi-continuous setup, and they can vary from 6 at 1 mL min^{-1} up to 152 at 24 mL min^{-1}. In the conditions used for the preparation of the Au colloid (6 mL min^{-1}), a Dean number of 38 was obtained, showing that under such conditions even small Dean numbers can result in efficient mixing. DLS analysis of the colloidal solutions were in accordance with STEM analysis for all the printed connections and reactors. UV-Vis analysis, on the other hand, does not show significant

changes in the surface plasmon resonance, with the broad plasmon peak centred at ca. 500 nm for all the colloids produced (Figure 3.29).

Table 3.10: Reactor shape effect on Au plasmonic resonance, particle dimension and metal loading.

Reactor	Particle size [nm]		Metal loading [wt%]
	DLS	STEM	
T-shape	5.9 ± 1.7	7.0 ± 1.9	0.95
Helix	5.2 ± 1.6	6.3 ± 1.3	0.96
Plait-like	5.8 ± 1.7	7.5 ± 2.5	0.94

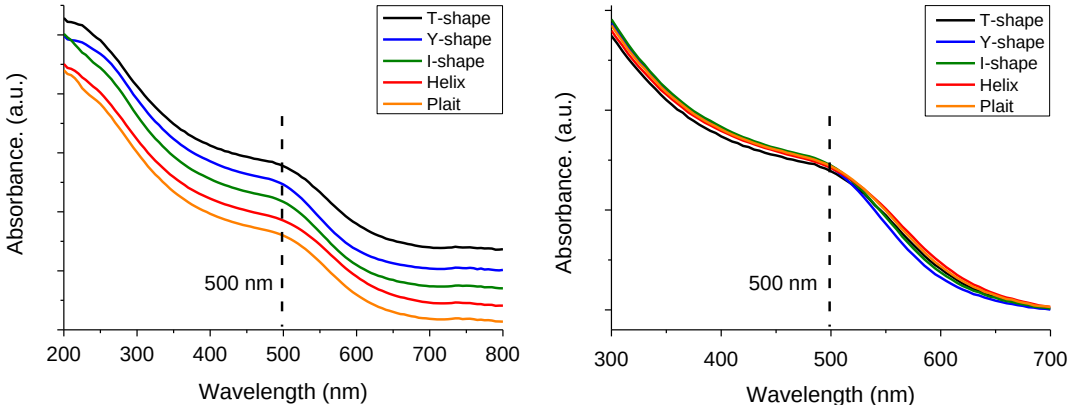

Figure 3.29: Comparison between the Au plasmonic resonance of the nanoparticles prepared using the different 3D printed connections and reactors (left); the spectra have been vertically shifted in order to avoid complete overlap. On the right, a zoom-in on the plasmonic region of the overlapped spectra. Reaction conditions: total flow rate 6 mL min^{-1}, reactor length 80 cm (residence time 8 s), Au concentration 0.127 mmol L^{-1}, PVA : Au weight ratio 0.65, $NaBH_4$: Au molar ratio 5, temperature 25 °C.

3.3.5. Tubing reuse

As already mentioned before, Au deposition was seen on the inner walls of the tubing during the colloid synthesis. The Au layer is very thin, MP-AES analysis revealed an average of 27 µg of Au per gram of catalyst produced, and it is not enough to block the tubing; however, the Au deposit can act as nucleation spot for new nanoparticles, decreasing the quality of the colloid produced reusing the tubing multiple times.

To evaluate this phenomenon, a 30 cm tube was used to synthesise 5 mg of Au nanoparticles (that correspond to 0.5 g of 1 wt% supported Au catalyst) up to 5 times. With the last tube reuse, big nanoparticles were produced (23.4 nm) with a very broad particle

size distribution (± 8.7 nm). UV-Vis and DLS analysis suggests that the nanoparticles size increases immediately after the first use. The surface plasmonic resonance, in fact, shifts towards higher wavelengths after the first use and then maintains its position for further reuses (Figure 3.30). It is interesting to notice that the plasmon resonance undergoes only a very small shift, in contrast with what usually observed. This phenomenon might be due to the presence of a broad nanoparticle size distribution. The formation of bigger nanoparticles is confirmed by DLS analysis (Table 3.11); with the first reuse, the average hydrodynamic diameter was twice as large compared to nanoparticles produced with the new tube (from 5.5 ± 1.7 nm to 10.7 ± 2.2 nm). A second reuse led to an additional twofold increase in dimension, from 10.7 ± 2.2 nm to 27.5 ± 2.8 nm, while further reuses seem to not affect the nanoparticles dimension anymore.

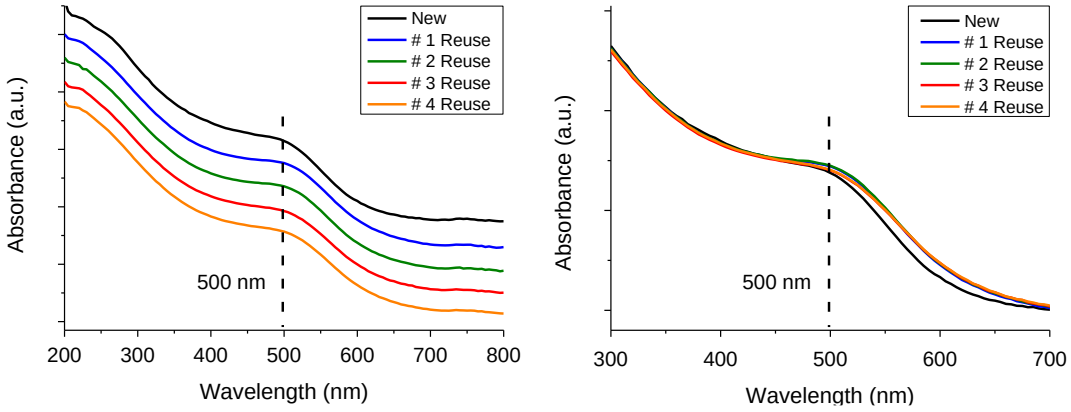

Figure 3.30: Comparison between the Au plasmonic resonance of the nanoparticles prepared using the tubing multiple times (left); the spectra have been vertically shifted in order to avoid complete overlap. On the right, a zoom-in on the plasmonic region of the overlapped spectra. Reaction conditions: total flow rate 6 mL min^{-1}, reactor length 80 cm (residence time 8 s), Au concentration 0.127 mmol L^{-1}, PVA : Au weight ratio 0.65, $NaBH_4$: Au molar ratio 5, temperature 25 °C.

Table 3.11: Tubing reusability effect on Au plasmonic resonance, particle dimension and metal loading.

# Run	Particle size [nm]		Metal loading [wt%]
	DLS	STEM	
New	5.5 ± 1.7	6.5 ± 1.7	0.94
1st reuse	10.7 ± 2.2	n.a.	n.a.
2nd reuse	27.5 ± 2.8	n.a.	n.a.
3rd reuse	25.7 ± 3.2	n.a.	n.a.
4th reuse	28.9 ± 3.1	23.4 ± 8.7	0.94

To further extend the tubing lifetime, a diluted solution of aqua regia was used to clean the internal walls from any metal deposit (10 mL of a solution 30 vol%). The concentration was optimised in order to completely clean the internal wall using the smallest amount of acid possible. The tube was then reused up to 4 times, cleaning it every time before reuse. The results show that small nanoparticles can still be produced even after 4 experiments (Table 3.12). The slightly bigger mean value it is probably due to the change in surface chemistry of the inner walls of the tube when treated with aqua regia. UV-Vis analysis does not show any plasmon resonance shift, confirming the presence of Au nanoparticles in the same size range for all the 5 uses (Figure 3.31).

Table 3.12: Tubing reusability effect on Au plasmonic resonance, particle dimension and metal loading. The tubing were washed with a diluted solution of aqua regia (30 vol%) after every use.

# Run	Particle size [nm]		Metal loading [wt%]
	DLS	STEM	
New	5.5 ± 1.7	6.5 ± 1.7	0.94
1st reuse	5.7 ± 1.8	n.a.	n.a.
2nd reuse	5.5 ± 1.9	n.a.	n.a.
3rd reuse	5.9 ± 1.9	n.a.	n.a.
4th reuse	5.9 ± 1.5	6.9 ± 1.8	0.97

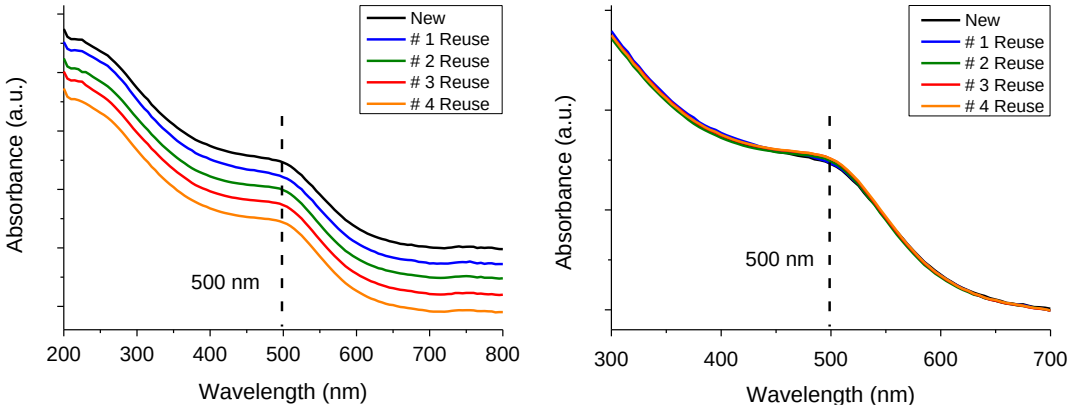

Figure 3.31: Comparison between the Au plasmonic resonance of the nanoparticles prepared using the tubing multiple times (left); the spectra have been vertically shifted in order to avoid complete overlap. On the right, a zoom-in on the plasmonic region of the overlapped spectra. The tubing were washed at the end of every catalyst synthesis with a 30 vol% solution of aqua regia. Reaction conditions: total flow rate 6 mL min^{-1}, reactor length 80 cm (residence time 8 s), Au concentration 0.127 mmol L^{-1}, PVA : Au weight ratio 0.65, $NaBH_4$: Au molar ratio 5, temperature 25 °C.

3.4. The continuous setup

3.4.1. Synthesis of Au/TiO_2 catalysts

The semi-continuous setup was further upgraded to generate the entire supported metal nanoparticle catalyst in a continuous one-step process. An additional peristaltic pump was added in order to integrate a continuous stream of support suspended in water to the Au colloid (Figure 3.32). The catalyst as produced was immediately filtered, washed with deionised water and dried at room temperature for 48 hours.

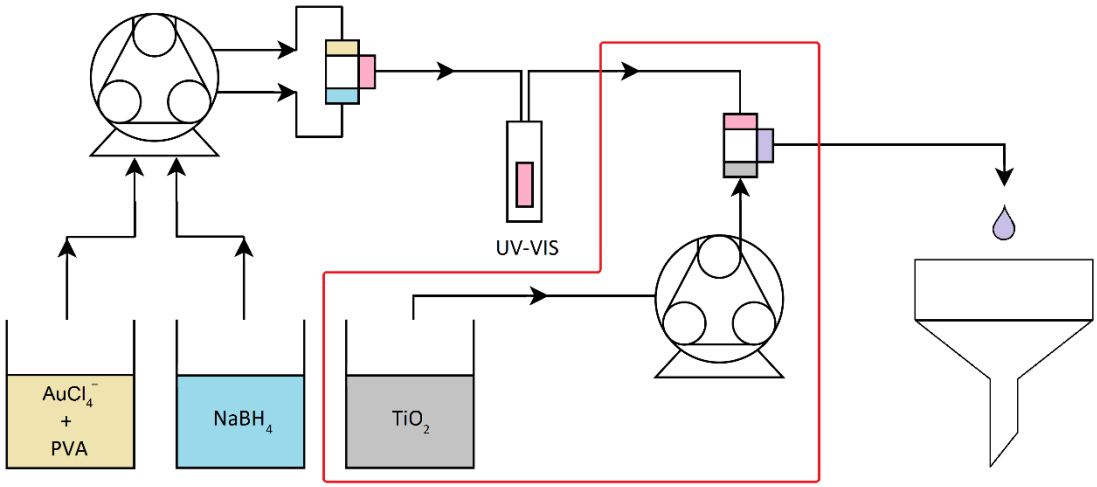

Figure 3.32: Schematic representation of the continuous setup for the synthesis of Au/TiO_2 catalyst; the additional pump and T-shape connection are highlighted by the red box. The catalyst produced was collected on a filter, washed with deionised water and dried at room temperature for 48 hours.

In these conditions, the Au NPs production rate varied in a range of 0.025 to 0.6 mg_{Au} min^{-1}, with a theoretical 1 wt% Au/TiO_2 catalyst production rate of up to 3.6 g h^{-1} when a flow rate of 24 mL min^{-1} was used. Figure 3.33 shows a picture of the continuous setup.

Figure 3.33: Picture of the continuous setup during the synthesis of a Au/TiO_2 catalyst. The colloid stream is merged to a stream of support suspended in water, and the final catalyst is immediately filtered and washed.

The as produced continuous catalyst was then compared with the batch sol-immobilisation benchmark and the materials produced with the optimised semi-continuous setup (8 mL min^{-1} flow rate, 80 cm reactor with PFA T-shape connection, 0.65 PVA : Au molar ratio, 5 $NaBH_4$: Au molar ratio, 0.127 mol L^{-1} Au concentration, pH 3.6) and the results are reported in Table 3.13. The continuous addition of support facilitated the production of very well-defined Au NPs with small particle size and narrow particle size distribution as determined by STEM analysis. Comparison with the batch and the semi-continuous catalysts showed that the mean NPs size decreased from 5.4 nm of the semi-continuous and 5.6 nm of the batch to only 4.5 nm with the continuous setup. It is clear that the immediate deposition of Au colloid onto the support is highly beneficial and this positive outcome can be ascribed mainly to two effects: firstly, the absence of stirring present in the batch synthesis minimises agglomeration phenomena to a high degree, and secondly the immediate removal of the remaining $NaBH_4$ in solution which can interfere with the PVA thus reducing the stabilising effect of the polymer[48]. It is also important to notice that the metal loading of both the semi-continuous and continuous catalysts is comparable to the one of the batch benchmark (0.94 – 0.96 %, within the experimental error), confirming again that the metal deposition on the internal tubing wall is negligible.

Table 3.13: Au plasmonic resonance, particle dimension and metal loading of the catalysts prepared with different technique: batch, semi-continuous and continuous.

Catalyst	Plasmonic resonance [nm]	Particle size [nm]		Metal loading [wt%]
	DR-UV-Vis	DLS	STEM	
Batch	540	5.6 ± 1.7	5.6 ± 1.6	0.94
Semi-continuous	542	5.5 ± 1.7	5.4 ± 0.9	0.94
Continuous	537	5.4 ± 1.6	4.5 ± 1.3	0.96

UV-Vis analysis, as expected, show no difference between the plasmonic peak of the semi-continuous and the continuous catalyst (Figure 3.34). The difference between the two catalysts, in fact, is in the deposition of the Au colloid rather than its formation. Diffuse reflectance UV-Vis analysis were performed on the three catalysts and the results (Figure 3.35) are in accordance with STEM analysis. The plasmonic resonance of the continuous catalyst was very small and broad compared to both batch and semi-continuous, and the maximum intensity was at shorter wavelengths (537 nm, compared to 540 nm of the batch and 542 nm of the semi-continuous). It is interesting to notice that all the peaks were shifted towards longer wavelengths and this effect is well known in literature and it is due to interaction between the Au nanoparticles and the support[27].

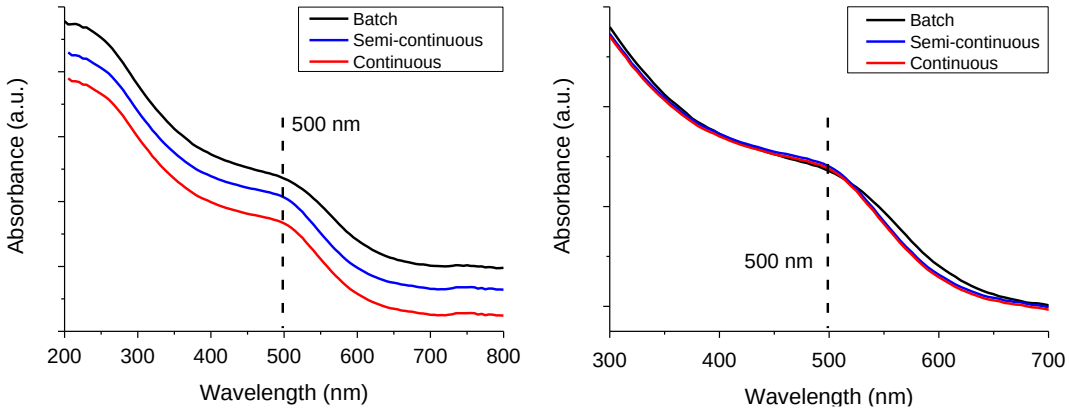

Figure 3.34: Comparison between the Au plasmonic resonance of the nanoparticles prepared using different synthetic techniques (left); the spectra have been vertically shifted in order to avoid complete overlap. On the right, a zoom-in on the plasmonic region of the overlapped spectra. Reaction conditions: total flow rate 6 mL min^{-1}, reactor length 80 cm (residence time 8 s), Au concentration 0.127 mmol L^{-1}, PVA : Au weight ratio 0.65, $NaBH_4$: Au molar ratio 5, temperature 25 °C.

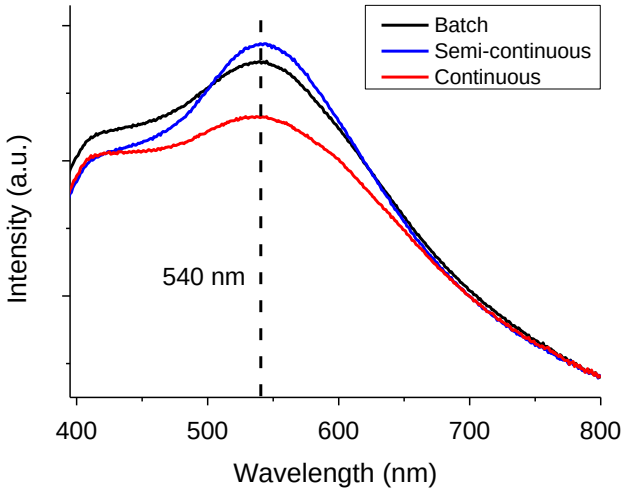

Figure 3.35: Diffuse reflectance analysis of the catalysts prepared using different synthetic techniques.

XPS and CO-DRIFT analysis were performed in order to assess any difference in electronic structure, oxidation state and coordination state of the supported Au nanoparticles. The XPS Au(4f) spectra of all three samples showed the presence of metallic Au, with Au $4f_{7/2}$ binding energy values (BE) in the range of 83.6-83.7 eV (Table 3.14), in agreement with previous reports[60]. No difference in the Au electronic structure was detected among the three samples analysed.

Table 3.14: Particle dimension, Au $4f_{7/2}$ binding energy and peripheral-to-top step sites ratio of the catalysts prepared with different technique: batch, semi-continuous and continuous.

Catalyst	**Particle size [nm]**		**BE Au $4f_{7/2}$ [eV]**	**Peripheral/top step sites ratio**
	DLS	**STEM**		
Batch	5.6 ± 1.7	5.6 ± 1.6	83.6	0.17
Semi-continuous	5.5 ± 1.7	5.4 ± 0.9	83.7	0.22
Continuous	5.4 ± 1.6	4.5 ± 1.3	83.6	0.73

CO molecules can bind selectively to transition metal atoms depending on their coordination and surrounding (Chapter 2.5.7). The shift in the position of the C-O stretching vibration band, in particular, can be associated with oxidation and coordination state of the metal on which CO is adsorbed on[27]. The CO-DRIFT spectra of batch, semi-continuous and continuous catalysts were recorded at a CO partial pressure of 1 % and are reported in Figure 3.36.

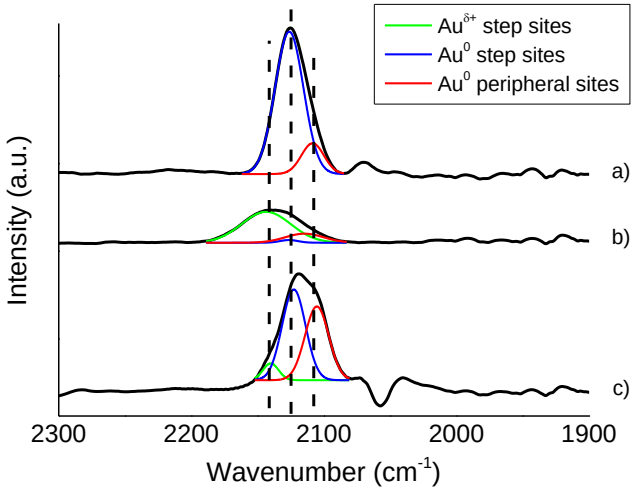

Figure 3.36: CO-DRIFT analysis of the catalysts prepared using different techniques. In particular a) batch, b) semi-continuous and c) continuous.

The batch catalyst showed a sharp peak centred at 2125 cm^{-1} that can be deconvoluted into two smaller peaks at 2126 cm^{-1} and 2108 cm^{-1} respectively. The former peak has been assigned to linearly adsorbed CO molecules on Au^{0} step sites on top of nanoparticles, while the latter has been assigned to linearly adsorbed CO molecules on peripheral Au^{0} sites (Figure 3.37)[61,62].

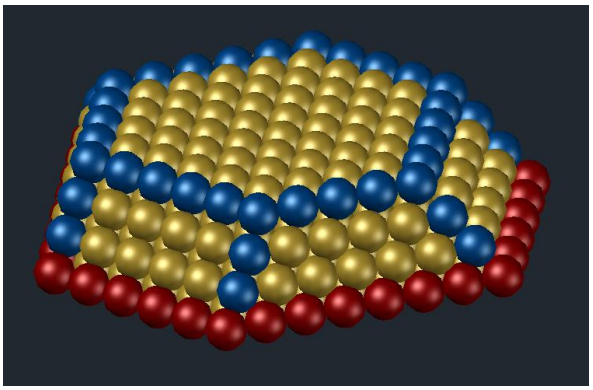

Figure 3.37: Representation of step (blue) and peripheral (red) sites in a flattened Au nanoparticle. The particle geometry does not represent the actual geometry of all the nanoparticles.

Interestingly, the semi-continuous catalyst showed a broad peak composed of 3 superimposed sub-peaks, respectively at 2143 cm^{-1}, 2126 cm^{-1} and 2113 cm^{-1}. The latter two peaks correspond to Au^{0} step sites and Au^{0} peripheral sites as already mentioned for the batch catalyst, while the new peak has been assigned again to Au step sites on top of nanoparticles. The strong shift at higher wavenumbers can be due to a partial positive charge present on the nanoparticles, as suggested by previous studies[62]. XPS analysis did not show

any $Au^{\delta+}$ in the catalyst, although the presence of any potentially unstable positive species can be easily reduced by the XPS beam and thus not been seen.

The continuous catalyst also showed a broad peak composed of 3 components. As for the semi-continuous catalyst, the peaks at 2140 cm^{-1} and 2123 cm^{-1} can be assigned to $Au^{\delta+}$ and Au^0 step sites on top of nanoparticles respectively, while the peak at 2106 cm^{-1} is peripheral Au^0 step sites. It is clear from Figure 3.36 that every species is present in a different amounts. The batch catalyst, for example, contains mostly step sites and relatively lower amount of peripheral atoms, while the continuous catalyst contains a much higher amount of peripheral sites. The ratios between the peak area of peripheral sites versus the peak area of step sites (both Au^0 and $Au^{\delta+}$) is reported in Table 3.14. Small nanoparticles have higher ratios due to the relative higher abundance of peripheral atoms compared to step atoms. The higher value for the semi-continuous catalyst compared to the batch catalyst, even though the particle size is smaller, might be due to a higher degree of surface order. A flatter particle surface, in fact, is capable of adsorbing less CO molecules compared to a surface full of low coordination sites such as step atoms, kinks and adatoms.

3.4.2. Synthesis of other monometallic catalysts

The same setup used for the continuous production of supported Au colloids was used to prepare supported Pd nanoparticles. The synthetic conditions were kept similar: flow rate 8 mL min^{-1}, $NaBH_4$: Pd ratio 5 mol : mol and PVA : Pd ratio 0.65 wt : wt. The metal concentration was increased to 0.235 mmol L^{-1} in order to maintain constant the volume of solution used. Palladium is another plasmonic metal; due to its intrinsic nature, however, the surface plasmonic resonance is much weaker than other metals such as Au and Ag.[63–65] For this reason, UV-Vis spectra are not very useful as analytical tool in the synthesis of Pd nanoparticles. The in-line UV-Vis cuvette was then removed and the reactor length decreased to 50 cm.

Pd colloids were efficiently synthesised as confirmed by DLS and TEM analysis (Table 3.15) and continuously immobilised onto TiO_2. A high value of hydrodynamic diameter was obtained with the DLS for Pd colloids compared to Au nanoparticles, although TEM analysis confirmed the presence of small particles (2.8 ± 0.9 nm). It is possible that the higher diameters obtained for Pd particles with DLS analysis were caused by a wrong value of refractive index used during the analysis. For this reason, DLS values should be used only to compare metal particles of the same nature. As for the synthesis of Au nanoparticles, small

metal deposition was noticeable just after the T-shape connection. The final metal loading, however, was very close to the nominal value of 1 wt%, indicating that the metal lost by deposition is only a very small amount. MP-AES analysis on the filtrate solution confirmed the complete deposition of the metal nanoparticles on the support.

In a similar way, using the continuous setup, Au and Pd colloids were immobilised onto activated carbon, in order to demonstrate the applicability of this one-step synthesis to other type of supports. Small metal nanoparticles were efficiently immobilised onto activated carbon (Figure 3.38). It was not possible to calculate the exact final metal loading due to the strong resistance to dissolution of Au and Pd in aqua regia when supported on carbonaceous supports. However, no traces of noble metals were found in the waste solution after filtration.

Table 3.15: Au particle dimension and metal loading of different catalysts prepared with the continuous setup.

Catalyst	**Particle size [nm]**		**Metal loading [wt%]**
	DLS	**TEM**	
Pd/TiO_2	10.2 ± 2.4	3.0 ± 1.0	0.97
Pd/AC	9.7 ± 2.4	3.1 ± 1.1	n.a.
Au/AC	6.7 ± 1.8	4.6 ± 1.3	n.a.

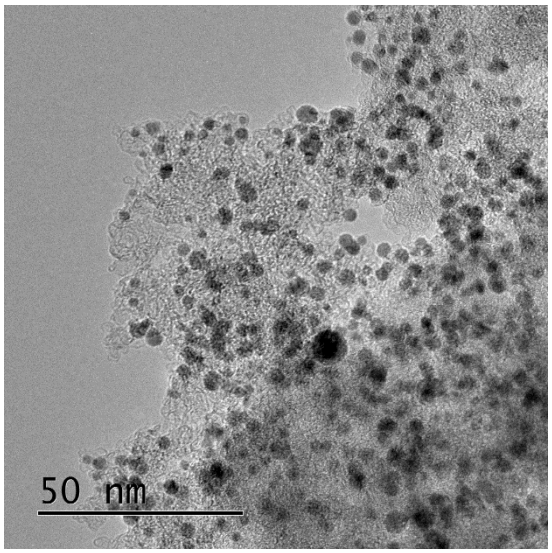

Figure 3.38: Representative TEM micrograph of the Pd/AC catalyst.

3.4.3. Synthesis of bimetallic gold-palladium catalysts

The continuous setup was used to prepare supported bimetallic AuPd nanoparticles. The Au and Pd precursors were mixed together in the same feed from the very beginning, in order to have simultaneous reduction of the two metals and thus produce uniform random alloy nanoparticles. The synthetic conditions were kept similar to the production of monometallic Pd catalyst (flow rate 8 mL min^{-1}, reactor length 80 cm and $NaBH_4$: Pd ratio 5 mol : mol) For the same reason explained before, the total metal concentration was changed to 0.160 mmol L^{-1}. Moreover, the PVA : (Au + Pd) ratio was changed to 1.2 wt : wt to have a better comparison with the batch catalyst that was optimised in previous studies with the same stabiliser-to-metals ratio[66].

The catalyst produced was compared with the batch sol-immobilisation AuPd benchmark, and the results are reported in Table 3.16. From TEM analysis, the nanoparticle size and distribution were in the same range, respectively 2.1 ± 0.7 nm for the batch and 2.0 ± 0.7 nm for the continuous. Also DLS analysis gave similar results, with higher values compared to the Au colloids due to the greater amount of PVA used and probably the same error in refractive index as explained for Pd catalysts. XPS analysis were performed on both catalysts to observe any electronic difference caused by the different synthetic methods (Figure 3.39). The Au ($4f_{7/2}$) peaks were between 83.0 - 83.2 eV, lower than that of bulk gold (ca. 84.0 eV)[67]. This decrease in binding energy (BE) is due to particle size effects and to electronic interaction between Au and Pd, confirming the presence of small alloy nanoparticles[68]. Since TEM analysis confirmed the presence of similar particle size distribution for the two catalysts, the shift from 83.2 eV to 83.0 eV might be caused by a better interaction between the two metals (more homogeneous AuPd composition). In accordance with these results, slight downshift was observed in the metallic Pd ($3d_{5/2}$) band as well, from 335.0 of pure Pd to 334.6 – 334.7 eV, with the batch catalyst being the one with lower shift[69–71]. No Pd^{2+} species were observed at ca. 337.0 eV, confirming the metallic state of the nanoparticles.

Table 3.16: Particle dimension, metal loading and binding energy of different AuPd bimetallyc catalysts prepared with the batch and continuous technique.

Catalyst	Particle size [nm]		Metal loading [wt%]	BE [eV]	
	DLS	TEM		Au $4f_{7/2}$	Pd $3d_{5/2}$
AuPd/TiO_2 - Batch	7.7 ± 2.1	2.1 ± 0.7	0.95	83.2	334.7
AuPd/TiO_2 – Cont.	7.6 ± 2.3	2.0 ± 0.7	0.94	83.0	334.6

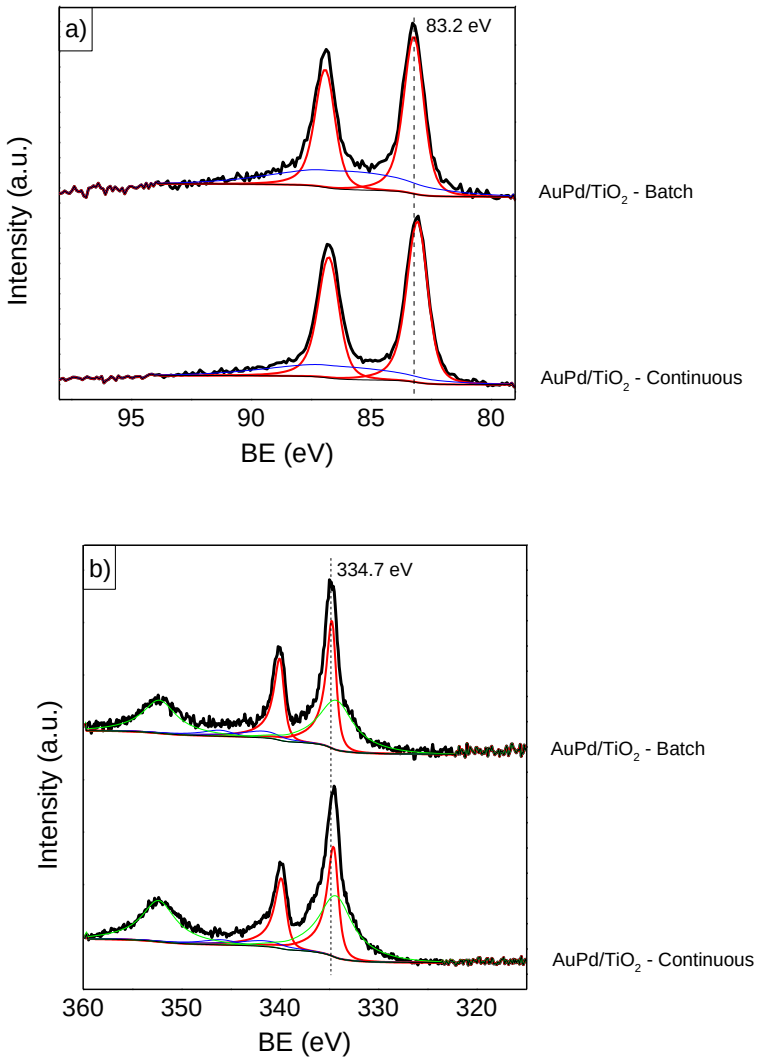

Figure 3.39: a) Au $4f_{7/2}$ and b) Pd $3d_{5/2}$ XPS analysis of the bimetallic AuPd catalysts prepared with the batch and continuous techniques.

The alloy composition was investigated by use of an aberration corrected STEM equipped with an energy dispersive X-ray detector (EDX); this instrument enabled single nanoparticles composition analysis. Previous studies showed how the Au-Pd relative composition of single nanoparticles was size dependant: small nanoparticles (ca. 2 nm) were mainly Au-rich, while bigger nanoparticles (ca. 6 nm) showed a Pd-rich composition (Figure 3.40)[72,73]. Single particle EDX analysis were performed on more than 40 nanoparticles and the results clearly show a much better alloy composition compared to the standard PVA batch benchmark (Figure 3.40). The average composition was ca. 35 wt% in Pd, that correspond to a Au:Pd molar ratio of 1:1, in great agreement with the nominal value.

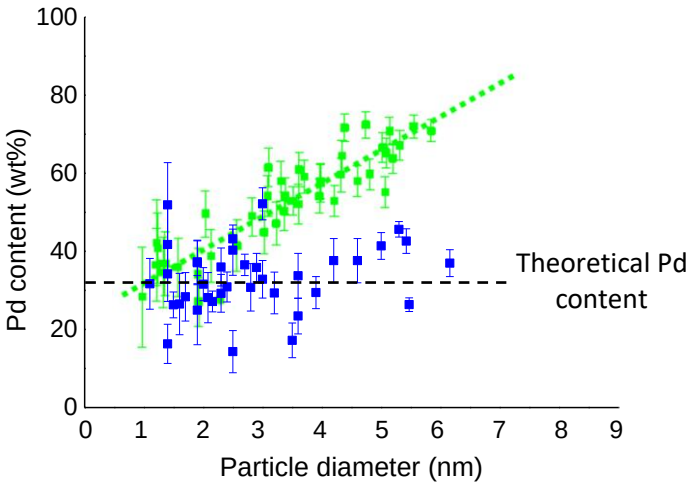

Figure 3.40: Composition distribution of AuPd catalysts prepared with the batch (green) and continuous (blue) procedure.

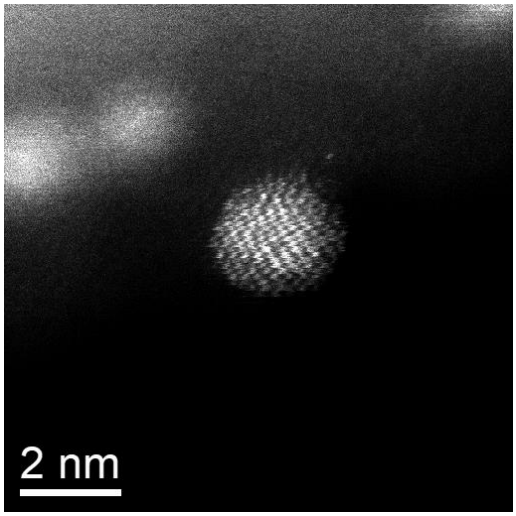

Figure 3.41: Dark field TEM image of a bimetallic AuPd nanoparticle prepared with the continuous setup.

This difference in behaviour can be explained by the very fast deposition of AuPd nanoparticles on the support that "freezes" their structure after only a few seconds from the formation. It is possible in fact that Ostwald ripening process takes place once the colloid is formed and causes composition rearrangements to form the more stable small Au-rich and big Pd-rich nanoparticles. Composition rearrangement can be hypothesised by analysis of the UV-Vis spectra of a Au colloid over time (Figure 3.42). Subtle changes in the absorption intensity (blue line) and shift (green line) of the plasmon resonance maxima indicate modification of either the nanoparticles structure or the surrounding environment. $NaBH_4$ undergoes decomposition without any change in the UV-Vis spectra, therefore the only cause of intensity variation must be due to nanoparticles structure modifications.

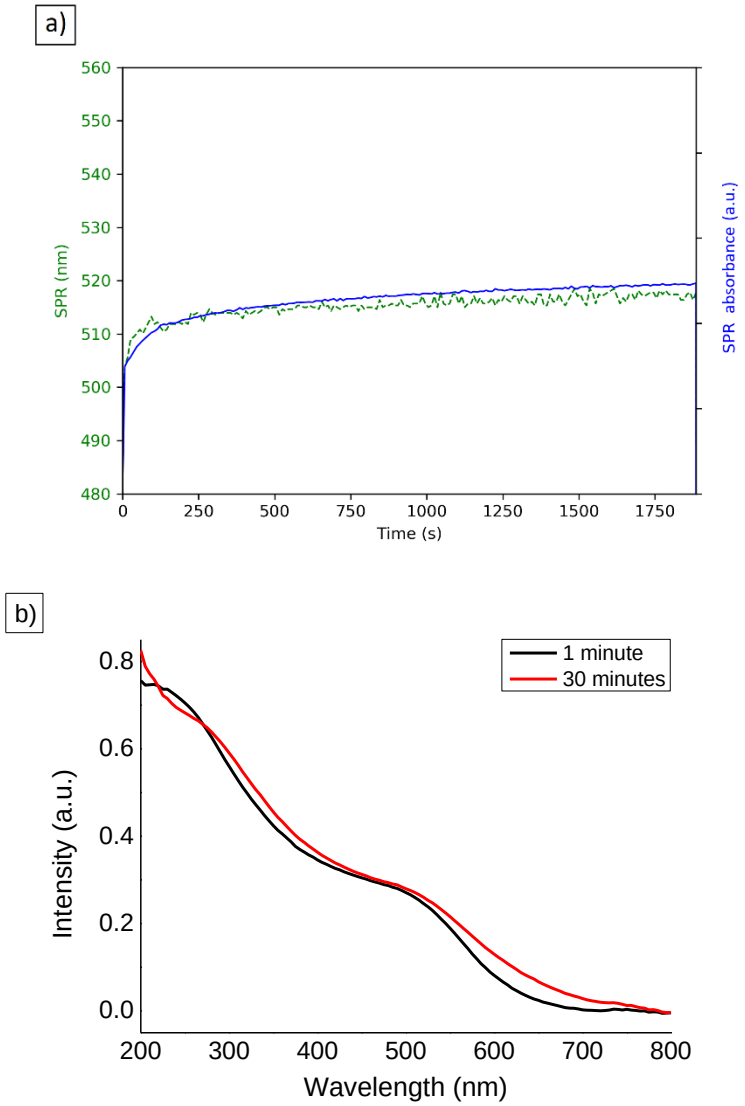

Figure 3.42: a) Change in surface plasmon resonance (SPR) position and intensity in function of ageing time in the batch synthesis; higher peak intensities and wavelengths indicate the presence of bigger nanoparticles. b) Difference in plasmonic resonance from the colloid after 1 minute from the addition of $NaBH_4$ and after 30 minutes.

This is further confirmed by experiments performed preparing separately Au and Pd colloids. Upon mixing the two preformed colloids, the plasmon resonance peak of the Au colloid is slowly dampened by the presence of Pd atoms in solution (Figure 3.43). After 100 min, the Au plasmon resonance completely disappeared, indicating the formation of a more stable AuPd colloid. This might happen also when preparing a AuPd colloid directly. In a first stage, random alloy AuPd particles are produced. Over time, however, the particles undergo chemical rearrangement to a more stable configuration (*i.e.* small particles Au rich and large particles Pd rich). In any case, more detailed TEM-EDX analysis should be performed in order to confirm this mechanism.

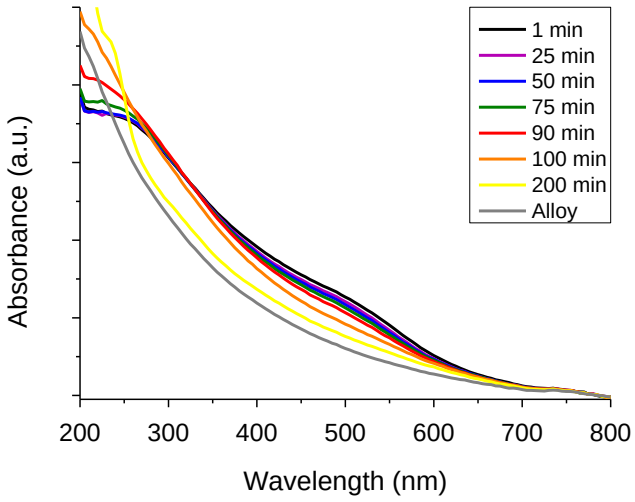

Figure 3.43: UV-Vis spectra of a physical mixture of a Au and Pd colloid over time. The inset highlights the change in surface plasmon resonance of the Au colloid dampened by the presence of Pd.

The catalytic performance of the Au/TiO_2 and $AuPd/TiO_2$ materials prepared by the batch and continuous methods were then evaluated for the hydrogenation of various nitroarenes to aminoarenes.

3.5. Application of materials as catalysts

Nitroarenes are generally highly toxic, mutagenic and many of them carcinogens[74–76]. They can often be found in agricultural and industrial waste water as by-products of herbicides, pesticides and synthetic dyes, and their presence, even in small concentrations, is of great concern from an environmental point of view[77]. On the other hand, the products of nitroarenes hydrogenation can generate aminoarenes, important chemicals widely used in industry. For example, aminoarenes are used by the pharmaceutical industry as analgesics, antipyretics and chemotherapeutics and in agriculture as fungicides and pesticides[78,79]. Moreover, many aminoarenes are also used as intermediates in the synthesis of polymers (polyurethanes), dyes, pigments, photographic chemicals and corrosion inhibitors[78,79].

The nitroarenes (NAR) used in this study were 4-nitrophenol (4-NPH), 3-nitrophenol (3-NPH), 2-nitrophenol (2-NPH), nitrobenzene (NBZ), 4-nitroaniline (4-NAL), 4-nitrotoluene (4-NTL) and 4-nitrobenzyl alcohol (4-NBA) and are represented in Figure 3.44.

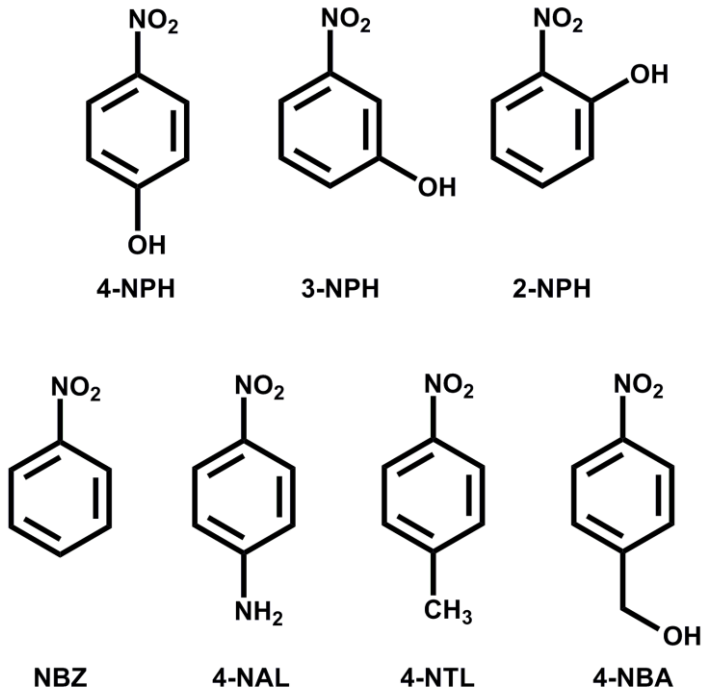

Figure 3.44: Nitroarenes substrates used for the catalysts comparison: 4-nitrophenol (4-NPH), 3-nitrophenol (3-NPH), 2-nitrophenol (2-NPH), nitrobenzene (NBZ), 4-nitroaniline (4-NAL), 4-nitrotoluene (4-NTL) and 4-nitrobenzyl alcohol (4-NBA).

The reduction of 4-nitrophenol (4-NPH) with $NaBH_4$, in particular, has been frequently used as a model reaction to investigate the catalytic activity of supported metal nanoparticles having controlled size and shape[80,81] and it will be extensively described and studied in Chapter 4. The nitroarene reduction reactions were conducted in a quartz cuvette at room temperature (25 °C) and monitored by UV-Vis spectroscopy, measuring the decrease in intensity with time of the substrate peak (typically at ca. 350-400 nm for the different nitroarenes). The catalysts activity was measured in terms of rate constant of the reaction (k_{NAR}, see Chapter 4.2). Since the $NaBH_4$ was present in excess, it was assumed that the reaction rate depended only on the concentration of nitroarenes, allowing us to approximate the kinetic data with a first-order rate law[81]. The reaction constant was then determined based on the kinetic equations described in Chapter 4.2 and below (Equation 3.4), and used to compare the activity of the different catalysts.

$$\ln\frac{C_t}{C_0} = \ln\frac{A_t}{A_0} = -k_{NAR} \times t \qquad Equation\ 3.4$$

Where C_t and A_t are respectively the NAR concentration and absorbance after a reaction time "t", while C_0 and A_0 are the NAR concentration and absorbance at the beginning

of the reaction. The experimental reaction procedure is finally fully described in Chapter 2.5.1.

3.5.1. Batch versus continuous: catalytic comparison

Transition metals are generally very active in the reduction of nitroarenes. Among them, noble metal nanoparticles such as Au, Pd and alloys of these two metals have shown remarkable activity when both unsupported or supported on various materials[82–85]. It is widely accepted that the reaction rate is strongly influenced by the metal particle size, with small nanoparticles being more active than large ones. For this reason, the monometallic Au/TiO_2 catalyst prepared with the continuous setup should result in more active catalysts compared to those prepared in batch. The continuous catalyst, in fact, showed the presence of smaller nanoparticles compared to the batch one (by STEM analysis, 4.5 ± 1.3 nm versus 5.6 ± 1.6 nm respectively).

As expected, the catalyst prepared in a continuous fashion consistently showed higher activity compared to the batch produced material (Table 3.17). This increase in activity can be better quantified in terms of the percentage difference in reaction constant (Δk_{NAR}) between the k_{NAR} values obtained for the batch and continuous derived catalysts. For the various substrates studied, the Δk_{NAR} value was in the 12 – 50 % range in favour of the continuously derived catalyst material, with the 4-NBA and NBZ substrates showing the lowest and highest measured activity increase respectively.

Table 3.17: Catalytic activity of the batch and continuous Au/TiO_2 catalysts in the nitroarene reduction reaction. Reaction conditions: molar ratio Au : NAR : $NaBH_4$ of 1 : 2.5 : 250, total volume 3 mL, room temperature.

Substrate	k_{NAR} [-10^3 s^{-1}]		Δk_{NAR} [%]
	Batch	Continuous	
4-NPH	12.1	16.8	28
3-NPH	8.9	10.3	14
2-NPH	6.2	11.6	47
NBZ	4.7	9.4	50
4-NAL	35.7	42.9	17
4-NTL	2.6	3.1	16
4-NBA	7.4	8.4	12

Table 3.18 shows the catalytic activity comparison in term of k_{NAR} between the two bimetallic AuPd/TiO_2 continuous and batch catalysts. Contrary to monometallic Au, the bimetallic catalysts showed comparable particle size from TEM analysis (2.1 ± 0.7 nm and 2.0 ± 0.7 nm for the batch catalyst and continuous catalyst respectively). Therefore, any difference in activity cannot be attributed to particle size differences but rather to a different alloy composition of the single nanoparticles. As shown in Figure 3.39 and 3.40, in fact, the bimetallic AuPd catalyst prepared in continuous showed a more uniform alloy composition of the single nanoparticles, while the batch catalyst showed by previous results a size dependent composition, with small nanoparticles being Au-rich and large nanoparticles being Pd-rich[72,73]. Differences in activity can therefore be attributed to this absence of Au-rich and Pd-rich nanoparticles in the material. The Δk_{NAR} value was in a narrower range compared to the monometallic Au catalysts (6 – 27 %), despite the 4-NBA and NBZ substrates showing again the lowest and highest measured activity increase respectively.

Table 3.18: Catalytic activity of the batch and continuous AuPd/TiO_2 catalysts in the nitroarene reduction reaction. Reaction conditions: molar ratio AuPd : NAR : $NaBH_4$ of 1 : 2.5 : 250, total volume 3 mL, room temperature.

Substrate	**k_{NAR} [-10^3 s^{-1}]**		**Δk_{NAR} [%]**
	Batch	**Continuous**	
4-NPH	24.4	28.9	16
3-NPH	15.2	17.0	10
2-NPH	11.0	14.1	22
NBZ	9.8	13.5	27
4-NAL	38.7	46.2	16
4-NTL	4.6	5.6	18
4-NBA	14.9	15.9	6

3.6. Conclusions

A new approach for the synthesis of metallic colloids in continuous mode was studied in this chapter. Gold was chosen as test metal due to its wide applicability in several catalytic reactions and to its ease of characterisation with UV-Vis spectroscopy. The setup, in fact, was equipped with in-line UV-Vis flow cell for the real-time analysis of the Au plasmonic resonance. The colloids were then immediately immobilised onto a support, specifically titanium oxide, in order to make a supported metal nanoparticle catalyst. Various operational parameters, such as reaction conditions, residence time and mixing, were studied and the best conditions for the synthesis of small and narrowly distributed metal nanoparticles were found.

Four reaction conditions were taken into consideration, namely the stabiliser concentration, the reducing agent concentration, the metal precursor concentration and the solution pH. The complete absence of stabilising agent led to the production of relatively big nanoparticles due to coalescence phenomena. The addition of PVA (PVA : Au wt ratio 0.65 and 1.3) increased the stability against coalescence and this resulted in small and uniform nanoparticles (6.0 ± 1.4 nm). An optimum value of 5 $NaBH_4$: Au mol : mol ratio was experimentally identified. Lower concentrations of reducing agent resulted in an inefficient reduction of the metal precursor; a molar ratio of only 1 was not even enough to fully reduce all the Au^{3+} in solution. High concentrations of reducing agent (7.5 $NaBH_4$: Au) led to large nanoparticles due to particle destabilisation caused by the excess in electrolytes concentration.

The metal precursor concentration was then varied between 0.102 and 0.254 mol L^{-1}. The particle dimension was not strongly affected; a minimum average size dimension was obtained with an intermediate concentration of 0.127 mmol L^{-1}, while more concentrated and diluted systems resulted in larger nanoparticles according to DLS analysis. Moreover, a good correlation was observed between the UV-Vis absorbance intensity at 400 nm and the Au nanoparticles concentration, and a molar attenuation coefficient value of 2.81 L $mmol^{-1}$ cm^{-1} was obtained, in good agreement with previous reports. The principle capability of the absorbance at 400 nm to determine the concentration of Au(0) is attributed to the allowed interband transitions at 3.1 eV (single particle excitations from the occupied 5d valence band to the unoccupied levels of the 6s-6p conduction band of Au). At this wavelength, the plasmonic resonance contribute only in a small extent to the overall intensity, as well as organic and inorganic molecules present in solution (that typically absorb in the UV region).

Finally, the pH of the feeding Au precursor solution was varied in order to obtain different Au ionic species. In particular, the pH was varied from 3.6 to 6.9 and finally to 9.6, to obtain respectively $AuCl_4^-$, $AuCl_2(OH)_2^-$ and $Au(OH)_4^-$ as main precursor species; as expected, the particle size increased decreasing the reduction potential of the Au species.

The colloid residence time was varied by changing the reactor length. It was observed that increasing the reactor length, the nanoparticles slightly increased in size (from 5.7 ± 1.3 nm at 30 cm up to 7.2 ± 2.6 nm at 130 cm). This effect was attributed to coalescence phenomena enhanced by the destabilisation effect of the plastic tube on the polymeric stabiliser.

The feeding solution mixing was optimised by changing flow rate and reactor geometry. In these conditions, in particular, the flow regime was laminar for all the studied flow rates, with Reynolds numbers ranging from 13 at 1 mL min^{-1} to 320 at 24 mL min^{-1}. The mixing of the solution increased with increasing the flow rate due to the formation of Dean vortices in the T-shape connection. As a consequence, the particle dimension decreased from 15.1 ± 6.2 nm at 1 mL min^{-1} to 5.4 ± 0.9 nm at 8 mL min^{-1}; higher flow rates did not affect the average nanoparticles size, indicating that the mixing was already optimised at flow rates as low as 8 mL min^{-1}. Interestingly, when running the setup at very low flow rate (1 mL min^{-1}) $NaBH_4$ decomposition was observed after ca. 35 minutes of reaction and this phenomenon was accounted for the increased particle size and the decreased final metal loading.

Different connections and reactors were employed to further improve the mixing of the feeding solutions, namely Y-shape and I-shape connections, Helix and Plait-like reactors. Decreasing the contact angle between the two solutions (from the standard T-shape to the Y-shape connection) reduced the intensity of the Dean vortices and thus the overall mixing. Surprisingly, when a coaxial mixer was used (I-shape) the nanoparticle dimension decreased; this effect was attributed to a better contact area between the two streams and to a positive effective contact angle due to the particular geometry of the connection. Changing the reactor shape resulted in a smaller average particle dimension and better particle size distribution. In particular, the mixing was enhanced either by molecular diffusion (Plait-like) or by chaotic advection (Helix), with the latter being the most effective mechanism that led to the synthesis of nanoparticles as small as 6.3 ± 1.3 nm.

Au deposition on the internal walls of the tubing can affect the quality of the colloid produced. Simply by washing with a diluted solution of aqua regia, the tubing could be efficiently reused up to 4 times without any significant change in nanoparticle dimension.

The semi-continuous setup was then further upgraded integrating a stream of support suspended in water to the colloidal stream, so that the whole catalyst was produced in continuous. Comparing the continuous catalyst as produced, with the standard batch benchmark and the semi-continuous catalyst, smaller Au nanoparticles were deposited when the support was added in continuous (4.5 ± 1.3 nm). This finding, confirmed also by CO-DRIFT analysis, was ascribed to the minimised agglomeration phenomena caused by the absence of mechanical stirring and to the immediate removal of the remaining $NaBH_4$ in solution that can interfere with the PVA thus reducing the stabilising effect of the polymer. Overall, the maximum catalyst productivity of the continuous setup can be as high as 3.6 g h^{-1} of 1 wt% Au/TiO_2 catalyst when a flow rate of 24 mL min^{-1} is used.

The continuous setup was efficiently employed for the production of other supported metal nanoparticles, such as Pd/TiO_2, Pd/AC and Au/AC with small particle dimension and narrow size distribution. In particular, bimetallic AuPd nanoparticles were synthesised and deposited on TiO_2. The comparison with the standard $AuPd/TiO_2$ batch benchmark revealed the absence of a size-dependent alloy composition in the size range of nanoparticles produced. This result, also confirmed by XPS data, is in contrast with previous reports on batch catalysts, showing that PVA stabilised AuPd nanoparticles were composed of smaller Au-rich and bigger Pd-rich particles. The reason for this difference was explained by the very fast deposition of the nanoparticles that inhibits Oswald ripening process responsible for metal rearrangements over time.

Moreover, the catalysts prepared in a continuous fashion consistently showed higher activity in the nitroarenes reduction reaction compared to that of the corresponding batch produced materials. This increase in activity, quantified in terms of the percentage difference in reaction constant (Δk_{NAR}) between the k_{NAR} values obtained for the batch and continuous derived catalysts, was in the 6 – 50 % range in favour of the continuously derived catalyst materials, with the 4-NBA and NBZ substrates showing the lowest and highest measured activity increase respectively. In the case of the continuous derived Au/TiO_2 catalyst, the greater activity was attributed to the smaller mean Au nanoparticle size whereas, in the case of the continuous $AuPd/TiO_2$ catalyst, the more uniform alloy composition and absence of Au-rich and Pd-rich nanoparticles in the material was responsible for the improvement in performance.

This work represents a starting point for the efficient production of supported metal NPs with very uniform and reproducible chemical-physical properties and it can easily find application for the production of a range of monometallic and bimetallic supported metal

nanoparticles using a wide range of metals and supports. In addition, this technique could also be highly appealing for the industrial production of supported nanoparticle catalysts, especially due to the ease of scale-up (catalyst productivity up to 3.6 g h^{-1} in one reactor) and the relative low cost compared to other continuous flow techniques.

Dynamic light scattering and UV-Vis spectroscopy proved to be useful technique to characterise the metal colloids before deposition. Both techniques give an indication of the nanoparticle size for the colloid produced, although small changes in particle dimension are quite hard to detect and for an accurate size distribution analysis TEM remains the most reliable technique. Analysis of the plasmon resonance for Au nanoparticles, however, can be particularly useful especially on an industrial scale because it can be easily integrated in-line, giving the opportunity to monitor the particle dimension in real time and potentially avoid huge waste of chemicals and energy in case of plant malfunction (Figure 3.45).

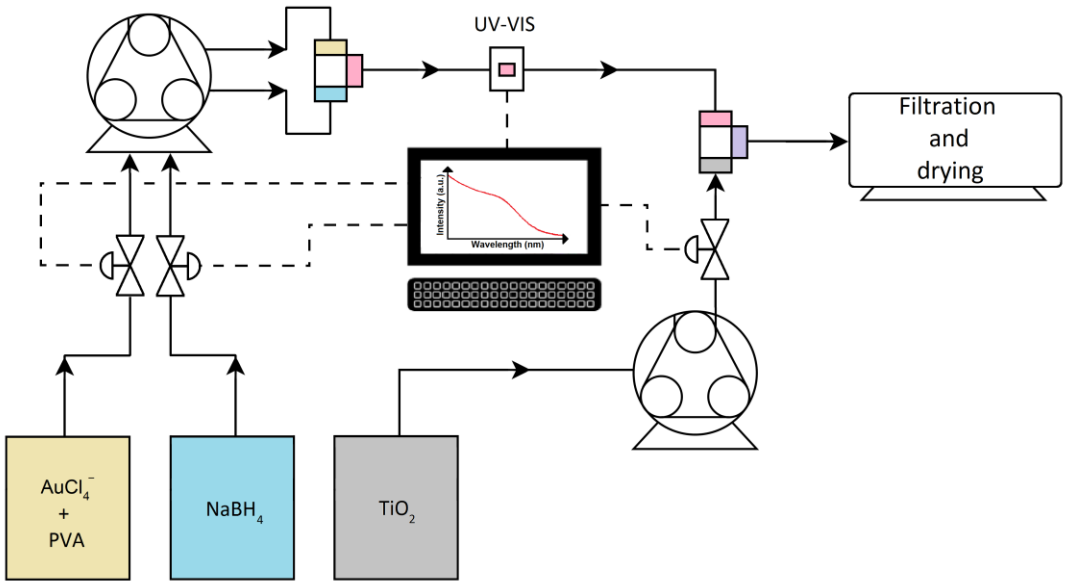

Figure 3.45: Example of an industrial setup for the synthesis of Au catalyst. The in-line UV-Vis is connected to valves that change the flux of the feeding streams in case the particle size does not meet the pre-set criteria.

3.7. References

1 J. DeMello and A. DeMello, *Lab Chip*, 2004, **4**, 11–15.

2 S. Marre and K. F. Jensen, *Chem. Soc. Rev.*, 2010, **39**, 1183–1202.

3 Y. Xia, Y. Xiong, B. Lim and S. E. Skrabalak, *Nanosctructures*, 2009, 60–103.

4 N. T. K. Thanh, N. Maclean and S. Mahiddine, *Chem. Rev.*, 2014, **3**, 7610–7630.

5 Y. Wang, J. He, C. Liu, W. H. Chong and H. Chen, *Angew. Chemie - Int. Ed.*, 2015, **54**, 2022–2051.

6 J. B. Edel, R. Fortt, J. C. deMello and A. J. deMello, *Chem. Commun.*, 2002, 1136–1137.

7 H. Wang, H. Nakamura, M. Uehara, M. Miyazaki and H. Maeda, *Chem. Commun.*, 2002, 1462–1463.

8 J. Wagner, T. Kirner, G. Mayer, J. Albert and J. M. Kohler, *Chem. Eng. J.*, 2004, **101**, 251–260.

9 J. M. Köhler, J. Wagner and J. Albert, *J. Mater. Chem.*, 2005, **15**, 1924–1930.

10 D. Zhang, F. Wu, M. Peng, X. Wang, D. Xia and G. Guo, *J. Am. Chem. Soc.*, 2015, **137**, 6263–6269.

11 A. Yepez, F. L. Y. Lam, A. A. Romero, C. O. Kappe and R. Luque, *ChemCatChem*, 2015, **7**, 276–282.

12 S. Appalakutti, S. Sonawane, B. A. Bhanvase, V. Mittal and M. Ashokkumar, *Chem. Eng. Process. Process Intensif.*, 2015, **89**, 28–34.

13 A. M. Karim, N. Al Hasan, S. Ivanov, S. Siefert, R. T. Kelly, N. G. Hallfors, A. Benavidez, L. Kovarik, A. Jenkins, R. E. Winans and A. K. Datye, *J. Phys. Chem. C*, 2015, **119**, 13257–13267.

14 L. Gomez, V. Sebastian, S. Irusta, A. Ibarra, M. Arruebo and J. Santamaria, *Lab Chip*, 2014, **14**, 325–332.

15 R. Gottesman, A. Tangy, I. Oussadon and D. Zitoun, *New J. Chem.*, 2012, **36**, 2456–2459.

16 K. S. Elvira, X. Casadevall i Solvas, R. C. R. Wootton and A. J. de Mello, *Nat. Chem.*, 2013, **5**, 905–915.

17 S. E. Lohse, J. R. Eller, S. T. Sivapalan, M. R. Plews and C. J. Murphy, *ACS Nano*, 2013, 4135–4150.

18 B. Kirby, *Micro- and Nanoscale Fluid Mechanics*, Cambridge University Press, 2013.

19 N.-T. Nguyen, *Micromixers, Second Edition*, 2012.

20 A. Günther, M. Jhunjhunwala, M. Thalmann, M. A. Schmidt and K. F. Jensen, *Langmuir*, 2005, **21**, 1547–1555.

21 A. S. Martin and K. F. Jensen, *Langmuir*, 2004, **20**, 8604–8611.

22 Y. Li, A. Sanampudi, V. Raji Reddy, S. Biswas, K. Nandakumar, D. Yemane, J. Goettert and C. S. S. R. Kumar, *Chem. Phys. Chem.*, 2012, **13**, 177–182.

23 H. Jun, T. Fabienne, M. Florent, P. Coulon, M. Nicolas and S. Olivier, *30th Anniv. Langmuir*, 2012, **28**, 15966–15974.

24 S. E. Davis, M. S. Ide and R. J. Davis, *Green Chem.*, 2013, **15**, 17–45.

25 N. Russo, D. Fino, G. Saracco and V. Specchia, *Catal. Today*, 2006, **117**, 214–219.

26 J. K. Edwards, A. F. Carley, A. A. Herzing, C. J. Kiely and G. J. Hutchings, *Faraday Discuss.*, 2008, **138**, 225–239.

27 A. Villa, N. Dimitratos, C. E. Chan-Thaw, C. Hammond, G. M. Veith, D. Wang, M. Manzoli, L. Prati and G. J. Hutchings, *Chem. Soc. Rev.*, 2016, **45**, 4953–4994.

28 P. Zhao, N. Li and D. Astruc, *Coord. Chem. Rev.*, 2013, **257**, 638–665.

29 X. Zhang, Y. L. Chen, R. S. Liu and D. P. Tsai, *Reports Prog. Phys.*, 2013, **76**, 046401, 1–41.

30 S. Linic, U. Aslam, C. Boerigter and M. Morabito, *Nat. Mater.*, 2015, **14**, 567–576.

31 M. Brust, M. Walker, D. Bethell, D. J. Schiffrin and R. Whyman, 2000, 801–802.

32 L. Prati and G. Martra, *Gold Bull.*, 1999, **32**, 96–101.

33 L. Prati and A. Villa, *Catalysts*, 2012, **2**, 24–37.

34 M. Daniel and D. Astruc, *Chem. Rev.*, 2004, **104**, 293–346.

35 S. M. Rogers, C. R. A. Catlow, C. E. Chan-Thaw, D. Gianolio, E. K. Gibson, A. L. Gould, N. Jian, A. J. Logsdail, R. E. Palmer, L. Prati, N. Dimitratos, A. Villa and P. P. Wells, *ACS Catal.*, 2015, **5**, 4377–4384.

36 G. L. Nealon, B. Donnio, R. Greget, J.-P. Kappler, E. Terazzi and J.-L. Gallani, *Nanoscale*, 2012, **4**, 5244–5258.

37 V. Amendola, R. Pilot, M. Frasconi, O. M. Maragò and M. A. Iatì, *J. Phys. Condens. Matter*, 2017, **29**, 203002, 1–48.

38 V. Amendola and M. Meneghetti, *J. Phys. Chem. C*, 2009, **113**, 4277–4285.

39 U. Kreibig and M. Vollmer, *Optical Properties of Metal Clusters*, 1995.

40 F. Bonaccorso, M. Zerbetto, A. C. Ferrari and V. Amendola, *J. Phys. Chem. C*, 2013, **117**, 13217–13229.

41 E. A. Coronado and G. C. Schatz, *J. Chem. Phys.*, 2003, **119**, 3926–3934.

42 S. Malola, L. Lehtovaara, J. Enkovaara and H. Häkkinen, *ACS Nano*, 2013, **7**, 10263–10270.

43 J. A. Scholl, A. L. Koh and J. A. Dionne, *Nature*, 2012, **483**, 421–427.

44 B. Chu, eds. R. Borsali and R. Pecora, Springer Netherlands, Dordrecht, 2008, pp. 335–

372.

45 T. Hendel, M. Wuithschick, F. Kettemann, A. Birnbaum, K. Rademann and J. Polte, *Anal. Chem.*, 2014, **86**, 11115–11124.

46 A. Villa, D. Wang, G. M. Veith, F. Vindigni and L. Prati, *Catal. Sci. Technol.*, 2013, **3**, 3036–3041.

47 H. I. Schlesinger, H. C. Brown, A. E. Finholt, J. R. Gilbreath, H. R. Hoekstra and E. K. Hyde, *J. Am. Chem. Soc.*, 1953, **75**, 215–219.

48 B. Corain, G. Schmid and N. Toshima, *Metal Nanoclusters in Catalysis and Materials Science: The Issue of Size Control*, 2008.

49 S. Wang, K. Qian, X. Bi and W. Huang, *J. Phys. Chem. C*, 2009, **113**, 6505–6510.

50 M. L. Machesky, W. O. Andrade and A. W. Rose, *Chem. Geol.*, 1992, **102**, 53–71.

51 S. Gómez-de Pedro, M. Puyol and J. Alonso-Chamarro, *Nanotechnology*, 2010, **21**, 415603, 1–6.

52 M. Luty-Błocho, K. Fitzner, V. Hessel, P. Löb, M. Maskos, D. Metzke, K. Pacławski and M. Wojnicki, *Chem. Eng. J.*, 2011, **171**, 279–290.

53 J. Boleininger, A. Kurz, V. Reuss and C. Sönnichsen, *Phys. Chem. Chem. Phys.*, 2006, **8**, 3824–3827.

54 P. M. Ligrani, *A Study of Dean Vortex Development and Structure in a Curved Rectangular Channel With Aspect Ratio of 40 at Dean Numbers up to 430*, 1994.

55 A. D. Stroock, S. K. W. Dertinger, A. Ajdari, I. Mezić, H. A. Stone and G. M. Whitesides, *Science*, 2002, **295**, 647–651.

56 M. G. Olsen, J. G. Santiago, R. J. Adrian, R. H. Liu, M. A. Stremler, K. V Sharp, M. G. Olsen, J. G. Santiago, R. J. Adrian, H. Aref and D. J. Beebe, *J. Microelectromech. Syst.*, 2000, **9**, 190–197.

57 F. Schönfeld, V. Hessel and C. Hofmann, *Lab Chip*, 2004, **4**, 65–69.

58 J. Branebjerg, P. Gravesen, J. P. Krog and C. R. Nielsen, in *Proceedings of Ninth International Workshop on Micro Electromechanical Systems*, 1996, pp. 441–446.

59 D. Bothe, C. Stemich and H.-J. Warnecke, *Chem. Eng. Sci.*, 2006, **61**, 2950–2958.

60 N. Dimitratos, J. A. Lopez-Sanchez, D. Morgan, A. F. Carley, R. Tiruvalam, C. J. Kiely, D. Bethell and G. J. Hutchings, *Phys. Chem. Chem. Phys.*, 2009, **11**, 5142–5153.

61 M. Manzoli, A. Chiorino and F. Boccuzzi, *Surf. Sci.*, 2003, **532**–**535**, 377–382.

62 D. A. Panayotov, S. P. Burrows, J. T. Yates and J. R. Morris, *J. Phys. Chem. C*, 2011, **115**, 22400–22408.

63 A. Klinkova, A. Ahmed, R. M. Choueiri, J. R. Guest and E. Kumacheva, *RSC Adv.*, 2016, **6**, 47907–47911.

64 H. Gao, J. Henzie, M. H. Lee and T. W. Odom, *Proc. Natl. Acad. Sci. U. S. A.*, 2008, **105**, 20146–20151.

65 H. Gao, J. M. McMahon, M. H. Lee, J. Henzie, S. K. Gray, G. C. Schatz and T. W. Odom, *Opt. Express*, 2009, **17**, 2334–2340.

66 S. Cattaneo, S. J. Freakley, D. J. Morgan, M. Sankar, N. Dimitratos and G. J. Hutchings, *Catal. Sci. Technol.*, 2018, **8**, 1677–1685.

67 Au 4f7/2 XPS data, https://srdata.nist.gov/xps/, (accessed 1 May 2018).

68 Y. Lee and Y. Jeon, *J. Korean Phys. Soc.*, 2000, **37**, 451–455.

69 W. F. Egelhoff, *Surf. Sci. Rep.*, 1987, **6**, 253–415.

70 J. Hedman, M. Klasson, R. Nilsson and C. Nordling, *Phys. Scr.*, 1971, **4**, 195–201.

71 Z. Li, F. Gao, Y. Wang, F. Calaza, L. Burkholder and W. T. Tysoe, *Surf. Sci.*, 2007, **601**, 1898–1908.

72 J. Pritchard, L. Kesavan, M. Piccinini, Q. He, R. Tiruvalam, N. Dimitratos, J. A. Lopez-Sanchez, A. F. Carley, J. K. Edwards, C. J. Kiely and G. J. Hutchings, *Langmuir*, 2010, **26**, 16568–16577.

73 R. C. Tiruvalam, J. C. Pritchard, N. Dimitratos, J. A. Lopez-Sanchez, J. K. Edwards, A. F. Carley, G. J. Hutchings and C. J. Kiely, *Faraday Discuss.*, 2011, **152**, 63–86.

74 G. Sunahara, G. Lotufo, R. Kuperman and J. Hawari, *Ecotoxicology of Explosives*, 2009.

75 P.-G. Rieger and H.-J. Knackmuss, ed. J. C. Spain, Springer US, Boston, MA, 1995, pp. 1–18.

76 V. Purohit and A. K. Basu, *Chem. Res. Toxicol.*, 2000, **13**, 673–692.

77 United States Environmental Protection Agency, *Priority Pollutant List*, 2014.

78 P. F. Vogt and J. J. Gerulis, *Ullmann's Encycl. Ind. Chem.*, 2005, 1–21.

79 S. C. Mitchell and R. H. Waring, *Ullmann's Encycl. Ind. Chem.*, 2005, 1–20.

80 P. Zhao, X. Feng, D. Huang, G. Yang and D. Astruc, *Coord. Chem. Rev.*, 2015, **287**, 114–136.

81 T. Aditya, A. Pal and T. Pal, *Chem. Commun.*, 2015, **51**, 9410–9431.

82 Y. Wu, M. Wen, Q. Wu and H. Fang, *J. Phys. Chem. C*, 2014, **118**, 6307–6313.

83 Q. Wang, W. Jia, B. Liu, A. Dong, X. Gong, C. Li, P. Jing, Y. Li, G. Xu and J. Zhang, *J. Mater. Chem. A*, 2013, **1**, 12732–12741.

84 P. Zhang, C. Shao, Z. Zhang, M. Zhang, J. Mu, Z. Guo and Y. Liu, *Nanoscale*, 2011, **3**, 3357–3363.

85 S. K. Ghosh, M. Mandal, S. Kundu, S. Nath and T. Pal, *Appl. Catal. A Gen.*, 2004, **268**, 61–66.

Chapter 4

Catalytic reduction of 4-nitrophenol

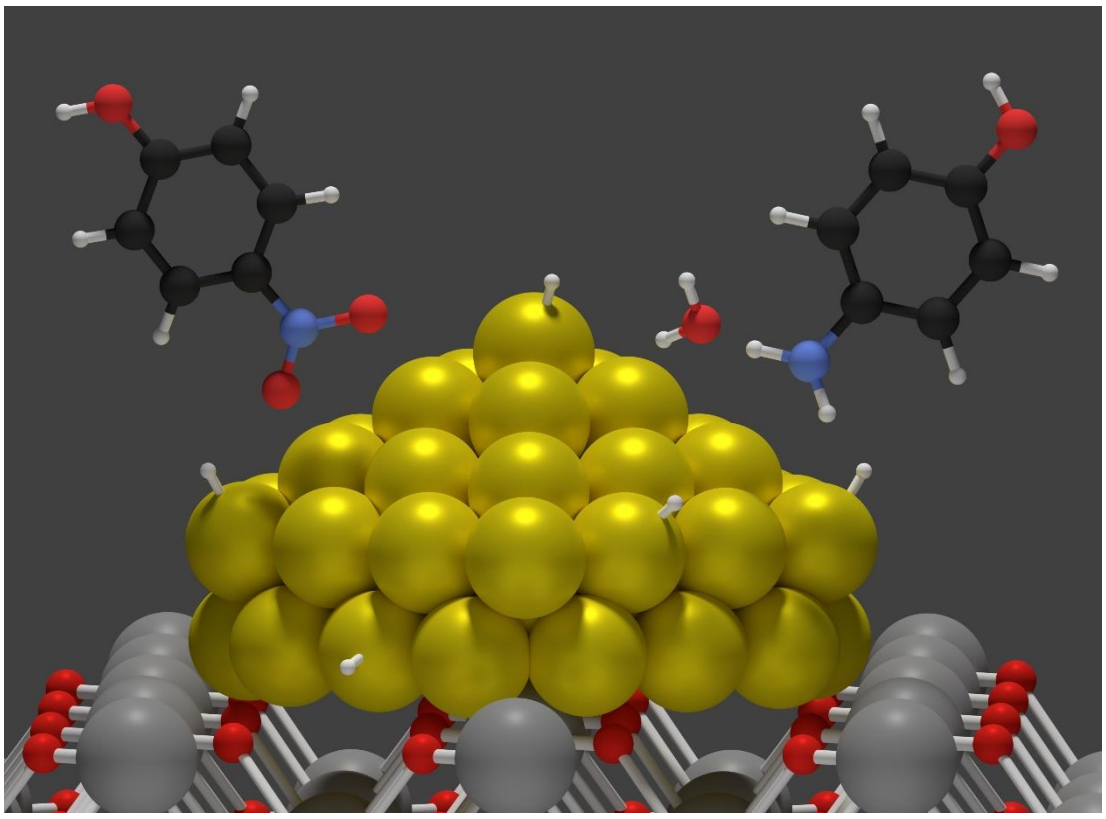

4.1. Introduction

4.1.1. Nitrophenols reduction as a model reaction

Nitroaromatic compounds, also known as nitroarenes, are a class of organic molecules composed of one or more nitro group (-NO_2) attached to an aromatic ring (usually a benzene ring). The combination of two electron-deficient oxygen atoms bonded to a partially positive nitrogen confer a strong electronegativity to the nitro group. Moreover, charge delocalisation is possible due to the π-electrons of the benzene ring, resulting in a partial positive charge at *ortho* and *para* positions[1].

Nitroarenes are generally highly toxic, mutagenic and many of them are human carcinogens[2–4]. They can often be found in industrial and agricultural waste water as by-products of pesticide, herbicide and synthetic dye production, and their presence, even in small concentrations, is a great concern from an environmental point of view. Indeed, several nitroarenes, such as nitrobenzene, dinitrotoluene and nitrophenol, are listed on the U.S. Environmental Protection Agency's list of priority pollutants[1,5]. In 2005, nitroarenes suddenly received great attention due to the explosion of a chemical manufacturing plant in China; in addition to the death of 6 workers and the injury of more than 70 people, 100 tons of benzene and nitrobenzene leaked into the river Songhua, heavily contaminating the environment and forcing the government to cut off water supplies to approximately 10 million people[6].

The hydrogenation of nitroaromatic compounds generates aminoarenes, important chemicals widely used in pharmaceutical industry as analgesics, antipyretics and chemotherapeutics, in agriculture as fungicides and pesticides and as intermediates in the synthesis of polymers (polyurethanes), dyes, pigments, photographic chemicals and corrosion inhibitors[7,8]. The products of hydrogenation of the nitrophenol isomers (aminophenols), in particular, are among the most extensively used nitroarene derivatives (Figure 4.1). 2-aminophenol, for example, is commonly used as photographic developing agent and as intermediate in the synthesis of dyes, while 3-aminophenol is mostly used in the synthesis of pharmaceuticals but finds application also as hair dye colorant and as stabiliser for chlorine-containing thermoplastics[7]. Finally, the 4-aminophenol is widely used in the synthesis of antipyretics and analgesics and as dyeing agent for fur and feathers[7].

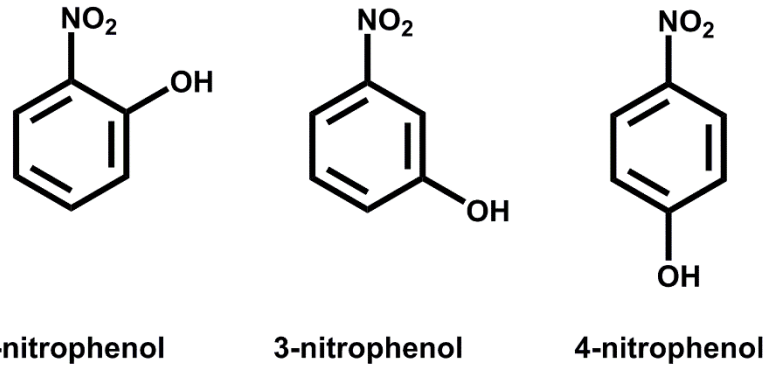

Figure 4.1: Nitrophenol isomers.

The reduction of 4-nitrophenol (4-NPH) to 4-aminophenol (4-APH) is often used as a model reaction to assess the catalytic activity of metal nanoparticles[9,10]. In order to be classified as such, a reaction should meet certain criteria. Firstly, the reaction should produce only one product in the presence of the catalyst without any side reaction taking place, meaning that the reaction rates can be easily measurable with good precision. Moreover, no conversion should be detected in absence of the catalyst. Secondly, temperature changes should not affect the reaction mechanism, therefore the activation energy should be easily derivable from Arrhenius plots. Finally, the reaction should proceed under mild conditions, for example at room temperature and water as solvent, and should be easy to monitor. The catalytic reduction of 4-NPH with sodium borohydride ($NaBH_4$) meets all the criteria above reported. The reaction, in fact, proceeds through the formation of various unstable intermediates and finally yields 4-APH as the only stable product. Moreover, the reaction can be carried out in water at room temperature and it can be easily monitored by UV-Vis spectroscopy due to the presence of conjugated π-electrons[9].

Much debate is reported on the exact mechanism of the reaction. The most accredited proposal is the Langmuir-Hinshelwood mechanism (LH), that dictates that both of the reactants, 4-NPH and $NaBH_4$, must be adsorbed onto the metal surface of the catalyst[11–14]. According to this mechanism, the borohydride ions react with the metal particle surface to generate adsorbed active hydrogen, while the 4-NPH molecules interact on the same active sites through the electronegative nitro group[15]. The substrates adsorption step is fast and reversible and it can be described by a Langmuir isotherm model, where all the active sites are equivalent and competition occurs between the two reagents. The diffusion of the substrates to the particle surface is very fast, thus the limiting step is the reaction between the adsorbed active hydrogen and 4-NPH[10]. Generally, the reaction is performed with $NaBH_4$ in high excess (therefore the concentration of $NaBH_4$ is considered constant over time), so that the kinetics can be easily described by a first-order rate law (Equation 4.1)[11,16,17]:

$$\frac{dC}{dt} = -k_R C_{NaBH4} C_t = -k_{NPH} C_t \qquad Equation\ 4.1$$

Where k_R is the rate constant of the reaction, C_{NaBH4} is the concentration of $NaBH_4$, C_t is the concentration of 4-NPH at time t and k_{NPH} is the apparent rate constant.

The reaction proceeds through the formation of several unstable intermediates that immediately react to produce 4-APH. The full reaction scheme is represented in Figure 4.2[18]. An adsorbed active hydrogen reacts first with the oxygen of the nitro group of the nitrophenolate ion to form a single hydroxyl-like intermediate (intermediate-1). A second active hydrogen reacts with the other oxygen of the nitro group to form a dihydroxy-like intermediate (intermediate-2) that decomposes removing a molecule of water and forming the nitrosophenol (intermediate-3). Next, two other hydrogen atoms react with the remaining oxygen (intermediate-4) and then with the nitrogen atom of the nitro group (intermediate-5, 4-hydroxylaminophenol). Finally, a second water molecule is formed and removed, and the last two hydrogen atoms react with the nitrogen atom to form the amino group through the intermediate-6.

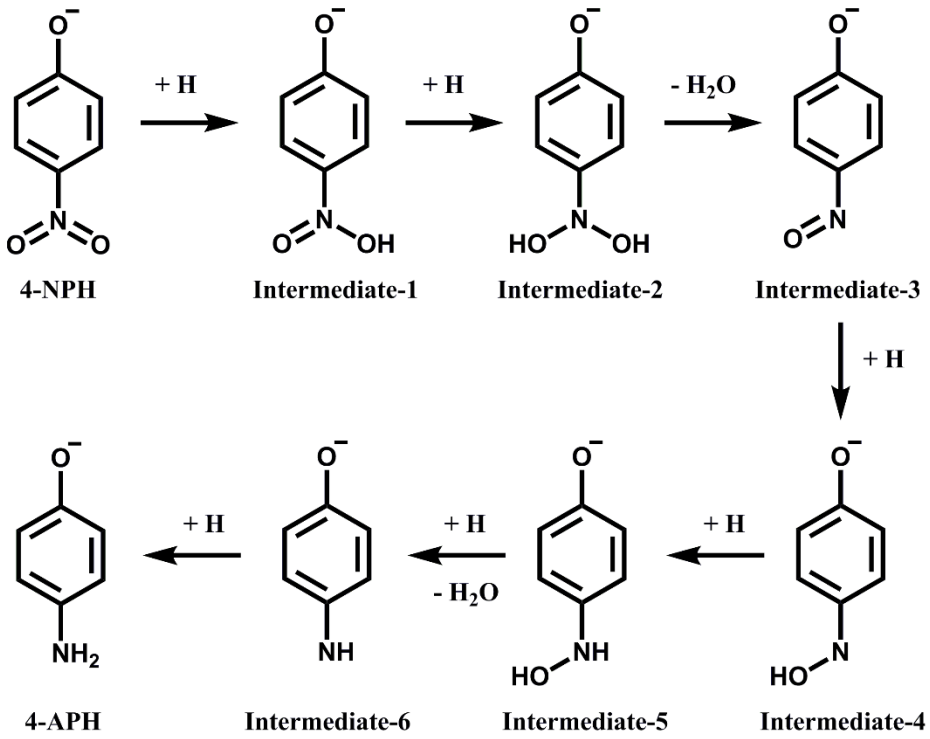

Figure 4.2: 4-NPH reduction mechanism as proposed by Kong et al. Image adapted from X. Kong et al., Chemical Physics Letters, 2017, 148-152.

Before the start of the reaction, upon addition of $NaBH_4$, several research groups have observed an induction time that can last several minutes[19,20]. This period used to be ascribed

to the diffusion time necessary for 4-NPH to reach the nanoparticles surface, but recent studies have disproved that[21]. Although no direct evidence has been reported in literature so far, the induction time is likely to be caused by surface restructuration necessary to make the metal nanoparticles active[17,22]. This reconstruction mechanism seems to directly involve 4-NPH, with at least two molecules of reactant necessary to induce the change in surface structure[17].

4.1.2. Gold and palladium catalysis in the 4-nitrophenol reduction

Transition metals are generally very active in the reduction of nitroarenes. Among them, noble metal nanoparticles such as Au, Pd and alloys of these two metals have shown remarkable activity when both unsupported or supported on various materials[23–26]. Au nanoparticles are the most tested catalyst in the 4-NPH reduction reaction, owing to their general high activity under mild reaction conditions and their structure sensitivity catalysis[10]. In addition to the particle size, the catalytic activity can be greatly influenced by the stabiliser agent used during the synthesis of the catalyst. The protective shell, in fact, can hinder the diffusion of the reactants to the particle surface and thus decrease the activity.

A wide range of stabilising agents have been reported in literature, including small organic molecules, polymers, peptides and dendrimers (Table 4.1)[10]. Yamamoto and co-workers, for example, reported the synthesis of Au_{13} clusters stabilised with N,N-dimethylformammide (DMF); the 4-NPH reduction reaction proceeded smoothly with a k_{NPH} of 7.0×10^{-3} s^{-1} only after a very long induction time of ca. 50 minutes[27]. The authors attributed this extended induction time to reactant diffusion limitation caused by the DMF layer surrounding the Au clusters. Polyvinylpyrrolidone (PVP) was used by Xiao et al. for the synthesis of Au@PVP hybrid nanogels, reporting high activity in the 4-NPH reduction ($k_{NPH} = 1.02 \times 10^{-2}$ s^{-1})[28]. The highest activity, however, was obtained by Biondi and co-workers employing a methyl-imidazolium-based ionic polymer ($k_{NPH} = 3.30 \times 10^{-2}$ s^{-1}) with the reaction reaching completion after only 4 minutes[29].

Since the catalytic activity of Au strongly depends on the size and shape of the particles, many anisotropic nanostructures have been specifically designed to enhance the number of active sites such as edges and corners. Polygonal particles, nanorods and hollow structures were then synthesised and tested on the 4-NPH reduction as a model reaction. Nanocages, in particular, showed interesting results from an activity point of view. Zeng and colleagues, in fact, reported that thinner nanocage walls had higher catalytic activity, with

the best performance achieved with structures having wall thickness of ca. 5 nm (k_{NPH} = 9.30 x 10^{-2} s^{-1})[30].

In order to improve the stability and applicability of Au nanoparticles, the active metal can also be immobilised onto different heterogeneous supports. Liu and colleagues, for example, tested 8 nm Au nanoparticles supported on carbon nanotubes/polyethyleneimine assembly (CNTs) reporting an activity of 1.5 x 10^{-3} s^{-1} in terms of apparent reaction constant[31]. Metal oxides are the most commonly used support for Au nanoparticles, and this is reflected by the great amount of literature available for this type of catalysts. Titanium dioxide was for instance employed by Ismail et al. to immobilise Au particles with different size[32]. The reported rate constant increased from 0.7 x 10^{-3} s^{-1} to 6.5 x 10^{-3} s^{-1} when the particle size was decreased from 300 to 10 nm, confirming that small nanoparticles are more active than large ones. Another very active metal oxide support is Fe_2O_3, as reported by Chang and colleagues[33]. The synthesised catalyst, in particular, combined high activity (k_{NPH} = 1.47 x 10^{-2} s^{-1}), with easy recoverability thanks to the magnetic property of the magnetite.

Table 4.1: Au based catalysts tested in the 4-NPH reduction reaction.

Catalyst	**Particle size [nm]**	**k_{NPH} [10^{-3} s^{-1}]**	**k_R [10^{-3} L mol^{-1} s^{-1}]**	**Ref.**
Au/DMF	1-2	7.0	35	[27]
Au/PVP	10	10.2	2170	[28]
Au/ionic-polymer	2-4	33.0	7857	[29]
Au nanocages	50 (5)[a]	93.0	2214	[30]
Au/CNTs	8	1.5	115	[31]
Au/TiO_2	300	0.7	7	[32]
Au/TiO_2	10	6.5	65	[32]
Au/Fe_2O_3	3	14.7	4454	[33]

[a]The number in brackets refers to the wall thickness.

As already mentioned above, besides Au, Pd nanoparticles are very active in the 4-NPH reduction reaction. Pd, in fact, can be even more active than Au if properly stabilised against agglomeration and leaching. The hindering effect of the support was studied by Johnson and co-workers using Pd clusters stabilised by various concentration of dendrimers[34]. The authors reported a decrease in activity with the increased amount of support due to steric crowding that inhibited free mass transport to the metal particle surface (Table 4.2). Very fast 4-NPH conversion was observed by Wang et al. when 3 nm Pd particles were supported on core-shell mixed oxides (k_{NPH} = 1.60 x 10^{-2} and 1.05 x 10^{-2} s^{-1} when Fe_3O_4@CeO_2 and

Fe_3O_4@SiO_2@CeO_2 were employed respectively)[25]. Carbon nanotubes (CNTs) were finally tested as support by Gu and colleagues, reporting a maximum activity of 1.05 x 10^{-2} s^{-1} in terms of k_{NPH}[35]. The nanotubes were previously functionalised with hydroxyl groups to improve both dispersion in water and interaction with the Pd nanoparticles, which in turns prevented particle agglomeration.

Table 4.2: Pd based catalysts tested in the 4-NPH reduction reaction.

Catalyst	Particle size [nm]	k_{NPH} [10^{-3} s^{-1}]	k_R [10^{-3} L mol^{-1} s^{-1}]	Ref.
Pd/dendrimer - 10/1	1	110	2895	[34]
Pd/dendrimer - 50/1	1	530	13947	[34]
Pd/Fe_3O_4@CeO_2	3	16.0	1260	[25]
Pd/Fe_3O_4@SiO_2@CeO_2	3	10.5	827	[25]
Pd/CNTs	1-2	10.5	652	[35]

Bimetallic nanoparticles have recently attracted much attention mostly because they often show enhanced catalytic performance compared to their monometallic counterparts. The simultaneous presence of two distinct metals adds an additional variable in the study of the property of a catalyst. As already discussed in Chapter 1.2, in fact, the two metals can be completely alloyed or segregated, drastically changing the catalytic behaviour of a particular reaction. For this reason, the use of a model reaction as test for bimetallic catalyst is of a great interest in the research community, and this is reflected in the amount of work published in literature in the last 10 years[10]. Particular attention was focused on AuPd alloy nanoparticles, due to the high activity of both monometallic Au and Pd. Enhanced activity was found by Meng's and Ballauff's workgroups when 1-4 nm particles were supported on either nanoporous carbon spheres[36] (NCS) or polyelectrolyte brushes[37] (Table 4.3). In both cases, the authors ascribed the enhanced catalytic activity to the synergistic effect of the two metal, such as electron transfer and structural rearrangements caused by differences in lattice parameters. Wang and colleagues, on the other hand, found no catalytic enhancement when using AuPd particles while screening several mixed metal oxides based catalysts[25]. Their work, however, was mostly focused on the properties of the mixed metal oxides rather than the bimetallic interaction, thus no explanation was given to the observed phenomenon. Finally, Zhang et al. developed a synthetic route for the preparation of octadecyltrimethyl ammonium chloride (OTAC) AuPd particles with similar size (ca. 40 nm) but different shape (rhombic dodecahedron, trisoctahedron and hexoctahedron) and tested the catalysts in the

4-NPH reduction reaction[38]. The authors related variations in activity to changes in surface structure of the nanoparticles caused by the different shape.

Table 4.3: AuPd based catalysts tested in the 4-NPH reduction reaction.

Catalyst	Particle size [nm]	k_{NPH} [10^{-3} s^{-1}]	k_R [10^{-3} L mol^{-1} s^{-1}]	Ref.
Au/NCS	3-4	0.1	15	[36]
Pd/NCS	3-4	6.6	985	[36]
AuPd/NCS	3-4	14.6	2179	[36]
Au/polyel-brushes	1-3	0.16	21	[37]
Pd/polyel-brushes	1-3	0.055	7	[37]
AuPd/polyel-brushes	1-3	2.9	387	[37]
$Au/Fe_3O_4@SiO_2@CeO_2$	3	3.9	639	[25]
$Pd/Fe_3O_4@SiO_2@CeO_2$	3	10.5	1721	[25]
$AuPd/Fe_3O_4@SiO_2@CeO_2$	3	4.0	656	[25]
AuPd/OTAC	40	5.4	25	[38]

4.1.3. Aims and objectives of the Chapter

The aim of this chapter was to deeply investigate the metal particle size effect on the nitrophenol reduction reaction to aminophenol. Despite the large volume of research concerning this reaction, to date, the active sites responsible for the reduction of nitroarenes on metallic nanocrystals in aqueous medium and with $NaBH_4$ as reducing agent have not been clearly identified. The knowledge of the active sites for a specific reaction is crucial in heterogeneous catalysis, and it can help tailoring the catalyst's synthesis specifically for the desired reaction.

The term nitrophenol (NPH) can be used to identify one of the three isomers, namely 2-nitrophenol (2-NPH), 3-nitrophenol (3-NPH) and 4-nitrophenol (4-NPH), depending on the relative position of the two functional groups on the benzene ring. Initially, the three isomers were tested with three different catalyst (Au/TiO_2, Pd/TiO_2 and $AuPd/TiO_2$) to find the best substrate and active metal to use as model for the study. A wide range of catalysts with different particle size range were then employed in order to find a good and reliable correlation between geometrical properties of the metal nanoparticles and catalytic activity.

4.2. Nitrophenol reduction with supported metal nanoparticles

4.2.1. Kinetic considerations

As already mentioned above, one of the advantages of using the NPH reduction as model reaction is that it can be easily monitored by UV-Vis spectroscopy. All the three NPH isomers, in fact, show a light yellow colouration when dissolved in water. 4-NPH, in particular, display a peak with an absorption maximum at 317 nm[9]. Upon the addition of $NaBH_4$ (or any base), the NPH undergoes deprotonation, becoming nitrophenolate ion. The presence of additional free electrons strengthens the solution colouration and shifts the peak to higher wavelengths (400 nm in the case of 4-NPH). During reduction to APH, the absorption peak of the nitrophenolate ion decreases, followed by the simultaneous increase of another peak at shorter wavelengths and corresponding to the product APH (Figure 4.3).

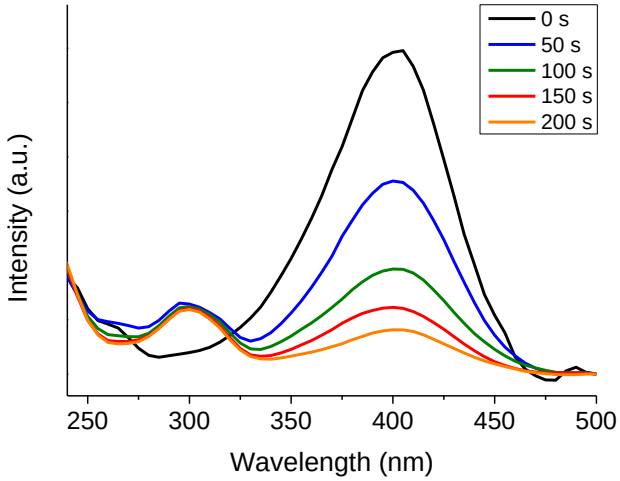

Figure 4.3: UV-Vis spectra of the evolution of a typical nitroarene reduction reaction (4-nitrophenol in this specific case).

The relation between absorbance (A) and concentration (C) is expressed by the Beer-Lambert law (Equation 4.2):

$$A = \varepsilon\, C\, l \qquad Equation\ 4.2$$

Where both the molar extinction coefficient (ε) and the light pathway (l) are constant, thus the absorbance is directly proportional to the concentration of the solution. For this reason, the substrate conversion (X) was calculated simply by the absorbance values at a given time t, according to the follow equation:

$$X = \frac{A_0 - A_t}{A_0} \times 100 \qquad Equation\ 4.3$$

Where A_0 is the absorption value of the nitrophenolate ion peak at the beginning of the reaction and A_t is the absorption value of the same peak after a reaction time "t".

An excess of $NaBH_4$ to nitrophenol was used for each reaction in the ratio $NaBH_4$: NPH of 100 : 1 in order to obtain pseudo-first order kinetics, as the activity is no longer dependent on the $NaBH_4$ concentration[9]. The apparent rate constant (k_{NPH}) can therefore be obtained from the Equation 4.4:

$$\ln\frac{C_t}{C_0} = \ln\frac{A_t}{A_0} = -k_{NPH}\ t \qquad Equation\ 4.4$$

Where C_t and A_t are respectively the NPH concentration and absorbance after a reaction time "t", while C_0 and A_0 are the NPH concentration and absorbance at the beginning of the reaction. In a more practical way, the k_{NPH} can be obtained from the relative kinetic graph as the gradient of the linear relationship (Figure 4.4).

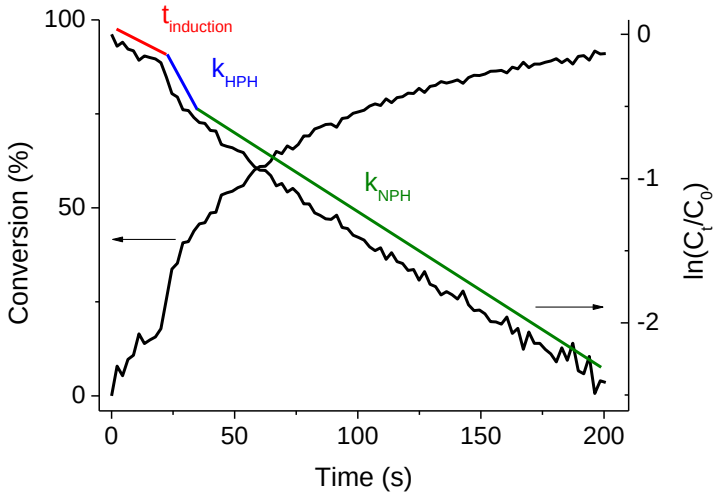

Figure 4.4: Time dependence of the conversion and the 4-nitrophenolate ions absorption at 400 nm for a typical reduction reaction. Emphasised with different colours the three parts of the reaction: induction time in red, 4-nitrophenol conversion into 4-hydroxylaminophenol in blue and the conversion of 4-hydroxylaminophenol into 4-aminophenol in green.

Figure 4.4 represents an example of a typical time dependence of the 4-nitrophenolate ions absorption at 400 nm. It is possible to observe three stages of the reaction, as pointed out by Ballauff and coworkers[39]. In the first stage, the reaction proceeds slowly and it is therefore characterised by a typical induction time ($t_{induction}$), that in some cases can last even several minutes (red line). The induction time, as already mentioned in the Introduction

section of this Chapter, is related to surface restructuring of the nanoparticles before the reaction starts: surface atoms rearrange to form new active sites such as corners and edges on the surface[17]. Subsequently, the reaction starts and a second induction time is necessary to finally reach a constant 4-NPH consumption[39]. In this second stage the 4-NPH is rapidly converted to the quasi-stable intermediate 4-hydroxylaminophenol (4-HPH), while only small amount of the final product 4-APH is produced[39]. The kinetic constant of the relative process (k_{HPH}) can be easily calculated from the graph and used to compare different catalysts. In the third and final stage, the 4-HPH concentration reaches a steady state and thus the kinetic constant of this process (K_{NPH}) is relative only to the reduction of 4-NPH to 4-APH.

4.2.2. Choice of substrate

As already explained in the Introduction section of this Chapter, the catalytic reduction of NPH isomers is very sensitive to active metal particle size variations. Preliminary tests on 2-NPH, 3-NPH and 4-NPH were conducted using a 0.5 wt% Au catalyst supported on TiO_2 and prepared with the standard batch sol-immobilisation technique. The catalyst was characterised with SEM/TEM and MP-AES beforehand to measure particle size and metal loading: small particles were efficiently synthesised and deposited on the support surface (Table 4.4).

Table 4.4: Particle size and metal loading of the 0.5 wt% Au/TiO_2 catalyst used with different substrates.

Catalyst	Particle size [nm]	Metal loading [wt%]
0.5 wt% Au/TiO_2	4.8 ± 1.1	0.48

The catalytic tests were repeated at least 3 times to ensure reproducibility of the results obtained. Figure 4.5 shows the time dependence of the NPH conversion with the different isomers. 3-NPH is more reactive compared to 2-NPH and 4-NPH. This can be explained by a lower electrostatic repulsion between the activated hydrogen from $NaBH_4$ and the nitro group when substituted in *meta*-position. Both species (hydride and nitro group) are electron rich and, according to the LH model, they are both adsorbed on the particle surface. The electron density on the nitro group is particularly high when the group is substituted in position *ortho* and *para* due to mesomeric effect. In this case, in fact, the negative charge of the phenoxide can be delocalised on the nitro group (Figure 4.6), making

the NO_2 more electron rich. For this reason, the repulsion between H^- and NO_2 will be higher when charge delocalisation is possible, and as a consequence the reaction rate will be lower.

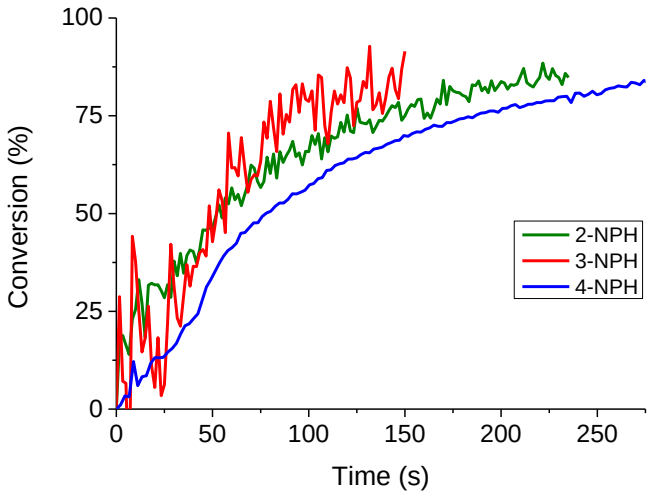

Figure 4.5: Conversion rates of different substrates using a 0.5 wt% Au/TiO_2 catalyst. Reaction conditions: molar ratio Au : NPH : $NaBH_4$ of 1 : 2.5 : 250, total volume 3 mL, room temperature.

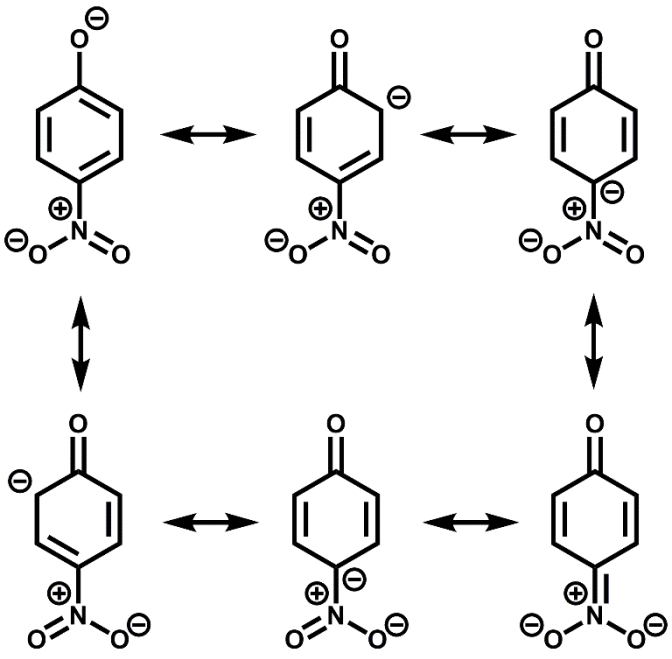

Figure 4.6: Mesomeric effect on the 4-NPH. The negative charge can be delocalised on the nitro group.

When 2-NPH and 3-NPH were used as substrates, the bubbling caused by $NaBH_4$ decomposition influenced the UV-Vis analysis and thus making the first 30 seconds of reaction difficult to interpret; k_{HPH} where therefore not possible or hard to calculated (Figure 4.7). The k_{NPH} values, on the other hand, were obtained for every isomer and are reported in Table 4.6. Due to the problematic calculation of both k_{HPH} and k_{NPH} caused by the vigorous

bubbling when 2-NPH and 3-NPH were used, 4-NPH was chosen as test substrate for this study.

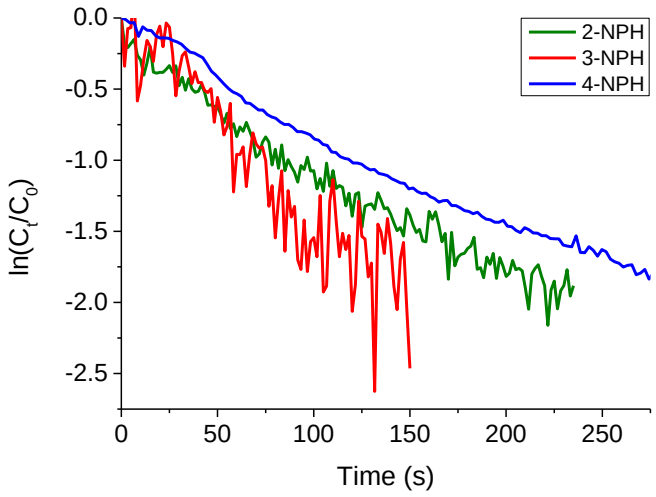

Figure 4.7: NPH conversion over time with different substrates. Reaction conditions: molar ratio Au : NPH : $NaBH_4$ of 1 : 2.5 : 250, total volume 3 mL, room temperature.

Table 4.5: Kinetic constants relative to the reduction reaction using different substrates.

Substrate	**k_{HPH} [-10^{-3} s^{-1}]**	**k_{NPH} [-10^{-3} s^{-1}]**
2-NPH	9.5	8.4
3-NPH	n.a.	19.4
4-NPH	15.6	6.7

4.2.3. Choice of metal

A monometallic Pd and a bimetallic AuPd catalysts were then synthesised with the standard batch sol-immobilisation technique in order to obtain a metal loading of 0.5 wt%. The catalysts metal loading was measured by MP-AES analysis and the results are reported in Table 4.7. The bimetallic AuPd, as for the previously reported Au catalyst, had an experimental metal loading very close to the theoretical value (0.46 wt%), confirming the effective deposition of all the metals on the support surface. In particular, the experimental Au : Pd molar ratio was very close to the nominal 1 : 1. The monometallic Pd catalyst, however, displayed a metal loading lower than expected (0.38 %), probably due to an error during the catalyst synthesis. Particle size and size distribution for the Pd and AuPd catalysts

were very similar, with nanoparticles in a 2 – 5 nm range. Slightly bigger nanoparticles were obtained with the Au catalyst (average diameter, 4.8 nm).

Table 4.6: Particle size, metal loading and metal composition of the three synthesised catalysts.

Catalyst	Particle size [nm]	Metal loading [wt%]	Metal content [%]	
			Au	Pd
Au/TiO_2	4.8 ± 1.2	0.48	100	-
Pd/TiO_2	3.3 ± 1.1	0.38	-	100
$AuPd/TiO_2$	3.1 ± 0.9	0.46	51	49

Figure 4.8 shows the comparison between the activities of the three catalysts in terms of reaction constant k_{HPH} and k_{NPH}. Contrary of the observations by Meng and Ballauff, the bimetallic catalyst was not the most active[36,37]. The Pd catalyst, in fact, showed a very high activity, approximatively 8 times higher than Au and 5 times higher than the bimetallic AuPd (Table 4.7). The high activity of Pd in this type of reaction has already been reported in literature and it is usually related to the better hydrogen storage property of this noble metal[10]. Activated hydrogen atoms can in fact diffuse inside the Pd structure, leaving more surface active sites available for the adsorption of NPH molecules. Higher activity can also result from leaching phenomena, with dissolved Pd atoms acting as homogeneous catalysts. MP-AES analysis on the reaction solution was performed in order to evaluate the extent of leaching (Table 4.7). When the Au and AuPd catalysts were used, the metal leaching was very low (less than 0.2 % of Au and less than 0.7 % of Pd). With the Pd catalyst, however, significant leaching was observed (3.61 %); it is therefore possible that Pd ions in solution were in part responsible for the very high boost in activity.

Another explanation for the high activity of the Pd-based catalyst can be attributed to the higher metal dispersion on the support surface. If on one hand the lower metal loading of the Pd/TiO_2 catalyst results in a lower amount of available active sites, on the other hand the better dispersion of the metal nanoparticles on the TiO_2 surface can reduce the electrostatic interactions and thus improve the accessibility of the active sites from the substrate. Moreover, it should be noted that the lower activity of the Au catalyst can be explained in part by the presence of bigger metallic particles on the support surface as revealed by STEM analysis (Table 4.6).

Au was chosen as active metal for the study for several reasons. Firstly, the Au/TiO_2 catalyst was relatively stable, with the lowest metal leaching among the catalysts compared

(Table 4.7). In addition, the UV-Vis signal was more stable using Au as active metal (Figure 4.8) and therefore the calculation of k_{NPH} and k_{HPH} can be more accurate and reliable. The reason for this signal instability was attributed to a faster decomposition of $NaBH_4$ on Pd atoms with consequent enhanced bubbles evolution. Finally, Au nanoparticles can be easily characterised by means of UV-Vis spectroscopy during the catalyst synthesis, due to the presence of plasmon resonance, otherwise not visible with Pd and AuPd nanoparticles.

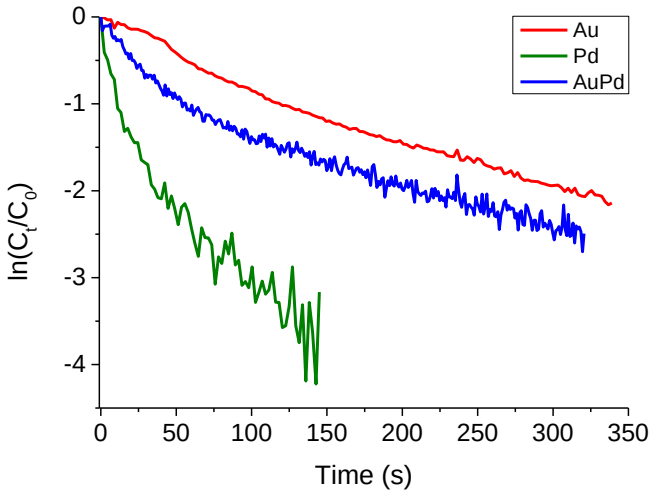

Figure 4.8: 4-NPH conversion over time using different catalysts. Reaction conditions: molar ratio Me : 4-4-NPH : $NaBH_4$ of 1 : 2.5 : 250, total volume 3 mL, room temperature.

Table 4.7: Catalytic activity and metal leaching of the three different catalysts used.

Catalyst	k_{HPH} [-10^{-3} s^{-1}]	k_{NPH} [-10^{-3} s^{-1}]	Metal leaching [%]	
			Au	Pd
Au/TiO_2	15.6	6.7	0.12	-
Pd/TiO_2	110.6	57.1	-	3.61
$AuPd/TiO_2$	21.5	11.1	0.19	0.63

4.3. Identification of the active sites in the 4-NPH reduction reaction

4.3.1. Metal surface area versus catalytic activity

The catalytic reduction of 4-NPH with Au-based catalysts has been widely studied over the past decade[40]. Recent studies, in particular, have shown that the k_{NPH} is directly proportional to the metal nanoparticles surface area (S)[32,41–43]. The reaction rate (dC/dt) can then be expressed by the Equation 4.5:

$$\frac{dC}{dt} = -k_{NPH}C_t = -k_S S C_t \qquad Equation\ 4.5$$

Where k_S is the rate constant normalised to S and C_t is the concentration of 4-NPH at time t.

In order to verify this relation, the 4-NPH reduction reaction was conducted using the catalysts produced during the optimisation of the semi-continuous and continuous setup described in Chapter 3. Tables 4.8 and 4.9 report all the catalyst tested with relative reaction conditions used during the synthetic step.

Table 4.8: Catalysts studied with relative reaction conditions used during the synthetic step and catalytic activity towards the 4-NPH reduction reaction. In particular: BATCH is the catalyst prepared in batch, SCxx are the catalysts prepared in semi-continuous and CONT is the catalyst prepared in continuous. In bolds are highlighted the parameters changed during the synthetic step. All the catalysts were prepared at pH 3.6 and Au concentration of 0.127 mmol L^{-1}.

Catalyst	Connection /Reactor	Flow rate [mL min^{-1}]	Reactor length [cm]	PVA/Au [wt/wt]	$NaBH_4$/Au [mol/mol]	Particle size[a] [nm]	Metal loading [wt%]	k_{NPH} [-10^{-3} s^{-1}]	k_R[b] [10^{-3} L mol^{-1} s^{-1}]	k_{HPH} [-10^{-3} s^{-1}]
BATCH	-	-	-	0.65	5	5.6 ± 1.6	0.94	12.1	1210	35.4
SC01	T-PFA	6	80	**0**	5	14.5 ± 8.7	0.97	3.9	390	5.7
SC02	T-PFA	6	80	**0.65**	5	6.5 ± 1.7	0.94	7.7	770	18.8
SC03	T-PFA	6	80	**1.3**	5	6.0 ± 1.4	0.93	4.4	440	9.2
SC04	T-PFA	6	80	0.65	**1**	22.9 ± 8.2	0.41	2.8	280	3.6
SC05	T-PFA	6	80	0.65	**2.5**	9.0 ± 2.8	0.90	3.9	390	5.5
SC06	T-PFA	6	80	0.65	**7.5**	11.3 ± 4.0	0.92	4.4	440	5.9
SC07	T-PFA	6	**130**	0.65	5	7.2 ± 2.6	0.92	4.0	400	6.4
SC08	T-PFA	6	**105**	0.65	5	7.0 ± 2.1	0.95	4.3	430	9.9
SC09	T-PFA	6	**30**	0.65	5	5.7 ± 1.3	0.95	9.0	900	18.3
SC10	T-PFA	**1**	80	0.65	5	15.1 ± 6.2	0.81	4.0	400	6.9
SC11	T-PFA	**2**	80	0.65	5	6.7 ± 1.5	0.87	5.2	520	8.1
SC12	T-PFA	**4**	80	0.65	5	7.0 ± 2.0	0.88	6.1	610	8.0
SC13	T-PFA	**8**	80	0.65	5	5.4 ± 0.9	0.92	11.2	1120	19.2
SC14	T-PFA	**24**	80	0.65	5	5.6 ± 1.3	0.94	10.4	1040	18.5
SC15	**T-Print**	6	80	0.65	5	7.0 ± 1.9	0.95	7.1	710	17.6
SC16	**Y- Print**	6	80	0.65	5	7.4 ± 2.2	0.97	7.0	700	16.8
SC17	**I- Print**	6	80	0.65	5	6.4 ± 1.5	0.96	7.4	740	21.6
SC18	**Helix- Print**	6	80	0.65	5	6.3 ± 1.3	0.96	8.8	880	26.6
SC19	**Plait- Print**	6	80	0.65	5	7.5 ± 2.5	0.94	5.4	540	20.6
CONT	T-PFA	6	80	0.65	5	4.5 ± 1.3	0.96	16.8	1680	38.7

[a]Particle size calculated by STEM. [b]Calculated considering a concentration of $NaBH_4$ of 1 x 10^{-2} mol L^{-1}.

Table 4.9: Catalysts studied with relative reaction conditions used during the synthetic step and catalytic activity towards the 4-NPH reduction reaction. In particular, SCxx are the catalysts prepared in semi-continuous. In bolds are highlighted the parameters changed during the synthetic step. All the catalysts were prepared with a PVA : Au weight ratio of 0.65 and a $NaBH_4$: Au molar ratio of 5.

Catalyst	Connection /Reactor	Flow rate [mL min^{-1}]	Reactor length [cm]	C_{Au} [mmol L^{-1}]	pH	Particle size[a] [nm]	Metal loading [wt%]	k_{NPH} [-10^{-3} s^{-1}]	k_R[d] [10^{-3} L mol^{-1} s^{-1}]	k_{HPH} [-10^{-3} s^{-1}]
SC20	T-PFA	6	80	**0.102**	3.6	8.0 ± 1.7	0.94	5.7	570	12.3
SC21	T-PFA	6	80	**0.169**	3.6	7.4 ± 1.5	0.93	4.0	400	11.8
SC22	T-PFA	6	80	**0.254**	3.6	7.4 ± 1.5	0.96	4.4	440	10.3
SC23	T-PFA	6	80	0.127	**6.9**	6.3 ± 1.8	0.95	5.0	500	16.1
SC24	T-PFA	6	80	0.127	**9.6**	7.5 ± 2.4	0.97	4.9	490	13.1
SC25-1[b]	T-PFA	6	80	0.127	3.6	10.7 ± 2.2	n.a.	6.1	610	12.1
SC26-2[b]	T-PFA	6	80	0.127	3.6	27.5 ± 2.8	n.a.	5.3	530	10.9
SC27-3[b]	T-PFA	6	80	0.127	3.6	25.7 ± 3.2	n.a.	4.7	470	6.4
SC28-4[b]	T-PFA	6	80	0.127	3.6	28.9 ± 3.1	0.94	4.8	480	5.7
SC29-1[c]	T-PFA	6	80	0.127	3.6	5.7 ± 1.8	n.a.	7.9	790	21.2
SC30-2[c]	T-PFA	6	80	0.127	3.6	5.5 ± 1.9	n.a.	8.7	870	20.8
SC31-3[c]	T-PFA	6	80	0.127	3.6	5.9 ± 1.9	n.a.	7.1	710	19.2
SC32-4[c]	T-PFA	6	80	0.127	3.6	5.9 ± 1.5	0.97	8.6	860	18.1

[a]Particle size calculated by DLS. [b]Catalyst produced after reuse of the tubing. [c]Catalyst produced after washing and reuse of the tubing.

[d]Calculated considering a concentration of $NaBH_4$ of 1 x 10^{-2} mol L^{-1}.

The k_{NPH} values were firstly plotted against the average particles diameter calculated from STEM analysis as represented in Figure 4.9; particle size values obtained with DLS were used for those catalysts were STEM analysis had not been performed (blue data). It is interesting to notice that the catalyst activity drastically drops with increasing the particle size in the 4 – 10 nm range, after which large changes in average particles diameter result in small activity variations. It is clear from this graph that the k_{NPH} values are not directly proportional to the average Au particle size, but rather follow an exponential trend.

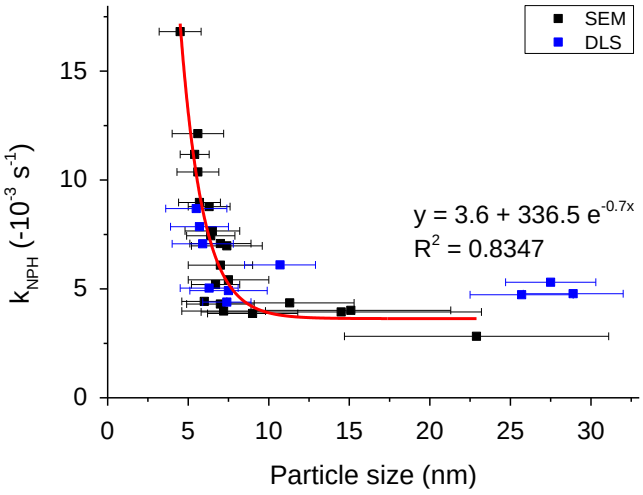

Figure 4.9: Activity versus particle size for the various catalysts synthesised. The colours refer to the different techniques used to calculate the particle size: black for STEM and blue for DLS. The red line represents the exponential trend that best fits the data; equation and coefficient of determination (R^2) are also reported.

The use of average particles diameter values, however, is not a reliable way to show size-dependent behaviours of the catalysts studied. According to Lu and colleagues, in fact, the catalytic activity of Pt and Ag nanoparticles is directly related to the theoretical specific surface area of metal particles, in their work calculated by approximation of the metal nanoparticles to perfect spheres[41–43]. Surface area values were therefore calculated using the average particle diameter obtained from STEM analysis (S_A, Equation 4.6). Half-spheres were considered as geometrical figures instead of full spheres, as the Au particles are strongly supported on the metal oxide and therefore assume a flattened structure[44].

$$S_A = \frac{\bar{A}}{\rho_{Au}\bar{V}} \times wt\% \qquad Equation\ 4.6$$

Where $\bar{A}$ and $\bar{V}$ are the half-area and half-volume of the nanoparticles calculated using the average particle diameter, while ρ_{Au} is the bulk density of Au (19.3 g cm^{-3}). The surface area values were normalised to the unit mass of the system, considering that the metal

loading (wt%) was not exactly 1 wt% for all the catalysts. In addition to S_A, two additional values were calculated considering the higher and lower limit of the standard deviation on the average particle diameter, respectively called S_{A+} and S_{A-}. For example, the catalyst named "BATCH" had an average particle diameter of 5.6 ± 1.6 nm (5.6 nm average diameter, 7.2 nm higher limit and 4.0 nm lower limit); the S_A, S_{A+} and S_{A-} values calculated using Equation 4.6 are therefore 55.5 $m^2 g^{-1}$, 43.1 $m^2 g^{-1}$ and 77.6 $m^2 g^{-1}$ respectively. The surface area values of the respective catalyst are reported in Table 4.10; only the catalysts analysed with STEM were considered, since DLS analysis does not allow a precise surface area calculation.

Table 4.10: Surface area values of the different catalysts studied along with average particle size, metal loading and catalytic activity.

Catalyst	Particle size[a] [nm]	Metal loading [wt%]	S_{A+} [$m^2 g^{-1}$]	S_A [$m^2 g^{-1}$]	S_{A-} [$m^2 g^{-1}$]	S_R [$m^2 g^{-1}$]
BATCH	5.6 ± 1.6	0.94	40.5	52.1	52.1	46.2
SC01	14.5 ± 8.7	0.97	13.0	20.8	20.8	10.6
SC02	6.5 ± 1.7	0.94	35.6	44.9	44.9	38.9
SC03	6.0 ± 1.4	0.93	39.0	48.1	48.1	47.1
SC04	22.9 ± 8.2	0.41	4.1	5.6	5.6	2.0
SC05	9.0 ± 2.8	0.90	23.7	31.1	31.1	25.4
SC06	11.3 ± 4.0	0.92	18.7	25.3	25.3	19.7
SC07	7.2 ± 2.6	0.92	29.2	39.7	39.7	27.8
SC08	7.0 ± 2.1	0.95	32.4	42.1	42.1	36.4
SC09	5.7 ± 1.3	0.95	42.1	51.8	51.8	47.6
SC10	15.1 ± 6.2	0.81	11.8	16.7	16.7	11.4
SC11	6.7 ± 1.5	0.87	32.9	40.3	40.3	32.2
SC12	7.0 ± 2.0	0.88	30.4	39.0	39.0	32.0
SC13	5.4 ± 0.9	0.92	45.4	52.9	52.9	47.8
SC14	5.6 ± 1.3	0.94	42.3	52.1	52.1	47.9
SC15	7.0 ± 1.9	0.95	33.1	42.1	42.1	37.4
SC16	7.4 ± 2.2	0.97	31.4	40.7	40.7	36.5
SC17	6.4 ± 1.5	0.96	37.7	46.6	46.6	46.1
SC18	6.3 ± 1.3	0.96	39.2	47.3	47.3	44.9
SC19	7.5 ± 2.5	0.94	29.2	38.9	38.9	33.6
CONT	4.5 ± 1.3	0.96	51.4	66.3	66.3	60.3

[a]Particle size calculated by STEM.

Figure 4.10a shows the catalyst activity in terms of k_{NPH} plotted against the theoretical Au surface area S_A. The values calculated using the average particles diameter show a very broad standard deviation (difference between S_{A+} and S_{A-}) caused by propagation of uncertainty on the average particle diameter. A better way to avoid this uncertainty is to

calculate the surface area values considering the contribution of every single nanoparticle measured by STEM (S_R, Equation 4.7).

$$S_R = \frac{\sum A_i}{\sum \rho_{Au} V_i} * wt\% \qquad Equation\ 4.7$$

Where A_i and V_i are the half-area and half-volume of every measured nanoparticle calculated as already mentioned approximating the particles to perfect half-spheres and ρ_{Au} is again the bulk density of Au (19.3 g cm^{-3}). In this case, no error bar is needed, since the resulting value is not an average value of the system. The surface area values of the respective catalyst are reported in Table 4.10; for the same reason already mentioned, only the catalysts analysed with STEM were considered. Figure 4.10b shows the catalyst activity in terms of k_{NPH} plotted against the theoretical Au surface area S_R. In this case, all the values seem to follow an exponential trend similar to the one observed plotting k_{NPH} against the average diameter (Figure 4.9). Only one point seems to be out of trend (blue square). This catalyst was the one prepared with excessive amount of stabilising agent (PVA). The low catalytic activity can be explained by an enhanced steric effect of the PVA, that obstructs the substrate from reaching the active sites on the metal nanoparticles.

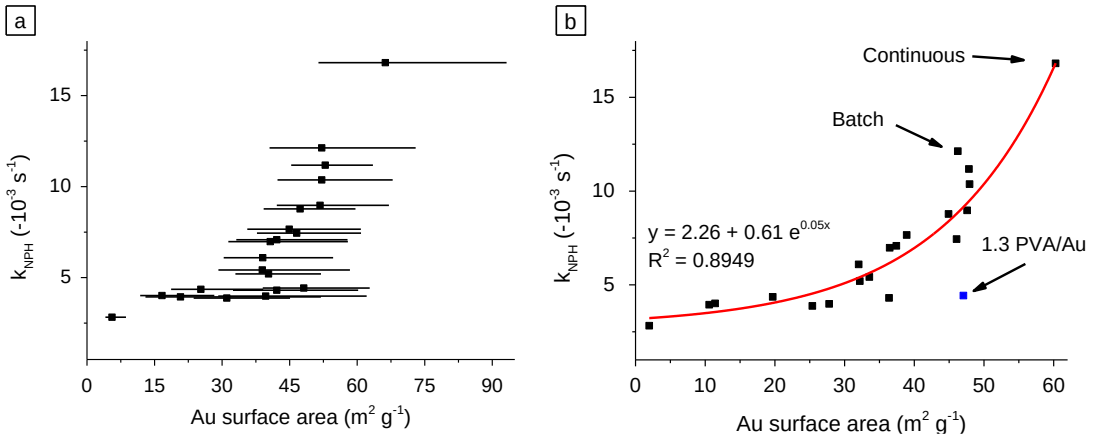

Figure 4.10: Activity versus metal surface area a) S_A and b) S_R normalised to the unit mass of the system for the various catalysts synthesised. The red line represents the exponential trend that best fits the data (excluding the blue square); equation and coefficient of determination (R^2) are also reported.

4.3.2. Low-coordination atoms versus catalytic activity

It is clear from these results that the active sites for the 4-NPH reduction on supported Au nanoparticles are not all the atoms present on the particle surface. It is well known that surface atoms are not all the same. In particular, the nanoparticle surface can present low-

coordination atoms such as adatoms, kink atoms, step atoms and surface atoms (Figure 4.11). It is however impossible to fully characterise and evaluate the relative amount of surface defects in a catalyst containing roughly 10^{15} – 10^{17} particles per gram. For this reason, simplifications need to be adopted.

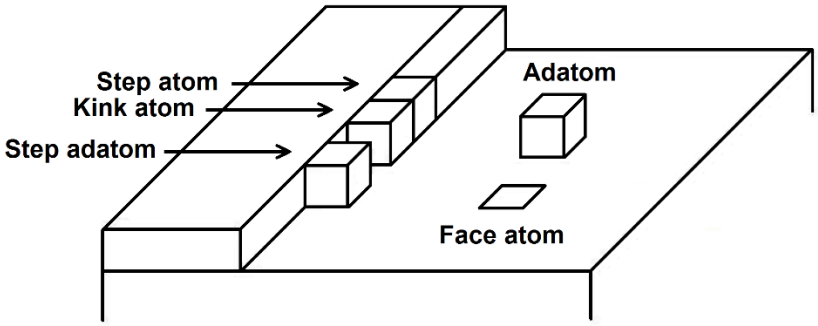

Figure 4.11: Schematic representation of surface features present on a nanoparticle surface.

A mathematical model was applied in order to calculate the percentage of atoms that lay at the faces, edges, vertices and surface of the Au nanoparticles within a specific size range; peripheral atoms (those Au surface atoms directly in contact with the support) were also calculated. The number of atoms contained in nanoparticles of a certain size, in fact, can be estimated from geometrical considerations. It has been shown that Au nanoparticles prepared by sol-immobilisation mostly assume icosahedral and cuboctahedral shapes, with minor portions of decahedral particles[44–48]. Previous studies showed that a hemi-spherical Mackay icosahedral model can well represent the geometry of Au nanoparticles generated during a sol-immobilisation synthetic procedure[44]. Therefore, for this work, such model was applied as well.[49]. In this model, all the nanoparticles were approximated to perfect hemi-icosahedron composed of "n" shells. The number of atoms in the particle (N_{TOT}) and at the surface (N_{SURF}) were calculated by the Equation 4.8 and 4.9.

$$N_{TOT} = \frac{5}{3}n^3 + \frac{5}{2}n^2 + \frac{11}{6}n \qquad Equation\ 4.8$$

$$N_{SURF} = 5n^2 + 1 \qquad Equation\ 4.9$$

It should be pointed out that, in the calculation of N_{TOT}, the real mathematical formula should include the addition of half atom corresponding on the atom at the very centre of the nanoparticle. For obvious reason, it has been decided to approximate the calculation not considering this "half atom" and therefore assuming there is a small void at the centre of the nanoparticles.

The surface atoms were then further divided in vertex atoms (N_{VERT}, 6 atoms independently by the particle dimension), edge atoms (N_{EDGE}), periphery atoms (N_{PERIPH}) and face atoms (N_{FACE}), and they were calculated by Equation 4.10, 4.11 and 4.12 respectively.

$$N_{EDGE} = 15(n-1) - 10 \qquad Equation\ 4.10$$

$$N_{PERIPH} = 5n \qquad Equation\ 4.11$$

$$N_{FACE} = N_{SURF} - N_{VERT} - N_{EDGE} - N_{PERIPH} \qquad Equation\ 4.12$$

The physical dimension of every shell (that represent the actual particle size) was calculated considering the most stable Au crystal structure and the relative lattice parameter. It is well known, in fact, that the crystal structure for Au at room temperature is face-centred cubic (FCC, Figure 4.12), with a lattice parameter (a) of 4.065 Å[50]. The minimal atomic distance (interatomic distance), however, does not correspond to the lattice parameter but to the distance between an atom at the vertex of the cube and an atom at the centre of the face of the cube. This distance can be easily calculated geometrically using the Pythagorean Theorem (Equation 4.13), resulting in an interatomic distance of ca. 2.874 Å.

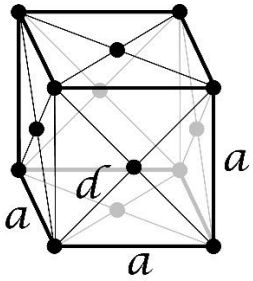

Figure 4.12: Face-centred cubic (FCC) structure of a Au crystal, where "a" is the lattice constant and "d" is the interatomic distance.

$$d = \frac{a}{\sqrt{2}} \qquad Equation\ 4.13$$

This distance is therefore the actual distance between nearby atoms in every shell of the hemi-spherical Mackay icosahedral model. The particle size can finally be calculated considering that an icosahedron is simply a platonic solid composed of 20 equilateral triangles, and therefore the particle's radius can be considered as the radius of the circle circumscribed onto a pentagon (Figure 4.13).

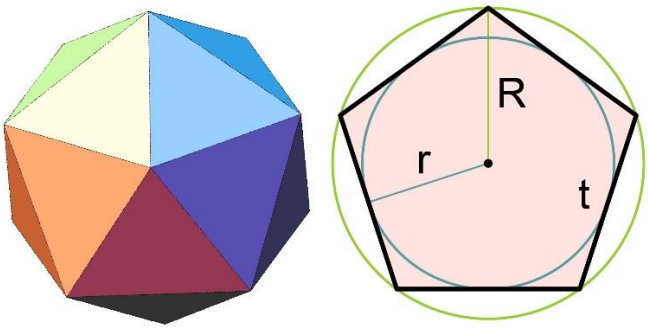

Figure 4.13: A nanoparticle's radius (R) can be represented as the radius of a circle circumscribed onto a pentagon, where "t" is the distance between two atoms at the vertices of an equilateral triangle that form the icosahedron.

The particle's radius (R) can therefore be easily calculated using the Equation 4.14:

$$t = R \times \sqrt{\frac{5-\sqrt{5}}{2}} \qquad Equation\ 4.14$$

That can be approximated in:

$$R = 0.850 \times t \qquad Equation\ 4.15$$

For the first shell, the parameter "t" is simply the interatomic distance (d), and therefore the particle's diameter is ca. 4.89 Å, corresponding to 0.489 nm. The particle size was calculated for all the shells and an example of the model for the first 5 shells is reported in Table 4.11, along with the values of N_{TOT}, N_{SURF}, N_{EDGE}, N_{PERIPH} and N_{FACE}.

Table 4.11: Example of particle size, number of surface atoms, edge atoms, peripheral atoms and face atoms for the first 5 shells of the Mackay icosahedral model.

Shell	Particle size [nm]	N_{TOT}	N_{SURF}	N_{EDGE}	N_{PERIPH}	N_{FACE}
1	0.489	6	6	0	5	0
2	0.978	27	21	5	10	0
3	1.466	73	46	20	15	5
4	1.955	154	81	35	20	20
5	2.444	280	126	50	25	45

It should be pointed out, however, that the bond distances calculated in the Mackay icosahedral model are not the same as the atomic distances in a bulk FCC Au crystal, since it is not possible to perfectly fit a FCC packing into the icosahedral morphology. In reality, interatomic distances in the Mackay icosahedral model are longer due to lattice strain. The

difference in length, however, is very small and for this reason it has not been considered in this study.

From the N_i values, the surface fraction (X_{SURF}), edge fraction (X_{EDGE}), peripheral fraction (X_{PERIPH}) and face fraction were calculated simply dividing the number of atoms relative to the specific site by the number of atoms in the particle (Table 4.12). Equation 4.16 gives an example on how to calculate a generic X_i.

$$X_i = \frac{N_i}{N_{TOT}} \qquad Equation\ 4.16$$

Table 4.12: Example of surface fraction, edge fraction, peripheral fraction and face fraction for the first 5 shells of the Mackay icosahedral model.

Shell	X_{SURF}	X_{EDGE}	X_{PERIPH}	X_{FACE}
1	1	0.000	1.000	0.000
2	0.778	0.185	0.370	0.000
3	0.630	0.274	0.205	0.068
4	0.526	0.227	0.130	0.130
5	0.450	0.179	0.089	0.161

Figure 4.14 shows an example of hemi-icosahedral Au particle composed of 3 shells supported on TiO_2.

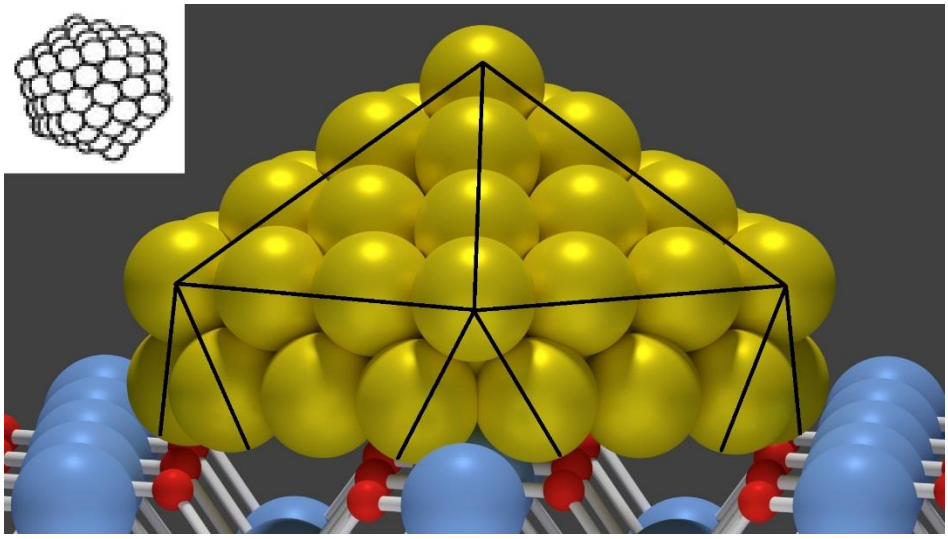

Figure 4.14: Schematic representation of a hemi-icosahedral Au nanoparticle composed of 3 shells and supported onto a TiO_2 surface. The black lines highlight the icosahedral edges.

The Mackay icosahedron chosen to best represent each binning interval was that which had the closest value to the median value of the binning interval. For example, a particle with a measured diameter of 2.5 nm (by STEM analysis) would be approximated to an icosahedron with 5 shells (Table 4.11). Clearly, using this binning approximation, an error is introduced. The difference between the real value of particle size measured by STEM and the shell size where the particle was allocated was calculated for each particle analysed (Δ_i) and the standard deviation was calculated as reported in Equation 4.17. This error (σ_x) is reported for each catalyst in Table 4.13.

$$\sigma_x = \sqrt{\frac{\sum_{i=1}^{N}(\Delta_i - \bar{\Delta})^2}{N-1}} \qquad Equation\ 4.17$$

Where $\bar{\Delta}$ is the average value of Δ_i and N is the number of particles counted.

Finally, in order to calculate the effective percentage of atoms at the surface ($\%_{SURF}$), at the edge ($\%_{EDGE}$), at the periphery ($\%_{PERIPH}$) and at the face ($\%_{FACE}$), the Equation 4.18 was applied.

$$\%_i = \sum \left(\frac{N_{TOT}\frac{Au_n}{\sum Au_n}}{\sum\left(N_{TOT}\frac{Au_n}{\sum Au_n}\right)} X_i \times 100 \right) \times wt\% \qquad Equation\ 4.18$$

Where Au_n is the number of Au particles with dimension approximated to the icosahedron with "n" shells, wt% is the experimental catalyst metal loading and the subscript "i" indicates one of the possible parameters to calculate (surface, edge, periphery and face). In other words, the result of Equation 4.18 can be imagined as a percentage of the total number of atoms at the surface, edge, periphery or face of the nanoparticles in respect to the total number of atoms present in the system. Also in this case, as for the calculation of the surface area S_R, no error bar is needed, since the resulting value is not an average value of the system. The $\%_i$ values were calculated for all the catalysts in Table 4.10 and are reported in Table 4.13.

Table 4.13: $\%_i$ values calculated for all the catalysts studied.

Catalyst	**$\%_{SURF}$ [%]**	**$\%_{EDGE}$ [%]**	**$\%_{PERIPH}$ [%]**	**$\%_{FACE}$ [%]**	Error [nm]
BATCH	18.9	3.9	1.5	13.3	0.143
SC01	4.7	0.3	0.1	4.3	0.132
SC02	16.7	3.1	1.2	12.3	0.139
SC03	18.1	3.6	1.4	13.0	0.146
SC04	2.0	0.1	0.0	1.9	0.136
SC05	11.4	1.5	0.6	9.2	0.143
SC06	8.8	0.9	0.3	7.5	0.144
SC07	13.2	2.1	0.8	10.2	0.148
SC08	15.1	2.5	1.0	11.5	0.141
SC09	19.6	4.1	1.6	13.8	0.142
SC10	5.4	0.4	0.2	4.9	0.137
SC11	15.5	2.8	1.1	11.5	0.144
SC12	14.3	2.4	0.9	10.9	0.136
SC13	20.8	4.6	1.8	14.1	0.143
SC14	19.5	4.1	1.6	13.6	0.142
SC15	15.8	2.7	1.0	12.0	0.140
SC16	14.7	2.4	0.9	11.4	0.145
SC17	17.8	3.4	1.3	13.1	0.139
SC18	17.9	3.5	1.3	13.0	0.149
SC19	13.9	2.2	0.8	10.8	0.140
CONT	22.6	5.5	2.3	14.6	0.138

As expecting, plotting the $\%_{SURF}$ values against the catalyst activity in terms of k_{NPH} (Figure 4.15), the resulting trend is very similar to the one obtained approximating the nanoparticles to perfect spheres (Figure 4.10b). This confirms the validity of the approximation adopted by Lu and colleagues[41–43]. Also in this case, the data referred to the catalyst produced with high amount of stabilising agent is off the trend (blue square). A similar behaviour was observed plotting $\%_{FACE}$ versus k_{NPH} (Figure 4.16), suggesting that the reaction does not take place on the Au face atoms either. If that was the case, in fact, increasing the number of face atoms the reaction activity should have increased linearly.

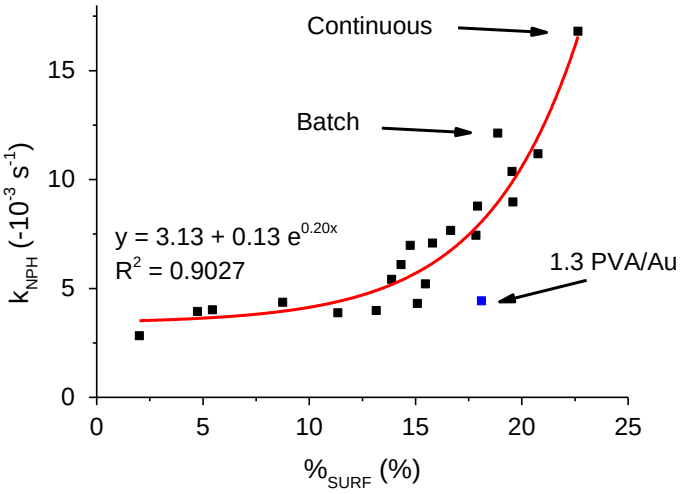

Figure 4.15: Activity versus percentage of Au surface atoms in the system for the various catalysts synthesised. Highlighted the continuous catalyst, the batch catalyst and the catalyst prepared with high stabiliser agent concentration. The red line represents the exponential trend that best fits the data (excluding the blue square); equation and coefficient of determination (R^2) are also reported.

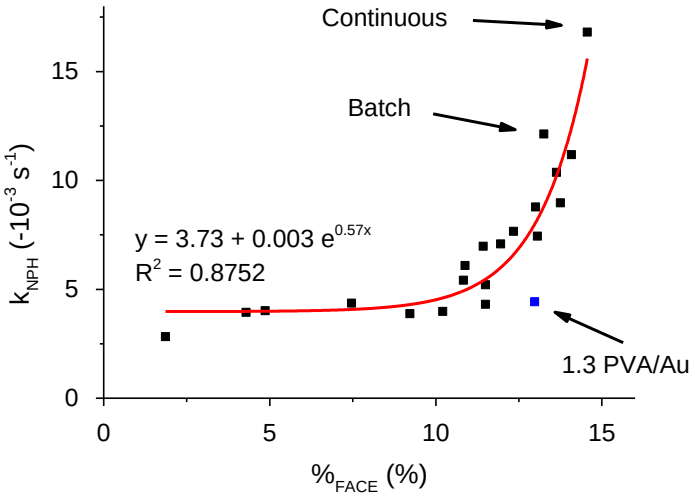

Figure 4.16: Activity versus percentage of Au face atoms in the system for the various catalysts synthesised. Highlighted the continuous catalyst, the batch catalyst and the catalyst prepared with high stabiliser agent concentration. The red line represents the exponential trend that best fits the data (excluding the blue square); equation and coefficient of determination (R^2) are also reported.

All these results suggest that the activity could be associated to low coordination Au atoms, such as edges, vertices or even peripheral atoms[51]. A linear trend should therefore be observed plotting $\%_{EDGE}$ and $\%_{PERIPH}$ against k_{NPH}. Also in this case, however, an exponential trend was observed (Figure 4.17 and 4.18), although much less pronounced than what obtained plotting $\%_{SURF}$ and $\%_{FACE}$ against k_{NPH}. Considering that several studies reported activity of unsupported Au nanoparticles in the catalytic reduction of 4-NPH, it can be safely

assumed that edges atoms are involved in the reaction[27–29]. Regarding peripheral atoms, it is hard to tell whether they actually take part in the reaction or not due to the impossibility to fully isolate the specific sites.

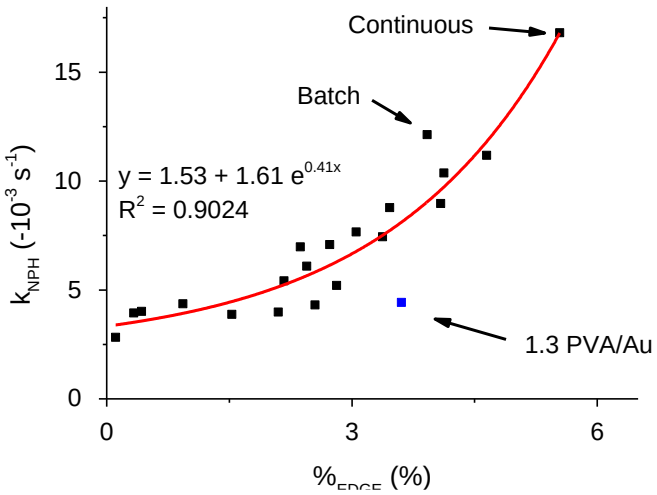

Figure 4.17: Activity versus percentage of Au edge atoms in the system for the various catalysts synthesised. Highlighted the continuous catalyst, the batch catalyst and the catalyst prepared with high stabiliser agent concentration. The red line represents the exponential trend that best fits the data (excluding the blue square); equation and coefficient of determination (R^2) are also reported.

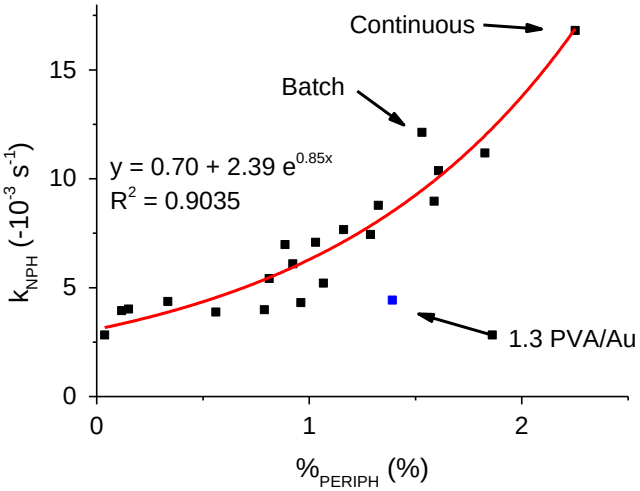

Figure 4.18: Activity versus percentage of Au peripheral atoms in the system for the various catalysts synthesised. Highlighted the continuous catalyst, the batch catalyst and the catalyst prepared with high stabiliser agent concentration. The red line represents the exponential trend that best fits the data (excluding the blue square); equation and coefficient of determination (R^2) are also reported.

By considering all the low-coordination sites (vertices and edges) and the peripheral atoms, it is possible to calculate the percentage of these sites in respect to the total number of atoms present in the system ($\%_{V\_E\_P}$) using Equation 4.18, with $N_{V\_E\_P}$ and $X_{V\_E\_P}$ calculated using Equation 4.19 and 4.20 respectively.

$$N_{V\_E\_P} = N_{VERT} + N_{EDGE} + N_{PERIPH} \qquad Equation\ 4.19$$

$$X_{V\_E\_P} = \frac{N_{V\_E\_P}}{N_{TOT}} \qquad Equation\ 4.20$$

The resulting $\%_{V\_E\_P}$ versus k_{NPH} plot (Figure 4.19), as expected, showed a similar trend compared to Figure 4.17 and 4.18. These results, however, do not conclusively prove that low coordination atoms are the only active sites in the hydrogenation of 4-nitrophenol to 4-aminophenol, and more studies need to be performed in order to better investigate the correlation between activity and specific active sites.

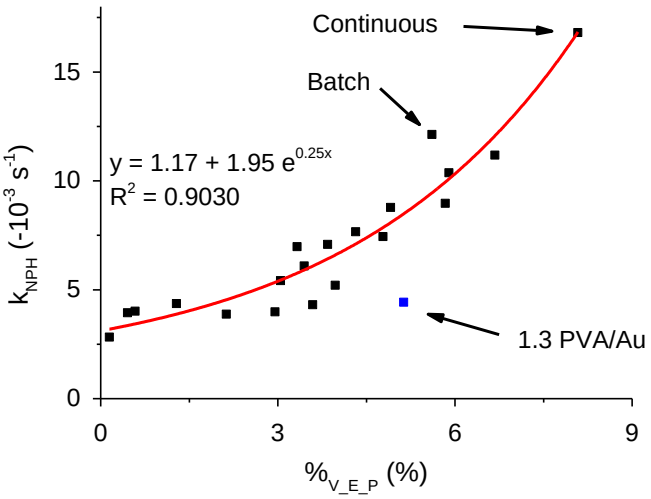

Figure 4.19: Activity versus percentage of Au atoms in vertex, edge and peripheral positions in the system for the various catalysts synthesised. Highlighted the continuous catalyst, the batch catalyst and the catalyst prepared with high stabiliser agent concentration. The red line represents the exponential trend that best fits the data (excluding the blue square); equation and coefficient of determination (R^2) are also reported.

In a similar way, the $\%_i$ values were compared to the reaction constant relative to the conversion to the quasi-stable intermediate 4-HPH (k_{HPH}). In all the cases the trends were similar to those obtained using k_{NPH} as kinetic parameter; in particular, a marked exponential correlation was observed when $\%_{SURF}$ and $\%_{FACE}$ were used (Figure 4.20), while a less pronounced exponential correlation was observed when $\%_{EDGE}$, $\%_{PERIPH}$ and $\%_{V\_E\_P}$ were used (Figure 4.21). In this last case, in particular, the coefficient of determination for a linear trend and for an exponential trend are very similar. The high uncertainty caused by the small

number of points available for the calculation of the reaction constant (Figure 4.4), however, makes the comparison challenging (as can be seen by the low coefficients of determination) and the only claim that can be safely extract from these trends is that similar active sites are involved for both 4-NPH and 4-HPH conversion.

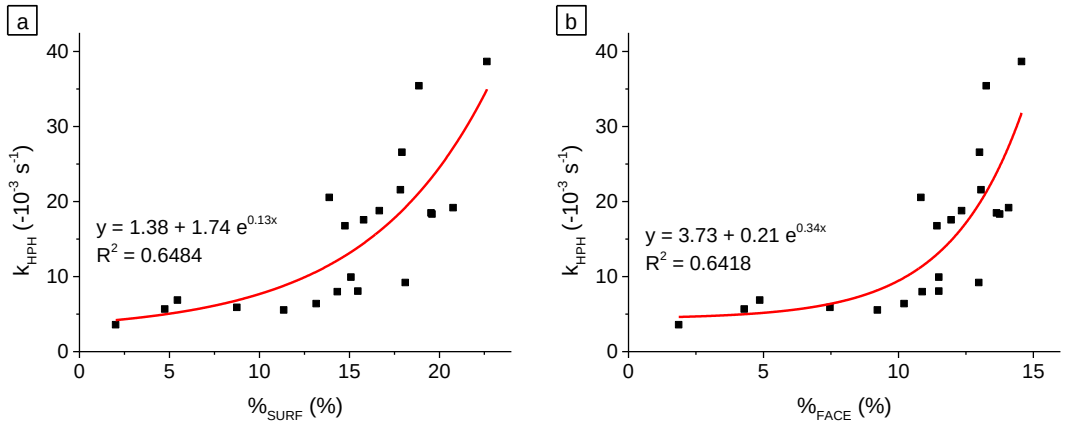

Figure 4.20: Activity versus percentage of Au a) surface atoms and b) face atoms in the system for the various catalysts synthesised. The red line represents the exponential trend that best fits the data; equation and coefficient of determination (R^2) are also reported.

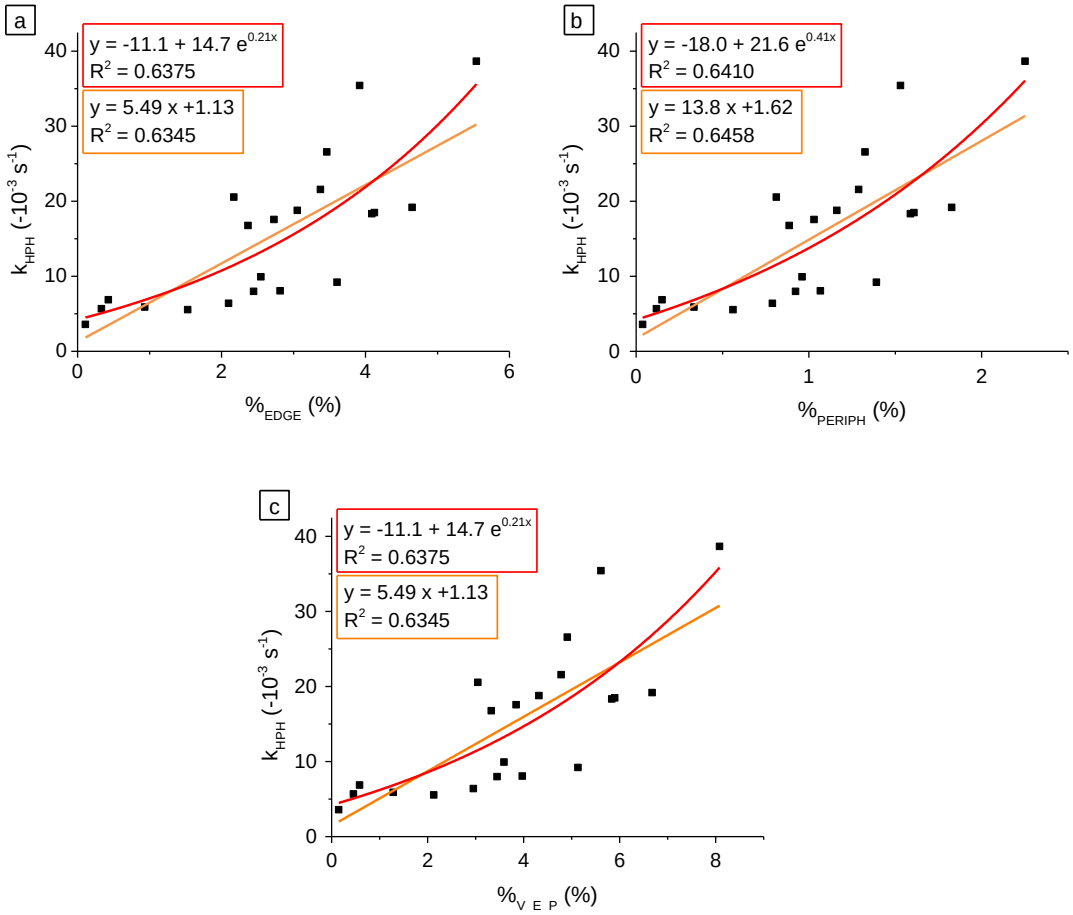

Figure 4.21: Activity versus percentage of Au a) edge atoms, b) peripheral atoms and c) sum of vertex, edge and peripheral atoms in the system for the various catalysts synthesised. The red and orange lines represent the exponential and linear trend respectively that best fit the data; equations and coefficients of determination (R^2) are also reported.

4.4. Conclusions

In this Chapter, the relation between metal particle size and catalytic activity was deeply investigated using the reduction of nitrophenol to aminophenol as model reaction. The reaction was performed in aqueous medium using sodium borohydride as reducing agent and followed by UV-Vis spectroscopy. 4-nitrophenol (4-NPH) was chosen among the nitrophenol isomers due to the problematic calculation of both k_{HPH} and k_{NPH} caused by the vigorous bubbling when 2-nitrophenol and 3-nitrophenol were used. Moreover, Au was chosen as active metal due to several reasons, such as a better stability against metal leaching, an easier calculation of the reaction constants due to less bubble formation and an easier nanoparticle characterisation due to the presence of plasmon resonance.

Several Au/TiO_2 catalysts were prepared with different particle size, ranging from 4 nm up to ca. 30 nm. The activity of all the catalysts was evaluated in terms of k_{HPH} and k_{NPH}, respectively the reaction constant for the conversion of 4-NPH into 4-HPH (4-hydroxylaminophenol) and for the conversion of 4-HPH into 4-APH. The catalytic activity in terms of k_{NPH} was initially correlated to the total metal surface area, and an exponential trend was observed. This result was in apparent contradiction to what previously reported by other authors, where a linear correlation was found and therefore the catalytic activity was attributed in general to surface Au atoms[41–43].

A mathematical model was then applied to the synthesised catalysts in order to calculate the amount of different low-coordination atoms relative to the total amount of Au atoms in the system. The model consisted of simplifying all of the Au nanoparticles to hemi-icosahedra in direct contact with the support. Purely from geometrical considerations, the number of Au atoms in vertex, edge, periphery and face positions were calculated; in all the cases, an exponential correlation was found between specific Au atom sites and catalytic activity in terms of k_{NPH}, in contrast to what previously reported in literature. A similar trend was also observed when correlating the same Au sites to the activity in terms of k_{HPH}, suggesting that similar active sites are involved for both 4-NPH and 4-HPH conversion. The exact identification of the active site, however, was not possible and more studies need to be performed in order to better investigate the correlation between activity and specific active sites.

4.5. References

1 K. Ju and R. E. Parales, *Microbiol. Mol. Biol. Rev.*, 2010, **74**, 250–272.

2 G. Sunahara, G. Lotufo, R. Kuperman and J. Hawari, *Ecotoxicology of Explosives*, 2009.

3 P.-G. Rieger and H.-J. Knackmuss, ed. J. C. Spain, Springer US, Boston, MA, 1995, pp. 1–18.

4 V. Purohit and A. K. Basu, *Chem. Res. Toxicol.*, 2000, **13**, 673–692.

5 United States Environmental Protection Agency, *Priority Pollutant List*, 2014.

6 D. Lague, *China blames oil company for benzene spill in river, New York Times*, 2005.

7 S. C. Mitchell and R. H. Waring, *Ullmann's Encycl. Ind. Chem.*, 2005, 1–20.

8 P. F. Vogt and J. J. Gerulis, *Ullmann's Encycl. Ind. Chem.*, 2005, 1–21.

9 T. Aditya, A. Pal and T. Pal, *Chem. Commun.*, 2015, **51**, 9410–9431.

10 P. Zhao, X. Feng, D. Huang, G. Yang and D. Astruc, *Coord. Chem. Rev.*, 2015, **287**, 114–136.

11 S. Wunder, F. Polzer, Y. Lu, Y. Mei and M. Ballauff, *J. Phys. Chem. C*, 2010, **114**, 8814–8820.

12 J. Harris and B. Kasemo, *Surf. Sci.*, 1981, **105**, L281–L287.

13 I. Langmuir, *Trans. Faraday Soc.*, 1922, **17**, 621–654.

14 C. N. Hinshelwood, *Annu. Reports Prog. Chem.*, 1930, **27**, 11–51.

15 H. U. Blaser, *Science*, 2006, **313**, 312–313.

16 P. Hervés, M. Pérez-Lorenzo, L. M. Liz-Marzán, J. Dzubiella, Y. Lu and M. Ballauff, *Chem. Soc. Rev.*, 2012, **41**, 5577–5587.

17 S. Wunder, Y. Lu, M. Albrecht and M. Ballauff, *ACS Catal.*, 2011, **1**, 908–916.

18 X. Kong, H. Zhu, C. Le Chen, G. Huang and Q. Chen, *Chem. Phys. Lett.*, 2017, **684**, 148–152.

19 S. Sarkar, A. K. Sinha, M. Pradhan, M. Basu, Y. Negishi and T. Pal, *J. Phys. Chem. C*, 2011, **115**, 1659–1673.

20 J. Zeng, Q. Zhang, J. Chen and Y. Xia, *Nano Lett.*, 2010, **10**, 30–35.

21 P. Hervés, M. Pérez-Lorenzo, L. M. Liz-Marzán, J. Dzubiella, Y. Lu and M. Ballauff, *Chem. Soc. Rev.*, 2012, **41**, 5577–5587.

22 X. Zhou, W. Xu, G. Liu, D. Panda and P. Chen, *J. Am. Chem. Soc.*, 2010, **132**, 138–146.

23 Y. Wu, M. Wen, Q. Wu and H. Fang, *J. Phys. Chem. C*, 2014, **118**, 6307–6313.

24 S. K. Ghosh, M. Mandal, S. Kundu, S. Nath and T. Pal, *Appl. Catal. A Gen.*, 2004, **268**, 61–66.

25 Q. Wang, W. Jia, B. Liu, A. Dong, X. Gong, C. Li, P. Jing, Y. Li, G. Xu and J. Zhang, *J. Mater.*

Chem. A, 2013, **1**, 12732–12741.

26 P. Zhang, C. Shao, Z. Zhang, M. Zhang, J. Mu, Z. Guo and Y. Liu, *Nanoscale*, 2011, **3**, 3357–3363.

27 H. Yamamoto, H. Yano, H. Kouchi, Y. Obora, R. Arakawa and H. Kawasaki, *Nanoscale*, 2012, **4**, 4148–4154.

28 C. Xiao, S. Chen, L. Zhang, S. Zhou and W. Wu, *Chem. Commun.*, 2012, **48**, 11751–11753.

29 I. Biondi, G. Laurenczy and P. J. Dyson, *Inorg. Chem.*, 2011, **50**, 8038–8045.

30 J. Zeng, Q. Zhang, J. Chen and Y. Xia, *Nano Lett.*, 2010, **10**, 30–35.

31 S. Liu, X. L. Zhou, M. M. Zhang, X. Lu, Y. J. Qin, P. Zhang and Z. X. Guo, *Chinese Chem. Lett.*, 2016, **27**, 843–846.

32 A. A. Ismail, A. Hakki and D. W. Bahnemann, *J. Mol. Catal. A Chem.*, 2012, **358**, 145–151.

33 Y. C. Chang and D. H. Chen, *J. Hazard. Mater.*, 2009, **165**, 664–669.

34 J. A. Johnson, J. J. Makis, K. A. Marvin, S. E. Rodenbusch and K. J. Stevenson, *J. Phys. Chem. C*, 2013, **117**, 22644–22651.

35 X. Gu, W. Qi, X. Xu, Z. Sun, L. Zhang, W. Liu, X. Pan and D. Su, *Nanoscale*, 2014, **6**, 6609–6616.

36 S. Tang, S. Vongehr, G. He, L. Chen and X. Meng, *J. Colloid Interface Sci.*, 2012, **375**, 125–133.

37 J. Kaiser, L. Leppert, H. Welz, F. Polzer, S. Wunder, N. Wanderka, M. Albrecht, T. Lunkenbein, J. Breu, S. Kümmel, Y. Lu and M. Ballauff, *Phys. Chem. Chem. Phys.*, 2012, **14**, 6487–6495.

38 J. Zhang, C. Hou, H. Huang, L. Zhang, Z. Jiang, G. Chen, Y. Jia, Q. Kuang, Z. Xie and L. Zheng, *Small*, 2013, **9**, 538–544.

39 S. Gu, S. Wunder, Y. Lu, M. Ballauff, R. Fenger, K. Rademann, B. Jaquet and A. Zaccone, *J. Phys. Chem. C*, 2014, **118**, 18618–18625.

40 A. Corma and P. Serna, *Science*, 2006, **313**, 332–334.

41 Y. Lu, Y. Mei, M. Ballauff and M. Drechsler, *J. Phys. Chem. B*, 2006, **110**, 3930–3937.

42 Y. Mei, G. Sharma, Y. Lu, M. Ballauff, M. Drechsler, T. Irrgang and R. Kempe, *Langmuir*, 2005, **21**, 12229–12234.

43 Y. Lu, Y. Mei, R. Walker, M. Ballauff and M. Drechsler, *Polymer*, 2006, **47**, 4985–4995.

44 Q. He, S. J. Freakley, J. K. Edwards, A. F. Carley, A. Y. Borisevich, Y. Mineo, M. Haruta, G. J. Hutchings and C. J. Kiely, *Nat. Commun.*, 2016, **7**, 12905, 1–8.

45 M. Brust, M. Walker, D. Bethell, D. J. Schiffrin and R. Whyman, 2000, 801–802.

46 A. Villa, N. Dimitratos, C. E. Chan-Thaw, C. Hammond, L. Prati and G. J. Hutchings, *Acc. Chem. Res.*, 2015, **48**, 1403–1412.

47 A. Villa, N. Dimitratos, C. E. Chan-Thaw, C. Hammond, G. M. Veith, D. Wang, M. Manzoli, L. Prati and G. J. Hutchings, *Chem. Soc. Rev.*, 2016, **45**, 4953–4994.

48 M. Sankar, N. Dimitratos, P. J. Miedziak, P. P. Wells, C. J. Kiely and G. J. Hutchings, *Chem. Soc. Rev.*, 2012, **41**, 8099–8139.

49 A. L. Mackay, *Acta Crystallogr.*, 1962, **15**, 916–918.

50 W. P. Davey, *Phys. Rev.*, 1925, **25**, 753–761.

51 R. A. Van Santen, *Acc. Chem. Res.*, 2009, **42**, 57–66.

Chapter 5

Selective catalytic hydrogenation of cinnamaldehyde

5.1. Introduction

5.1.1. Cinnamaldehyde hydrogenation background

α,β-unsaturated aldehydes are important molecules in the industrial synthesis of pharmaceuticals, fragrances and fine chemicals[1–4]. With an estimated production of 1.5 kton/year *via* the base-catalysed condensation of benzaldehyde and acetaldehyde[5], cinnamaldehyde (CAL) is one of the most significant fragrance aldehydes; in addition to its use in perfumery, it is also used as a polymerisation and corrosion inhibitor and in metal coatings[6]. α,β-unsaturated aldehydes are stabilised through resonance structures due to the presence of a conjugated vinyl group (C=C) and carbonyl group (C=O); this results in a delocalisation of the partial positive charge on the carbonyl carbon (Figure 5.1).

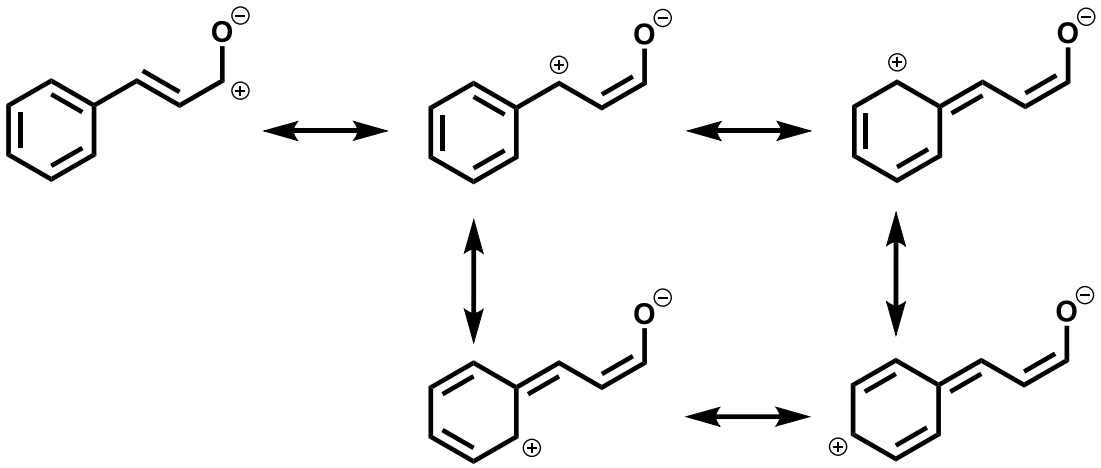

Figure 5.1: Charge delocalisation in the cinnamaldehyde molecule.

The hydrogenation of CAL follows different pathways depending on the reaction mechanism (Figure 5.2). There are three main reaction pathways, which depending on the adsorption mode and the hydrogenation position result in the final reaction product and determine reaction selectivity. 1,2-addition gives the unsaturated alcohol through hydrogenation of the carbonyl group, while both 3,4-addition and 1,4-addition give the saturated aldehyde, the former by hydrogenation of the vinyl group, and the latter through the formation of the enol followed by keto-enolic isomerisation. Both of these products are reported to be used as intermediates in HIV pharmaceuticals and perfumery products[5,7]. Side reactions can further complicate the reaction scheme. The most common is the over hydrogenation to hydrocinnamyl alcohol (HCOH) and the C-O hydrogenolysis to phenylpropane (PPR)[8]. All of these reactions are thermodynamically possible, however, the selective hydrogenation of the vinyl group is more favoured than the hydrogenation of the

carbonyl group by ca. 35 kJ/mol[3], and for this reason the selective synthesis of COH is more challenging.

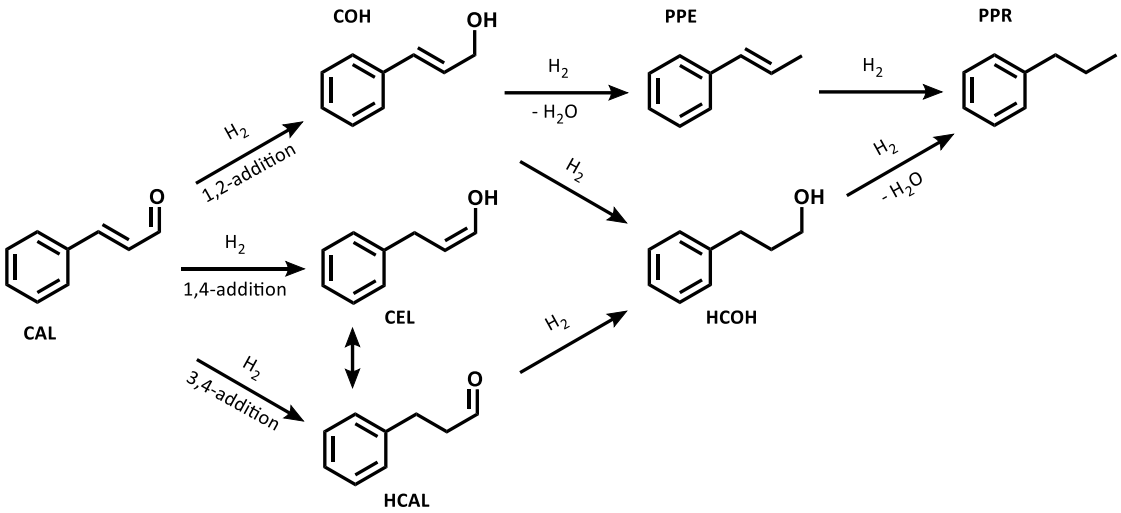

Figure 5.2: Cinnamaldehyde (CAL) hydrogenation reaction pathway. The possible products are cinnamyl alcohol (COH), cinnamenol (CEL), hydrocinnamaldehyde (HCAL), hydrocinnamyl alcohol (HCOH), phenylpropene (PPE) and phenylpropane (PPR).

Currently, several homogeneous and heterogeneous transition metal based catalysts have been reported in literature to be active in the selective hydrogenation of cinnamaldehyde[3,9]. The reaction takes place on the metal surface via a Horiuti-Polanyi mechanism[4]; this mechanism was first predicted by Juro Horiuti and Michael Polanyi in 1934 for ethane hydrogenation and it is nowadays still used to explain various hydrogenation reactions[10]. It consists of a 3-step process, schematically depicted in Figure 5.3[11]. In the first step, the substrate binds to the metal surface by a combination of π-electron donation to a single metal atom (π η^2) and σ-bonding to two adjacent metal atoms (di-σ η^2). This interaction, in the case of α,β-unsaturated aldehydes, can either be a single di-$\sigma_{C=O}$ η^2 plus a $\pi_{C=O}$ η^2 (interaction metal/carbonyl), a single di-$\sigma_{C=C}$ η^2 plus a $\pi_{C=C}$ η^2 (interaction metal/vinyl), or a combination of both di-$\sigma_{C=O}$ and di-$\sigma_{C=C}$ plus a di-$\pi_{C=O,C=C}$ η^2 (η^4, interaction metal/conjugated system in a planar fashion). In the second step, a hydrogen atom previously adsorbed dissociatively on the metal surface forms a σ-bond with a carbon atom; this step is reversible. Finally, the metal-substrate intermediate undergoes irreversible reductive elimination with a second hydrogen atom, to form the hydrogenated product. This third step is usually the rate-determining step. The nature of the metal and the type of face exposed strongly affect the adsorption mode of the substrate and thus the activity and selectivity of the reaction.

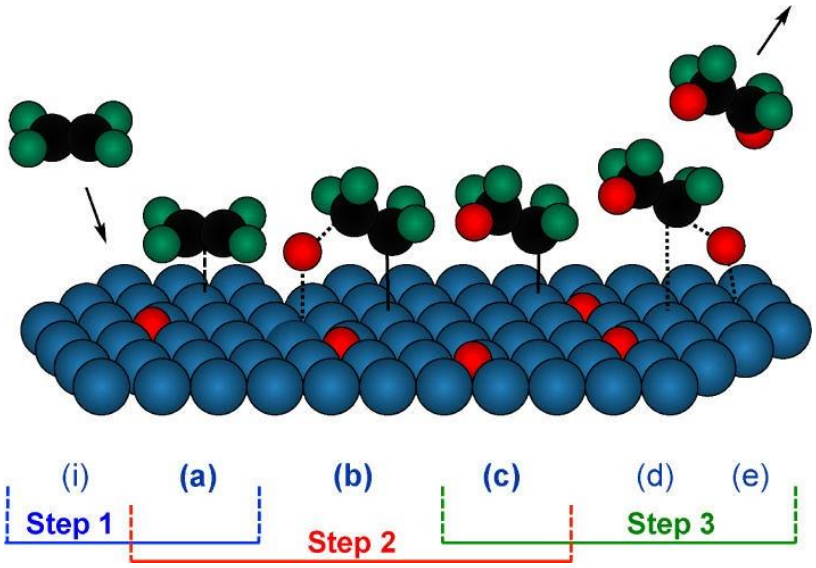

Figure 5.3: Hydrogenation of ethene by Horiuti-Polanyi mechanism. Substrate adsorption (Step 1), addition of a first hydrogen atom (Step 2) and addition of the second atom of hydrogen and consequent product desorption (Step 3). Image reprinted with permission from B. Mattson et al., J. Chem. Educ., 2013, 613-619.

Several factors can influence the selectivity and activity of the α,β-unsaturated aldehydes hydrogenation reaction[3,12,13], and in particular:

- Nature of the metal
- Electronic and steric influence of the support
- Metal-support interactions
- Metal particle size and morphology
- Selective poisoning
- Influence of a second metal
- Steric effect of substituents at the C=C double bond
- Reaction parameters

It is widely accepted that the selectivity in the hydrogenation of α,β-unsaturated aldehydes strongly depends on the competitive adsorption of the vinyl and carbonyl group on the metal surface[1,13]. Theoretical studies, for example, showed that a di-$\sigma_{C=O}$ adsorption modes is favoured on Pt(111) plane, a planar η^4 is favoured on Pd(111) and Pt(100) faces and a $\pi_{C=C}$ or planar η^4 modes are favoured on Pt(110) and on the steps of Pt(111)[14]. The selectivity is therefore affected by the relative binding energy between the C=O and C=C bonds and the metal surface. In the case of CAL, the presence of a bulky and electron rich substituent on the C=C bond (the benzene ring), strongly affects the C=C adsorption mode[15,16]. CAL, in fact, cannot adsorb with a parallel η^4 mode on the metal surface because of the steric repulsion of the aromatic ring. Theoretical calculations proved that due to this repulsion, the aromatic

ring cannot get closer than 0.3 nm to the metal surface, thus making the approach of the vinyl group to the metal surface more difficult compared to the carbonyl group[17]. For this reason, the selectivity can be affected by the particle size; large nanoparticles present flat surfaces that reduce the adsorption of the C=C bond, while small nanoparticles show a much smaller steric effect, as depicted in Figure 5.4.

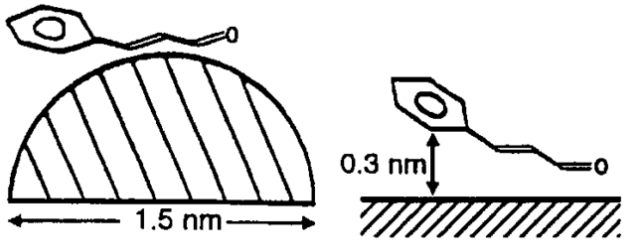

Figure 5.4: Cinnamaldehyde interaction with small pseudo-spherical (left) and large flat (right) metallic nanoparticles. Image reprinted with permission from P. Gallezot et al., Catal. Lett., 1990, 175-181.

Moreover, it has been demonstrated from both a theoretical and experimental point of view, that the selectivity can be tuned by choosing the metal according to its d-orbital bandwidth[3,14,18,19]. The larger the band, in fact, the stronger the repulsion with the four electrons of the C=C double bond and the lower is the adsorption energy of the vinyl group onto the metal surface. For this reason, metals with a large d-bandwidth such as osmium and iridium show a high selectivity towards the hydrogenation of the carbonyl bond, while metals with a small d-band such as rhodium, palladium, nickel and copper show a high selectivity towards the hydrogenation of the vinyl bond[1].

Several other experimental reaction parameters have been reported to strongly influence activity and selectivity of the CAL hydrogenation, such as reaction temperature, hydrogen pressure, solvent, nature of the support and addition of a second metal[12,19].

5.1.2. Palladium and gold catalysis in the cinnamaldehyde hydrogenation

Palladium is well known to be a metal that shows high selectivity to C=C double bond hydrogenation[20]. The reason for this high selectivity is the small d bandwidth of Pd, that affects the adsorption mode of the substrate. Pd, in fact, preferentially adsorbs conjugated systems in a planar η^4 way, with the carbon and oxygen atoms involved in σ-bonds with four different metal atoms[14]. For thermodynamic reasons, the vinyl bond is therefore hydrogenated faster than the carbonyl bond, resulting in a higher formation of HCAL compared to COH. Pd nanoparticles have been supported on several systems such as

carbonaceous materials (charcoal, nanofibers and nanotubes)[21–23], metal oxides (silica, alumina, ceria, titania and iron oxide)[24–26] and even polymers[27] as catalysts for the hydrogenation of cinnamaldehyde. In all the cases, the primary product was HCAL (Table 5.1). Ledoux and co-workers compared the performance of Pd nanoparticles supported on charcoal and carbon nanofibers, ascribing the better selectivity towards HCAL of the nanofibers (98 % versus 60 % at complete CAL conversion) to the high external surface area and the absence of any microporosity that can cause mass transfer limitations[21]. Multi-walled carbon nanotubes were tested by Liu *et al.* in CO_2-expanded liquids (a mixed solvent system composed of CO_2 gas dissolved in other organic solvents), reporting a selectivity to HCAL of 91 % at 100 % conversion[28]. After a metal loss of ca. 10 % after the first run, the catalyst was completely reusable up to 9 times. Metal oxides can also be used as support for Pd nanoparticles. Liu and co-workers compared a series of metal oxides (γ-Al_2O_3, SiO_2 and TiO_2) with carbonaceous support (activated carbon and graphene oxide), reporting higher conversion and selectivity to HCAL when γ-Al_2O_3 was used (92 % of selectivity at 100 % conversion)[26]; high amounts of HCOH, however, was reported when TiO_2 was used (27 % at 62 % conversion). Interestingly, the selectivity to HCAL was only 65 % when a commercial Pd/Al_2O_3 catalyst was used in ethanol as solvent and 40 bar of H_2[25]. The authors managed to improve the selectivity up to 88 % applying organic thiol coatings to the catalyst surface.

Table 5.1: Pd based catalysts used in the CAL hydrogenation reaction.

Catalyst	Solvent	Time [h]	P_{H_2} [bar]	T [°C]	Conv. [%]	Sel.[a] [%]	Ref.
5 wt% Pd/CNFs	1,4-Dioxane	30	1	80	100	98	21
5 wt% Pd/C	1,4-Dioxane	50	1	80	100	60	21
5 wt% Pd/MWCNT	TFEOH/CO_2	2	40	60	100	91	28
0.5 wt% Pd/γ-Al_2O_3	p-Xylene	6	20	80	100	92	26
0.5 wt% Pd/SiO_2	p-Xylene	6	20	80	100	82	26
0.5 wt% Pd/SiC	p-Xylene	6	20	80	35	84	26
0.5 wt% Pd/AC	p-Xylene	6	20	80	32	87	26
0.5 wt% Pd/TiO_2	p-Xylene	6	20	80	62	73	26
0.5 wt% Pd/GO	p-Xylene	6	20	80	64	80	26
Pd NPs	p-Xylene	6	20	80	64	86	26
5 wt% Pd/Al_2O_3	Ethanol	1	40	50	100	65	25
5 wt% Pd/Al_2O_3 (thiol coated)	Ethanol	1	40	50	100	88	25

[a] *Selectivity to HCAL.*

Transition metals of the group 8, 9 and 10 are generally considered to be active in hydrogenation reactions and in catalysis in general[3]. The reason is that they have partially filled d-orbitals, and so they can easily adsorb organic molecules. Moreover, the catalytic activity of a metal in hydrogenation reactions is determined by its ability to absorb and dissociate H_2[29]. In this regard, Au was for long thought to be not active, having a completely filled d-orbital ($5d^{10}$) and being unable to activate/dissociate H_2 on the surface. Despite this, Au proved to be moderately active in several hydrogenation reactions when finely dispersed (generally < 10 nm), including the hydrogenation of α,β-unsaturated aldehydes (Table 5.2)[30–34]. The reason for the activity was attributed to several factors, such as quantum-size effects, development of charge on nanoparticles, presence of defects (low coordination atoms), large surface area and largely available oxygen free surface[35]. In the selective CAL hydrogenation, Au usually requires harsh reaction conditions to obtain good conversion and it commonly hydrogenates only the carbonyl group leading to the formation of COH. Bus *et al.*, reported for example the conversion of CAL with Au/γ-Al_2O_3 to COH with a selectivity up to 89 % at 85 bar of H_2 and 100 °C[8]. In their studies, high selectivity to COH were produced from the initial stages of the reaction, and the selectivity remained unaltered up to 94 % of conversion, after which all the COH further convert into HCOH. Similar results were obtained by other research groups with different supports such as CeO_2[36], SiO_2[37] and α-Fe_2O_3[38], while CNT and Zr_2O_3 promoted the hydrogenation of the vinyl group[32,37]. Interestingly, Milone and co-workers, found high activity towards cinnamyl ethyl ethers when Au was supported onto TiO_2 and used in alcohol solvents[39].

Table 5.2: Au based catalysts used in the CAL hydrogenation reaction.

Catalyst	Solvent	Time [h]	P_{H_2} [bar]	T [°C]	Conv. [%]	Sel.[a] [%]	Ref.
0.5 wt% Au/γ-Al_2O_3	Ethanol	3	85	100	94	89	[8]
3 mol% Au/CeO_2	Water	14	1	80	n.a.	84[b]	[36]
1 wt% Au/SiO_2	Toluene	3	10	180	98	96[c]	[37]
3.5 wt% Au/FeOOH	Ethanol	n.a.	1	70	50	91	[38]
1.6 wt% Au/CNTs	Toluene	2	8	90	95	91[c]	[32]
1.5 wt% Au/TiO_2	Ethanol	n.a.	1	70	50	47	[39]
1.5 wt% Au/TiO_2 (heat treated)	Ethanol	n.a.	1	70	50	33[d]	[39]

[a]Selectivity to COH, [b] yield to COH, [c] selectivity to HCAL, [d] selectivity to ethers.

A plethora of studies using both Au and Pd on different supports, solvents and hydrogen sources have been reported in literature. However, very few articles have been focused the attention on the catalytic performance of AuPd bimetallic catalysts. Dash *et al.*, reported equimolar production of HCAL and HCOH using bimetallic nanoparticles stabilised in imidazolium ionic liquids when the Au/Pd molar ratio was 3:1 and 1:3, while over-hydrogenation to HCOH was observed when the two metals were present in the same molar amount[40]. Similar results were obtained by Szumelda and co-workers using AuPd/C catalysts prepared by reverse water-in-oil microemulsion method[41]. On the other hand, Parvulescu *et al.* observed an increase in COH production using AuPd colloids embedded in SiO_2[42], although little importance was given to the alloy composition and the reaction optimisation, since their report was more focused on general hydrogenation reactions. Very high selectivity towards HCAL was obtained by Yang *et al*. with bimetallic nanoparticles supported on mesoporous SiO_2[43]. A different approach to obtain HCAL in high selectivity was studied by Gu and co-workers[44]: separate deposition of Au and Pd nanoparticles was achieved onto ordered mesoporous carbon, and the authors ascribed the superior activity to the better H_2 dissociation properties of the Pd nanoparticles, while Au nanoparticles suppressed the deep hydrogenation process acting as hydrogen acceptors and diluting the Pd active sites. Severe sintering and aggregation phenomena were however observed during the heat treatments these catalysts undergone (NPs size varied from 2.3 ± 0.5 to 15 ± 5 nm), thus making difficult any comparison in term of activity.

Table 5.3: Bimetallic AuPd based catalysts used in the CAL hydrogenation reaction

Catalyst	Solvent	Time [h]	P_{H_2} [bar]	T [°C]	Conv. [%]	Sel.[a] [%]	Ref.
$1{:}3_{mol}$ AuPd	BMIM	1	1	40	n.a.	50	[40]
$1{:}1_{mol}$ AuPd	BMIM	1	1	40	n.a.	38	[40]
3.5 wt% $70{:}30_{mol}$ AuPd/C	Toluene	1	1	22	100	55	[41]
5 wt% $44{:}56_{mol}$ AuPd/C	Toluene	1.4	1	22	80	38	[41]
1 wt% $1{:}1_{mol}$ $AuPd/SiO_2$	i-Propanol	n.a.	20	80	n.a.	55	[42]
2.7 wt% $1{:}5_{mol}$ $AuPd/SiO_2$	Hexane	1	5	50	98	85	[43]
0.45 wt% $1{:}2_{mol}$ Au+Pd/C	i-Propanol	11	1	40	97	88	[44]

[a] *Selectivity to HCAL.*

5.1.3. Aims and objectives of the chapter

The aim of this chapter is to study in detail the AuPd alloy system in the cinnamaldehyde hydrogenation reaction. In order to do that, several parameters were considered, such as stirring speed, catalyst amount, hydrogen pressure and reaction temperature. Different relative concentrations of Au and Pd were then used to evaluate the importance of both metals in the overall performance of the catalyst. Moreover, several solvents and supports were also used to assess their effect on activity and selectivity. Finally, the AuPd benchmark catalyst was heat treated at various temperature to induce strong metal-support interactions and compared to the untreated one was shown to be stable to multiple reaction cycles. All the catalysts were opportunely characterised by means of UV-VIS, DLS, MP-AES, HRTEM, XPS, XRD, DRIFT and FTIR.

5.2. Catalysts characterisation

As previously mentioned, limited reports are present in literature regarding the hydrogenation of cinnamaldehyde using bimetallic AuPd based catalysts. Moreover, most of them make use of either carbon-based or silica-based materials as support. In our study we decided to use a different support, titanium dioxide. TiO_2 proved to be an active and selective support in CAL hydrogenation reactions when either Au or Pd nanoparticles where immobilised[26,39]. In addition, TiO_2 based catalysts are usually relatively easy to characterise and show interesting behaviour when treated in a reductive atmosphere at high temperature (strong metal-support interaction effects)[26]. For this reason, 1wt% Au_xPd_y/TiO_2 catalyst with different Au:Pd molar ratios (namely Au/TiO_2, $Au_{95}Pd_5/TiO_2$, $Au_{65}Pd_{35}/TiO_2$, $Au_{50}Pd_{50}/TiO_2$, $Au_{35}Pd_{65}/TiO_2$ and Pd/TiO_2) were synthesised by sol-immobilisation, thoroughly characterised and tested in the CAL hydrogenation reaction. Other supports were also used, such as activated carbon (AC), iron oxide (Fe_2O_3) and magnesium oxide (MgO). In this case, the Au:Pd molar ratio was kept constant at 50 : 50.

5.2.1. MP-AES analysis

All the catalysts were initially analysed by MP-AES in order to quantify the actual amount of metal deposited on the support surface and the Au/Pd molar ratio. The results are reported on Table 5.4. Both metal loadings and Au/Pd ratios are in good agreement with the theoretical values. Only the $Au_{65}Pd_{35}/TiO_2$ and $Au_{35}Pd_{65}/TiO_2$ catalysts show a slightly low

concentration of Pd compared to the theoretical values, probably simply due to experimental errors or incomplete digestion. The possible presence of metal precursor not immobilised on the support was checked with UV-Vis analysis of the filtrate solution. No metal traces were detected in the waste-water of all the catalysts during preparation.

Table 5.4: MP-AES analysis on the TiO_s supported catalysts

Catalyst	Metal loading [wt%]	Au/Pd ratio [mol/mol]	
		Theoretical	Experimental
Au/TiO_2	0.94	100 : 0	100 : 0
$Au_{95}Pd_5/TiO_2$	1.00	95 : 5	96 : 4
$Au_{65}Pd_{35}/TiO_2$	0.92	65 : 35	68 : 32
$Au_{50}Pd_{50}/TiO_2$	1.00	50 : 50	47 : 53
$Au_{35}Pd_{65}/TiO_2$	0.96	35 : 65	39 : 61
Pd/TiO_2	0.98	0 : 100	0 : 100

5.2.2. UV-Vis analysis

The metal colloids were analysed by UV-Vis prior to deposition onto the support in order to determine the presence or absence, position and intensity of the surface plasmon peak of gold. In Figure 5.5 the UV-Vis spectra of the Au and $Au_{50}Pd_{50}$ colloids are reported. It is clear from the spectra that the presence of a broad and low intensity Au plasmonic peak in the monometallic sample at ca. 505 nm, corresponding to nanoparticles of 2 - 6 nm in dimension is present. The bimetallic sample has no peak associated with Au surface plasmon resonance, confirming the formation of alloy AuPd nanoparticles.

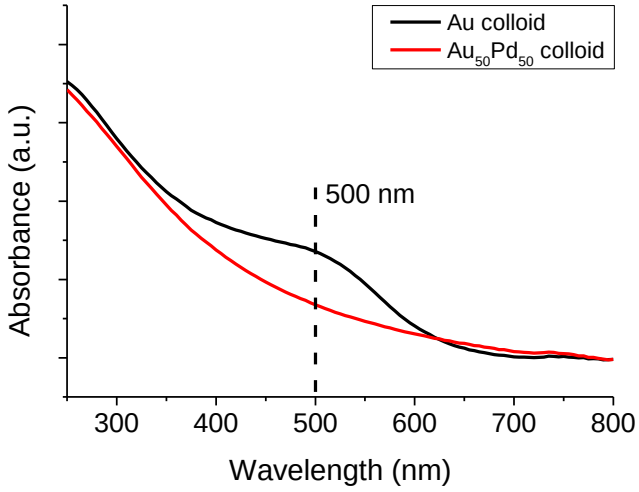

Figure 5.5: UV-Vis spectra of Au and $Au_{50}Pd_{50}$ colloids; at ca.500 nm the presence of the Au surface plasmon.

5.2.3. TEM and DLS analysis

TEM and DLS analysis were performed to determine the average particle size and particle size distribution. Representative bright field TEM micrographs as shown in Figure 5.6, were acquired to measure the particle size distributions and mean particle sizes of the supported monometallic and bimetallic nanoparticles. The particle size data are summarized in Table 5.5. The mean particle sizes of the supported Au_xPd_y nanoparticles were in the 2.1 nm (± 0.4) - 2.7 nm (± 1.0) range without observing any appreciable systematic size trend with variation of Au_xPd_y atomic composition in the chosen range. The average diameter of Au_xPd_y colloids using DLS was in the range 4-7 nm. Since the DLS measures the hydrodynamic diameter, the PVA layer and the water solvation shell that surrounds the colloidal nanoparticles are responsible of the differences in the order of 2.5 - 5.0 nm compared to TEM analysis.

Particle size and size distribution were also calculated for the $Au_{50}Pd_{50}$ nanoparticles supported on activated carbon (AC), α-iron oxide (α-Fe_2O_3) and magnesium oxide (MgO). The results are presented in Table 5.5. When the bimetallic colloid was immobilised on AC, the size was in the same range as reported for TiO_2 (2.5 nm ± 0.7). However, when α-Fe_2O_3 and MgO were used, the nanoparticles were slightly bigger, with an average dimension of 3.4 nm ± 1.0. It is possible that bigger nanoparticles are simply the result of a weaker interaction between the support and the metal.

Table 5.5: Particle size and size distribution calculated from TEM and DLS analysis.

Catalyst	Mean particle size and size distribution [nm]	
	TEM	**DLS**
Au/TiO_2	2.4 ± 0.7	5.6 ± 1.7
$Au_{95}Pd_5/TiO_2$	2.1 ± 0.4	5.8 ± 1.7
$Au_{65}Pd_{35}/TiO_2$	2.7 ± 0.7	6.2 ± 1.6
$Au_{50}Pd_{50}/TiO_2$	2.1 ± 0.6	4.1 ± 1.8
$Au_{35}Pd_{65}/TiO_2$	2.3 ± 0.8	7.1 ± 1.7
Pd/TiO_2	2.7 ± 1.0	6.0 ± 1.9
AuPd/AC	2.5 ± 0.7	n.a.
$AuPd/\alpha\text{-}Fe_2O_3$	3.4 ± 1.0	n.a.
AuPd/MgO	3.4 ± 0.8	n.a.

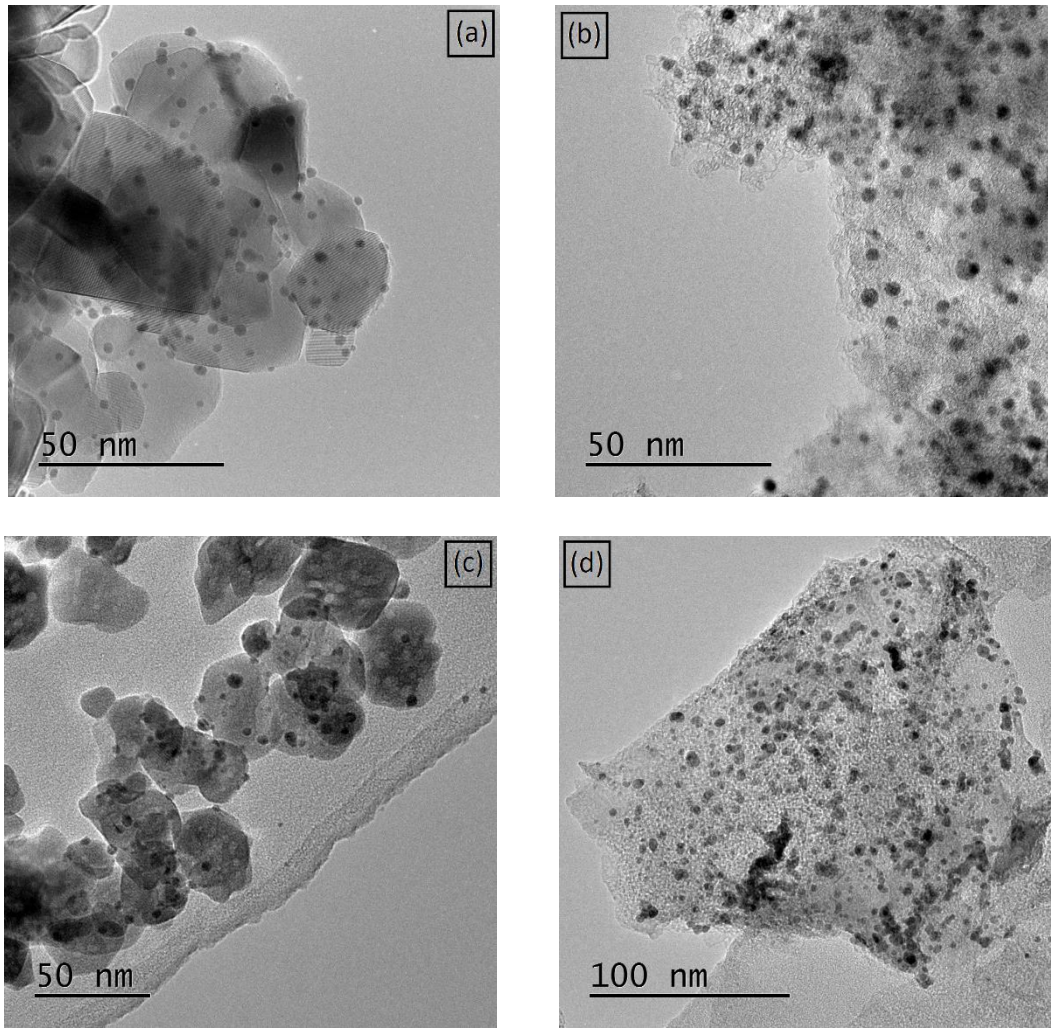

Figure 5.6: Representative bright-field TEM micrographs of (a) $Au_{50}Pd_{50}/TiO_2$, (b) AuPd/AC, (c) AuPd/α-Fe_2O_3 and (d) AuPd/MgO.

5.2.4. XRD analysis

The presence of small nanoparticles on the TiO_2 supported catalysts was also confirmed by XRD analysis. The Scherrer equation could not be applied for the calculation of the crystallite size due to the small signal to noise ratio caused by the very low intensity of Au (200) and Pd (200) diffraction peaks (Figure 5.7[a]). From the analysis of the whole XRD diffraction pattern, the catalyst shows the characteristic reflections of the anatase and rutile phases (Figure 5.7[b]), with a predominance of anatase as reported in literature for P25 TiO_2. XRD analysis were performed also on the $Au_{50}Pd_{50}$/MgO and $Au_{50}Pd_{50}/Fe_2O_3$ catalysts to verify the actual composition of the supports (Figure 5.8). Regarding MgO, as expected, since the catalyst had not been calcined at high temperature, the support presented the characteristic (001), (101), (102) and (110) peaks (at 19, 38, 51 and 59 ° respectively) of the

$Mg(OH)_2$ brucite phase[45–47]. XRD patterns of the Fe_2O_3 sample presented all the characteristic peaks of the haematite phase (α-Fe_2O_3), for example the (104) at 32 °, the (110) at 35 ° and the (116) at 55 °.

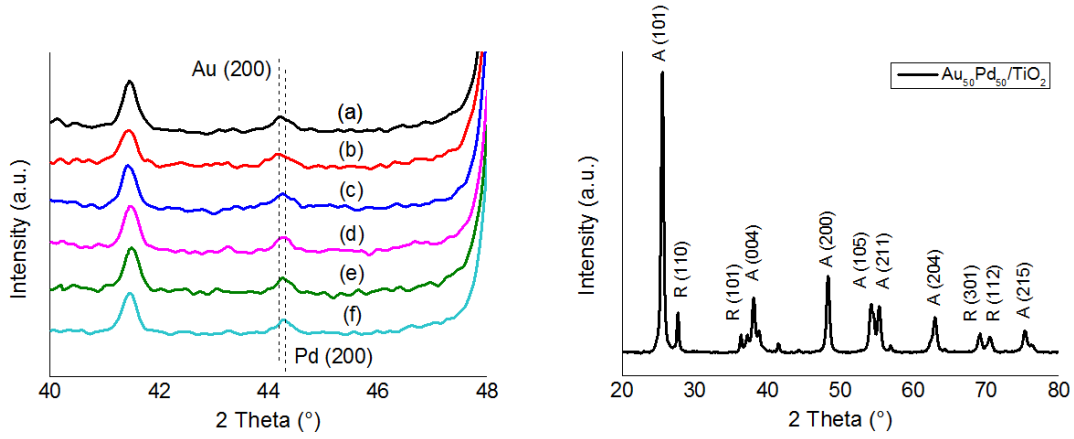

Figure 5.7: [a] XRD analysis of the catalysts with different Au/Pd molar ratio: (a) Au/TiO_2, (b) $Au_{95}Pd_5/TiO_2$, (c) $Au_{65}Pd_{35}/TiO_2$, (d) $Au_{50}Pd_{50}/TiO_2$, (e) $Au_{35}Pd_{65}/TiO_2$ and (f) Pd/TiO_2. [b] Whole XRD patterns of the $Au_{50}Pd_{50}/TiO_2$ catalyst showing the characteristic reflections of the anatase (A) and rutile (R) phase.

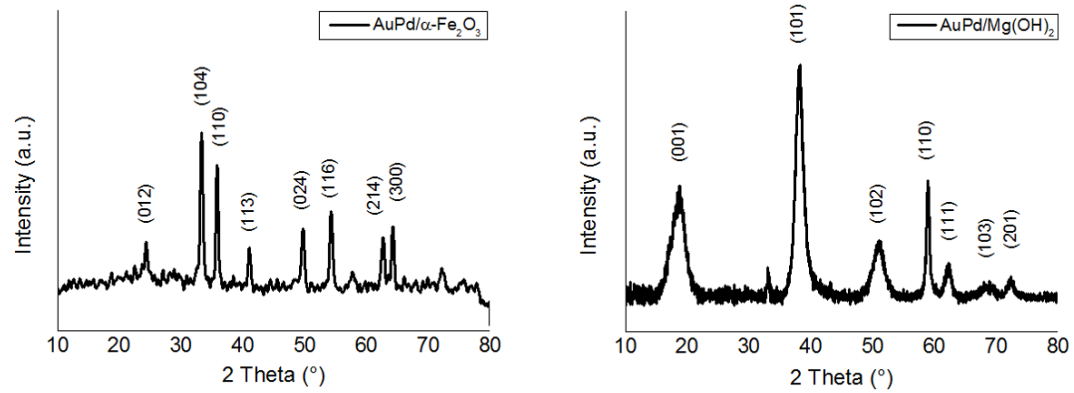

Figure 5.8: [a] XRD analysis of the AuPd/α-Fe_2O_3 catalyst showing the characteristic peaks of the haematite phase. [b] XRD analysis of the AuPd/$Mg(OH)_2$ catalyst showing the characteristic peaks of the brucite phase.

5.2.5. XPS analysis

XPS analyses were conducted on the supported monometallic and bimetallic catalysts to determine their electronic states and evaluate the metal surface composition. The Au/Pd molar ratios calculated from XPS are in good agreement with both theoretical and MP-AES experimental values. For the whole series of samples, the Au ($4f_{7/2}$) peak was recorded between 83.3-83.7 eV confirming that Au is in the metallic state (Figure 5.9)[48]. The Pd ($3d_{5/2}$)

spectra showed the presence of metallic Pd (334.9 eV) as the major species and minor contributions of Pd^{2+}, attributed to PdO (337.0 eV) since no chloride is detected, (Figure 5.10). For the monometallic Au/TiO_2 sample the binding energy (BE) of Au was 83.7 eV, lower than that of bulk gold (ca. 84.0-84.2 eV). This slight decrease in BE is be attributed to (i) particle size effects and (ii) charging of Au particles (presence of Au with partially negative charge $Au^{\delta-}$). The addition of Pd to the Au samples caused a downward shift in the BE of Au from 83.7 to 83.3 eV indicating an electronic interaction between the Au and Pd, as noted by Lee et al[49]. In common with that study the Pd BE shifts were no greater than 0.2 eV, which are in the experimental confidence limit for absolute BE (Figure 5.10). With the small size of the nanoparticles, the photoelectron attenuation lengths are of the same order as the particle sizes, therefore absolute information on the presence of either random alloy or core-shell is difficult to obtain. However, previous reports showed that AuPd nanoparticles prepared via a sol-immobilisation technique are in a random alloy state[50].

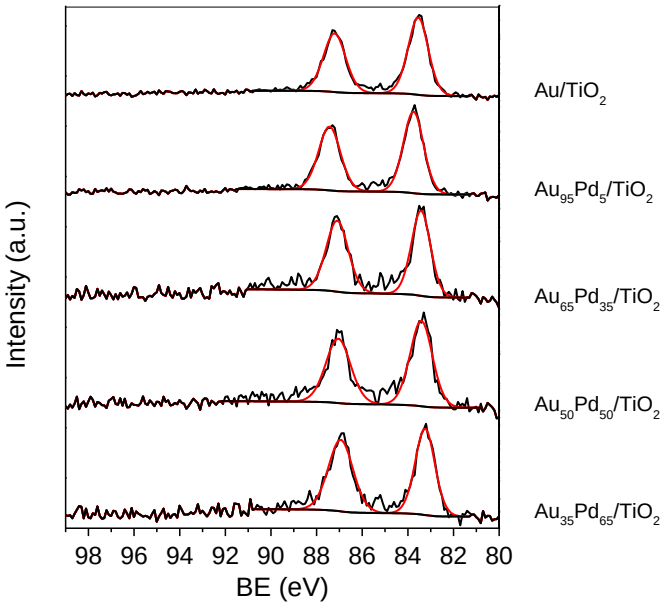

Figure 5.9: Au $4f_{7/2}$ spectra of the TiO_2 supported catalysts.

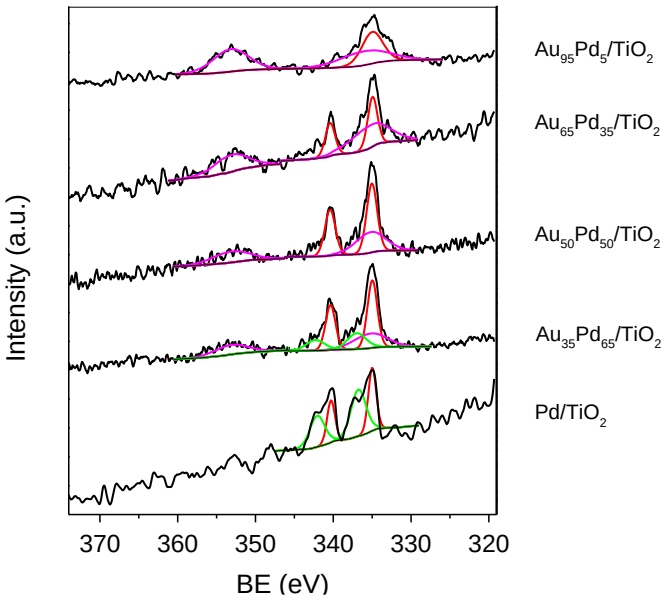

Figure 5.10: Pd $3d_{5/2}$ spectra of the TiO_2 supported catalysts.

5.2.6. CO-DRIFT analysis

CO-DRIFTS analyses were performed on the TiO_2 supported catalysts. The results are reported in Figures 5.11. The monometallic Au catalyst (Figure 5.12) shows a primary peak at around 2120 cm^{-1} comprised by two peaks at 2124 and 2115 cm^{-1} and assigned according to previous reports to CO linearly bonded on Au^0 step sites on top of nanoparticles and on peripheral Au^0 step sites respectively[51,52]. The presence of the latter peak, in particular, confirm the presence of very small nanoparticles on the catalyst surface. The peak at 2072 cm^{-1}, on the other hand, has been assigned to linear CO adsorbed on $Au^{\delta-}$ species[53]. These partially negative species seem to form during the gradual reduction of Au^0 to $Au^{\delta-}$ caused by CO when present in high concentration[54]. Analysis at low CO partial pressure, in fact, confirmed this hypothesis, although from XPS analysis the presence of small portion of $Au^{\delta-}$ species cannot be excluded (Figure 5.12). The better stability of partially negative Au atoms in a CO rich atmosphere has been ascribed to the greater π-back-donation of the latter species[55]. Finally, the broad peak centred at 2055 cm^{-1} has been assigned to bridge bonded CO on $Au^{\delta-}$ species[53].

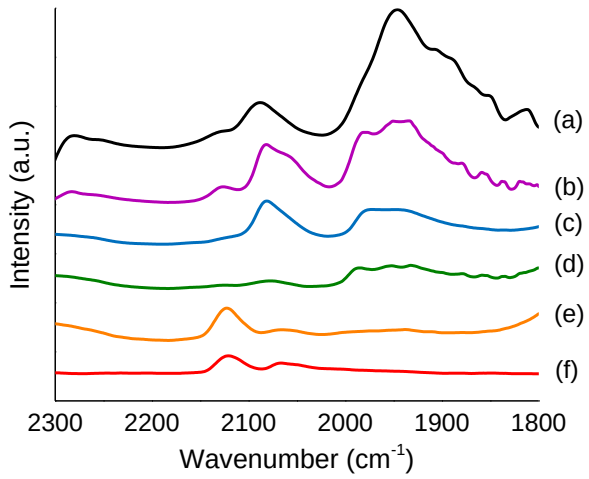

Figure 5.11: CO-DRIFT spectra of (a) Pd/TiO_2, (b) $Au_{35}Pd_{65}/TiO_2$, (c) $Au_{50}Pd_{50}/TiO_2$, (d) $Au_{65}Pd_{35}/TiO_2$, (e) $Au_{95}Pd_5/TiO_2$ and (f) Au/TiO_2.

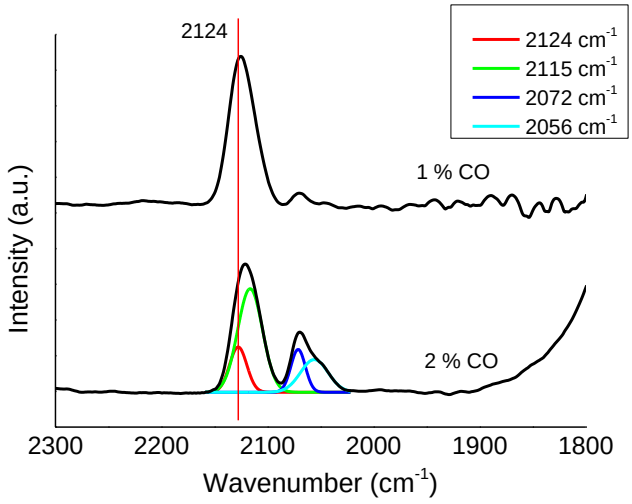

Figure 5.12: CO-DRIFT spectra of the Au/TiO_2 catalyst recorded at different CO concentrations.

The monometallic Pd catalyst (Figure 5.13), presents two broad groups of peaks. The first group, is comprised by 3 peaks at 2128, 2083 and 2065 cm^{-1}; the latter two peaks have been assigned to linear CO coordinated on Pd^0, while the peak at 2128 cm^{-1} indicates the presence of Pd^+ species[56–58]. These positive charged Pd species are not present originally in the catalyst, as confirmed by XPS analysis, but are most likely the result of partial reduction of Pd^{2+} species by the coordinated CO molecules. The second group at lower wavenumbers, is comprised by multiple and broad peaks assigned to μ_2 bridge bonded CO (ca. 1980-1930 cm^{-1}) and μ_3 bridge bonded CO (ca. 1930-1820 cm^{-1}) in accordance with previous literature[56,58].

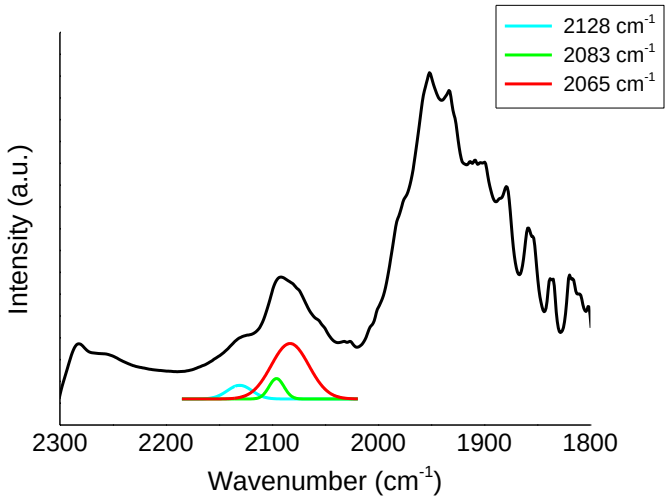

Figure 5.13: CO-DRIFT spectrum of the Pd/TiO_2 catalyst.

Regarding bimetallic AuPd catalysts, it has been previously reported that Pd carbonyls are much more stable than Au carbonyls due to the higher π-back-donation of the Pd-CO bond[59]. For this reason, the typical Pd-CO bands dominate the DRIFTS spectra in AuPd alloys when Pd is present in significant amounts and it is therefore difficult to observe bands related to the presence of Au sites. Indeed, in the $Au_{35}Pd_{65}$, $Au_{50}Pd_{50}$ and $Au_{65}Pd_{35}$ catalysts, all the CO-Pd features listed above for the monometallic Pd catalyst are present, and the only difference among these catalysts is the intensity of the peaks[60]: as expected, increasing the amount of Pd, the intensity of the CO-Pd peaks increases (Figure 5.14[a]). Interestingly, when the Au/Pd ratio is 95:5, the CO stretching peaks are dominated by the CO-Au interactions (Figure 5.14[b]) rather than CO-Pd. The appearance of a strong peak at 2123 cm^{-1} with a small shoulder at 2103 cm^{-1} is evident and these peaks are characteristic of linear CO bonded on Au^0 step sites on top of nanoparticles and of peripheral Au^0 step sites, as previously discussed.

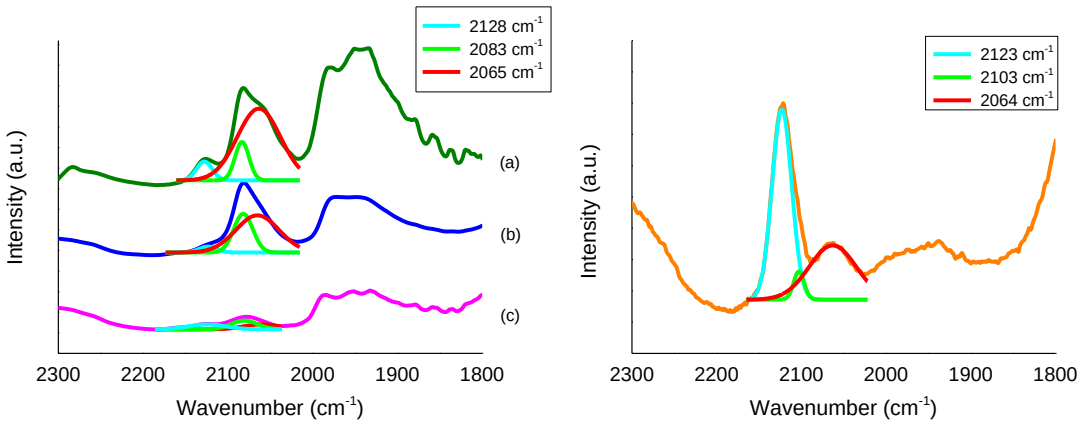

Figure 5.14: [a] CO-DRIFT spectra of the (a) $Au_{35}Pd_{65}/TiO_2$, (b) $Au_{50}Pd_{50}/TiO_2$ and (c) $Au_{65}Pd_{35}/TiO_2$ catalysts. [b] CO-DRIFT spectrum of the $Au_{95}Pd_5/TiO_2$ catalyst.

5.2.7. Pyridine-DRIFT analysis

Pyridine-DRIFTS was used to evaluate the presence of Lewis and Brønsted sites on bimetallic AuPd catalysts on different supports. The lone electron pair on the nitrogen of the pyridine molecule can form coordinative bonds to Lewis acid sites or interact with acidic surface protons to form the pyridinium ion. Additionally, pyridine can physically adsorb or bond through a hydrogen bond. The infrared spectrum of these four species are different and usually clearly distinguishable.

Figure 5.15 shows the comparison between the spectra of $Au_{50}Pd_{50}$ nanoparticles supported on activated carbon (AC), titanium oxide (TiO_2), iron oxide (Fe_2O_3) and magnesium oxide (MgO) in vacuum at 30 °C after 15 minutes of saturation in a pyridine/N_2 atmosphere. It should be firstly pointed out that the MgO spectrum in pure N_2 (Figure 5.16), shows the characteristic features of $Mg(OH)_2$; this is not surprising, since no calcination was performed on the catalyst. In particular, the peaks at 3706 and 3736 cm^{-1} are single vOH of $Mg(OH)_2$ and isolated OH group respectively, while the broad peak at 3600-3000 cm^{-1} was assigned to the presence of adsorbed H_2O and hydrogen bound hydroxyl groups[61].

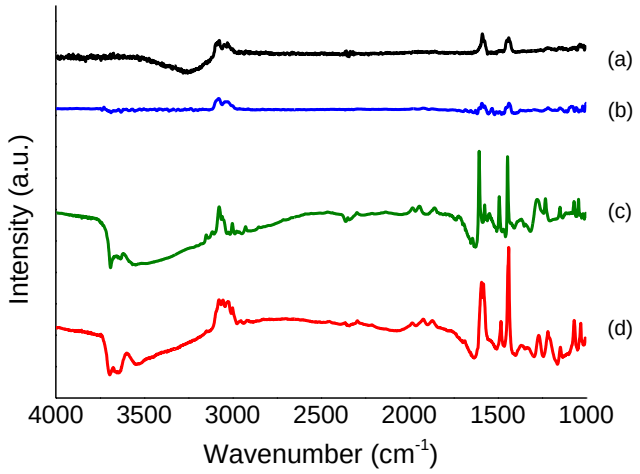

Figure 5.15: Py-DRIFT spectra of the (a) AuPd/AC, (b) AuPd/Mg(OH)$_2$, (c) AuPd/TiO$_2$ and (d) AuPd/α-Fe$_2$O$_3$ catalysts.

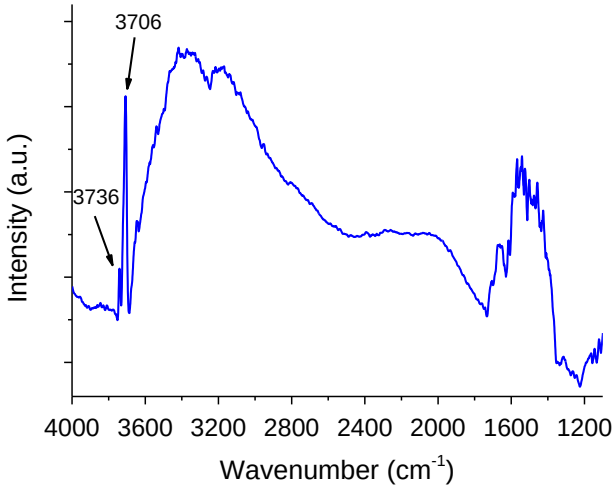

Figure 5.16: DRIFT spectrum of the AuPd/Mg(OH)$_2$ catalyst.

Both carbon and magnesium hydroxide show two peaks of small intensity at 1590 and 1440 cm^{-1} relative to non-specifically adsorbed liquid-like pyridine molecules[61,62]. These peaks deplete by increasing the temperature up to 80 °C. No other peaks relative to Lewis or Brønsted sites were detected. Titanium oxide and iron oxide, on the other hand, show interesting peaks. The former, in particular, shows strong peaks at 1603, 1573, 1494 and 1444 cm^{-1} characteristic of Lewis acid species[63,64]. These peaks are very stable to high temperature outgassing (Figure 5.17) and are indicative of coordinatively unsaturated metal sites on the surface of the support, as reported by Zaki and colleagues[64]. In the same study, the authors ascribed the small peak at 1594 cm^{-1} to H-bonded pyridine molecules, thus indicating the availability of H-bond donor sites on the TiO$_2$ surface. Finally, the peaks at 1640 and 1545

cm^{-1} are Brønsted acid sites[64–66]; in this case, as per the H-bond sites, the peaks are not stable at high temperature outgassing (Figure 5.17)[64–66]. No basic sites or acid-base pair sites are present on the catalyst surface, as confirmed by the absence of α-pyridone and O^{2-} sites peaks, at 1680-1650 and 1260-1250 cm^{-1} respectively[64].

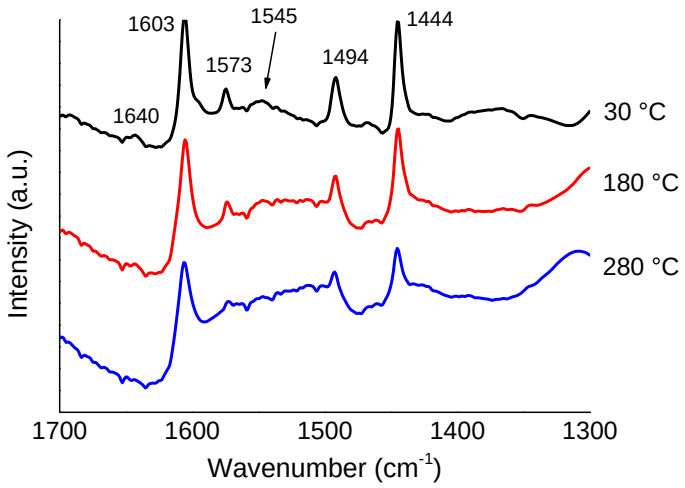

Figure 5.17: Py-DRIFT spectra of the AuPd/TiO_2 catalyst degassed at different temperature.

Regarding the Fe_2O_3 catalyst, the 4 main peaks at 1592, 1581, 1482 and 1438 cm^{-1} can be assigned to Lewis acid species[67]. Every main peak, however, has at least one shoulder that may be ascribed to slightly different acidic sites, according to a previous report[63]. The Lewis acid peaks, in particular, are divided in 4 main groups as follow: (a) 1602 and 1592 cm^{-1}, (b) 1581 and 1576 cm^{-1}, (c) 1489 and 1482 cm^{-1} and (d) 1443 and 1438 cm^{-1}. Increasing the outgassing temperature, only the strongest Lewis acid sites are able to coordinate with the pyridine, and thus it is easier to identify the 4 main peaks at 1602, 1576, 1489 and 1443 cm^{-1} (Figure 5.18).

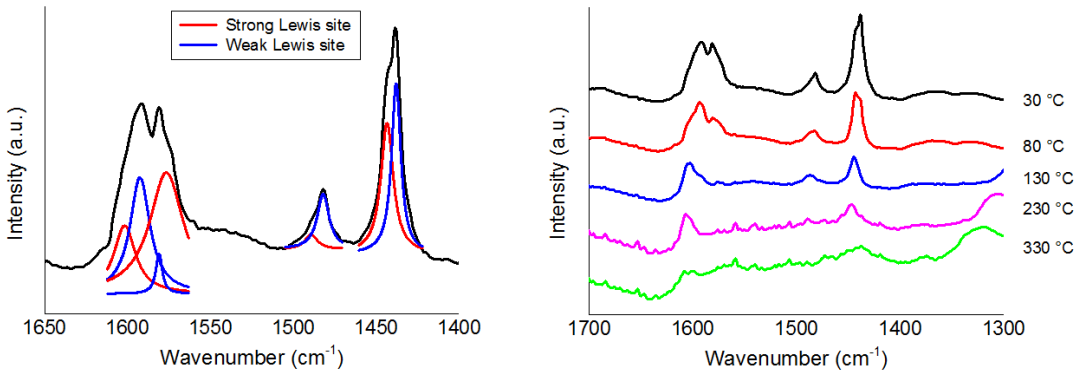

Figure 5.18: [a] Py-DRIFT spectrum of the AuPd/α-Fe_2O_3 catalyst showing two different type of Lewis sites. [b] Py-DRIFT spectra of the AuPd/α-Fe_2O_3 catalyst degassed at different temperature.

5.3. Cinnamaldehyde hydrogenation

5.3.1. Identification of the kinetic regime

Prior to obtaining any kinetically relevant data, it is important to verify the absence of any mass transfer limitations and to ensure that the reactions are conducted under a kinetic regime. Typically, this is verified simply by varying the stirring speed and/or the catalyst amount. In this way, one can check the presence of mass transfer resistance of H_2 from the gas to liquid phase and the transport of reactant from the liquid phase to the catalyst surface. In absence of any mass transfer limitation, increasing the stirring speed the reaction rate should remain constant, while increasing the catalyst amount the reaction rate should increase of the same magnitude.

Cinnamaldehyde (CAL) hydrogenation reactions were initially performed in toluene at 100 °C and under 1 bar of H_2 using a bimetallic gold-palladium catalyst ($Au_{50}Pd_{50}/TiO_2$, 1 wt.%) as our chosen model catalyst, and the main products observed were hydrocinnamaldehyde (HCAL) and hydrocinnamyl alcohol (HCOH), with cinnamyl alcohol (COH) and phenylpropane (PPR) present only in small amount as side products (Figure 5.19).

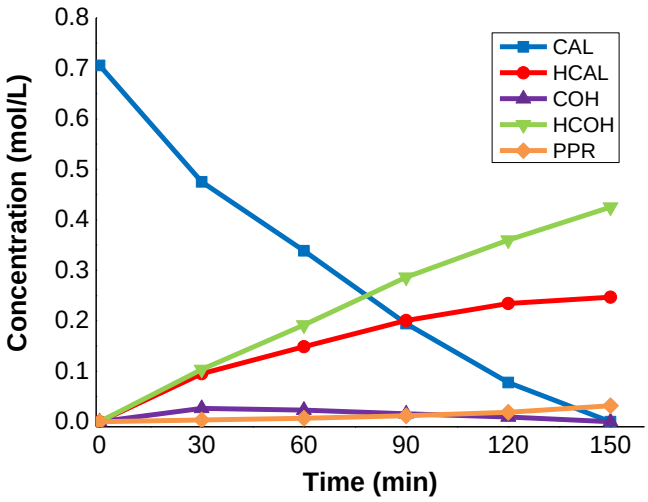

Figure 5.19: CAL hydrogenation reaction profile. Reaction conditions: 100 °C, 1 H_2 bar, 50 mg of catalyst, 4 mmol of CAL (substrate/metal ratio 1200:1), 5 mL of toluene, 1000 rpm stirring.

Experiments to determine the conditions in order to avoid diffusion limitations and identify the kinetic regime were then carried out. The stirring rate effect was studied in the range of 250 and 1250 rpm, maintaining all the other parameters constant (catalyst amount = 50 mg, CAL = 4 mmol, CAL/Metal molar ratio = 1200 : 1, toluene = 5 mL, reaction time = 30

– 150 min). Figure 5.20 shows the performance of the catalyst at various stirring rates in terms of activity expressed as turnover frequency numbers (TOF). The TOF was calculated according to Equation 5.1.

$$TOF = \frac{mol_{CONV}}{mol_{Me} \times t} \qquad Equation\ 5.1$$

Where mol_{CONV} are the moles of substrate converted after a reaction time "t" and mol_{Me} are the moles of active metal in the catalyst. The results in Figure 5.20 showed no mass transfer limitations in the rage 750-1250 rpm, while a further decrease in the stirring rate leads to a decrease in hydrogenation activity. Fittings these data separately results in the identification of two regimes, mass transfer limited regime and kinetically limited regime respectively (presented as two straight lines). The two regimes intersect at around 550 rpm: this value can be considered as the minimum stirring speed necessary in order to avoid any diffusion limitations.

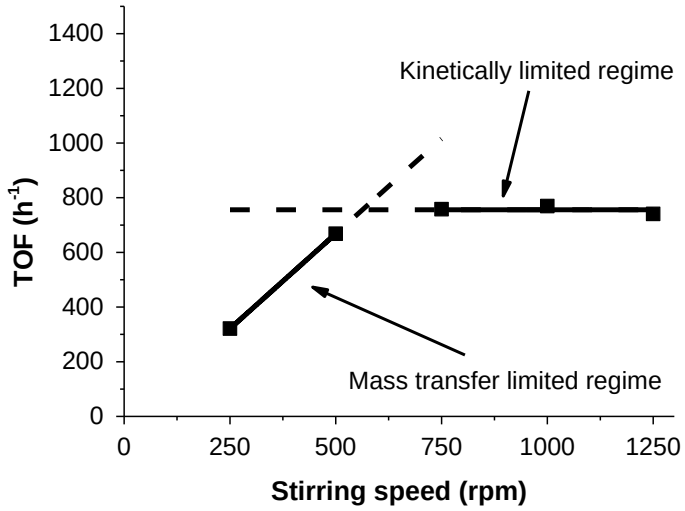

Figure 5.20: Effect of stirring speed on the TOF of the reaction. Reaction conditions: 100 °C, 1 H_2 bar, 50 mg of catalyst, 4 mmol of CAL (substrate/metal ratio 1200:1), 5 mL of toluene.

The substrate to metal ratio was then varied between 800 and 6000 (mol/mol) using stirring speed of 1000 rpm in order to study the effect of the catalyst amount (substrate to metal molar ratio). In practical terms, the amount of catalyst was varied between 10 to 70 mg. Changes in substrate/metal molar ratios in the chosen range seem to not affect the activity in terms of TOF (Figure 5.21); indeed, the conversion follows a linear increase or decrease as the catalyst amount was varied. Therefore, for the chosen catalyst amount range, no mass transfer limitations were present and the reactions were thus performed in a chemically controlled regime.

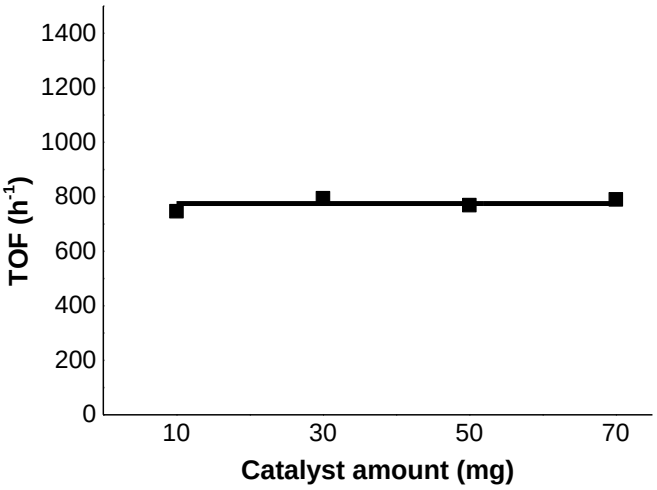

Figure 5.21: Effect of catalyst amount on the TOF of the reaction. Reaction conditions: 100 °C, 1 H_2 bar, 4 mmol of CAL, 5 mL of toluene, 1000 rpm stirring.

For both stirring speed and catalyst amount, any variation led solely to changes in activity, while the selectivity calculated at 30 % iso-conversion remained constant (Figure 5.22); HCAL and HCOH were the two main products and produced in comparable amount (42 – 46 %) while the selectivity towards the unsaturated alcohol COH remained constant at 15 %. Only traces of PPR were found at these reaction conditions (< 2 %).

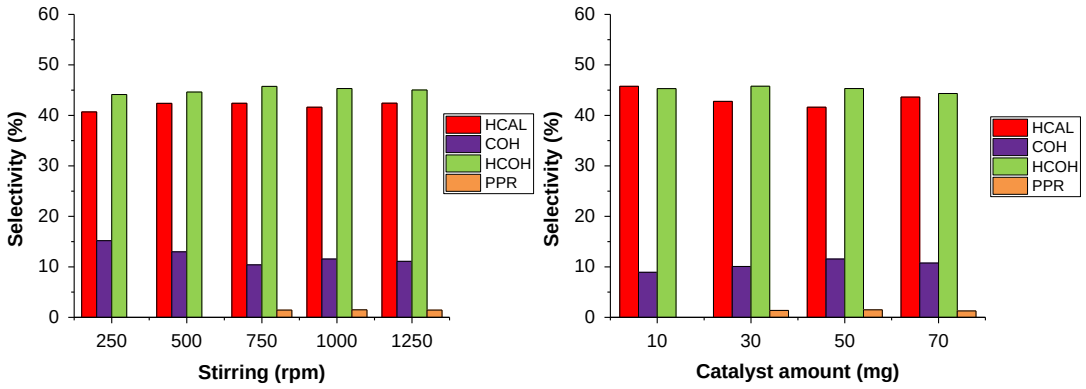

Figure 5.22: Stirring effect (left) and catalyst amount effect (right) on the selectivity at iso-conversion (30 % conversion). Reaction conditions as reported above.

5.3.2. Hydrogen pressure and temperature effect

The influence of hydrogen pressure on both activity and selectivity was also analysed. Reactions were carried out varying the hydrogen pressure from 1 to 3 bar and using the optimised reaction conditions reported above. Higher value of hydrogen pressure could not be investigated due to reactor pressure limitations. The increase of H_2 pressure enhances the solubility of the gas into the reaction medium, increasing the accessibility of H_2 molecule. Figure 5.23 shows that the TOF for cinnamaldehyde hydrogenation increased linearly as the partial pressure increased in the studied range, confirming that the reaction is a first order in respect of the hydrogen partial pressure[43,68].

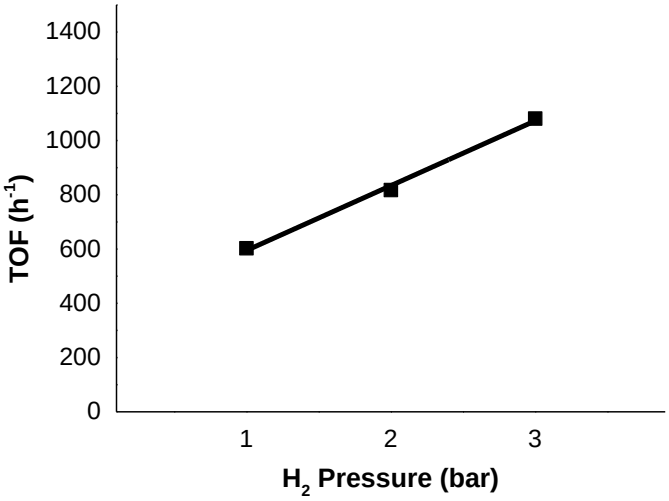

Figure 5.23: Effect of hydrogen pressure on the TOF of the reaction. Reaction conditions: 100 °C, 50 mg of catalyst, 4 mmol of CAL (substrate/metal ratio 1200:1), 5 mL of toluene, 1000 rpm stirring.

The reaction temperature effect was subsequently evaluated by varying the reaction temperature from 40 to 100 °C and maintaining the hydrogen partial pressure constant at 1 bar. It is well known that hydrogenation rates usually increase with increasing temperatures[3], and indeed, as expected, decreasing the temperature, the TOF decreased linearly as shown in Figure 5.24. It should be noted, however, that the hydrogenation selectivity to HCAL at iso-conversion level over the $Au_{50}Pd_{50}/TiO_2$ catalyst remained unchanged with variation of both H_2 pressure and reaction temperature (Figure 5.25, 40 – 45 % selectivity at 30 % of iso-conversion). This behaviour is in agreement with previous studies on bimetallic systems[43,69,70].

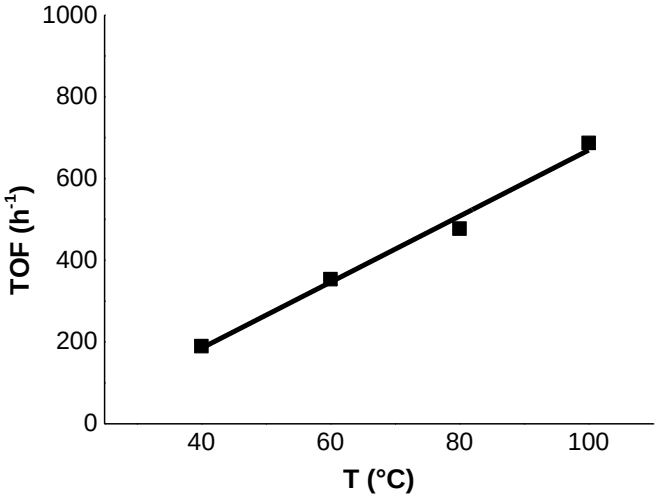

Figure 5.24: Effect of reaction temperature on the TOF of the reaction. Reaction conditions: 1 H_2 bar, 50 mg of catalyst, 4 mmol of CAL (substrate/metal ratio 1200:1), 5 mL of toluene, 1000 rpm stirring.

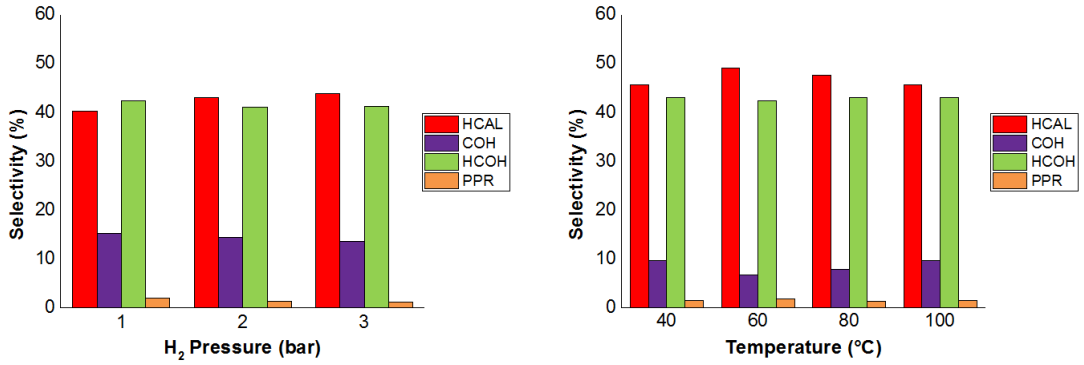

Figure 5.25: [a] Hydrogen pressure effect and [b] reaction temperature effect on the selectivity at iso-conversion (30 % conversion). Reaction conditions as reported above.

The apparent activation energy was calculated from Arrhenius plot and the value obtained was 24 kJ mol^{-1} (Figure 5.26). This value is in good agreement with the data reported in the literature for various metal based catalysts (Table 5.6)[4,68,70–72].

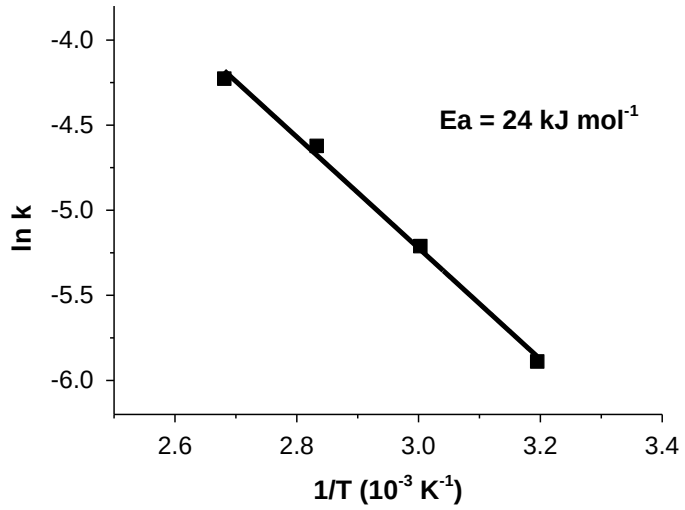

Figure 5.26: Arrhenius plot for the $Au_{50}Pd_{50}/TiO_2$ catalyst.

Table 5.6: CAL hydrogenation activation energy for different catalysts.

Catalyst	Activation Energy [kJ mol^{-1}]	Ref.
5 % Pd/SiO_2	30.1	4
Co-B	18	68
Raney-Co	35	
CoPt	17.3	70
2 % Pt/SBA-15	21	71
5 % Ir/C	37	72

5.3.3. Au/Pd molar ratio effect

The effect of Au/Pd molar ratio on cinnamaldehyde hydrogenation activity and the selectivity towards to the C=O or C=C group hydrogenation was studied. A series of catalysts with different Au/Pd metal molar ratios were prepared (Au, $Au_{95}Pd_5$, $Au_{65}Pd_{35}$, $Au_{50}Pd_{50}$, $Au_{35}Pd_{65}$, and Pd). From TEM analysis, all the catalysts have nanoparticles in a very narrow range (2.1 ± 0.4 - 2.7 ± 1.0) without any appreciable systematic size trend with variation of Au_xPd_y atomic composition. Thus, any change in activity and selectivity cannot be related to changes in nanoparticle size.

Monometallic Au/TiO_2 and bimetallic $Au_{95}Pd_5/TiO_2$ catalysts were inactive in the reaction conditions used (Figure 5.27); an increase of catalytic activity based on TOF was observed only with a further addition of Pd, meaning that a minimum amount of this noble metal is required to achieve measurable reaction rates. This is in agreement with the CO-

DRIFT results (Figure 5.14[b]), where no Pd features were detected in the $Au_{95}Pd_5$ catalyst, probably due to an extremely Au-rich surface. When the molar ratio between Au and Pd was approximately 50:50, the activity reached a maximum with a TOF of 836 h^{-1}, and a further addition of Pd decreased the catalytic performance. Activity enhancement due to alloying effect between Au and Pd were also reported by other groups, but no effect on selectivity was reported[4,73]. Only Parvulescu et al. reported an increase in COH selectivity using AuPd colloid embedded in SiO_2 as catalyst[42], while Szumelda and co-workers observed a progressive decrease in both activity and selectivity towards HCAL starting from a Pd/C catalyst and increasing the amount of Au[41]. In both cases, changes in selectivity are explained as geometric and electronic effects.

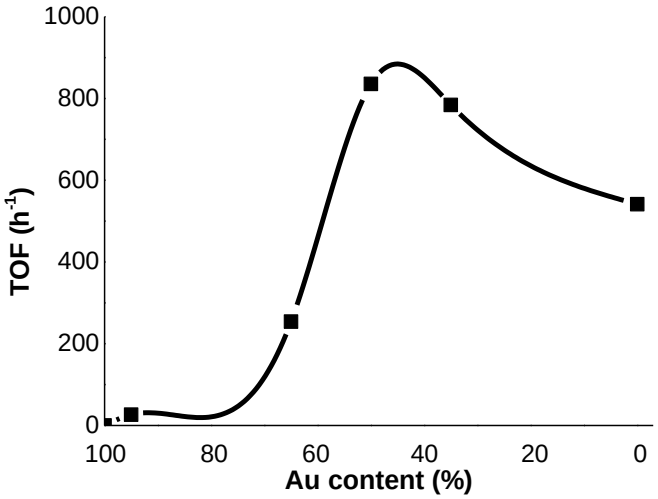

Figure 5.27: Au/Pd molar ratio effect in the CAL hydrogenation reaction. Reaction conditions: 100 °C, 1 H_2 bar, 50 mg of catalyst, 4 mmol of CAL (substrate/metal ratio 1200:1), 5 mL of toluene, 1000 rpm stirring.

It is clear from these results that Au, although totally inactive when present alone under our experimental conditions, plays an important role when alloyed with Pd, increasing the catalytic activity with respect to the monometallic Pd from 541 to 836 h^{-1}. In terms of selectivity, contrary of what previously reported by *Parvulescu* and co-workers for AuPd on SiO_2, an increase in the content of Pd leads to higher production of HCAL up to 82 % in selectivity, with a consequential decrease in HCOH selectivity at iso-conversion level (Figure 5.29). The reason for this inactivity of Au was already discussed in the introduction chapter as the presence of a completely filled d-orbital ($5d^{10}$) which affects the adsorption mode and thus the activity of the catalyst. The small d bandwidth, however, makes Pd compatible with a planar η^4 adsorption mode of CAL, with the vinyl bond being hydrogenated faster than the carbonyl bond. This explains the high activity and selectivity of Pd based catalysts. It has been

reported in literature that there is a positive effect of alloying a transition metal with a more electropositive one. Fe, for example, was added to a Pt catalyst to improve the selectivity of the C=O hydrogenation via electron transfer from the more electropositive metal to Pt[74]. The iron atoms acted as Lewis sites for the oxygen in the C=O bond, where the polarised carbonyl is easily hydrogenated by addition of hydrogen adsorbed on the nearby Pt atoms (Figure 5.28). In this case, however, a more electronegative metal (Au) was added to Pd, and thus this cannot be considered responsible for the improvement in activity.

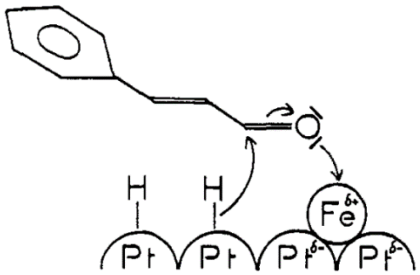

Figure 5.28: C=O activation due to action of an electropositive metal. Image reprinted with permission from D. Richard et al., Catal. Lett., 1989, 53-58.

To better understand how the second metal affects activity and selectivity, it is better to analyse the reaction considering the hydrogenation rate to COH and the hydrogenation rate to HCAL. Comparing the reactions performed with $Au_{65}Pd_{35}$, $Au_{50}Pd_{50}$, $Au_{35}Pd_{65}$, and Pd catalysts at 40 % iso-conversion (Figure 5.29), the production of COH is very low and only noticeable with the $Au_{65}Pd_{35}$ catalyst (11 %). HCOH can be formed either by C=O hydrogenation of HCAL or by C=C hydrogenation of COH. To clarify which mechanism is predominant, reactions were performed using HCAL and COH as substrate. The results (Table 5.7) clearly show that all the HCOH comes from the very fast hydrogenation of COH. Thus, in a standard CAL hydrogenation reaction with a bimetallic AuPd catalyst, all the COH formed is readily converted to HCOH. Since this step is very fast, the rate determining step in the production of HCOH is the hydrogenation of the carbonyl group. The rate of COH formation can then be approximated to the sum of the actual COH formation plus the HCOH formation.

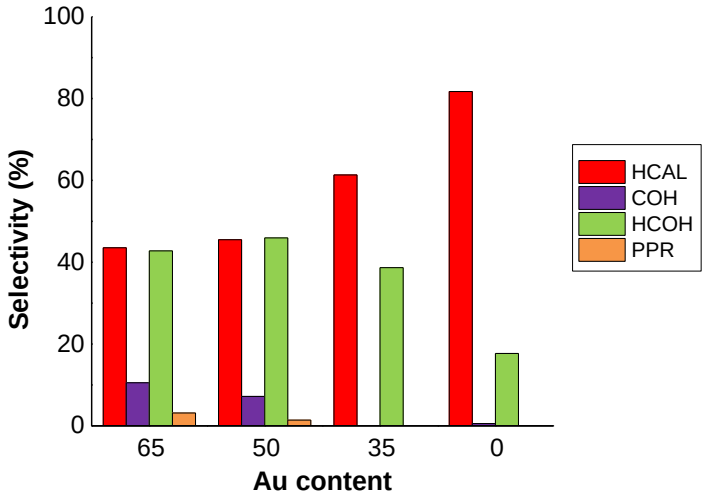

Figure 5.29: Au/Pd molar ratio effect on the selectivity. Reaction conditions: 100 °C, 1 H_2 bar, 50 mg of catalyst, 4 mmol of CAL (substrate/metal ratio 1200:1), 5 mL of toluene, 1000 rpm stirring.

Table 5.7: Catalytic tests performed using HCAL and COH as starting material. Reaction conditions: 100 °C, 1 H_2 bar, 50 mg of catalyst, 4 mmol of substrate (substrate/metal ratio 1200:1), 5 mL of toluene, 1000 rpm stirring.

Substrate	**Conversion[a] [%]**	**Selectivity[a]**	
		HCOH	**PPR**
HCAL	0	-	-
COH	100	92	8
CAL	35	46	1

[a] *Conversion and selectivity calculated at 30 minutes of reaction.*

In Table 5.8 are reported the rate of CAL conversion and of COH and HCAL formation. To prove that the conversion rate is not only dependent on the amount of Pd present in the catalyst, but that there is an alloying effect due to the presence of Au, the TOF was calculated as if only the Pd atoms were active in the hydrogenation reaction (TOF_{Pd}). In other words, during the calculation of the TOF, instead of considering the total metal moles present (Au + Pd), the amount of Pd only was taken into consideration (Equation 5.2). If Pd was the only responsible for the CAL hydrogenation, then the TOF_{Pd} should be the same with all the catalysts when normalised by the moles of Pd. However, that is not the case. The TOF_{Pd}, in fact, reaches a maximum with the $Au_{50}Pd_{50}/TiO_2$ as it happened with the standard TOF.

$$TOF_{Pd} = \frac{mol_{CAL}}{mol_{Pd} \times t} \qquad Equation\ 5.2$$

Where mol_{CAL} are the moles of CAL converted, mol_{Pd} the moles of Pd present in the catalyst and t is the reaction time in hours.

Table 5.8: Rate of CAL conversion and HCAL and COH formation calculated at iso-conversion (30 % conversion. Reaction conditions: 100 °C, 1 H_2 bar, 50 mg of catalyst, 4 mmol of CAL (substrate/metal ratio 1200:1), 5 mL of toluene, 1000 rpm stirring.

Catalyst	TOF [h^{-1}]	Reaction rate [mol L^{-1} h^{-1}]			TOF_{Pd} [h^{-1}]	
		CAL	HCAL	COH + HCOH[a]	CAL	HCAL
$Au_{65}Pd_{35}/TiO_2$	254	-0.137	0.059	0.072	726	310
$Au_{50}Pd_{50}/TiO_2$	836	-0.501	0.230	0.269	1671	783
$Au_{35}Pd_{65}/TiO_2$	784	-0.507	0.310	0.195	1206	737
Pd/TiO_2	541	-0.454	0.371	0.080	541	442

[a] *COH production rate calculated as sum of the COH and HCOH production rate.*

The boost in activity can be caused by either an increase of C=C hydrogenation, by an increase of C=O hydrogenation or by a simultaneous increase of both. The data in Table 5.8 show an increase in HCAL production rate increasing the Pd amount, again with a maximum at a AuPd composition of 50:50. Recalculating the TOF as before (considering the Pd atoms only), it is clear again that the reaction rate is faster when the Au/Pd molar ratio is 1:1. Similar results were obtained with the COH production rates. In this case, in fact, the boost in activity due to the alloying effect is evident, with a maximum in reaction rate when the $Au_{50}Pd_{50}/TiO_2$ catalyst was used.

Both hydrogenations of the carbonyl and vinyl group are enhanced by the addition of a second metal (Au) to an already active Pd/TiO_2 catalyst. The boost in activity reached a maximum when the Au/Pd molar ratio was 1:1 and then it decreased, showing a volcano-like plot. In this case, the enhanced activity could be attributed to a double concomitant effect. On one hand, the addition of a bigger element, such as Au, helps to space out the Pd atoms that have a better and stronger interaction in the new lattice conformation with the substrate. This is reflected in an increase of both C=C and C=O hydrogenation rates, since both of the double bonds are closer to the metallic centre and thus more prone to being hydrogenated. On the other hand, the addition of Au causes a progressive filling of the d-band, thus enriching the electron density on the metal surface. This effect, as reported in literature, decrease the C=C hydrogenation rate due to electron repulsion between the metal surface and the C=C in saturation. When the Au content is too high, however, the external d-band is completely filled and interaction between the alloy and the substrate is not

favourable anymore, and thus the overall activity greatly drops. From theoretical results, it has been reported that the Pd d-band can be completely filled with a Au concentration of ca. 60 mol%[75,76]. This is in accordance with our findings, since the overall CAL conversion strongly decreases with a relative Au concentration of ca. 65 mol%. More studies, such as DFT calculations, are however necessary to further confirm this hypothesis.

5.3.4. Solvent effect

Solvents can play a very important role in the selective hydrogenation of CAL. It has been reported in the literature that polar solvents enhance adsorption of non-polar substrates, while non-polar solvents enhance the adsorption of polar substrates. The reason for this is a double effect between the solvent and the substrate: competitive adsorption and differences in affinity. For this reason, toluene was initially employed as solvent. Different polar solvents were then used to evaluate their effect on the studied reaction. Ethanol (EtOH) and iso-propanol (i-PrOH), the most used polar solvents in literature for this reaction, were employed maintaining all the other experimental parameters constant[8,31,38,41,42]. The results (Figure 5.30) show an apparent small variation of CAL conversion (a variation of only ± 7 % conversion after 2 hours), while the selectivity was significantly varied. The reaction pathway is greatly complicated with formation of PPR and ethers when alcohols are used as solvent. A simplified analysis of COH and HCAL formation rates cannot be carried out as per the Au/Pd molar ratio effect due to this numerous side-products, so an accurate analysis of the solvent effect can only be hypothesised.

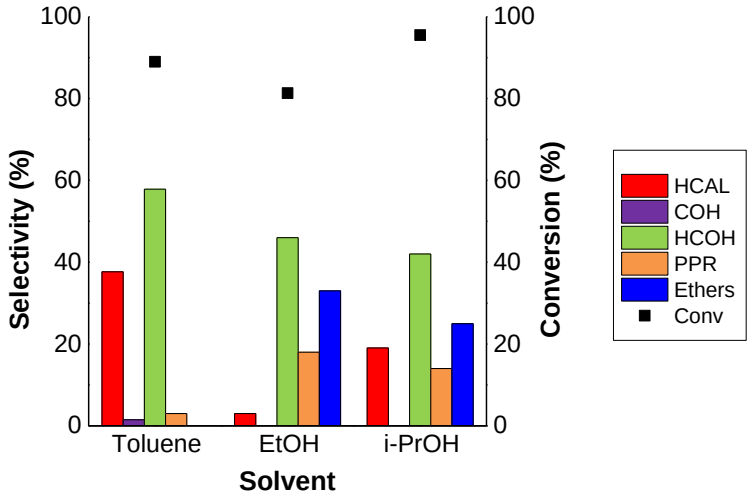

Figure 5.30: Solvent effect in the CAL hydrogenation. Reaction conditions: 100 °C, 1 H_2 bar, 50 mg of catalyst, 4 mmol of CAL (substrate/metal ratio 1200:1), 5 mL of solvent, 1000 rpm stirring.

The hydrogen solubility in a specific solvent affects the conversion of CAL (Table 5.9). It is well known that the coverage of hydrogen on the catalyst surface is directly related to the hydrogen concentration in the liquid phase[77]. Thus, a higher hydrogen solubility should lead to higher CAL conversion rates. This is in fact observed in the results, although the strong change in selectivity suggests that hydrogen solubility is not the major factor responsible for the change in CAL conversion. As previously shown, in fact, an increase in hydrogen pressure resulted in an increase in CAL conversion with no effect on the selectivity.

Table 5.9: Hydrogen solubility in the solvent used as reported by Young et al.[78]

Solvent	**Mole fraction of dissolved hydrogen [10^4 mol/mol][a]**
Toluene	3.15
Ethanol	2.06
i-Propanol	5.20

[a] *Measured at 1 bar of H_2 and 25 °C.*

From a selectivity point of view, it is interesting to notice the strong decrease in selectivity to HCAL, especially with ethanol (only 3 % is produced at 85 % conversion), and the presence of ethers when both EtOH and i-PrOH were used as solvents (33 % and 25 % respectively). It is clear that the presence of an alcohol as a solvent enables the possibility of a new reaction pathway. Milone and co-workers reported the synthesis of CAL ethers when a Au/TiO_2 catalyst was used in EtOH[39]. The mechanism suggested for the formation of the ether was through a C=O activation by the Lewis acid sites of the support, the formation of a

monoacetal by addition of a molecule of solvent and the hydrogenolysis of the C-O bond with elimination of a molecule of H_2O. A similar mechanism can happen with the $AuPd/TiO_2$ catalyst. The authors, however, did not report in their work the presence of products of further hydrogenolysis. It is possible that the more drastic hydrogenolysis of the C-O group in ethers can happen only in presence of Pd as active site. Thus, the complete mechanism is reported in Figure 5.31. It is not clear at which point the C=C bond have been hydrogenated. The presence of only the hydrogenated ether, however, suggests that the PPR comes from alcohol addition to the HCAL rather than the CAL.

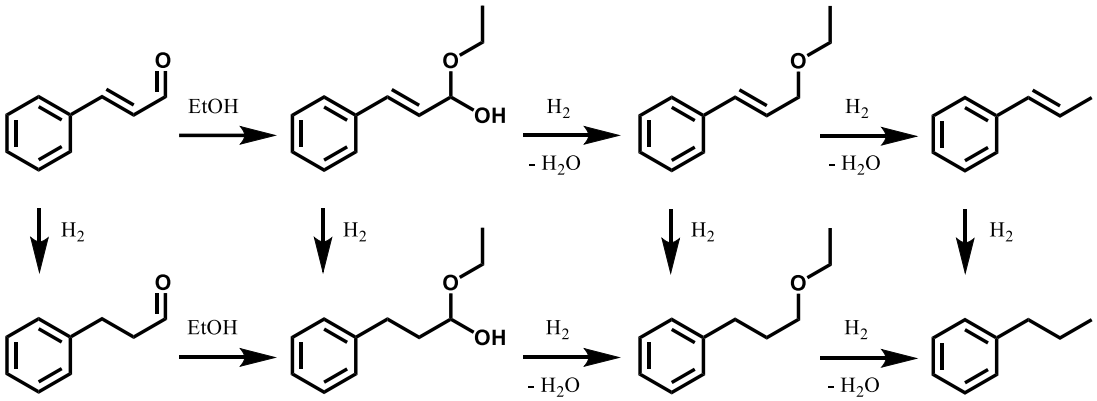

Figure 5.31: Proposed mechanism for the formation of products of etherification and hydrogenolysis.

5.3.5. Support effect

As shown in the introduction section of this chapter, the support has a great influence on the specific hydrogenation rate. The presence of acid/basic sites, the electron donation from the support to the metal and the presence of strong metal-support interactions (SMSI) are the most common factors that can tune both activity and selectivity in the CAL hydrogenation reactions. A range of three different supports with different electronical and acid/base properties were studied, namely iron oxide (α-Fe_2O_3), magnesium oxide (or more accurately magnesium hydroxide, $Mg(OH)_2$, as confirmed by DRIFT and XRD analysis) and activated carbon (AC), and compared to the $Au_{50}Pd_{50}/TiO_2$ reference. The results of the catalytic tests are reported in Figure 5.32. Despite being poorly active, α-Fe_2O_3 and $Mg(OH)_2$ seem to be very selective towards the C=C hydrogenation (HCAL selectivity of 79 % and 80 % respectively). AC shows an intermediate behaviour between TiO_2 and the two supports just mentioned, with a moderate overall activity (TOF 385 h^{-1}) and moderate selectivity to HCAL (61 %).

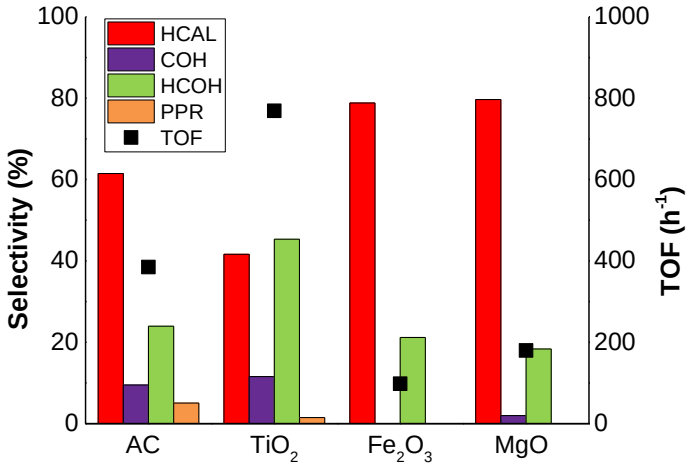

Figure 5.32: Support effect in the CAL hydrogenation. Reaction conditions: 100 °C, 1 H_2 bar, 50 mg of catalyst, 4 mmol of CAL (substrate/metal ratio 1200:1), 5 mL of toluene, 1000 rpm stirring.

It has been suggested in literature that basic OH sites on the support surface can decrease the hydrogenation rate of the C=C bond due to the electron repulsion between the vinyl group and the oxygen lone pairs thus hindering the adsorption of a planar η^4 conformation and favouring an atop approach[79]. However, this is not the case since high selectivity was obtained when $Mg(OH)_2$ was employed. The lower overall activity can be explained by the presence of numerous OH groups that creates a strong electron transfer to the metal nanoparticles that hinders the adsorption of CAL on the surface.

Using the results obtained with the pyridine-DRIFT setup, we tried to correlate the catalytic data to the Lewis/Brønsted acidity properties of the different supports. As discussed before, both TiO_2 and α-Fe_2O_3 have acid sites, however only the former has high activity towards the hydrogenation reaction, while the latter resulted the less active among the supports studied. Moreover, both $Mg(OH)_2$ and AC do not show any particular acid behaviour. Correlations between activity and Lewis/Brønsted acidity are therefore hard to draw, since no trend can be appreciated from the results obtained.

Fe_2O_3 is generally associated to higher COH selectivity due to the presence of the cationic Fe centres that act as acid Lewis sites[74]. The presence of Lewis sites on the support, in fact, in general should favour the adsorption of the electron rich aromatic ring and vinyl group, orienting the carbonyl group in the CAL towards the metal nanoparticles. This can explain the high C=O hydrogenation rate with TiO_2. At the same time, however, the intrinsic electron withdrawing behaviour of the α-Fe_2O_3, subtracts electrons from the metal

nanoparticles, reducing the metal/C=C repulsion and thus favouring a planar η^4 CAL adsorption. This could explain the higher HCAL selectivity of α-Fe_2O_3 compared to TiO_2.

The smaller metal particle size definitely plays a role in the higher overall activity of AC and TiO_2 compared to α-Fe_2O_3 and $Mg(OH)_2$. It worth also notice the PPR increase in selectivity when AC was employed, possibly due to its highly-functionalised surface. This is not unexpected, since activated carbon is known to enhance the hydrogenolysis mechanism in several reactions[80]. Different group functionalisation may be also responsible for the general aspecific selectivity of the carbon catalyst towards the hydrogenation of either the vinyl or the carbonyl group.

5.3.6. Catalyst stability

The $Au_{50}Pd_{50}/TiO_2$ catalyst was tested in multiple consecutive reactions in order to evaluate its reusability. The results are reported in Figure 5.33. After the first run, the conversion decreased from 73 % to 50 % and it stabilised at a value of 45 % for the following runs. The selectivity, however, changed accordingly to the conversion level (HCAL increased from 39 % to 49 %), indicating that the deactivation process affects mainly the catalytic activity rather than the selectivity. MP-AES analysis showed a significant loss (about 22 %) of the Pd content after 4 runs that partially explain the loss in activity. Pd leaching was also detected when the reaction was performed with the monometallic Pd/TiO_2 catalyst, with a 28 % loss after 4 consecutive reactions. A control experiment using the hot filtrate solution without catalyst confirmed that eventual leached species do not take active part to the reaction.

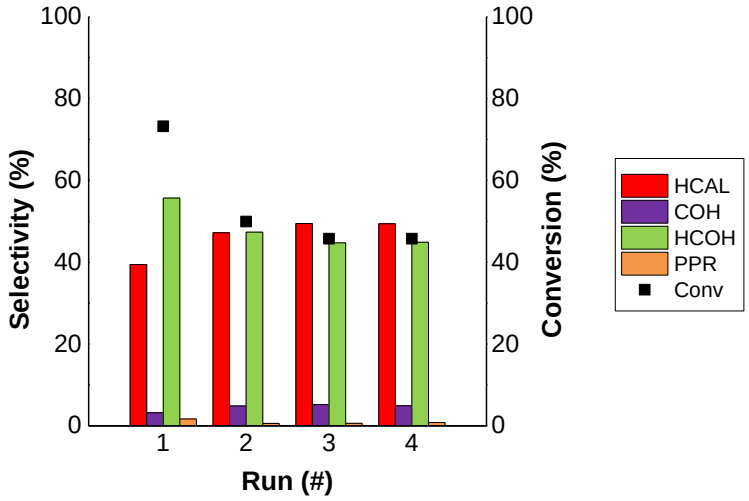

Figure 5.33: Reusability of the $Au_{50}Pd_{50}/TiO_2$ catalyst in the CAL hydrogenation. Reaction conditions: 100 °C, 1 H_2 bar, 50 mg of catalyst, 4 mmol of CAL (substrate/metal ratio 1200:1), 5 mL of toluene, 1000 rpm stirring.

Sintering of the metal nanoparticles or irreversible substrate/product adsorption could also be other reasons for catalyst deactivation. TEM analysis of the spent catalyst (Figure 5.34) showed an increase in the mean particle size as well as a broadening in size distribution. The FTIR spectra of the fresh and spent catalysts (Figure 5.35[a]), show a weak band at 1670 cm^{-1} accompanied by a broad band in the range of 3700-3000 cm^{-1} that can be attributed to the OH stretching and bending typical for the stabilising agent used. However, the enhanced peak at 1670 cm^{-1} in the spent catalyst can be also attributed to the alcoholic functional group of the CAL hydrogenation products; moreover, a series of small peaks at around 1500-1400 cm^{-1} typically account for the presence of aromatic C=C stretches that indicate the presence of either COH or HCOH adsorbed on the surface of the catalyst. FTIR spectra of the stabilising agent and substrate/products are reported here for comparison (Figure 5.35[b]). The stronger band at 3700-3000 cm^{-1} in the fresh catalyst is only due to adsorbed water remaining on the catalyst surface.

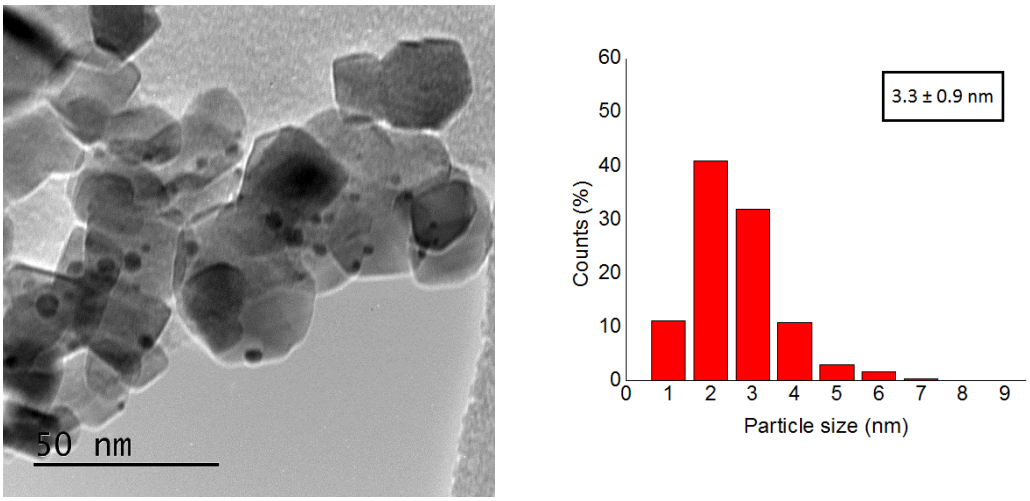

Figure 5.34: [a] Representative bright-field micrograph of the used $Au_{50}Pd_{50}/TiO_2$ catalyst and [b] relative particle size distribution.

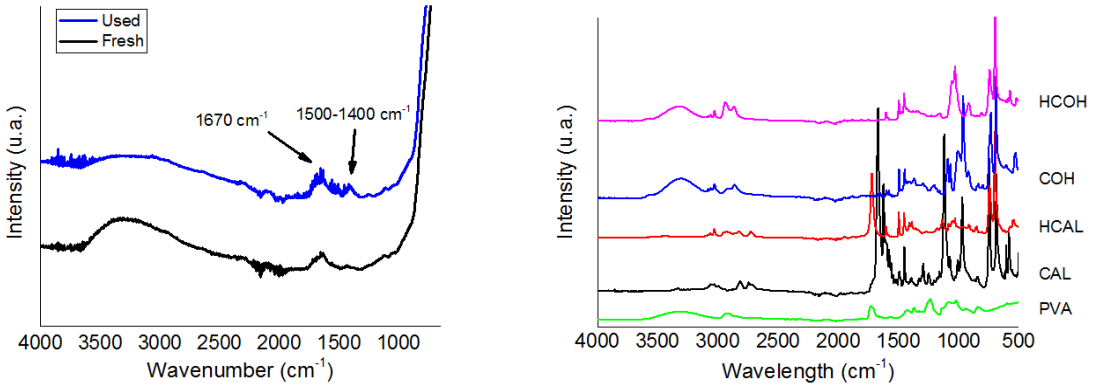

Figure 5.35: [a] FTIR spectra of the fresh and used $Au_{50}Pd_{50}/TiO_2$ catalyst and [b] of substrate/products as reference.

5.3.7. Catalyst heat treatments

In order to improve the catalyst reusability, the $Au_{50}Pd_{50}/TiO_2$ catalyst was treated at different temperatures: 200, 300 and 400 °C. In the first step, the catalyst was calcined in static air in order to remove residual chlorine ions remaining from the catalyst preparation and to remove the nanoparticles stabilising agent (PVA). In the second step, maintaining the same heating temperature, a 5 % mixture of H_2 in Ar was passed through the furnace chamber. The reductive atmosphere generates the ideal conditions for strong metal-support interactions (SMSI) to occur[81]. SMSI have been suggested to be responsible for stability and selectivity improvement in several reactions by a thin layer of TiO_x that moves over and partially covers supported metal nanoparticles[40]. This mechanism can happen even at temperature as low as 200 °C[82].

The TEM analysis of the effect of heat treatment are reported in Table 5.10. Increasing the reduction temperature decreases the activity from 73 % for the dried only sample to 50 % for the catalyst heated at 400 °C. However, the stability improves considerably: both AuPd/TiO_2–300 °C and AuPd/TiO_2–400 °C catalysts maintain the catalytic activity for 4 consecutive reactions. A small decrease in activity was observed for the AuPd/TiO_2–200 catalyst (from 70 to 58 %). MP-AES tests on the final reaction solutions revealed the absence of Pd, confirming that high temperature treatments help to increase the stability of the catalyst by increasing the metal-support interaction.

Table 5.10: Reaction rate and particle size distribution for catalysts heat treated at different temperature. Reaction conditions: 100 °C, 1 H_2 bar, 50 mg of catalyst, 4 mmol of CAL (substrate/metal ratio 1200:1), 5 mL of toluene, 1000 rpm stirring.

Catalyst	Run	Particle size (nm)	Conversion (%)	Reaction rate[a] [mol L^{-1} h^{-1}]		
				CAL	HCAL	HCOH
AuPd/TiO_2	1	2.1 ± 0.6	73	-0.344	0.136	0.192
AuPd/TiO_2	4	3.3 ± 0.9	46	-0.211	0.103	0.093
AuPd/TiO_2-200	1	2.5 ± 0.8	70	-0.329	0.299	0.149
AuPd/TiO_2-200	4	3.4 ± 0.8	58	-0.271	0.232	0.128
AuPd/TiO_2-300	1	3.7 ± 1.0	56	-0.264	0.213	0.047
AuPd/TiO_2-300	4	3.8 ± 0.8	55	-0.261	0.203	0.054
AuPd/TiO_2-400	1	5.3 ± 1.2	50	-0.235	0.193	0.038
AuPd/TiO_2-400	4	5.9 ± 1.3	49	-0.232	0.183	0.047

XPS data (Table 5.11) of the heat-treated catalysts do not suggest significant changes in surface metal composition with the heat treatment, even though, as mentioned before in Chapter 4.2.5, these data cannot be considered as a true representation of the real surface composition. The overall loss in activity with the increased reduction temperature is probably due to both the suppressed hydrogen chemisorption due to the SMSI and to the increase in mean particle size (Table 5.10); the measured average mean diameter, in fact, varies from 2.1 ± 0.6 nm to 5.3 ± 1.2 nm for the AuPd/TiO_2 and AuPd/TiO_2–400 °C catalysts respectively. On the other hand, the significant improvement in stability may be due to the protective TiO_x surface layer that prevents metal sintering phenomena during reaction (Figure 5.36). This is confirmed again by TEM analysis (Table 5.10): for high temperature treated catalysts, the nanoparticles dimension changes only slightly (from 5.3 ± 1.2 nm to 5.9 ± 1.3 nm for the AuPd/TiO_2–400 catalyst).

Table 5.11: Au/Pd molar ratio calculated by XPS.

Catalyst	Au/Pd ratio (mol/mol)
$AuPd/TiO_2$	47 : 53
$AuPd/TiO_2$-200-Used	49 : 51
$AuPd/TiO_2$-300-Used	44 : 56
$AuPd/TiO_2$-400-Used	47 : 53

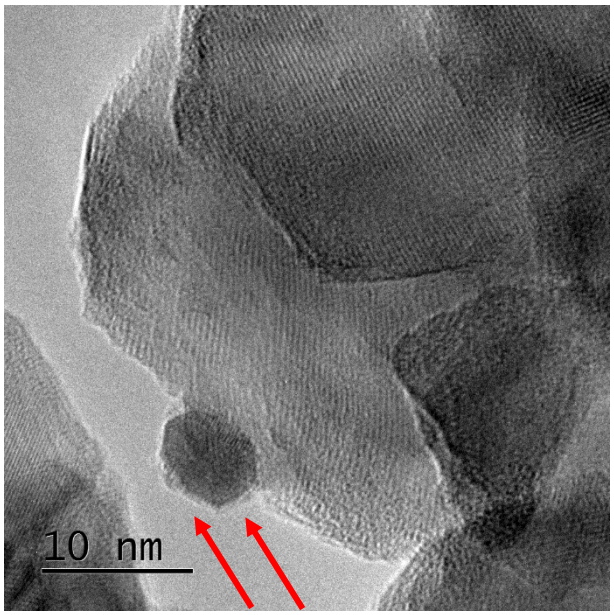

Figure 5.36: TiO_x surface layer formed during the heat treatment at 400 °C of the $Au_{50}Pd_{50}/TiO_2$ catalyst.

The high temperature treatments not only influence the activity of the catalysts, but also the selectivity: increasing the reduction temperature, the selectivity towards CAL increases drastically from 39 to 83 %, with $AuPd/TiO_2$ and $AuPd/TiO_2$–400 respectively. Comparing the values of hydrogenation rate (Table 5.10), it is clear that treating the catalyst at 200 °C on one hand it decreases the HCOH production rate, and on the other hand it increases the HCAL production rate. The C=C hydrogenation rate, however, decreases with the reuse of the catalyst. Higher temperatures make the catalyst more stable but at the same time decrease the vinyl hydrogenation rate. A good compromise between stability and selectivity is the catalyst treated at 300 °C. At this temperature the C=C hydrogenation rate is higher compared to the catalyst dried only (0.160 versus 0.102 mol L^{-1} h^{-1} respectively) and it is very stable after 4 reaction cycles.

Several works in literature reported the increase of C=O hydrogenation induced by SMSI. The enhanced COH selectivity was ascribed to cationic TiO_x species formed during the

heat treatment that are able to activate the carbonyl group by interaction with the strongly polarised oxygen atom (Figure 5.37)[83]. However, with our catalysts, a completely different behaviour was observed. It is well known that high temperature treatments in AuPd alloy systems may cause Pd segregation on the nanoparticles surface to form core-shell structures[84,85]. A recent report, in particular, shows that Pd segregation on AuPd/TiO_2 can start at temperatures as low as 200 °C[86].

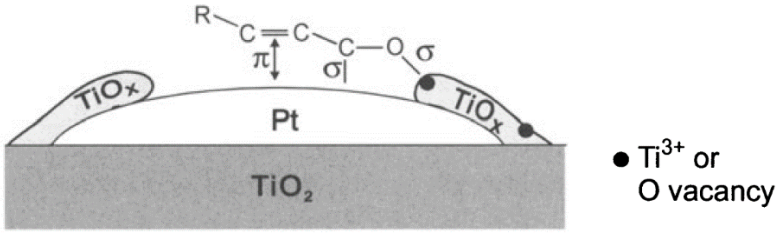

Figure 5.37: Proposed mechanism for the C=O activation by the TiO_x formed during the catalyst heat treatment. Image reprinted with permission from M. A. Vannice et al., J Catal., 1989, 115, 65-78.

It is possible that Pd segregation happened during the calcination step, thus enriching the nanoparticles surface in C=C selective Pd atoms. The Au-rich core still provides electron transfer to the Pd-rich shell, thus maintaining the activity higher than a normal monometallic Pd catalyst. The comparison of TOF_{Pd} between the heat treated catalysts and the Au_xPd_y catalysts confirms the persistence of the promotion effect generated by the presence of Au atoms (Table 5.12). XPS analysis cannot clear out all doubts, since the penetration depth of the X-ray is in the same order of magnitude of the nanoparticle dimensions, and the quantification analysis are good only to evaluate the overall content of the two metals. Single nanoparticle EDX analysis would ultimately confirm the bimetallic core-shell structure.

Table 5.12: CAL and HCAL TOF_{Pd} values for the heat treated catalysts. Reaction conditions: 100 °C, 1 H_2 bar, 50 mg of catalyst, 4 mmol of CAL (substrate/metal ratio 1200:1), 5 mL of toluene, 1000 rpm stirring.

Catalyst	**TOF_{Pd} [h^{-1}][a]**	
	CAL	**HCAL**
AuPd/TiO_2	1170	462
AuPd/TiO_2-200	1117	1016
AuPd/TiO_2-300	898	723
AuPd/TiO_2-400	792	658

[a] *TOF_{Pd} calculated after 90 minutes of reaction.*

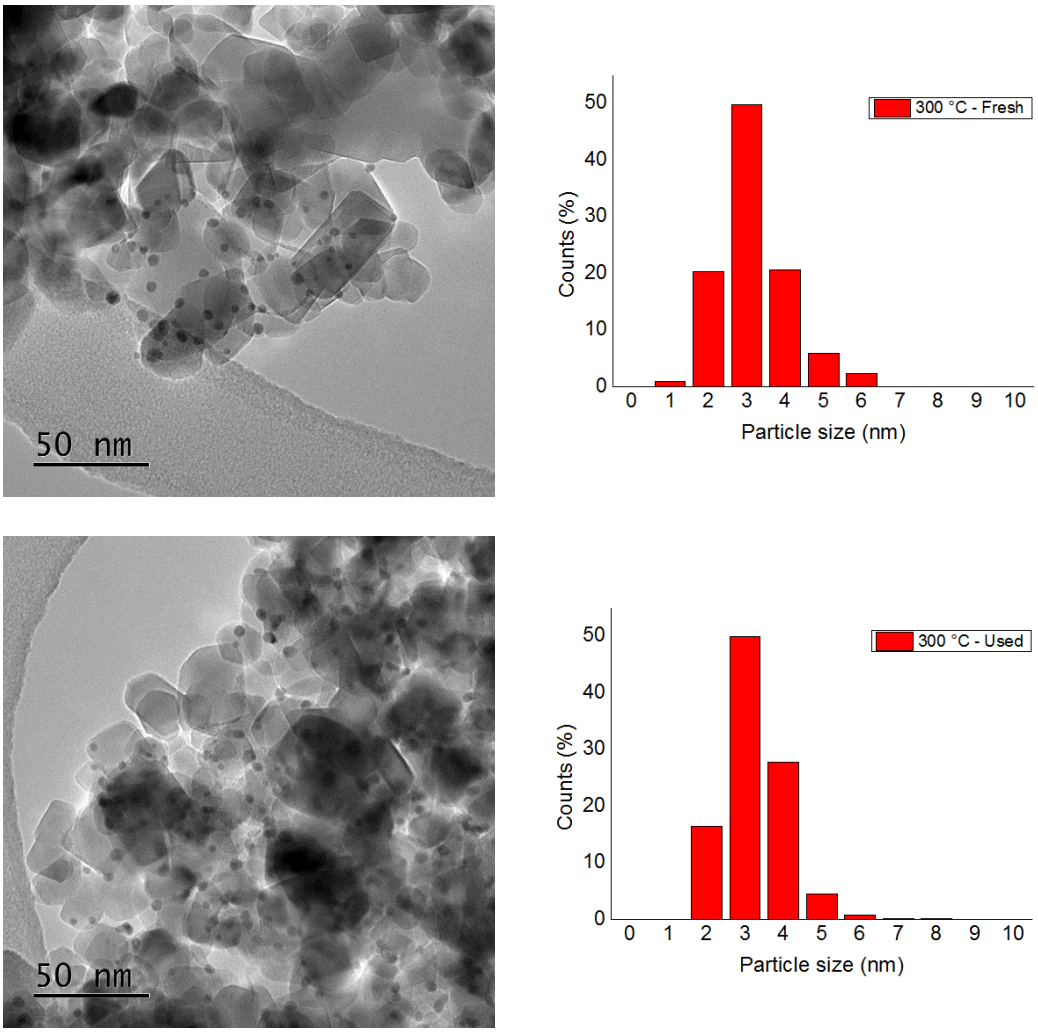

Figure 5.38: Representative Bright-field TEM micrographs and relative particle size distribution of the fresh and used AuPd/TiO_2 catalyst treated at 300 °C.

5.4. Conclusions

In this chapter, the selective catalytic hydrogenation of cinnamaldehyde has been investigated using supported AuPd nanoparticles prepared via sol immobilisation method. All the catalysts prepared were characterised with several techniques including TEM, XRD, XPS, CO-DRIFT and Pyridine-DRIFT. Systematic studies have been carried out to optimise catalyst properties and reaction conditions in respect to the selective hydrogenation of the carbonyl or the vinyl group of the substrate.

First of all, the conditions to work in the kinetic regime were identified. Mass transfer resistance of H_2 from the gas to liquid phase and transport of substrate from the liquid phase to the catalyst surface can strongly alter the kinetics of the reaction and mislead in the

interpretation of the results. To obtain reliable quantitative kinetics is then necessary to ensure the absence of any transport limitation. In particular, stirring speed and substrate to metal ratios were considered. The results highlighted the presence of mass transfer limitations only at stirring speed lower than ca. 550 rpm, while no diffusion limitations were identified in the range of substrate to metal ratio studied (from 800 to 6,000 mol/mol).

The influence of hydrogen pressure and reaction temperature was then analysed. A first order reaction was obtained in respect to the hydrogen partial pressure in the range 1 to 3 bar, while a linear increase in activity was observed when the temperature was varied between 40 and 100 °C. In both cases, changes in the catalytic activity did not occur with changes in the selectivity to specific products. The apparent activation energy was calculated from Arrhenius plot, obtaining a value of 24 kJ mol^{-1}.

Several catalysts with different Au/Pd molar ratios were prepared (Au, $Au_{95}Pd_5$, $Au_{65}Pd_{35}$, $Au_{50}Pd_{50}$, $Au_{35}Pd_{65}$, and Pd) and activity and selectivity towards the hydrogenation of the C=O or the C=C group were studied. The monometallic Au and the $Au_{95}Pd_5$ catalysts were found to be completely inactive for this reaction, proving that a minimum amount of Pd is required to initiate the reaction. Increasing the Pd content, the activity reached a maximum at a composition of 50 % Au and 50 % Pd, with the activity vs. composition plot showing a volcano-like behaviour. The reason for this enhanced activity due to the alloying was explained by a combination of electron transfer from the electron-rich Au atoms to the Pd and geometrical effect that enhanced substrate adsorption. In terms of selectivity, the hydrogenation of the C=C bond was favoured at high concentrations of Pd. This was again explained by a stronger η^4 adsorption of the CAL on the metal surface, that favours the hydrogenation of the thermodynamically favourable C=C bond.

The solvent effect was evaluated comparing toluene with ethanol and iso-propanol. The hydrogen solubility in the different solvents affected the hydrogenation activity. Moreover, it was hypothesised that alcoholic solvents open the doors for a new reaction pathway. The presence of ethers, formed by the interaction of CAL and HCAL with the solvent, was in fact detected and the increased production of PPR was attributed to the consequent hydrogenolysis of these ethers on the active Pd sites.

Different supports were then used in the CAL hydrogenation reaction. The presence of small metal nanoparticles was the main reason of higher activity of the TiO_2 and AC supports. In addition, the presence of Lewis acid sites on TiO_2 further increases the activity through a stronger adsorption of the electron rich aromatic ring and vinyl group. In addition to the

presence of bigger nanoparticles, the low catalytic activity of $Mg(OH)_2$ and α-Fe_2O_3 was explained by the presence of OH surface groups in the former and by the strong electron withdrawing behaviour of the latter. Finally, AC showed considerable amount of hydrogenolysis product.

The reusability of the very active $Au_{50}Pd_{50}/TiO_2$ catalyst was evaluated reusing the catalyst four times. The conversion dropped from 73 % to 45 % due to Pd leaching and nanoparticles sintering. Presence of adsorbed substrate/products were also detected on the used catalyst, even though it was hypothesised that the adsorption was reversible in reaction conditions.

Finally, in order to improve the catalyst reusability, the $Au_{50}Pd_{50}/TiO_2$ catalyst was exposed to heat treatments in an oxidant atmosphere first and then in a reductive atmosphere. The stability of the catalyst considerably improved after treatment at a temperature as low as 300 °C. The activity, however, decreased from 73 % to 56 %, probably due to an increase in nanoparticles dimension. Remarkable HCAL selectivity of 81 % was reached with the 300 °C treated catalyst and this result was explained with the formation of Pd surface segregation during the oxidation step, that generates a Au-rich core and Pd-rich shell structure of the nanoparticles.

5.5. References

1 P. Gallezot and D. Richard, *Selective Hydrogenation of α,β-Unsaturated Aldehydes*, 1998, vol. 40.

2 L. A. Saudan, *Acc. Chem. Res.*, 2007, **40**, 1309–1319.

3 P. Mäki-Arvela, J. Hájek, T. Salmi and D. Y. Murzin, *Appl. Catal. A Gen.*, 2005, **292**, 1–49.

4 S. Mahmoud, A. Hammoudeh, S. Gharaibeh and J. Melsheimer, *J. Mol. Catal. A Chem.*, 2002, **178**, 161–167.

5 *Ullmann's Encyclopedia of Industrial Chemistry*, 7th edn., 2014.

6 K. Shin, Preparation of acetals, US 4209643, 1978.

7 K. Konno, H. Sakagami, Y. Kawazoe and N. Yamamoto, AIDS therapeutic agents comprising polymers formed from cinnamic acid derivatives, US 5632980 A, 1997.

8 E. Bus, R. Prins and J. a. van Bokhoven, *Catal. Commun.*, 2007, **8**, 1397–1402.

9 M. B. Smith and J. March, *March's Advanced Organic Chemistry*, 2007.

10 I. Horiuti and M. Polanyi, *Trans. Faraday Soc.*, 1934, **30**, 1164–1172.

11 B. Mattson, W. Foster, J. Greimann, T. Hoette, N. Le, A. Mirich, S. Wankum, A. Cabri, C. Reichenbacher and E. Schwanke, *J. Chem. Educ.*, 2013, **90**, 613–619.

12 U. K. Singh and M. A. Vannice, *Appl. Catal. A Gen.*, 2001, **213**, 1–24.

13 S. Schimpf, J. Gaube and P. Claus, 2004, **75**, 85–123.

14 F. Delbecq and P. Sautet, *J. Catal.*, 1995, **152**, 217–236.

15 D. G. Blackmond, R. Oukaci, B. Blanc and P. Gallezot, *J. Catal.*, 1991, **131**, 401–411.

16 L. He, F.-J. Yu, X.-B. Lou, Y. Cao, H.-Y. He and K.-N. Fan, *Chem. Commun.*, 2010, **46**, 1553–1555.

17 A. Giroir-Fendler, D. Richard and P. Gallezot, *Catal. Letters*, 1990, **5**, 175–181.

18 P. Reyes, H. Rojas, G. Pecchi and J. L. G. Fierro, *J. Mol. Catal. A Chem.*, 2002, **179**, 293–299.

19 C. Mohr and P. Claus, *Sci. Prog.*, 2001, **84**, 311–334.

20 S. Nishimura, *Handbook of heterogeneous catalytic hydrogenation for organic synthesis*, 2001.

21 C. Pham-Huu, N. Keller, M. J. Ledoux, L. J. Charbonniere and R. Ziessel, *Chem. Commun.*, 2000, **170**, 1871–1872.

22 J. Zhu, Y. Jia, M. Li, M. Lu and J. Zhu, *Ind. Eng. Chem. Res.*, 2013, **52**, 1224–1233.

23 J. Qiu, H. Zhang, X. Wang, H. Han, C. Liang and C. Li, *React. Kinet. Catal. Lett.*, 2006, **88**, 269–276.

24 D. Das, K. Pal, J. Llorca, M. Dominguez, S. Colussi, A. Trovarelli and A. Gayen, *React. Kinet. Mech. Catal.*, 2017, **122**, 135–153.

25 K. R. Kahsar, S. Johnson, D. K. Schwartz and J. W. Medlin, *Top. Catal.*, 2014, **57**, 1505–1511.

26 F. Jiang, J. Cai, B. Liu, Y. Xu and X. Liu, *RSC Adv.*, 2016, **6**, 75541–75551.

27 K. Wąsikowska, P. Dmowska, N. Bączek, K. Strzelec, J. Pernak and B. Markiewicz, *Polish J. Chem. Technol.*, 2013, **15**, 28–32.

28 B.-H. Zhao, J.-G. Chen, X. Liu, Z.-W. Liu, Z. Hao, J. Xiao and Z.-T. Liu, *Ind. Eng. Chem. Res.*, 2012, **51**, 11112–11121.

29 R. I. Masel, *Principles of Adsorption and Reaction on Solid Surfaces*, 1996.

30 S. Fujiwara, N. Takanashi, R. Nishiyabu and Y. Kubo, *Green Chem.*, 2014, 3230–3236.

31 Z. Tian, X. Xiang, L. Xie and F. Li, *Ind. Eng. Chem. Res. 2013,* 2013, **52**, 288−296.

32 X. Zhang, Y. C. Guo, Z. Cheng Zhang, J. Sen Gao and C. M. Xu, *J. Catal.*, 2012, **292**, 213–226.

33 Y. Zhu, H. Qian, B. a. Drake and R. Jin, *Angew. Chemie - Int. Ed.*, 2010, **49**, 1295–1298.

34 J. Lenz, B. C. Campo, M. Alvarez and M. A. Volpe, *J. Catal.*, 2009, **267**, 50–56.

35 T. K. Hari and Z. Yaakob, *Chinese J. Chem. Eng.*, 2015, **23**, 327–336.

36 L. He, J. Ni, L. C. Wang, F. J. Yu, Y. Cao, H. Y. He and K. N. Fan, *Chem. - A Eur. J.*, 2009, **15**, 11833–11836.

37 H. Shi, N. Xu, D. Zhao and B.-Q. Xu, *Catal. Commun.*, 2008, **9**, 1949–1954.

38 C. Milone, C. Crisafulli, R. Ingoglia, L. Schipilliti and S. Galvagno, *Catal. Today*, 2007, **122**, 341–351.

39 C. Milone, M. C. Trapani and S. Galvagno, *Appl. Catal. A Gen.*, 2008, **337**, 163–167.

40 P. Dash, N. A. Dehm and R. W. J. Scott, *J. Mol. Catal. A Chem.*, 2008, **286**, 114–119.

41 T. Szumełda, A. Drelinkiewicz, R. Kosydar and J. Gurgul, *Appl. Catal. A Gen.*, 2014, **487**, 1–15.

42 V. I. Pârvulescu, V. Pârvulescu, U. Endruschat, G. Filoti, F. E. Wagner, C. Kübel and R. Richards, *Chem. - A Eur. J.*, 2006, **12**, 2343–2357.

43 X. Yang, D. Chen, S. Liao, H. Song, Y. Li, Z. Fu and Y. Su, *J. Catal.*, 2012, **291**, 36–43.

44 H. Gu, X. Xu, A. A. Chen, P. Ao and X. Yan, *Catal. Commun.*, 2013, **41**, 65–69.

45 J. Feng, C. Ma, P. J. Miedziak, J. K. Edwards, G. L. Brett, D. Li, Y. Du, D. J. Morgan and G. J. Hutchings, *Dalt. Trans.*, 2013, **42**, 14498–14508.

46 G. Zhan, Y. Hong, V. T. Mbah, J. Huang, A. R. Ibrahim, M. Du and Q. Li, *Appl. Catal. A Gen.*, 2012, **439**–**440**, 179–186.

47 D. Jin, X. Gu, X. Yu, G. Ding, H. Zhu and K. Yao, *Mater. Chem. Phys.*, 2008, **112**, 962–

965.

48 N. Dimitratos, J. A. Lopez-Sanchez, J. M. Anthonykutty, G. Brett, A. F. Carley, R. C. Tiruvalam, A. A. Herzing, C. J. Kiely, D. W. Knight and G. J. Hutchings, *Phys. Chem. Chem. Phys.*, 2009, **11**, 4952–4961.

49 Y. Lee and Y. Jeon, *J. Korean Phys. Soc.*, 2000, **37**, 451–455.

50 J. Pritchard, L. Kesavan, M. Piccinini, Q. He, R. Tiruvalam, N. Dimitratos, J. A. Lopez-Sanchez, A. F. Carley, J. K. Edwards, C. J. Kiely and G. J. Hutchings, *Langmuir*, 2010, **26**, 16568–16577.

51 M. Manzoli, A. Chiorino and F. Boccuzzi, *Surf. Sci.*, 2003, **532**–**535**, 377–382.

52 D. A. Panayotov, S. P. Burrows, J. T. Yates and J. R. Morris, *J. Phys. Chem. C*, 2011, **115**, 22400–22408.

53 M. Compagnoni, S. A. Kondrat, C. E. Chan-Thaw, D. J. Morgan, D. Wang, L. Prati, A. Villa, N. Dimitratos and I. Rossetti, *ChemCatChem*, 2016, **8**, 2136–2145.

54 K. Chakarova, M. Mihaylov, S. Ivanova, M. A. Centeno and K. Hadjiivanov, *J. Phys. Chem. C*, 2011, **115**, 21273–21282.

55 M. Mihaylov, H. Knözinger, K. Hadjiivanov and B. C. Gates, *Chemie-Ingenieur-Technik*, 2007, **79**, 795–806.

56 T. Lear, R. Marshall, J. A. Lopez-Sanchez, S. D. Jackson, T. M. Klapötke, M. Bäumer, G. Rupprechter, H. J. Freund and D. Lennon, *J. Chem. Phys.*, 2005, **123**, 174706, 1–13.

57 H. Zhu, Z. Qin, W. Shan, W. Shen and J. Wang, *J. Catal.*, 2004, **225**, 267–277.

58 S. M. Rogers, C. R. A. Catlow, C. E. Chan-Thaw, A. Chutia, N. Jian, R. E. Palmer, M. Perdjon, A. Thetford, N. Dimitratos, A. Villa and P. P. Wells, *ACS Catal.*, 2017, **7**, 2266–2274.

59 A. Villa, N. Dimitratos, C. E. Chan-Thaw, C. Hammond, G. M. Veith, D. Wang, M. Manzoli, L. Prati and G. J. Hutchings, *Chem. Soc. Rev.*, 2016, **45**, 4953–4994.

60 J. H. Carter, S. Althahban, E. Nowicka, S. J. Freakley, D. J. Morgan, P. M. Shah, S. Golunski, C. J. Kiely and G. J. Hutchings, *ACS Catal.*, 2016, **6**, 6623–6633.

61 F. Khairallah and A. Glisenti, *J. Mol. Catal. A Chem.*, 2007, **274**, 137–147.

62 X. Wang, S. Kim, C. Buda, M. Neurock, O. B. Koper and J. T. Yates, *J. Phys. Chem. C*, 2009, **113**, 2228–2234.

63 I. X. Green, C. Buda, Z. Zhang, M. Neurock and J. T. Yates, *J. Phys. Chem. C*, 2010, **114**, 16649–16659.

64 M. I. Zaki, M. a. Hasan, F. a. Al-Sagheer and L. Pasupulety, *Colloids Surfaces A Physicochem. Eng. Asp.*, 2001, **190**, 261–274.

65 V. V. Kumar, G. Naresh, M. Sudhakar, J. Tardio, S. K. Bhargava and A. Venugopal, *Appl.*

Catal. A Gen., 2015, **505**, 217–223.

66 G. a. M. Hussein, N. Sheppard, M. I. Zaki and R. B. Fahim, *J. Chem. Soc. Faraday Trans.*, 1989, **85**, 1723–1741.

67 K. J. A. Raj, M. G. Prakash, R. Shanmugam, K. R. Krishnamurthy and B. Viswanathan, *Indian J. Chem.*, 2011, **50**, 1050–1055.

68 H. Li, X. Chen, M. Wang and Y. Xu, *Appl. Catal. A Gen.*, 2002, **225**, 117–130.

69 K. Q. Sun, Y. C. Hong, G. R. Zhang and B. Q. Xu, *ACS Catal.*, 2011, **1**, 1336–1346.

70 W. O. Oduro, N. Cailuo, K. M. K. Yu, H. Yang and S. C. Tsang, *Phys. Chem. Chem. Phys.*, 2011, **13**, 2590–602.

71 L. J. Durndell, C. M. a. Parlett, N. S. Hondow, M. a. Isaacs, K. Wilson and A. F. Lee, *Sci. Rep.*, 2015, **5**, 9425, 1–9.

72 R. Liu, Y. Yu, K. Yoshida, G. Li, H. Jiang, M. Zhang, F. Zhao, S. ichiro Fujita and M. Arai, *J. Catal.*, 2010, **269**, 191–200.

73 D. I. Enache, J. K. Edwards, P. Landon, B. Solsona-Espriu, A. F. Carley, A. A. Herzing, M. Watanabe, C. J. Kiely, D. W. Knight and G. J. Hutchings, *Science*, 2006, **311**, 362–365.

74 D. Richard, J. Ockelford, A. Giroir-Fendler and P. Gallezot, *Catal. Letters*, 1989, **3**, 53–58.

75 A. Coupar and D. Eley, *Discuss. Faraday Soc.*, 1950, **8**, 172–184.

76 A. Maeland and T. B. Flanagan, *Can. J. Phys*, 1964, **42**, 2364–2366.

77 U. K. Singh and M. A. Vannice, *AIChE J.*, 2004, **45**, 1059–1071.

78 C. L. Young, *IUPAC Solubility data series*, 1981, vol. 5/6.

79 X. Zhang, H. Shi and B.-Q. Xu, *J. Catal.*, 2011, **279**, 75–87.

80 S. Nishimura, N. Ikeda and K. Ebitani, *Catal. Today*, 2014, **232**, 89–98.

81 M.-M. Wang, L. He, Y.-M. Liu, Y. Cao, H.-Y. He and K.-N. Fan, *Green Chem.*, 2011, **13**, 602–607.

82 Y. Li, Y. Fan, H. Yang, B. Xu, L. Feng, M. Yang and Y. Chen, *Chem. Phys. Lett.*, 2003, **372**, 160–165.

83 M. A. Vannice and B. Sen, *J. Catal.*, 1989, **115**, 65–78.

84 J. K. Edwards, A. F. Carley, A. A. Herzing, C. J. Kiely and G. J. Hutchings, *Faraday Discuss.*, 2008, **138**, 225–239.

85 L. Hilaire, P. Légaré, Y. Holl and G. Maire, *Surf. Sci.*, 1981, **103**, 125–140.

86 R. Sharpe, J. Counsell and M. Bowker, *Surf. Sci.*, 2017, **656**, 60–65.

Chapter 6

Conclusions and Future Work

As already discussed in the Introduction Chapter (Chapter 1), more than 70 % of chemical processes make use of heterogeneous catalysts. Therefore, the cost of production and regeneration of catalysts has a big impact on the overall cost of the final products. Among all the heterogeneous catalysts, in the last few decades supported metal nanoparticles have attracted much attention, and the study and optimisation of such catalysts is a very hot topic from both an academic and industrial point of view. Normally, supported metal nanoparticles are prepared by wet chemical methods, such as deposition-precipitation, impregnation or sol-immobilisation. This last technique, in particular, offers great control over nanoparticles size, size distribution and shape, since the metal nanoparticles are pre-formed in solution. However, sol-immobilisation synthesis are typically performed in conventional batch reactors, where inefficient mechanical mixing causes local concentration gradients of the reactants and therefore polydisperisty in nanoparticle size and shape and poor batch-to-batch reproducibility. In order to improve the reactant mixing and therefore achieve microscopic control over the reaction conditions, micro- and milli-fluidic reactors have been recently employed.

In Chapter 3, a milli-fluidic reactor was set up for the synthesis of metallic colloids in a continuous setup. The apparatus allowed precise control over the particle size simply by changing various operational parameters such as reaction conditions, residence time and mixing. Au nanoparticles of 5.4 ± 0.9 nm were produced and immobilised onto titanium dioxide (semi-continuous procedure). The setup was then further upgraded by integrating a stream of support suspended in water to the colloidal stream, so that the whole catalyst was produced in a continuous setup (continuous procedure). Smaller Au nanoparticles were observed when the support was added in continuous (4.5 ± 1.3 nm) compared to both semi-continuous (5.4 ± 0.9 nm) and batch (5.6 ± 1.6 nm) catalysts. This effect was attributed to the absence of mechanical stirring and to the immediate removal of the remaining $NaBH_4$ in solution which can interfere with the PVA thus reducing the stabilising effect of the polymer.

The optimised continuous procedure was then adapted for the production of bimetallic AuPd nanoparticles with random alloy composition and supported on TiO_2. STEM-EDX analysis revealed the absence of a size-dependent alloy composition in the size range of

nanoparticles produced typically observed in AuPd catalysts synthesised with a batch procedure. The reason for this difference was explained by the very fast deposition of the nanoparticles that inhibits Oswald ripening process responsible for metal rearrangements over time.

Finally, the mono- and bi-metallic catalysts prepared with the continuous procedure showed higher catalytic activity compared to that of the corresponding batch produced materials. The smaller mean nanoparticle size and the uniform alloy composition were responsible for the greater activity of the Au/TiO_2 and $AuPd/TiO_2$ catalysts respectively.

This work represents a starting point for the efficient production of supported metal nanoparticles with highly reproducible structural and compositional characteristics. The optimised continuous setup, in fact, could be used with many other metals (i.e. Pd, Pt, Ag) and supports (i.e. metal oxides, carbonaceous materials) in order to produce a wide range of supported metal nanoparticles. In addition, different bimetallic structures could be synthesised as well; for example, a synthetic approach for the production of core-shell Au@Pd nanoparticles is currently being optimised. Finally, this technique can be also highly appealing from an industrial point of view, especially due to the ease of scale-up (catalyst productivity up to 3.6 g h^{-1} per reactor) and the relative low cost compared to other continuous flow techniques.

The monometallic Au catalysts synthesised during the optimisation of the semi-continuous setup in Chapter 3 possessed a wide range of mean particle size (from 4 nm up to ca. 30 nm) and for this reason they were used to study of relation between metal particle size and catalytic activity in the 4-nitrophenol (4-NPH) reduction reaction (Chapter 4). As already discussed, this model reaction is very sensitive to metal particle size changes and the catalytic activity has been previously attributed to surface metal atoms. However, from the study carried on in Chapter 4, an exponential trend was observed between the rate constant of the reaction (k_{NPH}) and the total metal surface area, demonstrating that not all the Au surface atoms were involved in the conversion of 4-NPH.

Through the use of a mathematical model where supported Au nanoparticles were approximated to perfect hemi-icosahedrons, the number of Au atoms in vertex, edge, periphery and face positions were calculated. Also in this case, however, an exponential correlation was observed between k_{NPH} and the specific Au sites. Therefore, the exact identification of the active site was not possible and further studies need to be performed in

this direction in order to unravel the active sites involved in the hydrogenation of 4-nitrophenol to 4-aminophenol.

Finally, in Chapter 5 the selective catalytic hydrogenation of cinnamaldehyde was investigated using supported AuPd catalysts. A first systematic study was carried out in order to optimise both catalyst properties and reaction conditions in respect to the selective hydrogenation of the vinyl or the carbonyl group of the substrate. Parameters such as stirring speed and substrate to metal ratio were considered in order to ensure the absence of any transport limitation. Moreover, reaction temperature and hydrogen pressure were evaluated and a first order reaction was obtained in respect to the hydrogen partial pressure in the studied range (1 to 3 bar), while a linear increase in activity was observed when the temperature was varied between 40 and 100 °C. A new reaction pathway was observed when alcoholic solvents were used. This led to the formation of ethers and consequently to phenylpropane by hydrogenolysis mechanism. In addition, a wide range of supports with different properties were employed and differences in activity and selectivity were correlated to the presence or absence of Lewis acid sites and particle-support electron transfer.

The importance of the ligand and ensemble effect was demonstrated by tuning the Au/Pd molar ratio of the bimetallic catalysts; in particular, a maximum in activity was observed for a composition of 50 % Au and 50 % Pd. On the other hand, the hydrogenation of the C=C bond was favoured at high concentrations of Pd due to the strong η^4 adsorption of the substrate on the Pd surface. Deactivation phenomena were observed on the catalyst and were attributed to Pd leaching and particle sintering. However, good catalyst stability was reached treating the catalyst at high temperature (300 °C) and in a reductive atmosphere. In addition, after the heat treatment, an increase in selectivity towards the hydrogenation of the vinyl bond was observed and this was attributed to the formation of Pd surface segregation during the oxidation step. This hypothesis, however, still requires validation by specific characterisation techniques, such as single-particle STEM-EDX. Moreover, the synthesis and application of well-defined Au@Pd core-shell catalysts could further enhance the catalyst performance towards the selective hydrogenation of the vinyl bond.